The development of turbulent slender open-core annular jets

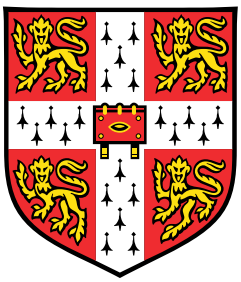

Shahid Anwar Padhani

Department of Engineering
University of Cambridge

This dissertation is submitted for the degree of
Doctor of Philosophy

Wolfson College

August 2018

Declaration

I hereby declare that except where specific reference is made to the work of others, the contents of this dissertation are original and have not been submitted in whole or in part for consideration for any other degree or qualification in this, or any other university. This dissertation is my own work and contains nothing which is the outcome of work done in collaboration with others, except as specified in the text and acknowledged below. This dissertation contains fewer than 65,000 words including appendices, bibliography, footnotes, tables and equations and has fewer than 150 figures.

Shahid Anwar Padhani
August 2018

Acknowledgements

I am extremely thankful to my supervisor Professor Gary R. Hunt for his advice, constructive criticism, patience, encouragement and friendship. His unending support was instrumental in the completion of this thesis and my development in both an academic and personal sense.

I would like to thank Dr Timothy N. Jukes for his guidance into the world of Particle Image Velocimetry, Thomas Blower for his technical input on nozzle design, Jimmy Livrat, Frederic Nicolas and Dr Ludovic Desvard for providing many interesting discussions on the subject of slender annular jets. In addition, I would like to show my gratitude to the aforementioned, and Dyson Technology Ltd, for allowing me the use of their experimental facilities and for their hospitality during my visits.

I would also like to thank my colleagues and friends in the Environmental and Industrial Fluid Mechanics Research Group and Fluid Dynamics Office for the many valuable discussions, technical support, motivation and friendship.

For the financial support, I would like to acknowledge Dyson Technology Ltd and the EPRSC Industrial Case Award programme.

Without the loving support of and the curiosity instilled in me by my Mum and Dad, it is likely that my life would be very different and for this, I am eternally grateful. I would also like to thank my sisters, Aliya and Sabiha, for their support, baking, fashion advice and the continual reminders that I would be richer had I gone into finance. Finally, I would like to thank my friends who were a continual source of laughter and who have made my years in Cambridge some of my best (so far). Special mention goes to Michael Friedman, Samuel Willis, Joachim Dias, Mila Araoz, Halan Hawizy, Georgios Drakakis, Alexandra Ross, Ram Loganathan, Antoine Debugne, Francesco Ciriello, Raghu Kesavan, Alain Kilajian, Anne Sauviat, Lucie Tavernier, Karlos Brown, Kirsten Barnes, Anthony Matthews, Sarah Coombes, Jamee Elder, Athiban Selvakadanko, Ashik Amlani and Asad Zaidi.

Abstract

The very first study of the development of the turbulent isothermal and incompressible air jet which issues at a constant velocity from a slender annular slot, circumnavigating an open core, into an otherwise quiescent and unbounded environment of the same density, is presented. The geometry of this source is defined by three diameters: the outer diameter of the slot D_o; the inner diameter of the slot D_i; and the diameter of the (circular) open core D_v. 'Slender' refers to a slot for which the inner and outer diameters are approximately equal, i.e. $D_i/D_o \approx 1$. Our focus lies in understanding the development of the time-averaged flow with distance downstream and the influence of the source geometry on the development of the jet.

Given the absence of information on jets issuing from the sources of interest, the investigation follows an approach reminiscent of the classic investigations into round jets. That is, it begins with the development of a nozzle and experimental set-up which are suitable for studying the slender open-core annular jet. In addition to the experimental measurements, a complementary mathematical model was developed to describe the unique near-field behaviour of the open-core jet. Measurements were acquired using flow visualisation and Particle Image Velocimetry. On examining the streamwise development of the flow, the slender almost fully open-core jet was delineated into four key regions and the characteristic scalings identified. The regions were as follows: a bounded induced-flow region; a near-source planar-jet region; a transitional region; and a far-field round-jet region. Fluid induced through the open core of the nozzle and subsequently entrained into the jet significantly enhanced the near-field dilution of the jet.

Following on from this, the influence of the diameter ratio D_i/D_o and ventilation ratio D_v/D_i on jet coalescence was examined. Over the range of diameter ratios examined ($0.845 \leq D_i/D_o \leq 0.981$), experimental measurements and the predictions from mathematical modelling indicated that D_i/D_o significantly influenced the volume flux induced through the core while the coalescing behaviour of the jet and the far-field region remained largely unchanged. Over the range of ventilation ratios examined ($0 \leq D_v/D_i \leq 0.90$), experimental measurements demonstrated that D_v/D_i controlled the restriction experienced by fluid induced through the open core and significantly influenced the far-field behaviour of the jet. Our findings suggest that jet of interest is then uniquely characterised by the momentum flux M_0, the diameter ratio D_i/D_o, and the ventilation ratio D_v/D_i.

Table of contents

Nomenclature

Symbol	Dimensions	Quantity
Θ		Temperature
L		Length
M		Mass
T		Time
$\hat{A}_a$	-	Ratio of the area of the core and the slot area, $= A_a/A_0$
A_0	L^2	Area of the source. For the annular slot $A_0 = \pi(D_o^2 - D_i^2)/4$
A_a	L^2	Total area of the core of the annulus, $= \pi(D_i/2)^2$
A_v	L^2	Area of the open core of the annulus, $= \pi(D_v/2)^2$
b	L	Jet width
B_0	L^4T^{-3}	Source buoyancy flux
b_i	L	Radial location of the inner shear layer
b_o	L	Radial location of the outer shear layer
$b_{\zeta i}$	L	Perpendicular distance between the high-velocity centreline and the edge of the inner shear layer
$b_{\zeta o}$	L	Perpendicular distance between the high-velocity centreline and the edge of the outer shear layer
c	LT^{-1}	Speed of sound in air, taken to be 343.4 m s^{-1} (Haynes, 2012)
c_1	-	Constant specifying the spreading rate of the round-jet width b

Symbol	Dimensions	Quantity
c_2	-	Constant specifying the decay of the round-jet axial velocity $\bar{u}_c$
C_D	-	Drag coefficient
D	L	Diameter of circular orifice from which a round jet issues
d_1	-	Constant specifying the spreading rate of the planar-jet width
d_2	-	Constant specifying the decay of the planar-jet centreline velocity
D_c	L	Mean diameter of the annular slot, $= (D_o + D_i)/2$
D_i	L	Inner diameter of the annular slot
D_o	L	Outer diameter of the annular slot
D_v	L	Diameter of the open core
e	-	Logarithmic constant, $\ln(e) = 1$
F_I	MLT^{-2}	Inertial force which projects the jet downstream
F_P	MLT^{-2}	Pressure force which causes the jet to curve inwards and ultimately to coalesce
g	LT^{-2}	Acceleration due to gravity
h	L	Width of the nozzle cavity
$I_{\zeta u}$	-	Turbulent intensity tangential to the high-velocity centreline
$I_{\zeta v}$	-	Turbulent intensity perpendicular to the high-velocity centreline
$I_{u,max}$	-	Maximum axial turbulent intensity
I_u	-	Axial turbulent intensity
I_v	-	Radial turbulent intensity
ISL	L^2	Surface area of the inner shear layer
L	L	Length of the nozzle along the x-axis
l	L	Slot width, $= (D_o - D_i)/2$
L_1	L	Internal diameter of the nozzle
L_2	L	External diameter of the nozzle
L_j	L	Jet length
M	$\mathrm{L}^4\mathrm{T}^{-2}$	Estimates of the momentum integral of the jet calculated using planar PIV measurements in the $x-y$ plane
M_0	$\mathrm{L}^4\mathrm{T}^{-2}$	Specific momentum flux of the source
M_θ	$\mathrm{L}^4\mathrm{T}^{-2}$	Estimates of the momentum integral calculated using stereoscopic PIV measurements by rotating a 'virtual' planar PIV plane about the x-axis

Symbol	Dimensions	Quantity
M_a	L^4T^{-2}	Momentum flux of the induced flow at $x = 0$
M_D	L^4T^{-2}	Momentum integral deficit
M_m	L^4T^{-2}	Mean component of the momentum integral
M_X	L^4T^{-2}	Estimates of the momentum integral of the jet calculated using stereoscopic PIV measurements along in $r-\theta$ plane
M_{tp}	L^4T^{-2}	Contribution to the momentum integral from the turbulence and the axial pressure gradient
OSL	L^2	Surface area of the outer shear layer
P_B	$ML^{-1}T^{-2}$	Pressure acting on section **BB′** of the control volume
P_C	$ML^{-1}T^{-2}$	Pressure acting on section **CC′** of the control volume
P_∞	$ML^{-1}T^{-2}$	Ambient pressure
Q	L^3T^{-1}	Volume flux of the jet
Q_0	L^3T^{-1}	Source volume flux of the jet
Q_a	L^3T^{-1}	Volume flux induced through the open core of the annulus
$Q_e(x)$	L^3T^{-1}	Volume flux entrained into the jet
R_c	L	Radius of curvature of the high-velocity centreline
r_c	L	Radial location of the high-velocity centreline
R_i	L	Radius of curvature of the inner entrainment surface
r_i	L	Radius of the inner entrainment surface
R_r	L	Spatial resolution of the velocity vectors
R_S	L	Radius of curvature of a thin planar jet as given by Sawyer (1960)
R_t	T	Temporal resolution of the velocity vectors
r_{CV}	L	Radius of the control volume
Re_D	-	Round-jet Reynolds number based on the diameter of nozzle, $= U_0 D/\upsilon$
Re_f	-	Reynolds number based on the square root of the slot area $\sqrt{A_0}$, $= \sqrt{M_0}/\upsilon$
Re_l	-	Reynolds number based on the slot width l, $= U_0 l/\upsilon$
S	-	Dimensionless swirl number
T_∞	Θ	Temperature of the ambient fluid
u	LT^{-1}	Instantaneous axial velocity
$\bar{u}$	LT^{-1}	Time-averaged component of the instantaneous axial velocity
$\bar{u}_c$	LT^{-1}	Axial velocity $\bar{u}$ along the high-velocity centreline

Symbol	Dimensions	Quantity
$\hat{U}_a$	-	Ratio of the induced and slot velocities, $= U_a/U_0$
u'	LT^{-1}	Fluctuating component of the instantaneous axial velocity
U_0	LT^{-1}	Velocity at which the jet issues from the source
$\bar{u}_\zeta$	LT^{-1}	Time-averaged velocity tangential to the high-velocity centreline
U_a	LT^{-1}	Velocity of the fluid induced through the open core of the annulus, $= Q_a/A_v$
$\bar{u}_i$	LT^{-1}	Average of $\bar{u}$ over the $r-\theta$ section and within the bounded induced-flow region
$\bar{u}_{\zeta_c}$	LT^{-1}	Time-averaged velocity along the high-velocity centreline
v	LT^{-1}	Instantaneous radial velocity
$\bar{v}$	LT^{-1}	Time-averaged component of the instantaneous radial velocity
v'	LT^{-1}	Fluctuating component of the instantaneous radial velocity
$\bar{v}_\zeta$	LT^{-1}	Time-averaged velocity perpendicular to the high-velocity centreline
v_e	LT^{-1}	Round-jet entrainment velocity
v_{ep}	LT^{-1}	Planar-jet entrainment velocity
w	LT^{-1}	Instantaneous azimuthal velocity
$\bar{w}$	LT^{-1}	Time-averaged component of the instantaneous azimuthal velocity
w'	LT^{-1}	Fluctuating component of the instantaneous azimuthal velocity
$x,\ r,\ \theta$	L	Cylindrical coordinate system with an origin in the centre of the nozzle on the plane of slot
$x,\ y$	L	Cartesian coordinate system centred on the longitudinal nozzle axis and corresponding to $\theta = \pi/2$
x_0	L	Virtual origin correction
$x_\zeta,\ y_\zeta$	L	Coordinate system aligned with the high velocity centreline
x_C	L	Axial location of downstream end of the control volume
x_m	L	Defines the merge point, i.e. the distance from the source to the location at which the inner shear layer begins merging
x_{re}	L	Defines the reattachment point, i.e. the distance from the source to the location at which the jet reattaches

Symbol	Dimensions	Quantity
y_E	L	Radial coordinate corresponding to edge of measurement domain
y_w	L	Radial location of jet perimeter used for calculations of volume fluxes, defined such that estimates of volume flux remain continuous between measurement windows

Greek Letters

α	-	Round-jet entrainment coefficient
α_p	-	Planar-jet entrainment coefficient
β	-	Ratio of the distances at the jet merges and reattaches points, $= x_m/x_{re}$
ΔT	Θ	Temperature difference between jet and ambient fluid
δ	L	Width of planar jet at $x = x_m$
ε	-	Tolerance of theoretical model
ε_{bias}	-	Systematic bias component of the total error in the PIV measurements
ε_{RMS}	-	Root mean square component of the total error in the PIV measurements
ε_{total}	-	Total algorithm error in the PIV measurements
η	-	Angle between the optical axis of the camera and a line which is perpendicular to the laser sheet
γ	L	The excess momentum flux at section $\mathbf{CC}'$, i.e. $= M(x_C)/M_0 - 1$
λ	-	Non-dimensional shift of the stagnation point
λ_{crit}	-	Critical non-dimensional shift of the stagnation point above which symmetry breaking behaviour occurs
ν_T	$\mathrm{L}^2\mathrm{T}^{-1}$	Turbulent viscosity
$\hat{\nu_T}$	-	Normalised turbulent viscosity
$\langle\hat{\nu_T}\rangle$	-	Bulk turbulent viscosity
ρ	ML^{-3}	Density of the jet and ambient fluid
σ_i	LT^{-1}	Standard deviation of of $\bar{u}$ over the $r-\theta$ section and within the bounded induced-flow region
σ_u	LT^{-1}	Standard deviation of the axial velocity fluctuations
σ_v	LT^{-1}	Standard deviation of the radial velocity fluctuations

Symbol	Dimensions	Quantity
σ_{ζ_u}	LT^{-1}	Standard deviation of the velocity fluctuations tangential to the high-velocity centreline
σ_{ζ_v}	LT^{-1}	Standard deviation of the velocity fluctuations perpendicular to the high-velocity centreline
τ	T	Characteristic flow timescale, $\tau = b/\sigma_{uc}$
υ	L^2T^{-1}	Kinematic viscosity of the fluid, taken to be 1.5×10^{-5} m^2 s^{-1} for air at $20°C$ (Batchelor, 1967)
Υ_i	-	Uncertainty associated with quantity i
FOV		Field of view - on which planar PIV measurements in the $x-y$ plane were made
NE		Nozzle exit field of view, on which planar PIV measurements in the $x-y$ plane and adjacent to the slot were made
PIV		Particle Image Velocimetry
PTU		Programmable timing unit
SLA		Stereolithography
STFOV		Stereoscopic field of view - on which stereoscopic PIV measurements in the r-θ plane were made
h/l	-	Contraction ratio
$(D_i/D_o)_S$	-	Critical slender diameter ratio
D_i/D_o	-	Diameter ratio
D_v/D_i	-	Ventilation ratio
F_I/F_P	-	Ratio of inertial and pressure forces

CHAPTER 1

Introduction

1.1 Overview and problem outline

Fluids are integral to human life; among other things we live in and breathe air, water is essential to our survival and blood is used to transport oxygen and nutrients throughout the body. Fluid flows are often turbulent in nature, from the large-scale atmospheric eddies which are a key component of global weather systems (Dosio et al., 2005) to smaller-scale human thermal plumes (Craven & Settles, 2006) - indeed the majority of naturally occurring flows and practical man-made flows are turbulent in nature.

One such canonical turbulent flow is that of the jet, in the purest case an isothermal flow driven solely by momentum from a relatively narrow orifice into an otherwise quiescent and unbounded environment of the same density. While the case of the 'pure' jet rarely occurs in nature, natural phenomena which are primarily driven by density differences far from the source, such as plumes or fountains (List, 1982; Hunt & Burridge, 2015), often exhibit some degree of near-source jet-like behaviour. Example of flows which exhibit near-source jet-like behaviour include plumes emerging from undersea geothermal vents and during explosive volcanic eruptions (Carazzo et al., 2008). Upon considering flows that we humans have utilised to our advantage, examples of jet and jet-like flows come more readily to mind (and cross our paths more often): the flows produced by hair-dryers, leaf blowers, hand dryers; the fluid exiting an aircraft engine; and effluent discharging into the ocean. The use of jets spans a wide range of applications. These applications include combustion (Li & Tankin, 1987) where jets are used to mix fuel with the air, heat transfer (Song et al., 2000) where an impacting jet is used to cool (or heat) a surface, fluid mixing and transport (Fischer et al., 1979), to name but a few.

As a result of the many applications, a substantial degree of research has gone into understanding the turbulent jet, including investigations of jets issuing from different source

geometries (e.g. jets issuing from circular (Ball et al., 2012) and planar nozzles (Thomas & Goldschmidt, 1986)). The current work will consider an incompressible, isothermal and turbulent jet issuing into an otherwise quiescent and unbounded environment of the same density from an unexplored source geometry, namely that of the slender open-core (or *ventilated*) annular jet. A slender annular source is one for which the width of the annular slot is thin compared to the diameter of the nozzle itself. In the 'purest' case, this source geometry, depicted schematically in figure 1.1(a-b), is comprised of a slender slot from which fluid issues and which circumnavigates an open core. More generally, even when the core of the annulus is partially blocked we refer to the source as having an open core, see for example figure 1.1(c-d). As we show later (§4), a jet issuing from a source with an open core induces a flow through the open core, and this *induced flow* is subsequently entrained into the jet itself. This region of induced flow is clearly seen on the flow visualisation presented in figure 1.2. On restricting ourselves to circular central openings, three diameters can be used to describe this source geometry (see figure 1.1): these are the outer diameter of the slot D_o; the inner diameter of the slot D_i; and the diameter of the central opening D_v. Using these three diameters, it is possible to non-dimensionally describe the source geometry in terms of a diameter ratio D_i/D_o and a ventilation ratio D_v/D_i. On considering these ratios, identifying a parameter space which encompasses the physical range of source geometries becomes trivial, this parameter space spans $0 \leq D_i/D_o \leq 1$ and $0 \leq D_v/D_i \leq 1$. At the limits of $D_i/D_o = 0$ and $D_i/D_o = 1$ the flow is a round jet and an idealised slender annular jet, respectively. Similarly, at the limits of $D_v/D_i = 0$ (figure 1.1e-f) and $D_v/D_i = 1$ (figure 1.1a-b), the core is fully closed (*unventilated*) and fully open (*ventilated*), respectively.

The idealised case in which the slot is at the slender limit ($D_i/D_o = 1$) and the core fully open ($D_v/D_i = 1$) is a fundamental source geometry which may be regarded as a line source 'wrapped' around the circumference of a circle. As the details of the flow produced by this particular variation on the annular source geometry are virtually unknown (see §1.3), our initial investigation explores the flow using experimental measurements and flow visualisation. The idealised case ($D_i/D_o = 1$ and $D_v/D_i = 1$) is unphysical, and so we investigate the jet discharging from a near-idealised, almost fully open-core, slender annular slot. We are aware of two applications which utilise the slender almost fully open-core source geometry: devices intended for personalised cooling and air treatment; and a hair-dryer (Mason et al., 2010).

Subsequent to obtaining an understanding of the idealised case, we examine the influence of the two parameters which define the large-scale geometry of the source, namely, the diameter ratio D_i/D_o and the ventilation ratio D_v/D_i. We find (§5-6), using simplified theoretical models and experimental measurements, that these key parameters heavily influence the flow issuing from a ventilated annular nozzle. The influence of these parameters is most obvious in the

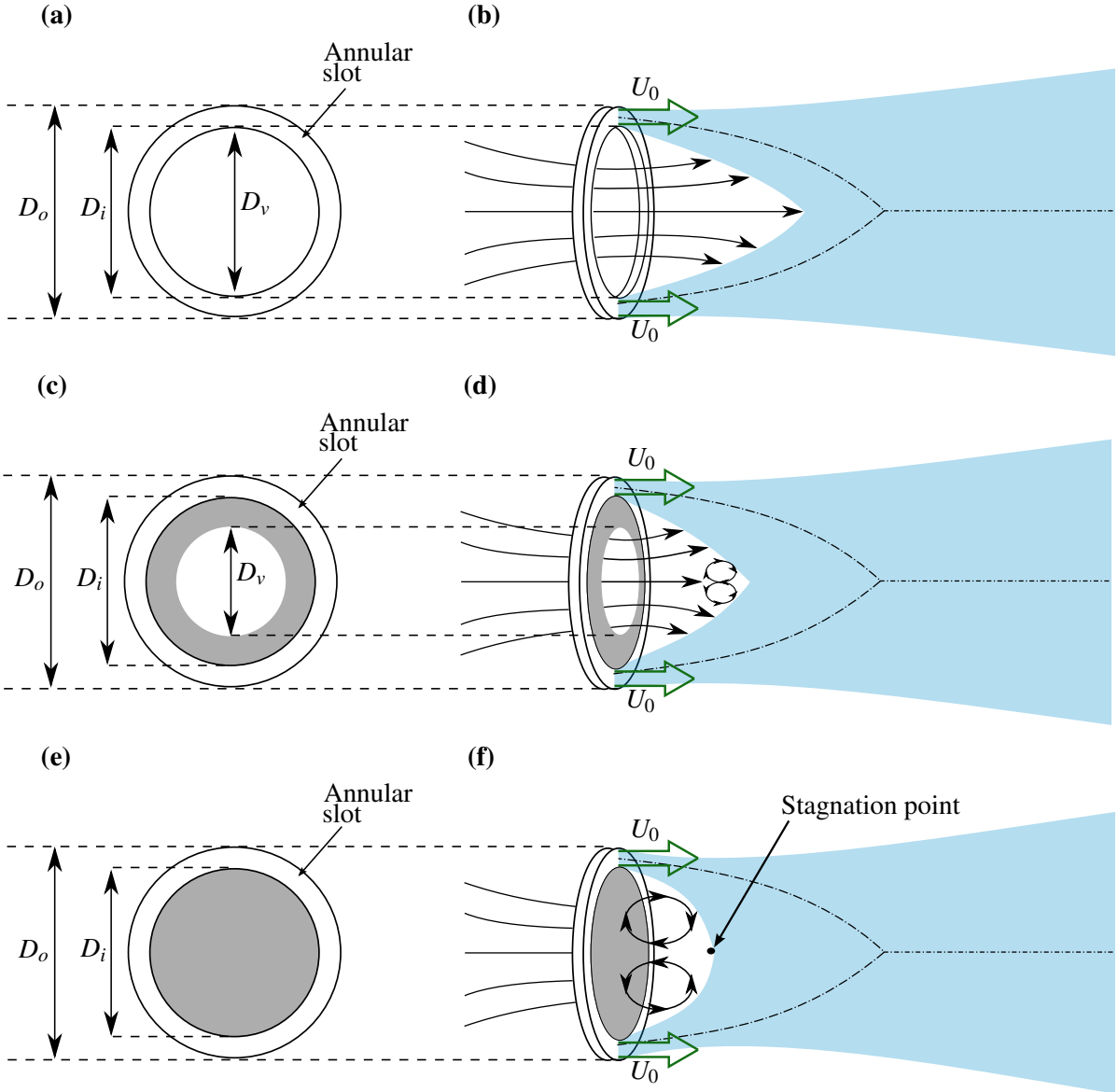

Fig. 1.1: Schematics depicting: (a-b) a fully open-core slender annular jet source ($D_v/D_i = 1$), (c-d) an open-core slender annular jet source ($0 < D_v/D_i < 1$) and (e-f) a closed-core annular jet source ($D_v/D_i = 0$). Figures (a,c,e) are shown face on to the slot, with exit slot width $l = (D_o - D_i)/2$ and with a circular central opening of diameter D_v. Figures (b,d,f) show, where appropriate, streamlines for the flow induced through the open core of the annulus, the recirculation, and a time-averaged streamwise section through the jet (shaded in blue). The region shaded in grey depicts the blocked area of the core. The steady exit velocity U_0 is perpendicular to the plane of the source as indicated. The dot-dashed lines represent the high-velocity centreline issuing from the slot.

near-field region of jet coalescence. For example, unlike for an open-core jet, a closed-core jet cannot drive an induced flow through the centre of the annulus and instead sets up a large-scale recirculation region adjacent to the source (figure 1.1e-f, §1.3). Thus, understanding the role of D_i/D_o and D_v/D_i may enable one to tailor the jet for specific purposes, e.g. if the geometry modifies the spreading rate of the jet, a device intended for personal cooling can be targeted at single or multiple users. This understanding has the potential to improve the current applications of the slender open-core annular jet, and may even reveal novel applications which have not yet been considered.

Flow visualisation (figure 1.2), carried out as part of this study, indicates that far from the nozzle the flow produced resembles that of typical round jet. This is confirmed using velocity measurements in §4. Such a round jet is shown in figure 1.3, taken from the study of Dimotakis et al. (1983). Nearer the nozzle, in the region where the jet coalesces, the flows differ significantly. This unique region of development is of particular interest and can potentially be exploited to our advantage. For example, our results in §4 suggest that the enhanced near-field dilution achieved by the ventilated annular source geometry may lend itself to wider applications, for example, those concerning pollutant discharges where rapid near-nozzle dilution of the source fluid may be desirable.

Fig. 1.2: Flow visualisation of a ventilated annular air jet issuing from an open-core slender annular source with $D_i/D_o = 0.981$, $D_v/D_i = 0.90$ and a Reynolds number based on the square-root of the slot area (defined in (1.2)) of $Re_f = 35,000$. For details of the nozzle dimensions and design see §2.1. The flow was visualised using a laser on the mid-plane of the jet with vaporised olive oil particles fed directly into the intake of the supply pump (for further information see §2.3).

Fig. 1.3: Flow visualisation of a round jet issuing from a circular source of diameter D with a Reynolds number based on D (defined in §1.4) of $Re_D = 10,000$. Reprinted from Dimotakis et al., Physics of Fluids, 26, 3185 (1983) with the permission of AIP Publishing.

1.2 Aim and objectives

1.2.1 Global aim

This investigation aims to gain a physical understanding of the turbulent jet issuing from a slender open-core annular slot into an otherwise quiescent unbounded environment, to identify the key regions and appropriate scalings for the jet, and to understand how the geometrical parameters (D_i/D_o and D_v/D_i) effect the development of the flow.

1.2.2 Objectives

A review of the literature (§1.3) reveals that the jets from the sources of interest are almost completely unstudied. Thus, this work forms the first study of its kind and follows a classic approach. This approach began with the development of an experimental nozzle which produces the flow of interest, the design of the experiments, and the validation that the flow produced is of good quality. Following this, the investigation of the fluid mechanics started in earnest. Investigations began with an in-depth experimental study on the time-averaged flow issuing from a source which is close to the idealised case. On obtaining an understanding of the idealised case, the work proceeded by investigating how the source geometry modified the flow produced. Simplified models were developed which enable the prediction of the quantities of interest. This approach and the global aim naturally led to the following objectives:

1. to design and fabricate an experimental nozzle that produces an open-core annular jet flow. We discuss the design of the nozzle in §2;

2. to design an experiment which allows for the capture of high-quality quantitative measurements of the flow issuing from the nozzle. We discuss the experimental procedure in §2;

3. to ensure, using simple diagnostics, that measurements of and the flow produced by the experimental nozzle are of good quality. We discuss the quality of our flow and measurements in §3;

4. to investigate the development of the flow produced by a near-idealised slender open-core annular source. This will allow us to obtain a physical understanding of the flow, identify the key regions and the appropriate scalings. This investigation is discussed in §4;

5. to investigate the effect of the source geometry (D_i/D_o and D_v/D_i) on the development of the flow. The aim of this investigation is to gain a physical understanding of how these

parameters influence the flow produced. The investigation into the effect of the diameter ratio D_i/D_o is presented in §5 and the investigation into the effect of the ventilation ratio D_v/D_i is presented in §6; and

6. to develop simplified models which allow us to predict how the quantities of interest vary with the geometrical parameters. For example, to predict how the near-field coalescing behaviour of the slender open-core jet changes with diameter ratio D_i/D_o. The models we have developed are presented in §5 and §6.

These objectives have been carefully chosen as they provide a solid foundation from which an understanding of slender open-core annular jets can be obtained.

1.3 Annular jets in the literature

While the literature directly pertinent to the investigation of slender open-core annular jets will be discussed in detail at the start of the relevant chapters, at this juncture the intention is to point the reader towards the key pieces of literature which have informed the current work. A summary of the specific source conditions (i.e. D_i/D_o, D_v/D_i, Re_l) and investigation type (numerical, experimental, or both) used in the literature discussed herein is given in table 1.1.

The vast majority of the scientific and engineering literature discussing annular jets focusses on the closed-core ($D_v/D_i = 0$) annular jet due to its wide use in combustion and mixing processes (Danlos et al., 2013). The main features of closed-core annular jets were captured by the experimental investigations of Chigier & Beer (1964a,b), Chan & Ko (1978) and Ko & Chan (1978, 1979). Key results included the identification of the wake-like nature of the flow (due to *wake vortices* shed from the recirculation region) and delineation of the annular jet into distinct regions. The regions identified were: a near field containing a large-scale recirculation and bounded downstream by a stagnation point (see figure 1.4); a transition region in which the jet completed coalescing (at the reattachment point, where the high-velocity centreline from the source merges); and a far-field round-jet-like region. The round-jet-like region was located by Chan & Ko (1978) using the linear growth in jet width and the inverse linear decay in streamwise velocity, this linear behaviour being typical of a classic round jet (cf. Hussein et al., 1994). A similar delineation proved useful for the current investigation into slender open-core annular jets.

Somewhat intuitively, and on comparing investigations by Chigier & Beer (1964b), Ko & Chan (1978), Kuhlman (1987), Celik & Bayazit (2011) and others, the diameter ratio was shown to be a key parameter which influenced the flow issuing from the closed-core nozzle (discussed in more detail later in this literature review) - amongst other things, controlling

Author	$\frac{D_i}{D_o}$	$\frac{D_v}{D_i}$	Re_l	Type	Focus
Celik & Bayazit (2011)	0.105-0.55	0	1-5$\times10^4$	N	Development
Ko (1980b)	0.35	0	6.0$\times10^4$	E	Wake vortices
Chan & Ko (1978)	0.45	0	(3.4, 5.7)$\times10^4$	E	Outer shear layer
Ko & Chan (1978)	0.45	0	(3.4, 5.7)$\times10^4$	E	Similarity
Ko & Chan (1979)	0.45	0	(3.4, 5.7)$\times10^4$	E	Inner regions
Del Taglia (2002)	0.54-0.99	0	2-57$\times10^3$	N&E	Symmetry breaking
Li & Tankin (1987)	0.56-0.85	0	0.1-4.3$\times10^3$	E	Reynolds number
V & V (2008)	0.65	0	7500	E	Swirl
Chigier & Beer (1964a)	0.66	0	$\sim 1.0\times10^5$	E	Flow description
Chigier & Beer (1964b)	0.66	0	1.1-5.5$\times10^4$	E	Swirl
Ko (1980a)	0.67	0	3.2$\times10^4$	E	Wake vortices
Warda et al. (1999)	0.67	0.42	2400	E	Development
Del Taglia et al. (2009)	0.71-0.94	0	50-400	N	Symmetry breaking
Kuhlman (1987)	0.75	0	2.9$\times10^4$	E	Core shape/location
Patte-Rouland et al. (2001)	0.905	0	(2.5, 7.7)$\times10^3$	E	POD
Danlos et al. (2013)	0.905	0	1.4-5.1$\times10^3$	E	Flow description
Del Taglia et al. (2004)	0.94	0	4.4$\times10^3$	N&E	Symmetry breaking
Gates & Cochran (1961)	0.99	0, 1	NA	E	Thrust augmentation

Table 1.1: Details of the annular jet nozzles used in the literature discussed in §1.3, listed in order of increasing D_i/D_o - the diameter ratios D_i/D_o, ventilation ratios D_v/D_i, and slot Reynolds numbers Re_l ($= U_0 l/\upsilon$, where l is the slot width, U_0 the source velocity and υ the kinematic viscosity of the source and ambient fluid, see (1.1)) have been extracted from the works cited. The penultimate column, entitled 'Type', indicates the nature of the study - experimental (E) and/or numerical (N). The entry V & V (2008) refers to Vanierschot & Van den Bulck (2008). The acronym POD refers to a data processing technique known as proper orthogonal decomposition.

the length of the recirculation region and the location of the reattachment point. The wake vortices, shed from the recirculation region, induced an additional train of vortices and excited the jet vortices themselves (Ko & Chan, 1979). Ko (1980a,b) showed that the diameter ratio regulated the effect of the wake vortices on the flow. This regulation occurred due to the relative axial extents (hereafter referred to as the length) of the potential core and recirculation region. The potential core refers to a region immediately downstream of the slot in which fluid has not directly interacted with the ambient and the velocities have not decayed. This region is eroded away by the shear layer that forms at the jet-ambient interface. The longer the potential core relative to the recirculation region, the more it 'shrouded' (Ko & Chan, 1979) the jet from the effect of vortex shedding. The length of the potential core scales on the slot width

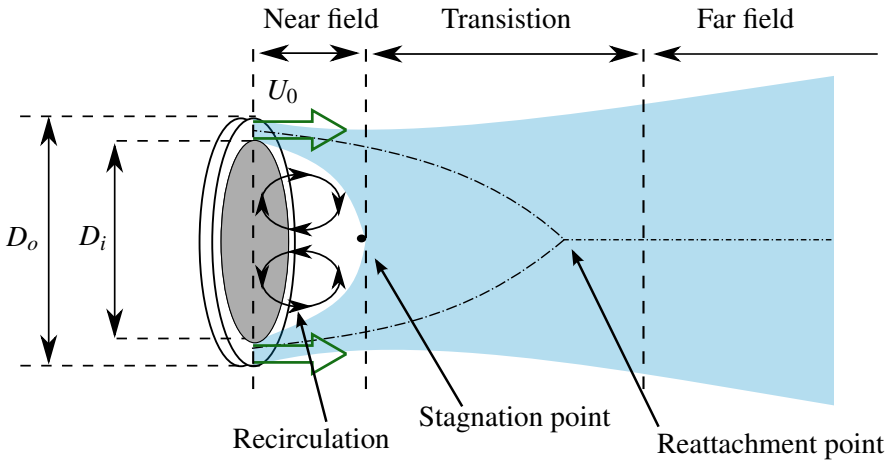

Fig. 1.4: An illustration (not to scale) of the flow issuing from a closed-core ($D_v/D_i = 0$) annular source. Indicated are the main features of the closed-core annular jets identified by Chigier & Beer (1964a,b), Chan & Ko (1978) and Ko & Chan (1978, 1979). The steady exit velocity U_0 is perpendicular to the plane of the source as indicated. The dot-dashed lines represent the high-velocity centreline issuing from the slot, and the (light) blue shaded region represent a section through the turbulent jet.

l ($= (D_o - D_i)/2$) (Thomas & Goldschmidt, 1986) and the recirculation region scales on the inner diameter of the nozzle D_i (Danlos et al., 2013). Since $2l/D_i = (D_o/D_i) - 1$, increasing D_i/D_o reduces the relative size of l/D_i. This reduction in l/D_i corresponds to a reduction in the length of the potential core relative to the recirculation region and, thus, the influence of the wake vortices on the flow increases. While the absence of a large-scale recirculation region in the fully open-core jet points to a different mechanism, we anticipate that D_i/D_o will play a significant role in the jet development. The results of Celik & Bayazit (2011) suggested that upstream of the reattachment point the influence of the diameter ratio was large, whereas downstream of this point the flow was independent of D_i/D_o. In other words, the round-jet behaviour in the far field is unaffected by the diameter ratio. Thus, modelling the far-field region of the jet becomes more straightforward.

The closed core does not necessarily need to be flat or flush with the plane of the slot exit, and Kuhlman (1987) observed in experiments that varying the shape and location of the central surface had the potential to significantly modify the growth of the jet width and decay of the centreline velocity. Kuhlman reasoned that the differences in the far-field behaviour were caused by how the different closed-core surfaces modified the wake vortices shed from the nozzle. The key result was that, despite variation due to the shape and location of the central surface, the entrainment rates of the closed-core annular jets examined always exceeded the

equivalent round jet. This work indicates that on examining the influence of the ventilation ratio D_v/D_i, the location at which we block the nozzle may influence our results. Indeed, in §6.3.1 we note that the location of the blockage significantly influences the flow.

If the momentum flux of the jet issuing from the slot has a circumferential (or azimuthal) component, the jet can be considered to have swirl. Vanierschot & Van den Bulck (2008) observed that, in closed-core jets, swirl shifts the coalescence of the jet further downstream. As the swirl was increased, they observed the formation of additional recirculating vortices, in addition to the single toroidal vortex observed in jets without swirl. When the swirl was sufficiently large, the annular jet did not coalesce. The current work focusses on non-swirling jets and thus the design of the experimental nozzle sought to minimise the circumferential component of momentum flux.

The source conditions of an annular jet are conventionally characterised by a specific momentum flux M_0 ($\propto l(D_o+D_i)U_0^2$) and a Reynolds number Re_l based on the slot width l (Chigier & Beer, 1964a; Ko & Chan, 1978)

$$Re_l = \frac{U_0 l}{\upsilon}, \tag{1.1}$$

where U_0 denotes the exit velocity and υ the kinematic viscosity of the source fluid and environment. Using source geometries with diameter ratios in the range $0.56 < D_i/D_o < 0.85$, Li & Tankin (1987) observed that the influence of the Reynolds number on the scale of the recirculation region and the jet envelope diminished for $Re_l > 800$. We might reasonably anticipate similar behaviour in open-core annular jets. As an additional note, in the near-field region, this definition of the Reynolds number is reasonable. However, further downstream, where the influence of the slot width is small (Celik & Bayazit, 2011), we suggest the use of a Reynolds number Re_f based on the source momentum flux M_0,

$$Re_f = \frac{Q_0}{\sqrt{A_0}\upsilon} = \frac{\sqrt{M_0}}{\upsilon}, \tag{1.2}$$

where Q_0 is the source volume flux and A_0 the slot area.

Comparatively few works have tackled the problem of the slender closed-core annular jet (Patte-Rouland et al., 2001; Del Taglia, 2002; Del Taglia et al., 2004, 2009; Danlos et al., 2013). This geometry is of particular interest given that it represents the closed-core limit of the slender annular jets which this thesis investigates. The majority of these works focus on a symmetry breaking behaviour, in which the vortex shedding occurred at a preferential location. This preferential vortex shedding prevents the jet from achieving statistical axisymmetry (within the extent of the measurement domain). Del Taglia (2002) was amongst the first to note symmetry

breaking behaviour in the annular jet and postulate a potential mechanism of action. Del Taglia considered the ratio of inertial and pressure forces at the stagnation point located at the downstream end of the recirculating region (see figure 1.1f). Del Taglia suggest that, if the pressure force dominates over the inertial force, a small perturbation of the jet at the source propagates downstream and causes the stagnation point to shift. If this shift is large relative to the jet width then the flow loses its symmetry. Del Taglia then formulated an equation relating the (non-dimensional) shift of the stagnation point λ to the slot Reynolds number Re_l and diameter ratio D_i/D_o,

$$\lambda = \left(1 - \frac{1}{Re_l\left(\frac{1}{D_i^2/D_o^2} - 1\right)}\right)\frac{1}{\frac{1}{D_i/D_o} - 1}, \tag{1.3}$$

and observed symmetry breaking behaviour for $\lambda > \lambda_{crit}$, where $3.18 < \lambda_{crit} < 16$. This result implies that the symmetry breaking behaviour only occurs for a range of high Reynolds number slender annular jets. While, at first, one may speculate that this behaviour could have been triggered by some large-scale defect in the nozzle, they demonstrate that this phenomenon also occurs in results from Large-Eddy Simulations. Numerical simulations allow for perfectly axisymmetric sources and in these cases the behaviour must, therefore, be triggered by extremely small numerical instabilities. Fabricating perfectly symmetrical and defect free sources is not possible, and so one would expect this symmetry breaking behaviour to occur for all experimental sources that meet the criteria. The open core of the annular sources of interest will reduce the pressure force at the stagnation point due to the connection between the region immediately downstream of the nozzle and the atmosphere. The larger the open area of the core, the larger the reduction of this pressure difference. Thus, for sufficiently large ventilation ratios D_v/D_i, the open core is expected to prevent the symmetry breaking behaviour. This prevention is confirmed on examining the symmetry of our slender, almost fully open-core, jet in §3.2.2. However, on restricting the open core to examine the influence of D_v/D_i, we may see evidence of the symmetry breaking behaviour. Indeed, in §6.3.1 we observe that, on blocking the annulus, the flow loses its symmetry - although the details are far more complex.

The subject of (partially or fully) open-core annular jets has almost been entirely neglected and, as such, there is an opportunity for a fundamental study. The study carried out by Warda et al. (1999) on a non-slender annular source ($D_i/D_o = 0.66$) investigates a source geometry that is partially ventilated ($D_v/D_i \approx 0.42$) and further restricted by a baffle as illustrated on figure 1.5. The restriction on the induced flow is considerable and, therefore, the flow resembles a closed-core annular jet in that it contains a large-scale recirculation region adjacent to the source (i.e. adjacent to and downstream of $x = 0$, see figure 1.5). They observed

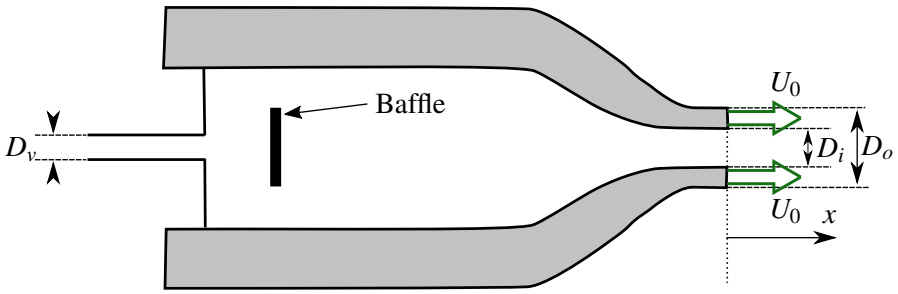

Fig. 1.5: A sketch of the experimental nozzle of Warda et al. (1999) with $D_i/D_o = 0.67$ and $D_v/D_i = 0.42$. Note the extremely restrictive nature of the ventilated opening D_v - compounded by the baffle located immediately downstream of the opening.

their jet coalescing further downstream than the closed-core jet of Chigier & Beer (1964a) ($D_i/D_o = 0.66$ and $D_v/D_i = 0$) and attribute this to the reduction of the pressure difference, due to the presence of a central opening, between the recirculation region and the ambient. The pressure difference is not entirely eliminated and drives an induced flow through the central opening. Enlarging the central opening would reduce the pressure difference and reduce the restriction experienced by the induced flow. At this stage, the relationship between the pressure difference, opening area, and induced volume flux is unknown. With regard to the volume flux induced through the opening, at the outset it was anticipated that the decreased restriction will more than offset the decreased pressure difference, and thus anticipate that increasing the area of the central opening will increase the volume flux driven through the core. If sufficiently large, this induced flow rate will notably reduce the degree to which the jet self-entrains and, thereby, reduce the size of the recirculation region.

Due to the geometrical similarities shared by annular and coaxial-jet nozzles, the latter referring to a central circular opening surrounded by an annular opening, the source conditions of interest herein may be regarded as a special case of a coaxial jet. Specifically, a coaxial jet in which the exit velocity of the outer jet is imposed (as U_0) and the 'exit' velocity of the inner jet is induced naturally as a result of entrainment into the outer jet (rather than imposed as is the norm). We anticipate that restricting the core of the open-core annular nozzle will reduce the volume flux induced through the core of the nozzle, and thus the research of Rehab et al. (1997) gives some indication of what might be expected as the restriction of the core is varied. Their work demonstrated that the size and location of the recirculation region are dependent on the balance between the volume flux through the core and the entrainment 'appetite' of the inner shear layer of the annular jet. If the volume flux supplied through the core is greater than the entrainment 'appetite' of the inner shear layer, no recirculation region exists. On reducing the flow rate through the core, at a critical volume flux equal to the entrainment appetite of

the jet, a stagnation point forms at the downstream end of the inner jet. This stagnation point serves to redirect the inner jet. Further reductions in the induced volume flux result in the formation and growth of a recirculation region (see figure 1.1b). If the volume flux through the central opening is set to zero, the coaxial jet resembles an unventilated annular jet, producing a large-scale recirculation region. For the annular jet, the volume flux through the core is not prescribed but rather controlled by the source geometry, i.e. by D_i/D_o and D_v/D_i. Thus, we anticipate that the restriction of the core (as characterised by D_v/D_i) will significantly influence the near-source behaviour of the jet.

An earlier military investigation into annular ejectors by Gates & Cochran (1961) briefly makes use of a slender open-core annular nozzle. An ejector is a device which uses a primary flow (the jet) to drive a secondary fluid (the flow of ambient fluid induced through the core). The focus of the investigation by Gates & Cochran (1961) was on the degree of thrust augmentation produced by the nozzle. Thrust augmentation (defined as a ratio of momentum fluxes) occurs because the jet expands into a self-induced region of sub-atmospheric pressure and, thus has a greater momentum flux at the exit plane of the nozzle when compared to a jet expanding into a region of ambient pressure (see Heiser, 2010). The investigation of Gates & Cochran (1961) does not examine *the jet* issuing from the slender open-core source but solely investigates thrust augmentation. They showed that, for their slender open-core annular nozzle, which was designed to maximise thrust augmentation, the degree of thrust augmentation was negligible ($< 4\%$). Therefore, we anticipate that, for our later experiments where the nozzle has not been designed to maximise this phenomenon, we may ignore the influence of thrust augmentation.

Despite the differences between the open- and closed- core annular nozzles, the existing literature on the closed-core case serves as a useful guide when considering the jet from open-core annular sources. For example, Ko & Chan (1978) established that the diameter ratio D_i/D_o controls the axial location of the reattachment point $x = x_{re}$. The reattachment point, at which the jet was regarded as having coalesced, was taken to be where the high-velocity centreline merges (figure 5.1b). Specifically, they observed that as D_i/D_o increased, x_{re}/D_o decreased. The reattachment point is likely to be a defining feature in the development of open core annular jets. Given the findings of Ko & Chan (1978), we anticipate that the diameter ratio will influence the location of the reattachment point for open-core annular jets.

The role of the diameter ratio on jet development can be better appreciated on considering the relative magnitudes of the forces that control the coalescing behaviour observed. The inertial force ($F_I \propto \rho(D_o^2 - D_i^2)U_0^2$) projects the jet downstream, U_0 denoting the source velocity of the jet and ρ the density of the jet and environment. Focussing for now on closed-core jets, the recirculation region is at a pressure below atmospheric, so that a pressure difference ΔP

pushes inwards on the jet. The area over which this pressure difference acts to cause the jet to merge is expected to scale with D_i^2; D_i being the length scale that characterises the distance between opposite sides of the inner shear layer as the jet emerges from the slot. Accordingly, the pressure force that causes the jet to curve inwards, and ultimately to coalesce, scales as $F_P \propto D_i^2 \Delta P$. With k denoting a constant of proportionality, the ratio of the inertial and pressure forces therefore scales as

$$\frac{F_I}{F_P} = k\left[\left(\frac{D_o}{D_i}\right)^2 - 1\right]\frac{\rho U_0^2}{\Delta P}, \tag{1.4}$$

(cf. Danlos et al., 2013) thereby highlighting the role of the diameter ratio on closed-core jet coalescence.

Prior to the current work, the role of the diameter ratio on open-core annular sources had not been established. Despite the absence of a large-scale recirculation region, on dimensional grounds the diameter ratio is also a key geometric parameter that influences the coalescing behaviour of these open-core annular jets. For the geometry of interest here (figure 5.1), a (steady) flow is induced through the circular open core because of the difference in pressure ΔP established by the jet between the exterior ambient and the bounded induced-flow region. In the absence of losses, straightforward application of Bernoulli's theorem along the streamline through the centre of the open core (from far upstream where the velocity is zero) yields $\Delta P = \frac{1}{2}\rho U_a^2$ and (1.4) becomes

$$\frac{F_I}{F_P} = 2k\left[\left(\frac{D_o}{D_i}\right)^2 - 1\right]\left(\frac{U_0}{U_a}\right)^2. \tag{1.5}$$

Thus, F_I/F_P and hence the coalescence of an open-core annular jet are expected to depend on the diameter ratio D_i/D_o and the velocity ratio U_0/U_a, the latter ratio is not prescribed but rather is a function of the diameter ratio ($U_0/U_a = f(D_i/D_o)$).

This brief overview of the limited literature available shows that the source geometry has a significant influence on the closed-core annular jet, particularly with regard to the near-field region of jet coalescence. In addition, it is clear that relatively little information exists on jets issuing from slender open-core annular sources (see table 1.1). In particular, there are no existing studies which investigate the jet issuing from the idealised slender fully open-core annular nozzle. Deviating from the idealised case, a significant proportion of the parameter space defined by the source geometry (D_i/D_o and D_v/D_i) remains unexplored. The exploration of the literature therefore informed the aim and objectives of the current work - first to investigate the idealised slender fully open-core annular jet and, then, to subsequently explore the influence of the source geometry. Before beginning our investigation (§2-7), classic

information and scalings from the literature on round jets are discussed to provide further insight into the behaviour of axisymmetric jets,

1.4 Orientation

While we have established (§1.3) that there is an absence of research on the slender annular jets of interest, our experimental results (§4) indicate that these jets share many characteristics with other momentum driven freely shearing flows (e.g. round jets and planar jets). Given that the annular source is axisymmetric, in this section we shall consider the literature on high Reynolds number axisymmetric jets. An examination of the axisymmetric jet literature provides a foundation from which an investigation of slender open-core annular jets can be launched. This includes identifying the governing equations (§1.4.1), the theoretical behaviour of the fully developed region (§1.4.2), the method by which the flow interacts with the surrounding environment (§1.4.3), and the time-averaged quantities in which the influence of the source geometry manifests (§1.4.4).

Before continuing further, it is necessary to develop the notation to be used when considering axisymmetric jets. The classic example of an axisymmetric jet is a round jet which issues from a circular source of diameter D. Therefore, in our consideration of axisymmetric jets, we consider a source of momentum flux M_0 and volume flux Q_0 issuing from a circular source into a quiescent environment with a uniform velocity U_0 ($= M_0/Q_0$), a schematic of which is shown in figure 1.6. For reference, the Reynolds number Re_D of round jets is typically based on the diameter D of the nozzle, i.e.

$$Re_D = \frac{U_0 D}{\upsilon}. \tag{1.6}$$

Given the circular nature of the nozzle, a cylindrical coordinate system (x, r, θ) is used to describe the flow, where the x-axis (illustrated on figure 1.6) is aligned with the longitudinal axis of the nozzle, with corresponding instantaneous velocity components (u, v, w). These instantaneous velocities can be represented by a combination of their mean (denoted by an overbar, $\bar{u}$, $\bar{v}$, $\bar{w}$) and fluctuating components (denoted by a prime, u', v', w') using a Reynolds decomposition, i.e. $u = \bar{u} + u'$, $v = \bar{v} + v'$ and $w = \bar{w} + w'$. Note that an axisymmetric jet is one in which the mean components of velocity have reached statistical axisymmetry, i.e. $\bar{u}$, $\bar{v}$, and $\bar{w}$ are independent of θ. Additionally, herein we are not concerned with swirling flows and thus $\bar{w}(x, r, \theta) = 0$.

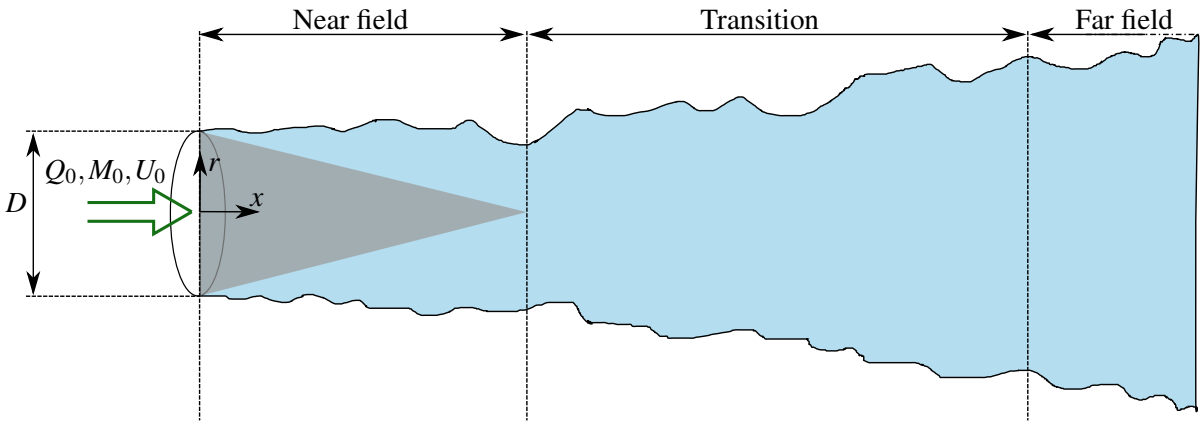

Fig. 1.6: An illustration (not to scale) of the flow issuing from a circular nozzle of diameter D depicting the three regions of the round jet. The (dark) grey shaded area represents a section (i.e. the $x-r$ plane) through the potential core and the (light) blue shaded region represents a section through the turbulent jet.

1.4.1 Governing equations

We begin by assuming that the dominant component of the time-averaged velocity is in the axial direction and, therefore, that the width of the jet, denoted as b, is small compared to the distance from its origin x, i.e. $b/x \ll 1$. This allows the use of the boundary layer equations when examining the jet (Schlichting, 1968; Davidson, 2004). Further reduction of these equations - assuming a steady, incompressible, high Reynolds number, axisymmetric, non-swirling flow issuing into an otherwise quiescent and unbounded environment - yields the axial momentum equation,

$$\bar{u}\frac{\partial \bar{u}}{\partial x} + \bar{v}\frac{\partial \bar{u}}{\partial r} = -\frac{1}{r}\frac{\partial}{\partial r} r\overline{u'v'} - \frac{\partial}{\partial x}\left(\overline{u'^2} - \frac{\overline{v'^2} + \overline{w'^2}}{2}\right), \tag{1.7}$$

and the continuity equation,

$$\frac{\partial \bar{u}}{\partial x} + \frac{1}{r}\frac{\partial r\bar{v}}{\partial r} = 0. \tag{1.8}$$

Note that in (1.7), on assuming $b/x \ll 1$, the radial momentum equation has been used to approximate the streamwise pressure gradient as $\partial P/(\rho \partial x) = \partial(\overline{v'^2} + \overline{w'^2})/(2\partial x)$ (Hussein et al., 1994). This assumption, that the jet is thin relative to its length, does not hold near the source. Thus, applying (1.7) near the source may result in inaccurate estimates of the momentum integral. Multiplying (1.8) by $\bar{u}$, combining with (1.7) and integrating across the jet

yields (to the second order)

$$2\pi\frac{d}{dx}\int_0^\infty\left(\bar{u}^2+\overline{u'^2}-\frac{\overline{v'^2}+\overline{w'^2}}{2}\right)r\,\mathrm{d}r=0, \tag{1.9}$$

or in words, the momentum integral in an axisymmetric jet does not vary with downstream distance. Thus

$$M(x)=2\pi\int_0^\infty\left(\bar{u}^2+\overline{u'^2}-\frac{\overline{v'^2}+\overline{w'^2}}{2}\right)\mathrm{d}r=M_0. \tag{1.10}$$

Given our interest in the unique near-field behaviour of the slender open-core annular jet, care must be taken on applying (1.10) near the source - in this region the jet is not thin relative to its length and therefore the treatment of $\partial P/(\rho\partial x)$ is incorrect. However, the dominant contribution to the momentum integral is from the mean momentum flux ($2\pi\int_0^\infty\bar{u}^2rdr$) (Hussein et al., 1994). Thus, on considering only first-order terms, the conclusion that momentum integral in the slender annular jet does not vary with distance downstream is valid. As discussed by Hussein et al. (1994), (1.10) is not a momentum flux because the term $(\overline{v'^2}+\overline{w'^2})/2$ represents the contribution from the streamwise pressure gradient.

1.4.2 The far field

The far field of round jets, typically for $x/D\gtrsim 30$ (Hussein et al., 1994), has undergone substantial study. In this region, the jet is fully developed and 'self-similar', where self-similarity is a property of the flow such that the radial profiles of the velocity statistics are identical when scaled appropriately. This implies that the time-averaged quantities and higher-order moments have reached a state of equilibrium and develop together.

Axial development

Far from the source, the volume flux entrained by the jet (§1.4.3) will greatly exceed the source volume flux. Given that momentum flux is conserved with distance downstream, it is then normally assumed that the jet can be treated as a point source of momentum flux (Fischer et al., 1979), such that

$$b=b(x,M_0), \tag{1.11}$$

$$\bar{u}_c=\bar{u}(x,M_0), \tag{1.12}$$

where $\bar{u}_c$ is the centreline velocity (i.e. along $r=0$). Using dimensional analysis, the following linear relationships are then obtained

$$b=c_1x, \tag{1.13}$$

$$\bar{u}_c^{-1} = c_2^{-1} M_0^{-1/2} x, \tag{1.14}$$

(Fischer et al., 1979) where c_1 and c_2 are constants that denote the spreading rate and the decay of the centreline velocity in a round jet, respectively. Given the axisymmetric nozzle geometry, far from the nozzle, we anticipate that the width and centreline velocity in a jet issuing from the slender annular source should follow (1.13) and (1.14).

An important point to note here is that experimental investigations on round jets recover a linear spreading rate and a linear velocity decay, however, the location of the point source of momentum flux does not coincide with the location of the physical nozzle. This finding led to the concept of a virtual origin $x = x_0$ (Kuethe, 1933). The virtual origin represents the location of the hypothetical point source of momentum flux, and is located by determining where linear fits to the jet width b and inverse centreline velocity $\bar{u}_c^{-1}$ intersect the x-axis. For a real jet, which is not a point source of momentum flux, (1.13) and (1.14) then become

$$b = c_1 (x - x_0), \tag{1.15}$$

$$\bar{u}_c = c_2 M_0^{1/2} (x - x_0)^{-1}. \tag{1.16}$$

A natural question that arises from these scalings concerns the values of the constants c_1, c_2 and the virtual origin x_0. Furthermore, one may wonder whether these constants are universal for all high Reynolds number incompressible axisymmetric jets, or whether there is a dependence on the source conditions and source geometry. This is a particularly pertinent question as the annular nozzle geometry considered within this thesis differs significantly from the circular geometry from which a round jet issues. Given (1.15) and (1.16), any far-field differences between the jet widths and centreline velocities of round and annular jets must manifest within c_1, c_2 and x_0. In considering the influence of the source on the far field of the jet, the literature has explored the nature of self-similarity.

Self-similarity

Observations of self-similar behaviour in the far field have been used by researchers (e.g. Schlichting, 1968; Tennekes & Lumley, 1972) to describe the radial profiles of time-averaged velocity and Reynolds stress $\overline{u'v'}$ in terms of a velocity scale (taken to be $\bar{u}_c$) and a non-dimensional radial coordinate,

$$\bar{u}(x,r) = \bar{u}_c G(\chi), \tag{1.17}$$

$$\overline{u'v'}(x,r) = \bar{u}_c^2 H(\chi), \tag{1.18}$$

where G and H represent shape functions and

$$\chi = r/b(x). \tag{1.19}$$

The continuity equation (1.8) can be solved to yield an expression for the radial velocity

$$\bar{v} = -\frac{1}{r}\int_0^r \frac{\partial \bar{u}}{\partial x} r \, \mathrm{d}r. \tag{1.20}$$

Substituting for (1.20) into (1.7) to eliminate $\bar{v}$, neglecting the second-order terms, and substituting for the derivatives of (1.17) and (1.18) gives

$$\frac{b}{\bar{u}_c}\frac{d\bar{u}_c}{dx}G^2 - \left[\frac{b}{\bar{u}_c}\frac{d\bar{u}_c}{dx} + 2\frac{db}{dx}\right]\frac{G'}{\chi}\int_0^\chi G\chi \, \mathrm{d}\chi = \frac{(\chi H)'}{\chi}, \tag{1.21}$$

where the prime $'$ represents the derivative with respect to χ. Combining the point source of momentum solutions (1.13) and (1.14) with (1.21) yields

$$-G^2 - \frac{G'}{\chi}\int_0^\chi G\chi \, \mathrm{d}\chi = \frac{(\chi H)'}{\chi} \tag{1.22}$$

where c_1 is chosen to be unity and the constant of proportionality is absorbed into $H(\chi)$. The elimination of the jet width b and centreline velocity $\bar{u}_c$ and their derivatives indicates that all axisymmetric jets reach an identical ('global') self-similar state regardless of the source conditions or source geometry. Much contention surrounds this result. Experimental investigations into axisymmetric jets consistently obtained differing far-field states, in part revealed by differing values for c_1 and c_2. For example, a review of the round-jet literature by Fischer et al. (1979) gives spreading rates ranging from $c_1 = 0.090$ to $c_1 = 0.130$, a difference of 45%. Such discrepancies between independent sets of measurements were customarily attributed to experimental uncertainty and some authors would conclude that their measurements were not far enough downstream for the jet to have reached true far-field behaviour (e.g. Wygnanski & Fiedler, 1969). As more data was accumulated, it became clear that these explanations were inadequate. George (1989) argued against the prevailing belief in a global self-similarity, disagreeing with the formulation posed in (1.18) and (1.22). In his derivation, the momentum integral (1.10) is recast using (1.17) yielding (to the first order)

$$M_0 = (\bar{u}_c b)^2 2\pi \int_0^\infty G^2(\chi)\chi \, \mathrm{d}\chi. \tag{1.23}$$

Then, by allowing the Reynolds stress to scale independently of the velocity (with a scaling variable R), i.e. by expressing

$$\overline{u'v'}(x,r) = RH(\chi), \tag{1.24}$$

and on noting, from (1.23), that $(\bar{u}_c b)^2$ is constant and therefore

$$\bar{u}_c \propto b^{-1}. \tag{1.25}$$

Following the steps outlined above that gave (1.22), George (1989) derives the alternate form, namely

$$\frac{db}{dx}\left(G^2 + \frac{G'}{\chi}\int_0^\chi G\chi \, \mathrm{d}\chi\right) = -\frac{R}{\bar{u}_c^2}\frac{(\chi H)'}{\chi}. \tag{1.26}$$

On not imposing point source of momentum solutions, the terms associated with b, $\bar{u}_c$, and R remain in (1.26) and allow for the source geometry and conditions to influence the self-similar state. Furthermore, George (1989) showed that the condition for (first-order) self-similarity, $db/dx \propto R/\bar{u}_c^2$, does not preclude solutions in which the growth rate or decay of centreline velocity are non-linear. George (1989) continued his analysis at the level of the turbulent kinetic energy, showing that it was possible to recover a non-unique linear solution. Thus, in short, this work indicated that each jet would reach its own 'local' source dependant self-similarity - and that knowledge of the source conditions was advected downstream within the turbulent quantities. Many subsequent investigations, both numerical (e.g. Boersma et al., 1998) and experimental (e.g. Ferdman et al., 2000; Mi et al., 2001), appear to indicate the existence of a local self-similarity and thus support the arguments of George (1989). The experimental study of Ferdman et al. (2000), where measurements were taken using hot-wires on air jets ($Re_D = 24{,}000$) with either a symmetric or an asymmetric fully developed velocity profile at the source, finds differences in both the spread of the width and centreline velocity decay with the different exit velocity profiles.

Not all studies agree with the conclusions of George (1989). The experimental investigation of Richards & Pitts (1993), where they measure the scalar concentration in turbulent (variable-density) jets using Rayleigh Light Scattering, appears to support the concept of a 'global' self-similarity. At the source, the density differences were significant such that the Boussinesq approximation could not be used (the Boussinesq approximation is the assumption that the density differences are only important in the buoyancy term (Turner, 1969)). The measurements, however, were made in a downstream region where momentum dominated and the entrainment of the ambient air rendered the Boussinesq approximation valid - thus permitting self-similar solutions. While they find evidence of a 'global' self-similarity, they also observe different virtual origins for the jet width and centreline concentration. The source dependence of their jets

is likely to manifest in these different virtual origins. The theoretical framework provided by Carazzo et al. (2006), based on the evolution of entrainment and the dynamic variables, implies far downstream a 'global' self-similarity is reached and also disagrees with the conclusions of George (1989). However, the reliance on complex shape functions and parameterisation makes physical interpretation difficult.

Despite the fact that both annular and round jets issue from axisymmetric source geometries, the geometries of the annular and circular sources differ considerably. Therefore, if the work of George (1989) is correct, we are likely to observe different values of c_1, c_2 and x_0 in the slender open-core annular jet when compared to the values typically observed in round jets. Furthermore, modifying the source geometry (D_i/D_o and D_v/D_i) of the slender open-core annular jet may also influence the values of these constants.

Velocity profiles

Several authors have closed (1.21) by relating the Reynolds stress term to the time-averaged velocity and, in doing so, have developed expressions for the velocity profiles. For example, Davidson (2004) uses an eddy viscosity approach and obtains an equation for the time-averaged axial velocity profile of the form

$$G = \frac{1}{(1 + const.\chi^2)^2}. \tag{1.27}$$

Information on different closure methods is given in Schlichting (1968). In practice however, most investigations, including our own (§4-6), use a Gaussian ($e^{-(r/b)^2}$) to describe the radial profile of time-averaged axial velocity $\bar{u}(r)$.

1.4.3 Entrainment

Entrainment is a multi-scale process by which the volume flux Q of a jet increases with distance downstream and is the primary means by which all jet flows (including those issuing from slender annular sources) interact with their environment.

Philip & Marusic (2012) provide a good description of the turbulent entrainment process that occurs between the turbulent shear layers of the jet and the irrotational ambient fluid. In their work, where they model the effect of large-scale eddies on entrainment in axisymmetric jets and wakes, they characterise entrainment as a "three-part-process". Illustrated on figure 1.7 are the three components: large-scale energy containing eddies '*induce*' and '*engulf*' irrotational ambient fluid, while smaller-scale eddies '*nibble*' irrotational fluid, engulfed by and otherwise in contact with the jet, and make it turbulent.

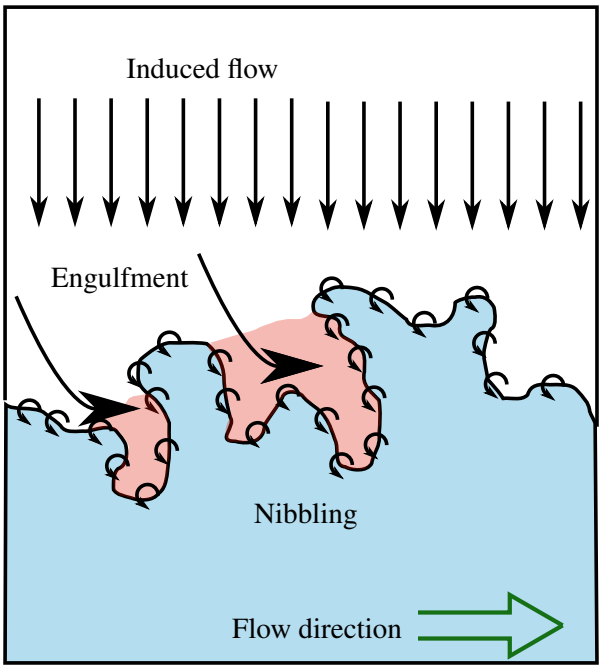

Fig. 1.7: A sketch of the turbulent/non-turbulent interface between the turbulent jet (shaded in blue) and the irrotational ambient (white or shaded in red when in the process of being engulfed) used to illustrate the processes occurring during turbulent entrainment. The straight arrows represent flow induced towards the jet, the curved arrows the engulfment of fluid and the smaller circular arrows the nibbling occurring on the jet boundary (after Philip & Marusic, 2012).

The first direct measurements of the entrainment into a round jet were made by Ricou & Spalding (1961). Their apparatus, which consisted of a round jet surrounded by a porous cylinder through which they could supply fluid, allowed them to measure the entrainment flow rate - the entrainment flow rate being equal to the flow rate through the porous cylinder which prevented the formation of an axial pressure gradient. Using this apparatus they took measurements over a range of Reynolds numbers $500 \leq Re_D \leq 80,000$ and axial distances $2.4 \leq x/D \leq 418$ and obtained

$$\frac{Q}{Q_0} = 0.32\frac{x}{D}, \tag{1.28}$$

confirming that far from the source the volume flux within the jet varied linearly with distance downstream. Given the axisymmetric source geometry, we anticipate that the volume flux in the far field of slender open-core annular jet will also vary linearly with distance downstream.

Morton et al. (1956) parameterised entrainment by means of an entrainment hypothesis, where, at a given axial location, they linked the radial velocity of the inflow $v_e(x)$ to the

time-averaged centreline velocity $\bar{u}_c$ by means of an entrainment coefficient α, i.e. $v_e(x) = \alpha\bar{u}_c$. Indeed, it was noted earlier that this approach could be applied to the non-buoyant jet (Priestley & Ball, 1955). Thus, for an axisymmetric jet we can write

$$\frac{dQ}{dx} = 2\pi b\alpha\bar{u}_c. \tag{1.29}$$

The coefficient α has been the subject of much interest - even at conception it was clear that α would be greater in plumes (when compared to jets) due to the greater rates of dilution measured in plumes. While many researchers (e.g. Priestley & Ball, 1955; Ezzamel et al., 2015) have sought to relate the entrainment coefficient to the local fluxes of mass, momentum and buoyancy, it is sufficient here to conclude from these works that in the far field of a non-buoyant jet the entrainment coefficient should remain unchanged with downstream distance. In other words, the entrainment coefficient should remain constant with downstream distance in the slender open-core annular jets of interest. Given the preceding discussion on self-similarity, however, we may expect the source geometry to influence the value of the entrainment coefficient in the jet.

1.4.4 The near field

Given that, in this work, we are interested in the influence of the source geometry on the jet issuing from the annular nozzle, it is prudent here to discuss how the source geometry may influence the round jet both near the source and further downstream.

The geometry upstream of an orifice controls the shape of the velocity profile at the nozzle exit (Quinn, 2006). Schematics of three circular nozzle geometries and corresponding time-averaged axial velocity profiles $\bar{u}(0,r)$ at the exit plane of the source are shown in figure 1.8. A smoothly contracting nozzle produces a 'top-hat' velocity profile (figure 1.8a), a jet issuing from a pipe of sufficient length will have a fully developed turbulent pipe flow velocity profile (figure 1.8b) and a sharp-edged orifice produces a profile that is 'saddle-backed' (figure 1.8c) (Quinn, 2006; Mi et al., 2001). The immediate effects of the differing velocity profiles are observed in the region of flow development. Specifically, the different velocity profiles result in potential cores of different (axial) lengths. The experiments of Quinn (2006), where the velocities of a round air jet were measured using hot wires, show that axisymmetric jets issuing with 'saddle-backed' velocity profiles have a shorter potential core than jets issuing with a 'top-hat' profile. They attribute this to the larger degree of shear present at the source in sharp-edged orifices jets when compared to jets issuing from smoothly contracting nozzles. The work of Mi et al. (2001) indicates that the potential core of jets with pipe flow profiles is longer than that of jets with 'top-hat' profiles, once again this is attributed to the degree of shear

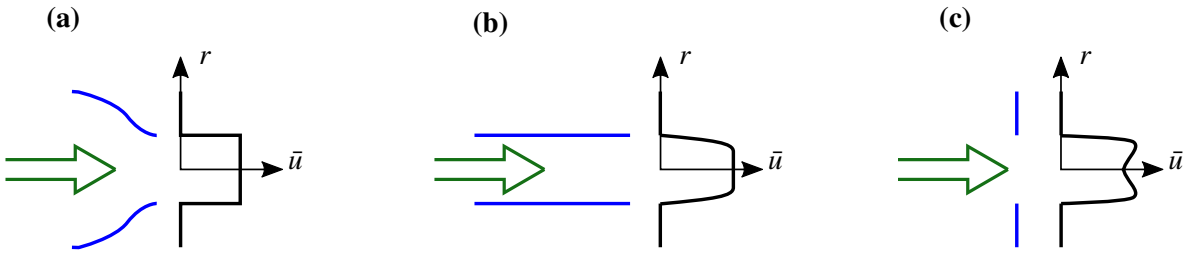

Fig. 1.8: An illustration of the time-averaged streamwise velocity profiles (thick black lines) produced by different nozzle geometries (blue lines). (a) A smoothly contracting nozzle produces a 'top-hat' profile (Quinn, 2006), (b) a pipe flow nozzle produces a (turbulent) pipe flow profile (Mi et al., 2001) and (c) a sharp-edged orifice produces a 'saddle-back' profile (Quinn, 2006).

present at the source. Far from the source, the differences in this region of flow development are reflected in the location of the virtual origin: the shorter the potential core, the further upstream the virtual origin is located (Quinn, 2006; Mi et al., 2001). Both sets of authors also observe the influence of the nozzle geometry in the far-field region by means of the coefficients c_1 and c_2, and attribute this to differences in the underlying turbulent structures which are ultimately related to differences in shear at the source. These far-field differences lend support to the conclusions of George (1989).

This overview of the near field indicates that far from the nozzle, the differences between the near fields of annular and round jets (see figures 1.2 and 1.3) will manifest in the virtual origin corrections x_0. The influence of the source geometry on the time-averaged far-field jet itself manifests in the spreading rate c_1 and decay rate c_2.

Indeed, on comparing round and slender open-core annular jets, we observe significant differences in the location of the virtual origin. These differences reflect the differing near-field development (cf. figures 1.2 and 1.3). Additionally, on modifying the ventilation ratio D_v/D_i we observe significant changes in the coefficients c_1 and c_2.

CHAPTER 2

Methodology

Preamble

The discussion that follows applies to the problem of interest, namely, investigating the development of the jet issuing from a slender open-core annular nozzle.

Before any theoretical or numerical work is undertaken, it is essential to gain a real physical understanding of the flow considered. In other words, the first step when considering a new problem is to carry out experiments in a real fluid. For this reason, given the lack of information on jets issuing from slender open-core annular sources, our primary method of investigation was through measurements obtained during an experimental campaign. Our objectives in this campaign (§1.2) were firstly to obtain an understanding of the flow and its development, from the source into the region in which the jet is fully developed and, secondly, to understand how the nozzle geometry effects the flow.

While many existing methodologies are suitable for studying momentum driven flows, the slender open-core annular jet had not previously been examined. Therefore, before commencing experiments, we first needed to design appropriate experimental nozzles. To successfully carry out the desired experiments, the nozzles and experimental set-up needed to be capable of:

1. producing a turbulent, non-swirling, momentum driven, axisymmetric flow issuing from slender annuli, i.e. annuli with $D_i/D_o \approx 1$. The intention is for the flow, within our measurement domain, to be momentum dominated and unaffected by the test chamber so that it approximates to a jet issuing into an infinite unbounded environment;

2. allowing fluid to pass through the centre of the annulus, unimpeded. In other words, having an almost fully open core ($D_v/D_i \approx 1$) and relatively low frictional losses when inducing a flow through the centre of the annular nozzle;

3. allowing an in-depth examination of the flow development, from the source into the region in which the jet is fully developed. Near the source, this capability is related to the spatial resolution of the measurements when compared to the size of the nozzle. Far downstream, this capability is related to the relative sizes of the nozzle and the experimental chamber;

4. allowing the investigation of slender annuli with a range of diameter ratios D_i/D_o; and

5. allowing subsequent modification of the nozzle ventilation.

The final nozzle design, source conditions and driving mechanism which these requirements led us to converge upon are detailed in §2.1 and §2.2. Figure 2.1 presents an image of one of the experimental nozzles used to perform the experiments described in this thesis (specifically, the image shows nozzle **N4** which has $D_i/D_o = 0.968$ and $D_v/D_i = 0.90$, see table 2.1). Two aspects of note are mentioned here. Firstly, the nozzle is designed such that fluid can easily be induced through the core of and around the outside of the nozzle. This design has resulted from our desire to minimise the influence of the nozzle on the flow induced through the open core. Secondly, the nozzle has been 3D printed. This technique allowed us to rapidly fabricate this complex nozzle geometry in a cost effective manner.

Simultaneously to designing the nozzle, we sought an appropriate fluid medium and measurement technique. Given the lack of literature on jets issuing from a slender open-core annular source, our focus was to investigate the primary flow features. By primary flow features, we refer to features that characterise the bulk time-averaged behaviour of the jet. An ideal measurement technique would be capable of obtaining, non-intrusively, high-resolution and accurate estimates of velocity across a section of the flow. To this end, we decided to carry out experiments in air and to make measurements using a combination of planar and stereoscopic particle image velocimetry (PIV), see §2.4. This allowed us to acquire high-resolution instantaneous measurements of velocity across streamwise and cross-stream sections of the jet. In addition, we recorded images using flow visualisation techniques, see §2.3, and thereby acquired a qualitative "picture" of the flow.

Prior to selecting the final fluid medium and measurement techniques, flow visualisation experiments in water were undertaken. This was logical, the Research Group has both access to a variety of water tanks, as well as extensive, and almost exclusive, experience in water tank experiments within the Cambridge University Engineering Department. Indeed, there are many advantages to carrying out experiments in water tanks (when compared to carrying out experiments in air). On assuming that the scale of the nozzle remains the same, these advantages include: easier isolation of the experimental chamber from thermal effects; lower flow rates and velocities required to achieve turbulent Reynolds numbers (as the kinematic

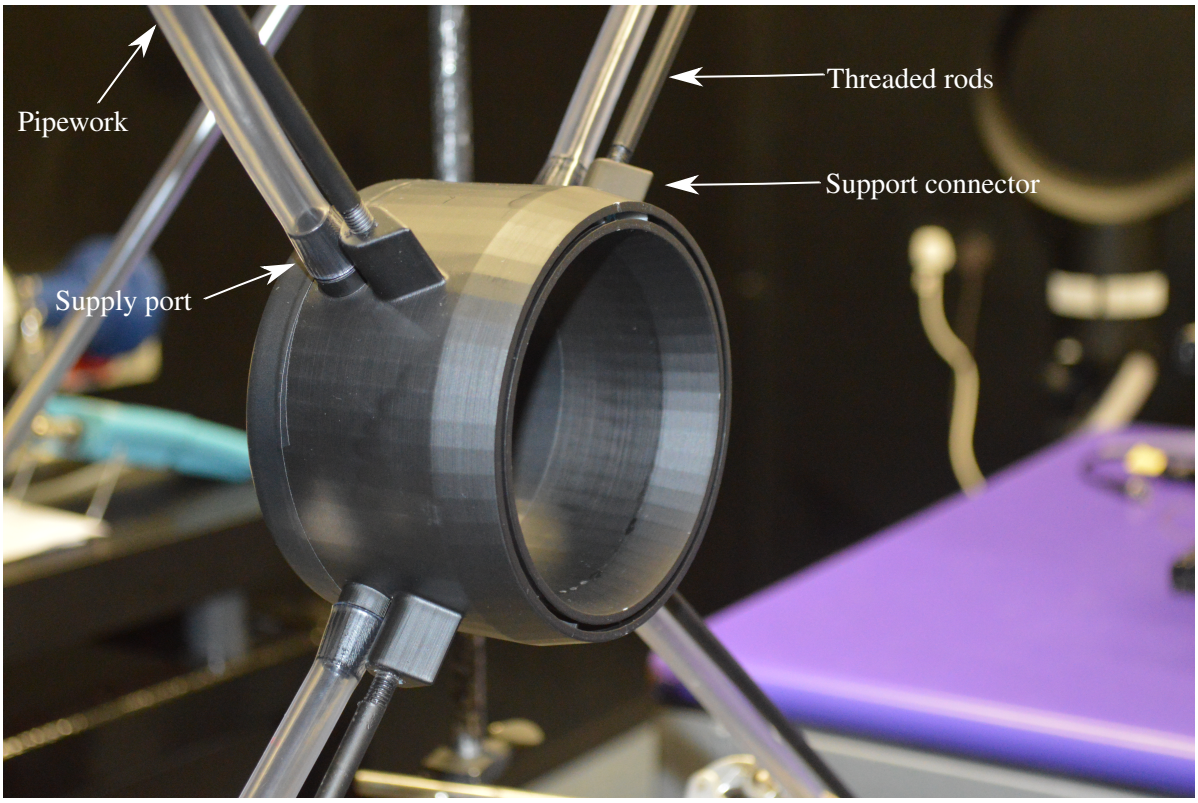

Fig. 2.1: An image of one of the experimental nozzles designed specifically to carry out the work described in this thesis. The nozzle is approximately 100 mm in diameter. The image shows nozzle **N4** which has $D_i/D_o = 0.968$ and $D_v/D_i = 0.90$, see table 2.1 for details.

viscosity of water is a factor 10 lower than that of air); and larger flow time scales (which would ease the acquisition of time-resolved images). However, although these experiments proved successful, a number of problems were encountered with the water tank set-up. The most pressing of these problems was that the 3D printed nozzle deformed when placed in water - it absorbed water as many plastics are wont to do, and subsequently swelled unevenly. While we were conducting these preliminary experiments, the industrial sponsor offered the use of their experimental facility. This facility was capable of flow visualisation and PIV experiments in air. Given this opportunity, we accepted their offer.

Measurements, forming an extensive dataset, were subsequently acquired in air for a variety of diameter ratios D_i/D_o, ventilation ratios D_v/D_i and slot Reynolds numbers Re_l. In the remainder of this chapter, the experimental details shared by these sets of measurements are discussed extensively. The purpose of this discussion is to provide the reader with assurance that the experiments are of good quality and to aid any who wish to carry out similar experiments.

	$\frac{D_i}{D_o}$	D_o (mm)	D_i (mm)	l (mm)	h (mm)	$\frac{h}{l}$	A_0 (mm^2)	L_1 (mm)	L_2 (mm)	$\frac{L_1}{D_i}$	$\frac{\sqrt{A_0}}{l}$
N1	0.845	108.67	91.87	8.40	13.0	1.55	2645	83.1	117.4	0.90	6.13
N2	0.894	105.91	94.73	5.59	11.0	1.97	1762	85.4	115.4	0.90	7.52
N3	0.947	103.08	97.66	2.71	7.90	2.92	855	88.4	112.2	0.90	10.8
N4	0.968	101.65	98.35	1.65	7.90	4.79	518	88.4	112.2	0.90	13.8
N5	0.981	109.56	107.44	1.06	8.70	8.21	361	96.3	121.7	0.90	17.9

Table 2.1: Dimensions of the five slender annular nozzles labelled **N1-N5**, listed in order of increasing D_i/D_o. The area of the nozzle exit has been calculated using $A_0 = \pi(D_o^2 - D_i^2)/4$. The distances were measured using digital vernier calipers to $\pm$ 0.01 mm and varied by $\pm$ 0.1 mm around the circumference of the annulus. Entries for D_i/D_o, D_o, D_i and l are given to three decimal places due to the relatively small differences in the diameter ratios investigated, all other entries given to two decimal places.

Details which are specific to each set of measurements will be considered within the relevant chapters.

2.1 Nozzle design

Experiments were performed in a test chamber of horizontal dimensions 5 m $\times$ 4 m and height 3 m using stereolithographic (SLA) 3D printed annular nozzles made of accura25 polyamide. Five nozzles, with slot widths l between 1.06 mm and 8.40 mm, were utilised. Due to the method of fabrication, the slot width varied by approximately $\pm$0.1 mm around the perimeter of the nozzle. Schematics, showing the design of the nozzles, are presented in figure 2.2 with dimensions given in table 2.1. To enable a study of the key flow features in both the near and far fields of the jet, given the dimensions of the room we converged on nozzles with a mean diameter of $D_c = (D_i + D_o)/2 \approx 100$ mm. We thereby achieved a range of slender diameter ratios between $D_i/D_o = 0.845$ and $D_i/D_o = 0.981$. Both $D_i/D_o = 0.968$ and $D_i/D_o = 0.981$ may be regarded as approximating to the limiting slender case (of $D_i/D_o = 1$). In a fully open-core annular source, the diameter of the central opening D_v and the inner diameter D_i of the slot are equal, i.e. $D_v/D_i = 1$. Although the fully open-core annular source was of primary interest, physical considerations, such as the presence of the nozzle, prevented the achievement of this fully open-core source geometry. Thus, the open core of our sources (of diameter L_1) is marginally restricted by the nozzles themselves, resulting in a ventilation ratio of $D_v/D_i = L_1/D_i = 0.90$ (we later further restrict the nozzle ventilation, see §6). Seeking to

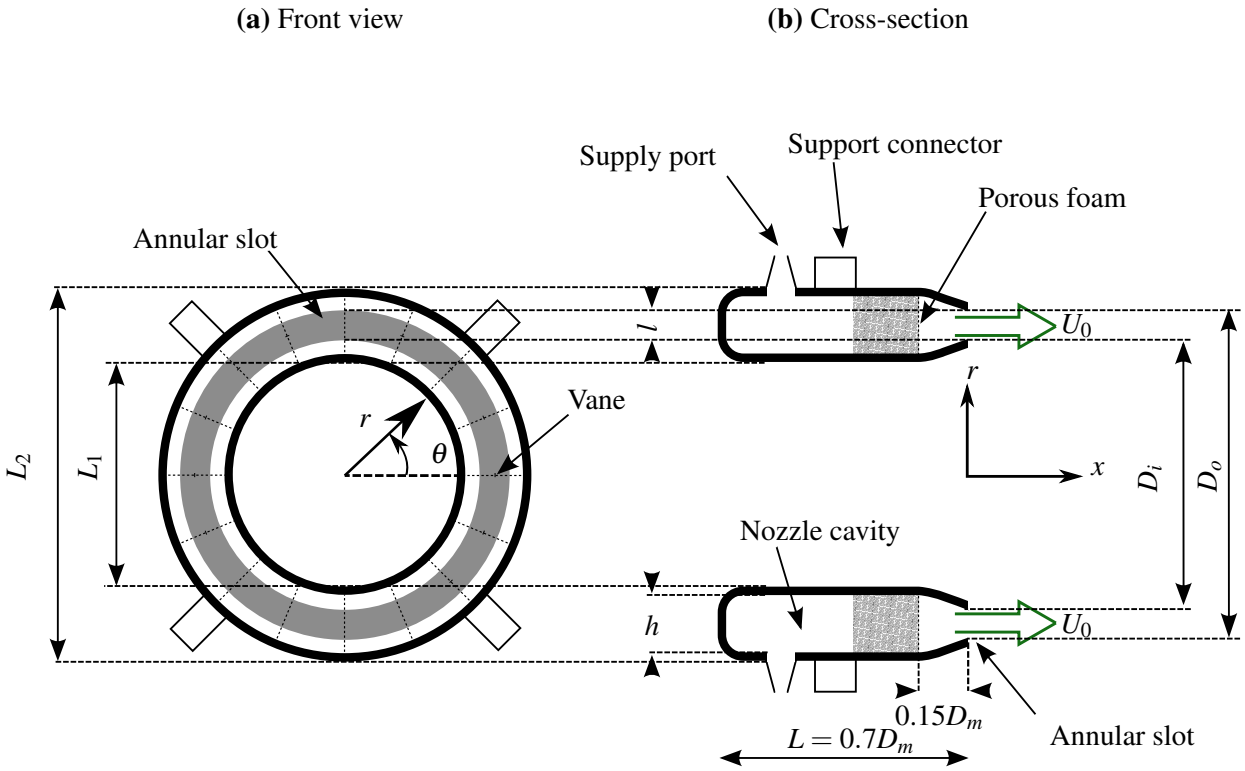

Fig. 2.2: Schematics showing the annular nozzle design (not to scale). The wall thickness (thick solid line) is approximately 2 mm. (a) Front view showing the swirl reducing vanes positioned at 22.5° intervals. The shaded ring represents the annular slot. (b) Section through the nozzle that bisects the air supply ports and the support connectors. Air pumped to the supply ports issues from the annular slot with mean velocity U_0 (m s^{-1}). Nozzle dimensions are given in table 2.1. The coordinate system (x, r, θ) is marked.

achieve uniform release conditions at the exit plane of the annulus, four air supply ports were located equidistant around the circumference of the nozzle (figure 2.1 and 2.2a) and the interior of the nozzle (of width h, see table 2.1) was lined with a 20 mm thick strip of porous foam. The foam aids the flow uniformity by increasing the pressure drop across the nozzle and, in addition, acts to damp out the turbulent fluctuations (Torrance et al., 2011). Moreover, 16 vanes were fabricated within the nozzle, one vane every 22.5°, in order to provide structure to the nozzle and to channel the air in a direction perpendicular to the exit plane, thereby reducing swirl (as quantified in §3.2.2). In order to maintain a ventilation ratio of $D_v/D_i = 0.90$, while preserving the symmetry of the nozzle cavity about the slot (about $r = D_c/2$), the contraction ratio of the nozzle h/l (table 2.1) varied with the diameter ratio. The details of the velocity profile at the slot exit and the effect of this varying contraction ratio is discussed in §3.5.3. The nozzles themselves were supported by threaded rods attached to the support connectors.

These rods, arranged in an X-shape, were themselves held rigidly by a combination of retort stands and clamps. The connections between the threaded rods and the support connectors, and between the pipework and air supply ports are visible in figure 2.1.

2.2 Experimental set-up

The design of the nozzle alone is not enough to achieve the capabilities set out at the start of this chapter. It is necessary to also consider the test chamber that this nozzle resides within and the experimental equipment used. Capability #3 (page 24), namely, that our set up should be capable of allowing an in-depth examination of the flow from the source and into the region in which the jet is fully developed, is clearly related to the dimensions of the test chamber and experimental set-up. In addition, capability #1, i.e within our measurement domain the flow produced should approximate to a jet issuing into an infinite unbounded environment, also has some dependence on the test chamber and experimental set-up. To achieve capability #1, the key considerations are to ensure that:

a. the return flow set up by the presence of the jet within the test chamber did not unduly influence the behaviour of the jet;

b. in the region of interest, the jet was not unduly effected by the boundaries of the test chamber; and

c. the method by which air was supplied to the nozzle resulted in a momentum dominated flow. This is a consideration due to the inevitable heating by the driving mechanism of the flow.

The remainder of this section outlines the experimental set-up used, which achieves the considerations laid out above.

A schematic showing a plan view of the test chamber **ABCD** is shown in figure 2.3, where the laser and camera are positioned for a single set of planar PIV measurements. The positioning of the laser and camera(s) varied between the experiments and between different recording techniques, and is discussed in more detail in §2.3-2.4.5. The location of the nozzle, approximately 1.2 m above the floor and approximately 1 m away from the nearest two walls, remained fixed for all flow visualisation and planar PIV experiments. For stereoscopic PIV experiments the location of the nozzle varied, see §2.4.5. The jet issued parallel to wall **CD** in the direction of wall **BC**. On accounting for the distance over which the laser had to travel before the expanding perimeter (due to the optics) of the laser sheet was of sufficient width for our measurements (i.e. extending past the boundaries of the jet), this set-up allowed us to

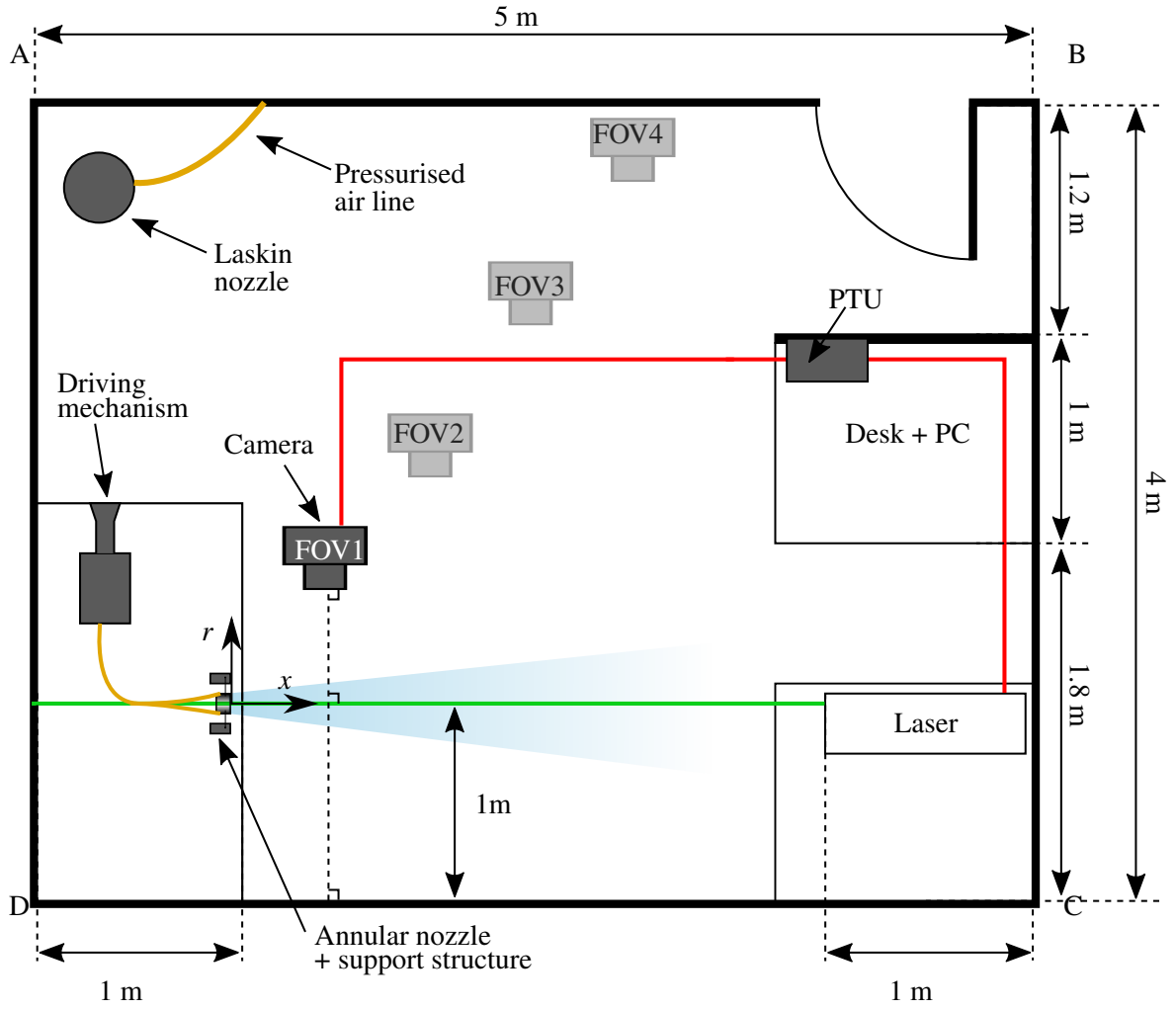

Fig. 2.3: A schematic showing a plan view of the test chamber, with key dimensions marked. The thick **black** lines represent the boundary **ABCD** of the test chamber. The **orange** lines illustrate pipework. The **green** line represents the vertical laser sheet. The **red** lines represent the wiring used to connect the camera, the programmable timing unit (PTU), and the laser for the PIV experiments. The laser and nozzle are shown positioned for planar PIV measurements (see §2.2); the camera indicated by the dark grey shading, wiring and PTU are positioned to capture measurements on a field of view close to the nozzle (FOV1) ; the cameras indicated by the light grey shading show the approximate positions of the camera when capturing FOV2-FOV4 (see §2.4.4). For planar PIV and flow visualisation experiments the jet (depicted by the shaded blue region) issued parallel to the wall **CD**.

obtain measurements in the jet for $0 \leq x \lesssim 16D_c$. Given that for our nozzle $D_c \approx D_o$, and that experiments on unventilated annular jets observe far-field behaviour from around $x \approx 9D_o$ (Ko & Chan, 1978), we expected the jet to approach fully developed far-field behaviour within this measurement domain. Through experiments (§4) we ascertained that at the downstream extent of the measurement domain, the time-averaged axial velocity had reached full self-similarity, whereas the time-averaged radial velocity and the turbulent statistics still showed evidence of development. At the downstream end of the measurement domain our measurements (cf. §4) indicated that the jet was approximately 850 mm from the nearest boundary, while having a diameter of approximately 300 mm. Thus, it was judged that the nozzle was sufficiently far from the boundaries of the test chamber that, within our measurement domain, the jet produced was deemed to be unaffected by their presence. This is confirmed by an examination of the jet symmetry and the streamwise variation in momentum flux, given in §3.2.1-3.2.2, which indicates that the boundaries of, and the return flow in, the test chamber had a negligible effect on the jet. At this stage, one may wonder why we did not situate the nozzle (and laser) at the midway point of wall **AD** (or, equivalently, wall **BC**). The placement of the nozzle was as chosen, because recording the largest field of view (FOV4, see §2.4.4) required the camera to be situated almost 3 m away from, and perpendicular to, the laser sheet. Therefore, the arrangement used, with the nozzle closer to wall **CD**, was the only feasible arrangement for capturing this particular FOV.

For the purposes of seeding, we employed a TSI 9307-6 Laskin nozzle oil droplet generator which was connected to a high pressure air line and used di-ethyl-hexyl-sebacat oil. This combination of generator and oil produced particles of approximately one micron in diameter (Raffel et al., 2007). The choice of seeding particle was informed by two considerations: firstly, for accurate PIV measurements, the particles must accurately follow the fluid motion; and secondly, the particles must scatter enough light to be accurately recorded. With regards to the seeding particle diameter, these two considerations represent opposing influences. Small particles will more accurately follow the flow, whereas larger particles will scatter more light. The diameter of di-ethyl-hexyl-sebacat oil is relatively small (approx. 1 µm, Raffel et al., 2007) and ensures that the particles will accurately follow the flow (Raffel et al., 2007), while images obtained from experiments confirmed that light scattered by the particles (and captured by the camera) was sufficient. The exact procedure for seeding the flow differed between flow visualisation and PIV experiments, and is discussed in §2.3 & §2.4. Without intervention the necessary presence of experimental equipment and researchers, both of which emit heat within the test chamber, may result in a non-uniform and stratified ambient environment. Therefore, to ensure uniform conditions within the test chamber, the air was completely purged and replaced

with external air prior to each experimental run. The air in the chamber was then allowed to settle before activating the jet and commencing an experiment.

2.2.1 Driving mechanism

Ambient air was fed to the nozzle, via a four-way manifold, by a mixed flow impeller fan controlled by a variable autotransformer (Variac). This mechanism of providing a supply of air to the ports resulted in an experiment dependent temperature difference ΔT between the jet and the ambient (recorded to ± 0.05°C using a RS51 digital thermocouple at the exit plane of the slot and in the ambient at the height of the nozzle, see figure 2.4). Measurements of the pressure difference ΔP between the ambient and ducting downstream of the bell mouth were made using a Digitron 2020P7 2.5 kPa digital manometer to ± 0.05 Pa (see figure 2.4). The reference background pressure was measured using an in-house barometer to ± 0.05 Pa. The ambient temperature T_∞ in the room was measured using an ATP DT-321 temperature and humidity meter to ± 0.05°C. These measurements, combined with the measurements of ΔT, allowed us to: estimate the source volume flux Q_0 from application of Bernoulli's theorem; apply corrections based on the bell mouth calibration (to an accuracy of approximately 1%); and account for the expansion of air passing through the fan (due to the temperature difference ΔT). The second step, to apply corrections based on the calibration of the bell mouth, was accomplished using an in-house spreadsheet. The final calculation, to account for the expansion of air, was accomplished using

$$Q_0 = Q_{0U}\frac{T_\infty + \Delta T}{T_\infty}, \tag{2.1}$$

where T and ΔT are in Kelvin, and Q_{0U} denotes the uncorrected flow rate. Pressure fluctuations during a given experiment were within ± 10 kg m^{-1} s^{-2} (i.e. within ± 10 Pa), indicating a variation in flow rate of ± 0.0002 m^3 s^{-1}.

If, at this point, we assume a uniform velocity profile at the slot exit (see §3.5.3), we can calculate the velocity of the fluid exiting the slot using $U_0 = Q_0/A_0$, where $A_0 (= \pi(D_o^2 - D_i^2)/4)$ denotes the slot area. The largest exit velocity examined, $U_0 \approx 35$ m s^{-1}, results in a Mach number of $U_0/c \approx 0.10$ (taking the speed of sound in air as $c = 343.4$ m s^{-1}, Haynes (2012)), indicating that the jet may be considered to be incompressible. In addition, the assumption of a uniform velocity profile at the slot exit allows an estimate of the source momentum flux as $M_0 = Q_0^2/A_0$.

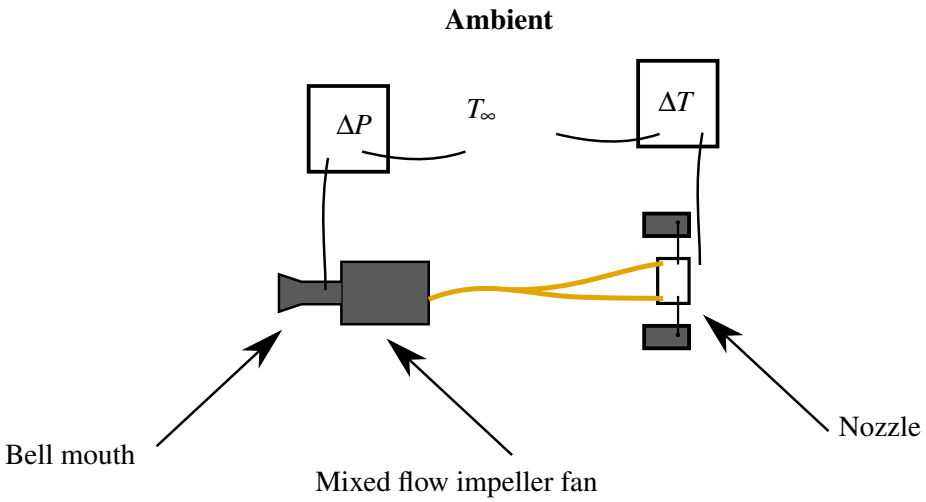

Fig. 2.4: A schematic showing the locations at which measurements of pressure difference ΔP, temperature difference ΔT and ambient temperature T_∞ were made. These measurements were used to calculate the source volume flux, see §2.2.1 for more details. The **orange** lines illustrate the pipework connecting the mixed flow impeller fan and the nozzle, and the black curved lines represent the piping used for manometer measurements (in the case of ΔP) or the wiring used for thermocouple measurements (in the case of ΔT).

2.2.2 Reynolds numbers

Five different slot Reynolds numbers Re_l have been targeted and are labelled **R1-R5** in ascending order, where the target values of Re_l associated with **R1-R5** are given in table 2.2. Between separate experiments targeting the same value of Re_l, there is a variation of ± 100 in slot Reynolds numbers. For the primary experiments (§4-6), where $2300 \lesssim Re_l \lesssim 3200$, the variation ($\pm 100$) between the achieved and target Reynolds number is small (<5%). Precise values for the Reynolds numbers and associated source conditions are given in the relevant sections.

Despite the use of similar source velocities, even our largest slot Reynolds number $Re_l \approx 3200$ is lower than the slot Reynolds numbers used in the unventilated-annular-jet studies of others, e.g. $Re_l = 6.8 \times 10^4$ in the experiments of Ko & Chan (1978). This is due to the significantly narrower slot width l of our nozzle that enabled us to explore both the near and far field of the jet within the test chamber. While not a primary focus of this work, in §3.4 we briefly explore the influence of the Reynolds number on the slender open-core annular jet using PIV measurements. These measurements confirm that, for our primary experiments (§4-6) in which $2300 \lesssim Re_l \lesssim 3200$, the influence of the Reynolds number on the measurements is small.

	$\frac{D_i}{D_o}$		Re_l		$\frac{D_v}{D_i}$
N1	0.845	**R1**	1100	**V1**	0.90*
N2	0.894	**R2**	1600	**V2**	0.75
N3	0.947	**R3**	2300	**V3**	0.50
N4	0.968	**R4**	2800	**V4**	0
N5	0.981	**R5**	3200		

Table 2.2: Notation and corresponding values of D_i/D_o, Re_l and D_v/D_i used to refer to the source conditions of the experiments. The ventilation ratio indicated using * represents the case where the nozzle ventilation has not been modified.

Prior to making experimental measurements, information provided in the literature can be used to evaluate the effect of the Reynolds number on the jet. As discussed in §1.3, the study of Li & Tankin (1987) indicated that the influence of the Reynolds number on the closed-core jet envelope diminished after $Re_l > 800$. Preliminary flow visualisations (on a jet issuing from the open-core source **N5** with $D_i/D_o = 0.981$) indicated that this held true for the slender open-core annular jet. Furthermore, the Reynolds number of the coalesced jet Re_f, calculated using (1.2), is a factor $\sqrt{A_0}/l$ larger than Re_l (see final column of table 2.1). Dimotakis (2000) argues that fully developed turbulence in jets, and quasi-independence of the flow from the Reynolds number, requires a Reynolds number based on the length scale of the nozzle to exceed $1-2\times10^4$. For our primary investigations, §4-6, $2200 \lesssim Re_l \lesssim 3200$ and $14000 \lesssim Re_f \lesssim 45000$. In the region near the nozzle, where the dominant length scale is the slot width l, $Re_l \ll 1-2\times10^4$ indicates that the influence of the Reynolds number may be significant. Further downstream however, where the dominant length scale is $\sqrt{A_0}$, the relatively large Reynolds number achieved herein, $Re_f \geq 1-2\times10^4$, indicates that the time-averaged quantities of interest in will be insensitive to Re_f.

2.2.3 Buoyancy

As a consequence of the temperature difference between the jet and the ambient (see §2.2.1), the jet was not perfectly isothermal. The jet length $L_j = M_0^{3/4} B_0^{-1/2}$ (Fischer et al., 1979), where $B_0 (= gQ_0\Delta T/T_0)$ denotes the source buoyancy flux and g the acceleration due to gravity, provides us with a measure of the distance from the source over which the dynamics of the jet are not expected to be influenced by this temperature anomaly. Papanicolaou & List (1988) observe momentum dominated behaviour in buoyant jets for $x < L_j$. Conservatively, we restrict

our measurement domain to $0.5L_j$ and therefore expect the influence of buoyancy on our measurements to be small. We confirm that the influence is indeed small in §3.2.3.

2.2.4 Nozzle ventilation

In §4-5 we examine slender annular jets with almost fully open cores, where the ventilation ratio of the source is determined by the geometry of the nozzle itself (i.e. $D_v/D_i = L_1/D_i = 0.90$). Subsequently, in §6 we consider the effect of restricting the ventilation on the slender annular jet and examine four different ventilation ratios $D_v/D_i = \{0,\ 0.50,\ 0.75,\ 0.90\}$. The four ventilation ratios are labelled **V1-V4** in descending order of D_v/D_i, see table 2.2. Details, including the method by which we restricted the source ventilation and the associated source conditions can be found in §6.2.

2.2.5 A note on source notation

The range of source conditions necessitates notation by which we can clearly and easily refer to a particular combination of D_i/D_o, Re_l and D_v/D_i. The precise source conditions associated with the combination of these three parameters are discussed in the relevant sections.

The diameter ratio D_i/D_o is referred to using the notation **N1-N5** introduced in table 2.1 for the nozzle geometry. The slot Reynolds number Re_l is labelled using **R1-R5** (see §2.2.2 and table 2.2), and the ventilation ratio with **V1-V4** (see §2.2.4). These three notations, summarised in table 2.2, are combined to refer to the source geometry and source conditions. For example, **N1R3V2** refers to a source with $D_i/D_o = 0.845$, $Re_l = 2300$ and $D_v/D_i = 0.75$. In addition, if only one of the source parameters is varying within a given experimental campaign, we can neatly refer to a range of sources, e.g. the sources denoted **N1-5R3V4** refer to sources with a range of diameter ratios $D_i/D_o = \{0.845,\ 0.894,\ 0.947,\ 0.968,\ 0.981\}$, a constant slot Reynolds number $Re_l = 2300$ and a constant ventilation ratio $D_v/D_i = 0$.

2.3 Flow visualisation

One method by which the flow was examined was through the use of flow visualisation, from which we obtained images along a longitudinal mid-section of the flow. An example of one of these images is displayed in figure 1.2, which presents an instantaneous snapshot of the flow produced by a slender open-core annular jet (specifically, that produced by source **N5R2V1**). In order to seed the jet flow, while the flow visualisation experiments were running, the output from the Laskin nozzle was fed directly into the bell mouth intake of the mixed flow impeller fan. To reduce errors in the recorded flow rate, associated with introducing a flow with momentum flux

directly into the bell mouth, a series of metal gauzes were placed over the entrance to the bell mouth. These gauzes reduced the momentum flux of the Laskin nozzle output.

The jet flow was illuminated using a vertical laser sheet with a width of approximately 1 mm. This laser sheet was produced by a near infra-red 808 nm pulsed diode laser (Oxford Lasers 'Firefly') with sheet forming optics and a maximum output of 3 Watts at a 1% duty cycle. Images were then captured using an IDT Y4-S2 high speed camera, capable of recording 1 mega-pixel images at up to 4500 frames per second. The camera was used to trigger the laser pulse, thereby synchronising these two pieces of equipment. A visual inspection of the recorded images led us to choose a laser pulse duration of 40 µs, while the pulse rate of the laser and the frame rate of the camera were dependant on the source volume flux and lay between 200 Hz and 600 Hz.

Flow visualisation was carried out in the $x-y$ plane, where y-axis corresponds to $r(\theta = \pi/2)$ (i.e. slices along the jet, see coordinate system marked on figure 2.2). For these recordings the laser was vertically aligned along the symmetry axis of the nozzle, and the camera was located perpendicular to the laser sheet such that the images captured extended between $0 \lesssim x/D_o \lesssim 5$.

2.4 Particle image velocimetry (PIV)

In this section the details of our particle image velocimetry experiments, which were used to obtain velocity measurements, are discussed. The intention is not to provide a discussion on the theory and analysis underpinning PIV, this has been discussed extensively in the literature and we point the interested reader to the work of Raffel et al. (2007). Rather, the goal of this section is to provide the reader with details specific to our experimental set-up and, thereby, provide a helpful tool for those who may wish to carry out similar experiments in the future.

The equipment used for both planar and stereoscopic PIV was identical. These two techniques instead differ in the arrangement of the equipment (see §2.4.4 and §2.4.5) and the algorithm used to process the recorded images. Firstly, with regards to seeding the test chamber for PIV measurements, provided the individual particles can be distinguished, increasing the number of particles within the PIV interrogation windows results in a greater probability of detecting valid velocity vectors and reduces the measurement uncertainty (Raffel et al., 2007). In order to seed the test chamber, prior to commencing experiments, we used a combination of the Laskin nozzle and a desk fan. The desk fan was used to mix the seeded air that issued from the Laskin nozzle with the ambient air in the chamber, and the Laskin nozzle itself was operated for approximately 20 seconds. This operating time, chosen through a process of trial and error, achieved an appropriate particle density. The jet flow was illuminated using a vertical laser sheet of approximately 1 mm in width which was produced by a 532 nm

Nd:YAG laser (Litron Lasers Nano L 200-15 PIV twin cavity) with sheet forming optics. The two cavities of the laser permitted two 10 ns pulses in rapid succession; each cavity had a maximum pulse rate of 15 Hz, with a power output of 200 mJ per pulse. Images of the flow were captured using 5.5 mega-pixel Imager sCMOS cameras. The number of cameras used and the details of the lenses used (e.g. focal length, aperture) varied between experiments (see §2.4.4 and §2.4.5 for further discussion). During image acquisition the camera lenses were fitted with a 532 nm narrowband filter. The narrowband filter ensured the camera only received light from the laser. The camera and laser were synchronised using a programmable timing unit (PTU) with a "double frame double exposure" method (LaVision, 2014). This recording method results in the two sequential laser pulses being recorded on two sequential frames. The duration between successive laser pulses was set so as to ensure a maximum particle displacement of approximately 7 pixels between successive images. The choice of particle displacement is a compromise between two competing influences. The absolute uncertainty in the particle displacement is approximately constant (for displacements greater than 0.5 pixels) and therefore the relative uncertainty reduces with greater particle displacements (Raffel et al., 2007). However, increased individual particle shifts make the displacement of the group of particles (contained within an interrogation window) more difficult to identify.

2.4.1 Calibration

Calibration of the PIV system was performed using the DaVis calibration tutorial, employing the LaVision two-level calibration plate (type 309-15) of dimensions 0.309 m $\times$ 0.309 m. Two methods of calibration were available - a pinhole camera model and, if the calibration plate spanned the whole field of view, a 3rd order polynomial model. For the majority of measurements a pinhole camera model was used, with the exception of stereoscopic PIV measurements with sufficiently small fields of view (i.e. close to the nozzle $x \leq 3D_o$). The choice of a 3rd order polynomial model for these measurements was informed by its improved accuracy for stereoscopic measurements (Fei & Merzkirch, 2004). The difference between these two calibration methods is discussed further and quantified in §3.3.3. The self-calibration procedure was iterated several times when performing stereoscopic PIV.

The average deviation, given by the DaVis software during the calibration procedure, quantified the quality of the calibration. In our experiments we ensured that the average deviation remained below 1 pixel. According to LaVision (2014), values below 1 pixel are considered to be good and thus, we can infer that the calibration was of good quality. In addition, when the pinhole camera method was applied, the calibration parameters were used to reconstruct (within the DaVis software) the relative locations of the camera and calibration plate. This allowed us to check the alignment of camera and calibration plate, as well as to

check the validity of the calibration by comparing the reconstructed locations to the actual experimental set-up.

2.4.2 Data acquisition

While a detailed discussion regarding the quality of our recorded vectors is given in §3, at this stage it is worth pointing out that all reasonable steps were taken to ensure that our data was of good quality. Prior to data acquisition, checks were made using the DaVis software to ensure strong correlation peaks and an absence of peak locking. Visual inspection revealed that spurious vectors, of which there were very few, were primarily situated at the corners of the domain and away from the region of interest. Furthermore, an almost identical experimental set-up, using a circular source with the same geometry and source conditions to those studied by Hussein et al. (1994), was used to validate our PIV measurement system (discussed in Appendix A). The close agreement between the results from these round-jet experiments and those of Hussein et al. (1994) provides a high degree of confidence in the experimental set-up and technique. To examine the differences between the jet issuing from a slender open-core annular source and the jet issuing from a circular source, in §4 the results obtained from the round-jet experiments are compared with the ventilated-annular-jet measurements.

The frame buffer was limited to capturing 2500 full resolution images in a single recording session. Therefore, for the planar PIV, where two images were required for each dataset, a total of 1250 datasets were acquired. For stereoscopic PIV, where 4 images were required for each dataset (two from each camera), a total of 625 datasets were acquired. All datasets were acquired at 15 Hz. This recording procedure was found to be sufficient for obtaining meaningful estimates of time-averaged quantities (specifically the time-averaged axial $\bar{u}$ and radial $\bar{v}$ velocities) and turbulent statistics (the standard deviation of the axial σ_u and radial σ_v velocity fluctuations), see §3.3.2.

2.4.3 Processing

"Double frame double exposure" PIV makes use of cross-correlation techniques, on a sequential image pair, to calculate the velocity vectors by determining the bulk motion of particles within the intensity fields, see Raffel et al. (2007) for details. The images of the seeded flow were processed and velocity vectors calculated using LaVision's DaVis 8.2.1 software as follows. Images were pre-processed with an 8 pixel sliding background subtraction, a high-pass filter which subtracts the local mean background values of intensity and, thereby, increases the strength of the correlations. Following this, a multi-pass cross-correlation algorithm was used, with one pass using an interrogation window size of 64×64 pixels, and then two passes at a size

of 32×32 pixels with a 50% overlap. A 'standard' PIV algorithm (via FFT, no zero-padding) was used for the first pass, and the second two passes used a 'normalised' algorithm in 'high accuracy' (B-spline-6 reconstruction) mode. The first two passes were post-processed by removing spurious vectors using a two-stage median filter and filling empty vectors using interpolation. No post-processing was applied to the final pass. For the planar PIV, the final passes were weighted using a 2:1 elliptical Gaussian weighting function along the x-axis.

2.4.4 Planar PIV

The majority of measurements were recorded were using planar PIV. Planar PIV allows the reconstruction of the in-plane velocity components from a single sequential image pair. For these measurements, the camera was positioned perpendicular to a vertical laser sheet aligned with the symmetry axis of the nozzle, see the schematic in figure 2.3. Data was thereby captured in a plane centred on the nozzles longitudinal axis, i.e. the u and v components captured on the $x-y$ plane, where the y-axis corresponds to $r(\theta = \pi/2)$. To capture the behaviour of the jet, both far from the source and in the near field whilst maintaining accuracy, up to four overlapping windows (referred to as FOVs, 'fields of view') of increasing size were used as depicted in figure 2.5 (the approximate coordinates of the FOVs are given in table 2.3). This arrangement enabled the time-averaged data collected to be combined into a single dataset spanning the entire measurement domain but with the penalty that the spatial resolution of the data decreased with increasing window size, see table 2.3. The exact location of the camera, in relation to the nozzle, depended on the window location and window size. For some experiments, an additional planar PIV measurement window (referred to as NE, 'nozzle exit') was located immediately downstream of the slot in order to examine the flow at the slot exit. For capturing the four overlapping main PIV windows, the camera was fitted with a Nikon 50 mm lens at f/4. For capturing the flow at the nozzle exit window, the camera was fitted with a Tokina 100 mm macro lens at f/8. The velocity vectors were then imported into MATLAB for analysis. Small vertical (< 10 mm) and rotational ($< 2^\circ$) corrections were made to align the measurements captured on the different field of views.

Alignment

The main aim of our planar PIV experiments was to obtain measurements along the symmetry axis of the flow. Therefore, a key part of acquiring useful results is to ensure that the jet, laser and camera are aligned. To align these components, at this stage, we assumed that the jet issues perpendicular to the face of the nozzle (i.e. perpendicular to the plane ($x = 0,\ r,\ \theta$) and therefore that we can align the nozzle in lieu of the jet. This assumption is implicitly confirmed

FOV	$\frac{x_{min}}{D_o}$	$\frac{x_{max}}{D_o}$	$\frac{y_{min}}{D_o}$	$\frac{y_{max}}{D_o}$	Vector resolution (mm)
NE	0.0	0.2	0.4	0.6	0.1
1	0.0	1.8	-0.8	0.8	1.1
2	1.5	4.5	-1.3	1.3	1.9
3	4.1	9.4	-2.3	2.3	3.4
4	8.7	16.1	-3.1	3.1	4.7

Table 2.3: Planar PIV measurement domains. Entries give the approximate coordinates for the fields of view (FOVs) used in these experiments (and illustrated on figure 2.5). NE refers to the field of view immediately adjacent to the *n*ozzle *e*xit. The vector resolution has been determined from the PIV data.

in §3.3.1, where we verify that we have aligned the flow and laser correctly. Given the number of components, and the degrees of freedom, the process of alignment was complex. The key steps are outlined below.

1. The laser was positioned as close to wall **BC** as practicable, so as to maximise the possible measurement domain, and the laser sheet then aligned such that it is parallel to wall **CD**.

2. Using the live images, the camera was positioned such that it would capture the required field of view. To align the camera perpendicularly to the laser sheet, a levelled calibration plate was placed in, and parallel to, the laser sheet. On the calibration plate, the point at which a straight line, drawn perpendicular to the laser sheet, would intersect the focal point of the camera was marked. Then, using a live feed from the camera, the pitch and yaw of the camera was adjusted so as to centre (within the camera image) the point at which we marked the calibration plate. Finally, we adjusted the roll of the camera, until the calibration marks on the live image were horizontal.

3. It was then necessary to focus the camera on the laser sheet. For this, the 532 nm narrowband filter was placed on the camera lens, the ambient air was seeded and the laser switched on. The live feed was then used to focus the camera on the seeding particles.

4. Aligning the nozzle was more complex due to its curved outer surface. First, the nozzle was adjusted such that the laser sheet bisected the face of the nozzle (to an accuracy of approximately $\pm$ 1 mm). Following this, we aligned the nozzle such that it was parallel to

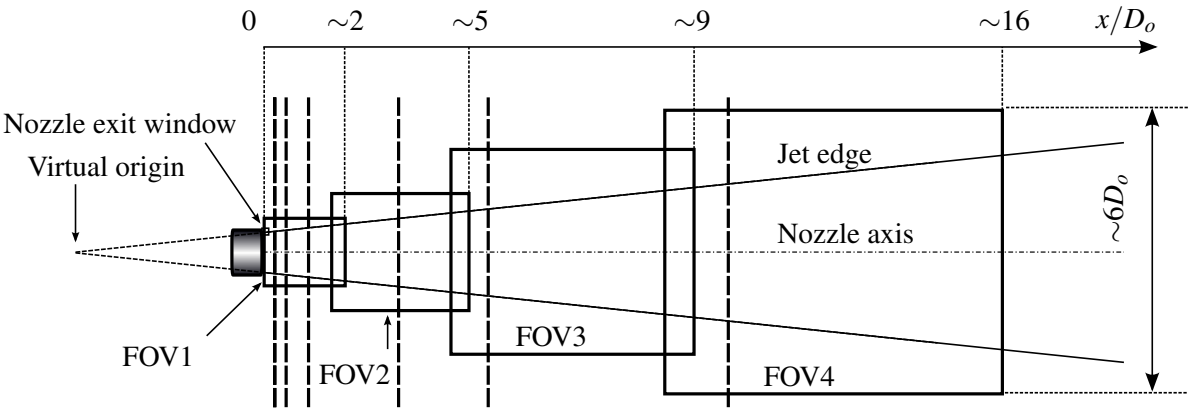

Fig. 2.5: The positions of the four overlapping rectangular planar PIV measurement windows (FOV1-FOV4) and the nozzle exit (NE) window; precise locations and window dimensions varied slightly between sets of experiments. The time-averaged jet perimeter and virtual origin are superimposed to indicate where the jet falls relative to each window. The location of $r-\theta$ sections, perpendicular to the x-axis of the nozzle and used for stereoscopic PIV, are marked by vertical dashed lines.

the floor, by aligning the face of the nozzle with the vertical edge of a levelled calibration plate. A rigid transparent cylindrical Perspex tube, of length 1 m and diameter 60 mm, was rested in the open core of the nozzle. This tube would naturally point along the x-axis of the nozzle. Therefore, by adjusting the nozzle such that the laser sheet simultaneously bisected (to an accuracy of approximately $\pm$ 1 mm) both ends of the Perspex tube and the nozzle itself, the nozzle was successfully aligned with wall **CD**.

This method of aligning the equipment for planar PIV measurements was validated and found to be good by making comparisons with stereoscopic PIV measurements, see §3.3.1. Furthermore, in §3.5.2 we show that the errors associated with misalignment are small.

2.4.5 Stereoscopic PIV

Where we deemed it necessary, our planar PIV measurements were complemented with stereoscopic PIV measurements made on $r-\theta$ planes. Stereoscopic PIV uses two sequential image pairs, acquired simultaneously from separate perspectives, to reconstruct all three velocity components on a plane. Thus, two cameras were required. As illustrated on figure 2.6, we positioned the cameras downstream of the laser sheet in a backward- forward- scattering

arrangement (i.e. on either side of the jet). This downstream placement ensured that the cameras would not influence our recorded measurements.

We chose to examine a number of $r-\theta$ planes along the length of our planar PIV measurement domain, at $x/D_o = \{0.25,\ 0.5,\ 1.0,\ 3.0,\ 5.0,\ 10.0\}$, positions indicated by vertical dashed lines on figure 2.5. For these measurements, the laser sheet was positioned such that it was perpendicular to the x-axis of the nozzle. The optical axes of the cameras were at an angle η to the normal of the laser sheet (and therefore at an angle η to the x-axis of the nozzle). According to LaVision (2014), for best results $30^\circ \lesssim \eta \lesssim 35^\circ$. For our measurements $26^\circ \leq \eta \leq 31^\circ$, deviating from the ideal angle range due to the constraints imposed by the experimental equipment and the test chamber itself. Positioning and aligning the cameras proved to be the most involved part of setting up stereoscopic PIV experiments. Therefore, in the interest of time, we utilised two (differently sized) fields of view (in which the cameras and laser remained stationary) and moved the nozzle to capture the desired $r-\theta$ sections. The smaller field of view, referred to as STFOV1, had an approximate size of $2.2D_o \times 1.8D_o$ and was used to capture $r-\theta$ sections at $x/D_o = \{0.25,\ 0.5,\ 1.0,\ 3.0\}$. For this field of view the cameras were at an angle $\eta = 31^\circ$ and a 3rd order polynomial model was used for calibration. The larger field of view, referred to as STFOV2, had an approximate size of $6.0D_o \times 5.0D_o$ and was used to capture $r-\theta$ sections at $x/D_o = \{3.0,\ 5.0,\ 10.0\}$. For this field of view the cameras were at an angle $\eta = 26^\circ$ and a pinhole camera model was used for calibration.

Both cameras were equipped with Nikon 50 mm lenses. It was necessary to vary the aperture of these lenses due to the forward- backward- scatter arrangement. With respect to figure 2.6, Camera 2 is recording light that is forward scattered and Camera 1 is recording light that has been backward scattered. The intensity of backward scattered light is lower when compared to the intensity of forward scattered light (LaVision, 2014). Therefore, to match the intensities recorded by the cameras, the aperture of Camera 1 was set to f/2.8 and the aperture of Camera 2 was set to f/5.6. A Scheimpflug mount (LaVision, 2014), placed between each lens/camera pair, permitted us to uncouple the image plane of the camera and the lens plane. Thus, we could align the focal plane of the camera with the laser sheet.

Alignment

Given the differences in the experimental set-up between the planar and stereoscopic PIV experiments, the process of alignment also differed. The key steps are outlined below.

1. The laser was positioned at the required plane and we ensured that the laser sheet was parallel to wall **AD**.

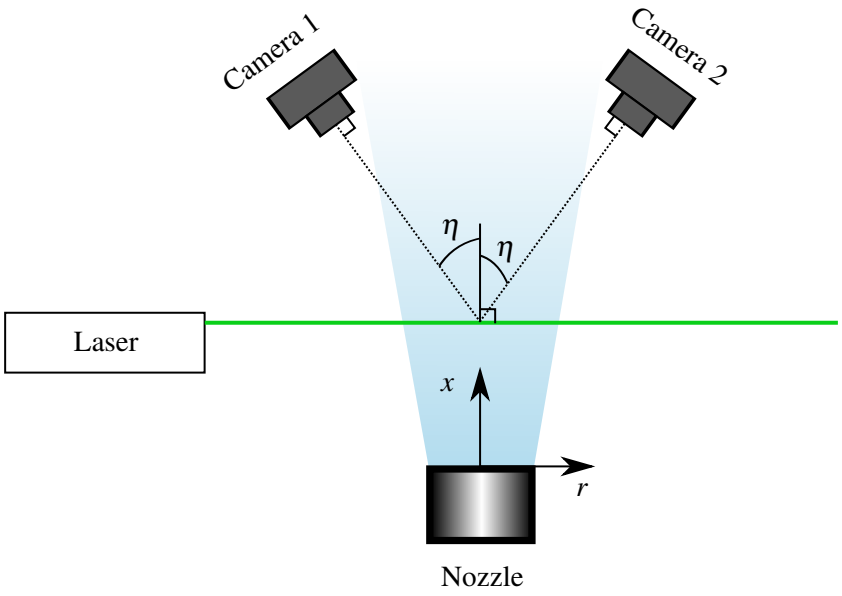

Fig. 2.6: A plan view schematic (not to scale) showing the layout of the cameras, laser and nozzle used for stereoscopic PIV. Camera 1, recording backward-scattered light, had an aperture of f/2.8. Camera 2, recording forward-scattered light, had an aperture of f/5.6. The **green** line represents the vertical laser sheet. The jet produced by the annular nozzle is represented by the shaded blue region.

2. Next, using a combination of the live feed from the camera and trigonometry, we positioned the cameras such that they were at the desired angles and would capture the desired field of view. A levelled calibration plate was placed in, and parallel to, the laser sheet. Then, both cameras were adjusted so that camera images were centred on the same point on the calibration plate (i.e. ensuring that the optical axes of the cameras intersected at plane of the laser sheet).

3. Using a live feed from the camera, we then adjusted the Scheimpflug mount such that the focal plane of the camera was parallel to the calibration plate (and thus the laser plane). It was then necessary to focus the camera on the laser sheet. For this, the 532 nm narrowband filter was placed on the camera lens, the ambient air was seeded and the laser switched on. The live feed from the camera was then used to focus the image on the seeding particles.

4. To align the source, we adjusted the nozzle until its face was parallel to wall **AD**, thereby ensuring that the x-axis of the nozzle was perpendicular to the laser sheet. Practically, this was achieved by measuring the distance between the wall and three points on the face of the nozzle. Given that the nozzle diameter ($\sim$ 100 mm) and the relatively low

accuracy of the tape measure ($\pm$ 1 mm at best), this method of alignment was likely to be less accurate than that discussed in §2.4.4. However, given that the stereoscopic measurements capture the entire cross-section of the jet, the relative influence of any small misalignments on our results will be less than the influence of *small* misalignments on the planar PIV results.

CHAPTER 3

Diagnostics and quality control

Preamble

Before presenting and analysing the results obtained using the experimental set-up outlined in §2, it is prudent to define the diagnostics used and to check that our measurements are of good quality. While some of the checks performed have been outlined in concert with the experimental set-up (e.g. the jet length, §2.2.3), those that are more involved, and require the use of data extracted from experiments, are discussed here. The checks here are threefold:

1. to determine what information can be usefully extracted from measurements made using the experimental set-up. In §3.1 we discuss the resolution of our measurements and define the key diagnostics used herein;

2. to ensure that the flow exiting from the nozzle meets capability #1 set out in §2. In other words, that the flow approximates to a non-swirling axisymmetric turbulent jet issuing into an unbounded environment. These checks are discussed in §3.2; and

3. to ensure that the data captured is suitable for our later analysis. This includes checking that our apparatus is aligned correctly and verifying that good estimates of the time-averaged quantities can be attained. These checks are discussed in §3.3.

These checks are best performed with measurements obtained using our experimental set-up to examine the flow of interest. To this end, even though we have not yet evaluated the flow issuing from a slender open-core annular nozzle, in §3.1-3.3 we primarily use data captured during the experiments outlined in §4. These experiments examined the slender open-core annular jet issuing from source **N4R5V1**, which has $D_i/D_o = 0.968$ and $D_v/D_i = 0.90$. Table 3.1 summarises the source conditions used. Where data from other experiments has been utilised

Source	D_i/D_o	D_v/D_i	Q_0 ($m^3\ s^{-1}$)	U_0 ($m\ s^{-1}$)	ΔT (°C)	Re_l	Re_f
N4R5V1	0.968	0.90	0.0153	29.5	15.0	$3200 \pm 5\%$	$45000 \pm 5\%$

Table 3.1: A summary of the source conditions used for the checks presented in §3.1-3.5. These source conditions were also used for the experimental results presented in §4, see tables 2.1 and 4.1 for more details. Reynolds numbers, $Re_l = U_0 l/\upsilon$ (1.1) and $Re_f = \sqrt{M_0}/\upsilon$ (1.2), are those estimated based on a kinematic viscosity for air at 20°C of $\upsilon = 1.5 \times 10^{-5}\ m^2\ s^{-1}$ (Batchelor, 1967) and on assuming a uniform exit velocity $U_0 = Q_0/A_0$.

(3.4-3.5), the source conditions are outlined in the relevant section. The vast majority of the quantitative information reported in this thesis has been extracted from PIV measurements, therefore the analysis presented here will focus on and use the PIV data. The results and conclusions of the quality control checks presented here are representative of all measurements reported herein.

Note that, while the quantities presented here have been used to ensure our experiments are of good quality, a subset provide key information on the flow of interest and are discussed in the relevant chapter. For example, estimates of the momentum integral, which in §3.2.1 are used to confirm that the boundaries of the test chamber do not unduly effect the flow, are discussed in more detail in §4.3.1.

This chapter also provides a good opportunity to examine aspects of the flow that are of incidental interest. For example, in §3.4, we examine the influence of the slot Reynolds number on the flow. Finally, in §3.5, we quantify the errors associated with our measurements.

Italicized text at the end of each subsection (with the exception of §3.1.1 and §3.5) provides a summary of the key points discussed therein.

3.1 Extraction

3.1.1 Definitions

The key diagnostics used are defined below. The time-averaged axial velocity $\bar{u}$ and the standard deviation of the axial velocity fluctuations σ_u are

$$\bar{u}(x,r,\theta) = \frac{1}{n_{av}} \sum_{n=1}^{n_{av}} u(x,r,\theta,n), \tag{3.1}$$

$$\sigma_u^2(x,r,\theta) = \frac{1}{n_{av}} \sum_{n=1}^{n_{av}} \big(u(x,r,\theta,n) - \bar{u}(x,r,\theta)\big)^2, \tag{3.2}$$

where u is the instantaneous axial velocity, n is the dataset number and n_{av} is the total number of datasets that were averaged; the time-averaged radial velocity $\bar{v}$, the time-averaged azimuthal velocity $\bar{w}$, associated standard deviations σ_v and σ_w are calculated similarly.

Denoting the radius of the flow induced through the core as $r_i(x)$, a sectional average for the mean streamwise velocity within the bounded induced-flow region $\bar{u}_i(x)$ and the associated standard deviation $\sigma_i(x)$ were evaluated as

$$\bar{u}_i(x) = \frac{1}{\pi r_i^2} \int_0^{2\pi} \int_0^{r_i} \bar{u}(x,r,\theta) r \, \mathrm{d}r \, \mathrm{d}\theta, \tag{3.3}$$

$$\sigma_i^2(x) = \frac{1}{\pi r_i^2} \int_0^{2\pi} \int_0^{r_i} \big(\bar{u}(x,r,\theta) - \bar{u}_i(x)\big)^2 r \, \mathrm{d}r \, \mathrm{d}\theta. \tag{3.4}$$

Note that at the source $r_i(0) = D_i/2$; elsewhere, we define r_i by $\sigma_u(x,r_i,\theta)/\bar{u}_{max}(x) = 0.05$, with $\bar{u}_{max}(x)$ denoting the maximum streamwise velocity on the $r-\theta$ plane.

The high-velocity centreline is located at $r = r_c$, the radial location on which the velocity magnitude $\sqrt{\bar{u}^2 + \bar{v}^2}$ is at a maximum. The width b of the external jet envelope is defined such that $\bar{u}(x,b) = \bar{u}_c(x)/e$ for $r > r_c$, where u_c is the axial velocity along the high-velocity centreline and $\ln(e) = 1$.

The key diagnostics used herein to describe the coalescing behaviour of the jet are marked on the schematic shown in figure 3.1 and defined below. The volume flux through the open core Q_a is evaluated by integrating the (time-averaged) velocities at the source

$$Q_a = \pi \int_{-D_i/2}^{D_i/2} \bar{u}(x=0) y \, \mathrm{d}y, \tag{3.5}$$

where the coordinate y has been used to highlight that this quantity has been estimated from planar PIV measurements. The velocity through the open core U_a is calculated by dividing the

induced volume flux Q_a by the area of the open core A_v $(= \pi(D_v/2)^2)$,

$$U_a = Q_a / A_v. \tag{3.6}$$

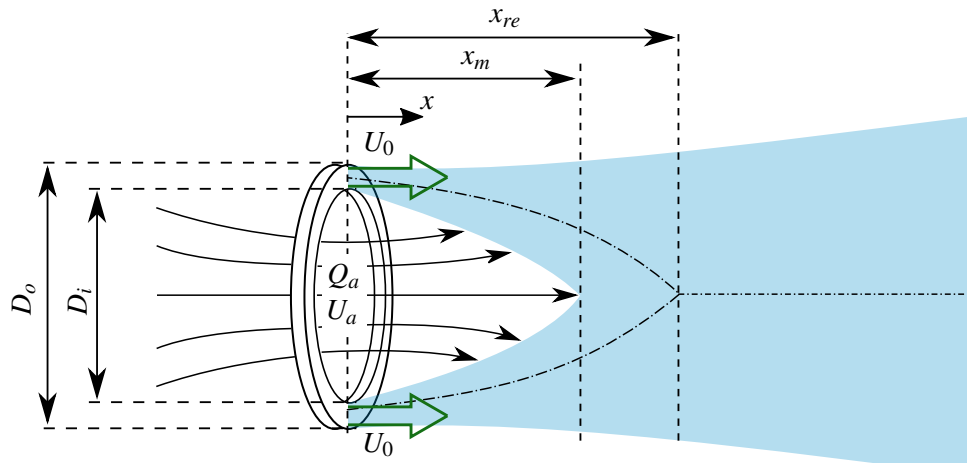

Fig. 3.1: Schematic depicting a time-averaged streamwise section through the jet issuing from a fully open-core annular source, showing the key diagnostic quantities (Q_a, U_a, x_{re} and x_m) used to describe coalescing behaviour of the flow. The shaded region indicates the main body of the jet. The high-velocity centrelines are indicated by the dot-dashed line. The steady exit velocity U_0 is perpendicular to the plane of the source as indicated. Relative locations at which the inner shear layers intersect ($x = x_m$) and at which the high-velocity centrelines intersect ($x = x_{re}$) are indicated.

The two length scales marked on figure 3.1 are defined as follows: the merge point, located at $x = x_m$, describes where the inner shear layer of the jet merges and; the reattachment point, located at $x = x_{re}$, describes where the jet has completed coalescing (i.e where the high-velocity centreline merges). As will be discussed in §4, there are multiple sensible definitions for the merge point. As per Warda et al. (1999), the reattachment point x_{re} is located where $\bar{u}(x,0)$ reaches a maximum; before the reattachment point the high-velocity centreline is coalescing and the velocity is increasing, subsequently, beyond the reattachment point the velocity begins to decay.

3.1.2 Resolution

A comparison of a length scale characteristic of the local turbulence with the spatial resolution of our data reveals that we are able to resolve, in detail, the velocity field of the annular jets issuing from our sources. Following Ezzamel et al. (2015), the length scale characteristic

FOV	b/R_r	τ/R_t	Average deviation (pixels)
NE	8	0.006	0.206
1	2-50	0.006-0.6	0.642
2	30-35	0.6-1.1	0.614
3	20-30	1.1-1.4	0.392
4	20-40	1.4-1.5	0.283

Table 3.2: The relative resolution and average deviation for the planar PIV windows (NE and FOV1-FOV4, see table 4.2) on which measurements of the jet issuing from source **N4R5V1** were recorded. The second and third columns show the ratio of the length scale for the flow b to the spatial resolution of the velocity vectors R_r and ratio of the timescale for the flow τ to the temporal resolution R_t (see §3.1.2). The fourth column shows the average deviation obtained during the calibration procedure (see §3.3.3).

of the local turbulence was taken to be the local jet width b. For the jet issuing from source **N4R5V1**, the jet width varied from a minimum of $b \approx l \approx 2$ mm adjacent to the nozzle (**N4** in table 2.1) to a maximum of $b \approx 180$ mm downstream (figure 4.17a). Accordingly, the spatial resolution R_r of the data is at least one order of magnitude less than the characteristic turbulent length scale in each field of view (second column of table 3.2). By contrast, a comparison of a characteristic flow timescale τ with the temporal resolution R_t of our data reveals that the resolution is not sufficient to extract turbulence spectra. A representative timescale for the flow ($\tau = b/\sigma_{uc}$) was estimated based on the local characteristic length and velocity scales, the latter taken to be the standard deviation of the horizontal centreline velocity (σ_{uc}); the subscript 'c' denotes centreline. The velocity scale was ~ 5 m s^{-1} adjacent to the source and ~ 0.5 m s^{-1} at the furthest measured downstream location (in FOV4). As a consequence, turbulent timescales are approximately $\tau = 1 \times 10^{-3}$ s adjacent to the source and $\tau = 0.1$ s at the furthest downstream measurement location. Therefore, at 15 Hz, the temporal resolution of our data was not sufficient to extract spectral information (see the penultimate column of table 3.2).

In short, the spatial resolution of our dataset allows us to extract detailed information regarding the spatial variation of velocity, while the temporal resolution is not sufficient for extracting spectral information.

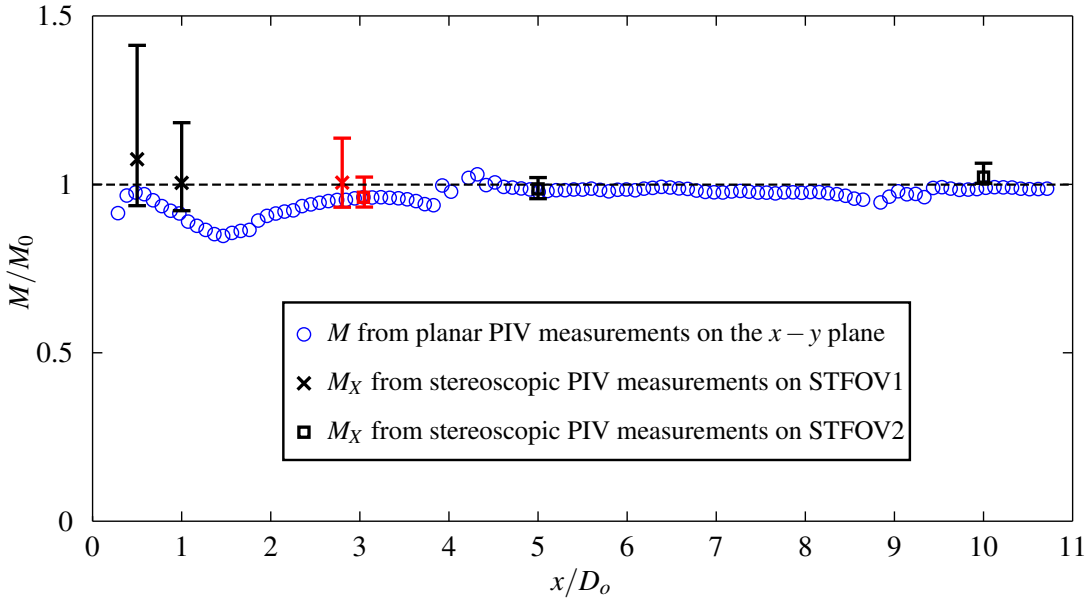

Fig. 3.2: The variation of specific momentum integrals with distance downstream x/D_o in the jet produced by source **N4R5V1**. The estimates of M/M_0 shown with the symbol '$\circ$' have been calculated using (3.7) on the $x-y$ plane captured by our planar PIV measurements. Estimates of M_X/M_0, calculated using (3.9), on the smaller stereoscopic $r-\theta$ section (STFOV1, see §2.4.5) are indicated with '$\times$' and estimates of M_X/M_0 obtained from the larger stereoscopic $r-\theta$ section (STFOV2) are indicated with '$\square$'. 'Handle bars' represent the range of values obtained when calculating the momentum integral M_θ/M_0 on a 'virtual' planar PIV slice rotated about the origin, see (3.8) and §3.2.2. The two stereoscopic measurements marked in red, '$\times$' and '$\square$', were both recorded at $x/D_o = 3$ and have been separated for clarity. The dashed line '- - - -' marks $M/M_0 = 1$.

3.2 The quality of the flow

3.2.1 A free jet

For an isothermal free jet we expect the momentum integral to be independent of the distance downstream. Hussein et al. (1994) note that a subset of experiments reported in the literature have been performed in test chambers of insufficient size, and are therefore significantly influenced by the return flow interacting with the jet, i.e. the momentum integral was not conserved with distance downstream. Estimates of the momentum integral can therefore be used to determine whether the flow has been influenced by the test chamber.

If our experiment is aligned correctly (§3.3.1) and the time-averaged flow is axisymmetric (§3.2.2), our planar PIV measurements reside upon a representative plane. We may then make estimates of the specific momentum integral from our planar PIV measurements using (1.10)

on assuming $\overline{v'^2} = \overline{w'^2}$ (Wang & Law, 2002), i.e. on the $x-y$ plane

$$M(x) = \pi \int_{-\infty}^{\infty} \bar{u}^2 y \, \mathrm{d}y + \pi \int_{-\infty}^{\infty} (\overline{u'^2} - \overline{v'^2}) y \, \mathrm{d}y. \tag{3.7}$$

The variation with x of the non-dimensional momentum integral M/M_0 for the jet produced by source **N4R5V1** is shown in figure 3.2 with the symbol '$\circ$'. For $x/D_o \lesssim 4$ estimates of the normalised momentum integral are significantly below unity. The discrepancy in the momentum integral estimates across the length of the jet ($\sim 10-15\%$) is smaller than the uncertainty in our measurements of momentum integral ($\pm$7-20%, see table 3.9). Thus it is not clear whether this discrepancy is real, or a result of experimental error. Adding to the confusion, there are several possible reasons for this discrepancy, which make it even more difficult to draw firm conclusions: near-source flow asymmetries (see §3.2.2); the dynamics of jet coalescence (the reattachment point falling at $x/D_o \approx 4.5$, see §4); the chosen fields of view (which overlap at $x//D_o \approx 4$, see §2.4.4); and the assumption that the jet is thin, made when deriving (3.7), which does not hold in the near-field of the jet (see §1.4.1). Further downstream, for $x/D_o \gtrsim 4$, the momentum integral is equal to unity (within experimental uncertainty) and remains constant with distance downstream.

Observations that the momentum integral is conserved with distance downstream confirm that the flow is not significantly influenced by the test chamber.

3.2.2 Symmetry and swirl

To determine whether the nozzle produced a time-averaged flow that could be regarded as axisymmetric, we have made the use of stereoscopic PIV measurements taken on several $r-\theta$ planes. We begin by making a qualitative assessment of the flow symmetry, before quantitatively examining how asymmetries would influence planar PIV measurements obtained on the $x-y$ plane.

Figure 3.3 presents contour plots of the time-averaged axial velocity $\bar{u}(x = const., r, \theta)$ in the jet issuing from source **N4R5V1**, obtained using stereoscopic PIV, on four $r-\theta$ sections located at $x/D_o = \{0.5,\ 1.0,\ 3.0,\ 5.0\}$. Near the source, at $x/D_o = \{0.5,\ 1.0\}$ (figure 3.3a-b), a series of local minima in the velocity are visible at intervals of approximately 22-23°, these coincide with the location of the flow-straightening vanes. The presence of these minima suggests that caution should be taken when interpreting results near the source. Despite this, the visual assessment indicates that the flow shows remarkable symmetry. Further downstream of the source, at $x/D_o = \{3.0,\ 5.0\}$ (figure 3.3c-d), the local minima are no longer present. In this region the flow appears to be more symmetrical. The reduction of the asymmetries with x is attributed to the mixing within, and the merging of, the flow.

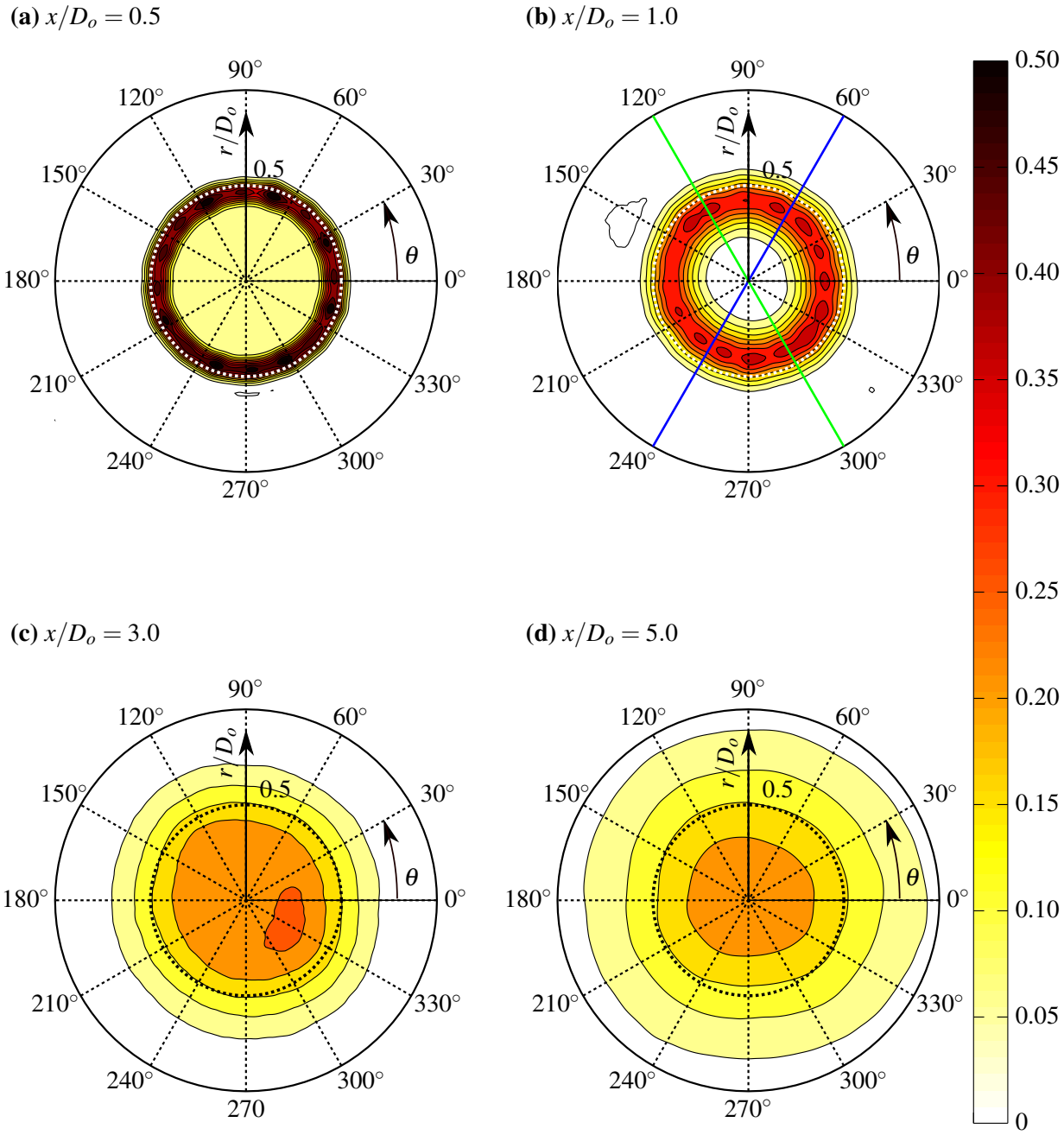

Fig. 3.3: Contour plots of the time-averaged axial velocity $\bar{u}(r,\theta)$, captured using stereoscopic PIV on $r-\theta$ planes located at $x/D_o = \{0.5,\ 1.0,\ 3.0,\ 5.0\}$ (a-d, respectively), in the jet issuing from **N4R5V1**. The colour bar indicates the non-dimensional axial velocity $\bar{u}/U_0$. The green and blue lines on (b) correspond to the lines of the same colour on figure 3.4.

To quantitatively assess the influence of the asymmetries on our planar PIV measurements, we calculate estimates of the specific momentum integral from our stereoscopic $r-\theta$ sections using (3.7) along lines of constant θ, while also varying θ between 0 and π. In other words, we have calculated momentum integral estimates along 'virtual' planar PIV slices, rotated about the origin. The full form of the equation used to calculated these momentum integral estimates is then

$$M_\theta(x,\theta) = \pi \int_{-\infty}^{\infty} \bar{u}(x,\tilde{y},\theta)^2 \tilde{y}\, \mathrm{d}\tilde{y} + \pi \int_{-\infty}^{\infty} [\overline{u'^2}(x,\tilde{y},\theta) - \overline{v'^2}(x,\tilde{y},\theta)]\tilde{y}\, \mathrm{d}\tilde{y}, \tag{3.8}$$

where the integral is formed by summing data along the line $\tilde{y} = r(\theta)$, $0 \leq \theta \leq \pi$ and $x/D_o = \{0.5,\ 1.0,\ 3.0,\ 5.0,\ 10.0\}$. The variation of M_θ with θ, for the stereoscopic plane located at $x/D_o = 1.0$ (figure 3.3b), is shown on figure 3.4. For the purposes of illustration, the 'virtual' planar PIV planes at $\theta = \{60^\circ,\ 120^\circ\}$ are indicated on figures 3.3(b) and 3.4 with blue and green lines. At this value of x/D_o, it is clear that the choice of angle θ at which the longitudinal planar PIV section bisects the nozzle may significantly influence estimates of the momentum integral made using (3.7). The range of M_θ (i.e. maximum peak to minimum trough), for each x/D_o location, is shown on figure 3.2 with 'handle bars'. These 'handle bars' indicate that asymmetries have the potential to significantly influence our measurements of the jet near the source, while further downstream the influence is negligible. Also marked, with '$\times$' and '$\square$', are estimates of the specific momentum integral calculated for each entire $r-\theta$ section using (1.10), i.e.

$$M_X(x) = \int_0^{2\pi}\int_0^{\infty} \bar{u}^2\, \mathrm{d}r\, \mathrm{d}\theta + \int_0^{2\pi}\int_0^{\infty} \left(\overline{u'^2} - \frac{\overline{v'^2}+\overline{w'^2}}{2}\right) \mathrm{d}r\, \mathrm{d}\theta. \tag{3.9}$$

On comparing '$\times$' and '$\square$' and the 'handle bars' in figure 3.2, it is clear that the value of M_X falls within the range encompassed by the 'virtual' planar PIV planes. The coincidence of the source momentum flux ('- - - -') and momentum integral estimates, obtained from both planar ('$\circ$') and stereoscopic PIV ('$\square$'), for $x/D_o \gtrsim 4$ indicates that, far downstream of the source, the chosen $x-y$ plane is representative of the flow. Note that, as $M \propto \bar{u}^2$ (to the first order), estimates of momentum integral accentuate the influence of the asymmetries on our measurements. Thus, the influence of the asymmetries on other quantities of interest (e.g. jet width, volume flux) will be less than on the momentum integral estimates.

The two estimates marked in red on figure 3.2 were both recorded at $x/D_o = 3.0$ and have been offset from each other for clarity. The estimate shown as '$\times$' was recorded on the smaller stereoscopic $r-\theta$ section (STFOV1, see §2.4.5), whereas the measurement shown as '$\square$' was recorded on the larger stereoscopic $r-\theta$ section (STFOV2). The momentum integral estimate

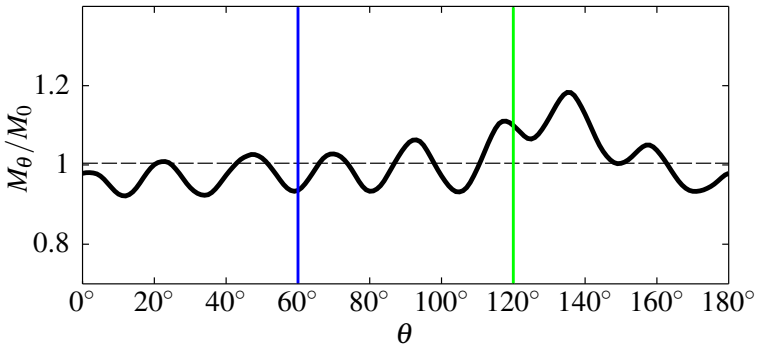

Fig. 3.4: The variation of M_θ with θ for the jet issuing from source **N4R5V1**, on the $r-\theta$ section located at $x/D_o = 1.0$. The horizontal dashed line '- - - -' represents M_X calculated from the whole stereoscopic section using (3.9). The vertical green and blue lines correspond to the lines (of the same colour) on figure 3.3(b).

calculated from STFOV1 is 4.5% larger than the estimate calculated from STFOV2. This difference is attributed to experimental uncertainty, the different resolutions of STFOV1 and STFOV2, and the difference between the calibration methods (see §2.4.1 and §3.3.3).

The planar PIV measurements presented capture the axial u and radial v velocity components on the $x-y$ plane. To establish whether the time-averaged circumferential velocity component $\bar{w}$ is significant, a measure of the degree of swirl within the jet was estimated from the stereoscopic PIV measurements on the $r-\theta$ planes. Chigier & Beer (1964b) compare time-averaged circumferential and streamwise momentum fluxes by means of a dimensionless swirl number S, defined as

$$S = \frac{\int_0^\infty \int_0^{2\pi} \bar{u}\bar{w}r \, \mathrm{d}\theta \mathrm{d}r}{\int_0^\infty \int_0^{2\pi} \bar{u}^2 r \, \mathrm{d}\theta \mathrm{d}r}. \tag{3.10}$$

A value of $S = 0$ corresponds to a section without swirl. Vanierschot et al. (2014) regard a value of $|S| > 0.12$ as corresponding to swirling flows. The largest swirl number we obtain, $|S| = 0.0155$ on the $r-\theta$ plane captured at $x/D_o = 1.0$, is one order of magnitude less than the Vanierschot et al. (2014) swirl number, from which we assert that the time-averaged circumferential velocity is negligible.

Here we have shown that the nozzle produces a time-averaged flow with a remarkably good degree of axisymmetry. The results indicate that caution must be applied when interpreting results for $x/D_o \lesssim 4$, but beyond this point, the chosen $x-y$ plane may be regarded as being representative of the flow. In addition, the influence of the time-averaged circumferential velocity is negligible, and thus, planar PIV measurements on the chosen $x-y$ plane are sufficient to examine the time-averaged flow.

3.2.3 Buoyancy

Given that the driving mechanism heats the source fluid (§2.2.3), it is necessary to check that the influence of this buoyancy may be regarded to be negligible over our measurement domain.

The jet issues, with a temperature of $T_\infty + \Delta T$, parallel to the floor into ambient fluid, of temperature T_∞. The resulting density difference will act to stabilise the jet-ambient interface on the "lower" half of the jet (the half closest to the floor), and destabilise the interface on the "upper" half of the jet (the half furthest from the floor), see figure 3.5. If the influence of buoyancy was non negligible we would expect to see differences in the growth rates of the two halves of the shear layer (i.e. $b_u > b_l$ on figure 3.5). To demonstrate that the source buoyancy flux does not influence our measurements, in figure 3.6 we compare the width of the "lower" ('$\circ$') and "upper" ('$\square$') halves of the shear layer (b_l and b_u, respectively) as measured along a section which vertically intersects the mid-plane of the jet issuing from source **N4R5V1**. The plot has been delineated, using vertical dashed lines, into four separate regions representing FOV1-FOV4, with the resolution of the measurements within each region shown using an error bar. While some systematic differences are observed far from the nozzle, these can be attributed to the resolution of the measurements. The growth rate of the two halves does not appear to differ (i.e. $b_l \approx b_u$) and thus we can conclude that the influence of buoyancy is small within our measurement domain.

Given that the width of the "upper" and "lower" halves of the shear layer do not diverge from one another at the furthest recorded downstream location, one can conclude that the influence of buoyancy is negligible within our measurement domain .

3.3 Validity

3.3.1 Alignment

The examination of stereoscopic PIV measurements recorded on $r-\theta$ sections, in §3.2.2, indicated that the time-averaged flow produced by our slender open-core annular nozzle was reasonably non-swirling and symmetric. Therefore, we can sensibly use planar PIV measurements to examine the development of the time-averaged jet, provided that our measurement plane bisects the jet. During the set up of the planar PIV experiments, described in §2.4.4, all reasonable steps were taken to align the equipment such that the data captured was in this representative plane. Subsequently, data acquired from the experiments in question could be used to verify whether the experiment was correctly aligned. In fact, the information presented in §3.2.1-3.2.2 is sufficient for this verification. As the $r-\theta$ sections capture the entire cross-section of the jet, the influence of any *small* misalignment on the cross-sectional

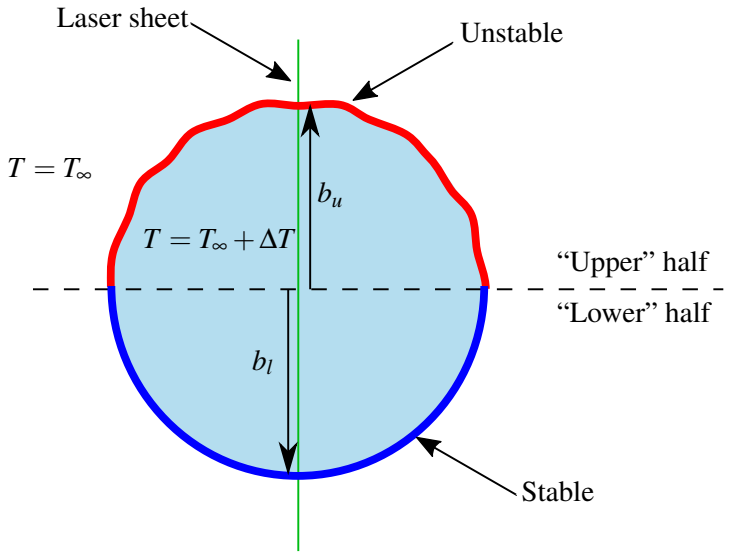

Fig. 3.5: Sketch showing the stable "lower" and unstable "upper" halves of a jet issuing with temperature $T_\infty + \Delta T$ into fluid of temperature T_∞. Also marked are the laser sheet, and the widths (along the laser plane) of the "upper" and "lower" halves of the jet b_l and b_u, respectively. The jet is shaded in light blue, the stable jet-ambient interface in dark blue and the unstable jet-ambient interface in red.

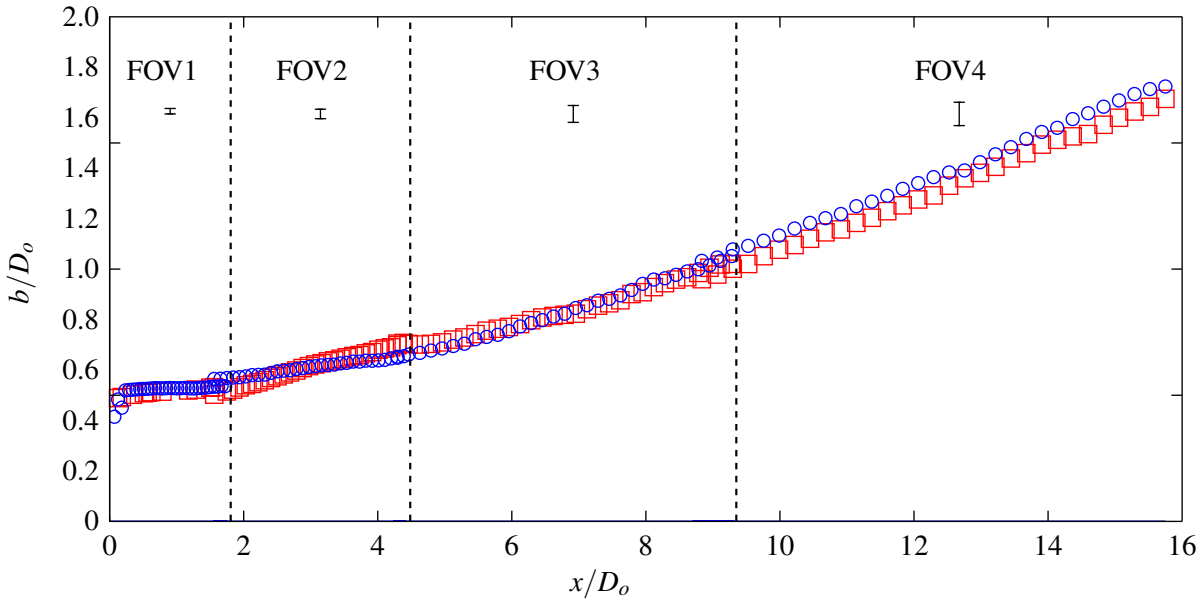

Fig. 3.6: A plot showing the width b_l of the "lower" ('○') half of the jet and the width b_u of the "upper" ('□') half of the jet, for the slender open-core annular jet issuing from source **N4R5V1**. The vertical dashed lines delineate the plot into four regions representing FOV1-FOV4, and the 'handle bars' represent the resolution of the measurements within each FOV.

measurements would be small. This allows one to assess the alignment of the planar PIV sections, by comparing, on figure 3.2, estimates of the momentum integral M calculated from the $x-y$ plane ('$\circ$') to estimates M_X calculated from the $r-\theta$ sections ('$\times$' and '$\square$'). Due to asymmetries near the nozzle (see §3.2.2), for $x/D_o \lesssim 4$, estimates of M and M_X are not coincident (differences as large as 10%). Further downstream, estimates of M concur with those of M_X (with differences less than 2%). This agreement confirms that our planar PIV measurement plane was correctly aligned.

For planar PIV measurements on the $x-y$ plane that have no corresponding stereoscopic PIV measurements on the $r-\theta$ plane, it is still possible to check the alignment of the nozzle using estimates of the momentum integral. The geometrical model presented in Appendix B predicts how misalignment, between the jet centreline and recording plane, would affect measurements of the mean momentum flux. The results of this model directly apply to our estimates of the momentum integral, given that the mean momentum flux is the dominant component of this integral (Hussein et al., 1994). Predictions indicate that angular misalignments result in underestimates of the momentum integral. In addition, if the recording plane and the longitudinal nozzle axis are parallel but not coincident, estimates of the momentum integral will vary with distance downstream. Values of M/M_0 estimated from our planar PIV measurements ('$\circ$' on figure 3.2) are equal to unity, lending support to the conclusion that the planar PIV plane was correctly aligned.

The coincidence of the momentum integral estimates obtained on the $x-y$ and $r-\theta$ planes confirms that the $x-y$ plane was correctly aligned. This confirmation is supported by the fact that estimates of the non-dimensional momentum integral calculated from the $x-y$ plane are conserved and equal to unity (within experimental uncertainty).

3.3.2 Time averaging

Much of the analysis presented herein is based upon a time-averaged 'picture' of the flow. Naturally, at this stage, one may question how we ensure that the time-averaged estimates obtained from our experiments are of good quality. For the purposes of illustration, consider measurements of a turbulent flow in the following two scenarios:

- two datasets, recorded instantaneously at times t and $t+\Delta t$,
- an infinite number of datasets, recorded between t and $t+\delta t$,

where Δt approaches infinity and δt approaches 0. Clearly, averaging the data acquired in either scenario will not yield a good estimate of the time-averaged flow. Both the time period over which data has been recorded and the number of measurements captured are important

in obtaining representative estimates of the time-averaged flow. The required time-averaging period will be a multiple of the local turbulent timescale τ.

To demonstrate that the time-averaged data presented herein is of good quality, here we examine the cumulative axial velocity statistics, $\bar{u}_n(n_{av})$ and $\sigma_{un}(n_{av})$, which represent values obtained using (3.1) and (3.2) while n_{av} is varied between 1 and 1250 (where 1250 is the total number of planar PIV datasets recorded). We calculate the relative difference between $\bar{u}_n$ and $\bar{u}$ using

$$\frac{\Delta\bar{u}_n(n_{av})}{\bar{u}} = \frac{\bar{u}_n(x,r,\theta,n_{av}) - \bar{u}(x,r,\theta)}{\bar{u}(x,r,\theta)}, \tag{3.11}$$

and calculate the relative difference between σ_{un} and σ_u using

$$\frac{\Delta\sigma_{un}(n_{av})}{\sigma_u} = \frac{\sigma_{un}(x,r,\theta,n_{av}) - \sigma_u(x,r,\theta)}{\sigma_u(x,r,\theta)}. \tag{3.12}$$

Six locations, spread throughout the jet issuing from source **N4R5V1**, were selected to investigate these relative differences. These locations are indicated by coloured symbols '$\circ$' overlaying a contour plot of time-averaged axial velocity $\bar{u}$ on figure 3.7(a). Note that the symbols correspond to lines of the same colour on figure 3.7(b-e).

Figure 3.7(b,d) plots $\Delta\bar{u}_n/\bar{u}$ and $\Delta\sigma_{un}/\sigma_u$ against non-dimensional time t/τ (given that the acquisition frequency was 15 Hz, $t \approx 0.0667 n_{av}$ seconds) and figure 3.7(c,e) plots $\Delta\bar{u}_n/\bar{u}$ and $\Delta\sigma_{un}/\sigma_u$ against n_{av}. These plots show the relative difference collapsing towards zero with increasing t/τ and n_{av}, demonstrating the good convergence of the cumulative axial velocity statistics. Locations further downstream appear to require a greater number of datasets to converge (or, equivalently, dimensional time), which is explained on considering the turbulent timescale τ. The turbulent timescale τ increases with distance downstream (cf. §3.1.2), and thus the same number of datasets represents a smaller range of non-dimensional time t/τ. For stereoscopic PIV measurements, our time-averaged dataset from which final velocity statistics were gathered was averaged over 625 instantaneous datasets, see §2.4.2. From figure 3.7(c,e) we observe that the velocity statistics have converged to within 4% of their final value within 625 recorded datasets (marked by the vertical dashed line). Similar results are observed when examining the cumulative radial velocity statistics. In §3.5.2 we quantify the uncertainty associated with obtaining estimates of our statistical quantities using a finite number of samples, including the uncertainty associated with our estimates of the Reynolds stress. Notably, while the uncertainty in our estimates of the Reynolds stress is larger than the uncertainties associated with $\bar{u}$, $\bar{v}$, σ_u, and σ_v, they remain of reasonable quality.

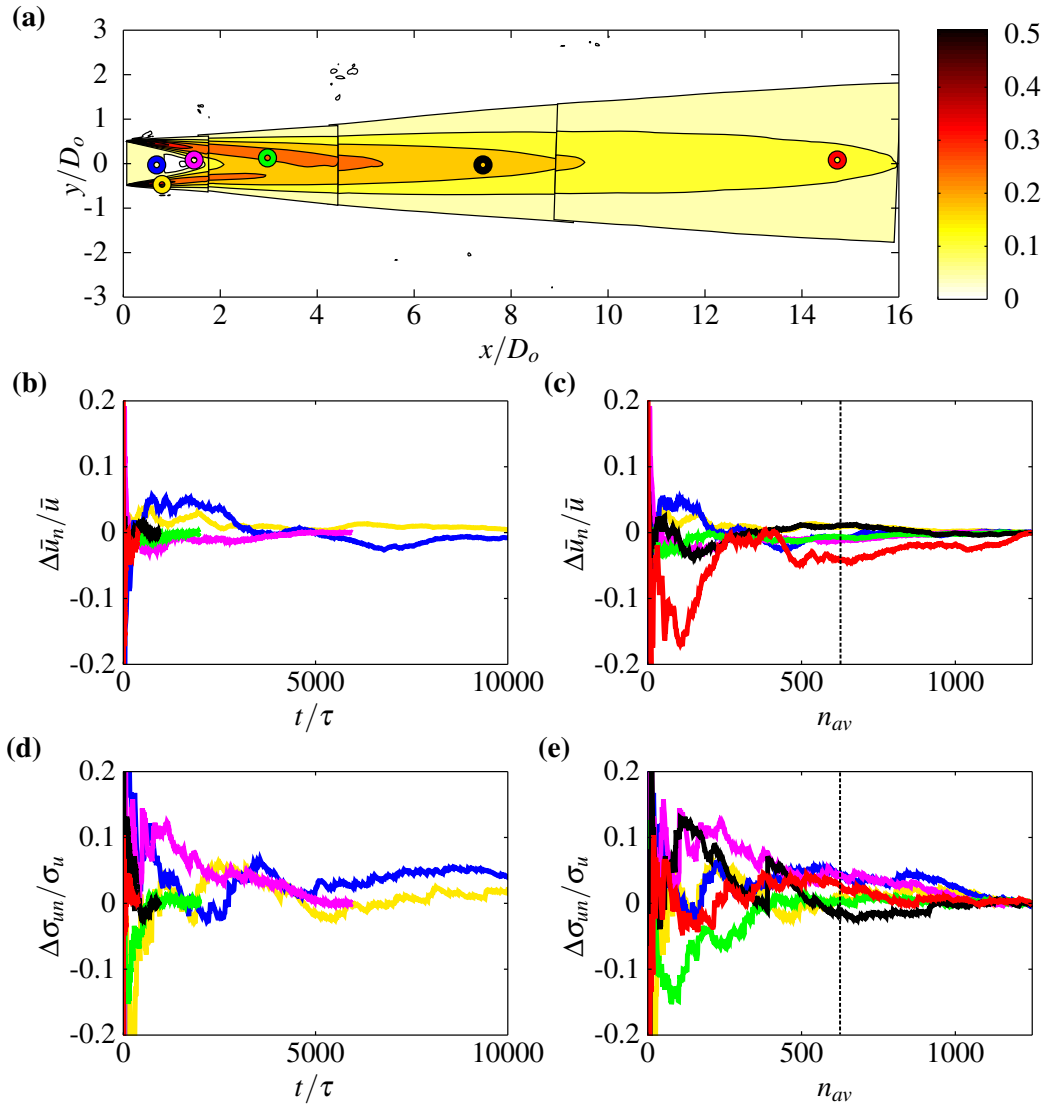

Fig. 3.7: Plots demonstrating the convergence of the cumulative axial velocity statistics (where n_{av} is varied between 1 and 1250) in the jet issuing from source **N4R5V1**. (a) Contour plot of the time-averaged axial velocity. The colour bar indicates the non-dimensional axial velocity $\bar{u}/U_0$. The symbols '$\circ$' correspond to the locations at which we examine the convergence of the velocity statistics, and correspond to lines of the same colour in (b-e). (b) The variation in $\Delta\bar{u}_n/\bar{u}$ with non-dimensional time t/τ. (c) The variation in $\Delta\bar{u}_n/\bar{u}$ with the number of averaging datasets n_{av}. (d) The variation in $\Delta\sigma_{un}/\sigma_u$ with non-dimensional time t/τ. (e) The variation in $\Delta\sigma_{un}/\sigma_u$ with the number of averaging datasets n_{av}. The vertical dashed lines on (c) and (e) are located at $n_{av} = 625$, the number of datasets over which the stereoscopic PIV images were averaged (see §2.4.2).

The analysis of the cumulative velocity statistics shows that a sufficient number of measurements have been captured over a long enough time period for the extraction of good quality and meaningful estimates of the velocity statistics.

3.3.3 Calibration

In §2.4.1 the calibration procedure which utilised the DaVis calibration tutorial and a two-level calibration plate was described. The average deviation for the different planar fields of view, given by the DaVis software during this procedure, is presented in table 3.2. We ensured these values remained under 1 pixel, and as such infer that the calibration is of good quality (LaVision, 2014).

More importantly when considering the calibration procedure, is the difference between the two different calibration methods used for stereoscopic PIV. As discussed in §2.4.1 and §2.4.5, stereoscopic measurements for $x/D_o \leq 3.0$ were captured using STFOV1 and calibrated using a 3rd order polynomial model, whereas measurements for $x/D_o \geq 3.0$ were captured using STFOV2 and calibrated using a pinhole camera model. Given these differences, we compare the two calibration methods. For this, the recordings of the jet issuing from source **N4R5V1** obtained at $x/D_o = 3.0$ on STFOV1 were processed using both the pinhole camera and 3rd order polynomial calibrations. This dataset was chosen as it allows one to relate the calibration method to the differences between the two datasets captured at $x/D_o = 3.0$ on STFOV1 and STFOV2, see §3.2.2. The estimate of the momentum integral, calculated using (3.9), from velocity vectors obtained using the 3rd order polynomial model is approximately 1.2% larger than the estimate calculated from velocity vectors obtained using the pinhole camera model. Thus, the majority of the 4.5% difference between the recordings taken at $x/D_o = 3.0$ on STFOV1 and STFOV2 is not due to the calibration method.

The difference between the two calibration methods used for stereoscopic PIV, compared using estimates of the specific momentum integral, is small.

3.4 Reynolds number effects

As discussed in §2.2.2, the primary investigations (§4-6) were carried out at a slot Reynolds number of $2100 \leq Re_l \leq 3200$. It is therefore sensible to ask ourselves if the differences in the Reynolds numbers of these experiments is likely to effect our results, and whether, and to what degree, our results will apply to turbulent slender open-core annular jets in general. To answer these questions, the experiment outlined in §4 was repeated with five different slot Reynolds

numbers $Re_l = \{1100,\ 1600,\ 2300,\ 2800,\ 3200\}$. Table 3.3 summarises the source conditions used in these experiments.

Source	Re_l	Re_f	Q_0 (m^3/s)	U_0 (m/s)	ΔT (°C)	L_j (m)	x_m/D_i	Q_a/Q_0
N4R1V1	1100	15000	0.0049	9.6	3.5	$48D_o$	1.16	1.36
N4R2V1	1600	22000	0.0076	14.5	7.2	$42D_o$	1.15	1.27
N4R3V1	2300	32000	0.0108	20.9	10.2	$52D_o$	1.14	1.24
N4R4V1	2800	37000	0.0127	24.6	15.3	$53D_o$	1.14	1.23
N4R5V1	3200	45000	0.0153	29.5	15.0	$64D_o$	1.11	1.21

Table 3.3: Details of source conditions for experiments investigating the effect of the Reynolds number on the flow, listed in order of increasing Reynolds number. These experiments, in which the flow issued from nozzle **N4**, were otherwise set up and performed in an identical fashion to those outlined in §4. Final two columns show estimates for the dimensionless merge point and the dimensionless induced volume flux, respectively.

Figure 3.8 plots the variation in the non-dimensional jet width b/D_o and inverse axial velocity $\bar{u}(x,0)^{-1}/U_0$ with distance downstream x/D_o. Far from the source, both quantities increase linearly with x. With regards to the jet width, figure 3.8(a), the far-field jet width increases slightly with increases in the Reynolds number for $Re_l \leq 2300$. The variation for $2300 \leq Re_l \leq 3200$ is small and indicates that estimates of the jet width in our primary experiments are unaffected by the variation in the Reynolds number. Similarly, there do not appear to be significant differences in the decay of centreline velocity $\bar{u}(x,0)$ as the Reynolds number is varied, figure 3.8(b).

Comparing the influence of the Reynolds number using these plots of the jet width and inverse centreline velocity focusses our attention on the far field where the appropriate Reynolds number Re_f is relatively large (see table 3.3 and the discussion in §2.2.2). Herein, to examine the influence of Re_l on the near field, we locate the upstream stagnation point $x = x_m$, which acts as an indicator for the size of the bounded induced-flow region (see §4), and the volume flux induced through the centre of the annulus Q_a (calculated using (3.5)). These quantities have been given in the final two columns of table 3.3. As the slot Reynolds number is increased from $Re_l = 1100$ to $Re_l = 3200$, the stagnation point shifts upstream by approximately 5%. Correspondingly, the volume flux induced through the centre of the annulus decreases by approximately 11%. These changes are attributed to changes in jet development over the transitional range of Reynolds numbers (with Reynolds number effects being most prominent for $Re_l \lesssim 2000$, see Suresh et al. (2008)). Over the range of Reynolds numbers used in the

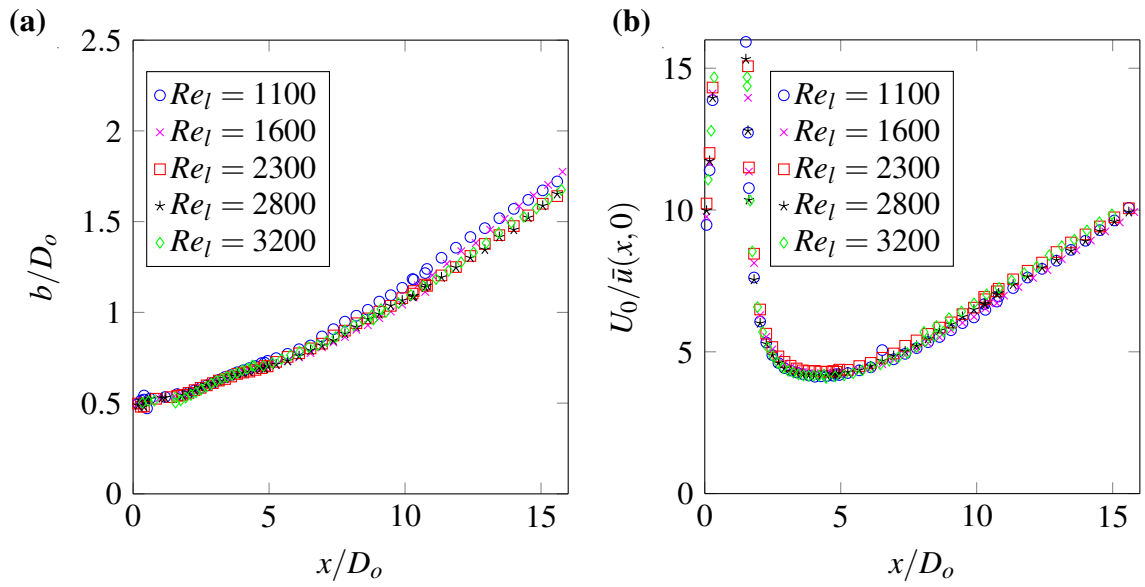

Fig. 3.8: The variation of dimensionless (a) jet width and (b) inverse axial velocity with distance downstream in the jets issuing from sources **N4R1-5V1**, i.e. at five different slot Reynolds numbers (see table 3.3 for the associated source conditions). On (a) the uncertainty is 1.9% (see the uncertainty in determining $\bar{u}/\bar{u}(x,0)$ on table 3.9) and (b) the maximum uncertainty is 4.9% (see table 3.9).

primary experiments (i.e. $2300 \leq Re_l \leq 3200$) the variation in these quantities is no greater than 3% and 2%, respectively. This variation is small and thus we can confidently compare estimates of these quantities obtained from our primary experiments in which the influence of the diameter ratio D_i/D_o and the ventilation ratio D_v/D_i are examined.

We do not expect the differing Reynolds numbers ($2100 \leq Re_l \leq 3200$*) of our primary investigations to significantly effect the results. The source conditions in our primary experiments may be regarded as high Reynolds number and the bulk quantities as independent of Reynolds number. In addition, the overall structure and behaviour of the flow remains unchanged. Given that the structure and behaviour remains unchanged, we expect that the key results presented in this thesis to be applicable to slender annular jets in general. As a consequence, the Reynolds number is not considered further.*

3.5 Errors

For accurate assessment of results, the errors associated with the measurements must be quantified. The final error in our results arise from multiple sources and are associated with

error and inaccuracies in: the measurement of the source dimensions; measurement of the source conditions; obtaining velocity vectors from the PIV technique; obtaining averaged and higher order measurements of the velocity through time averaging the data (see §3.3.2) and errors associated with integrating the velocity vectors to calculate the integral quantities. This section starts with a discussion of the PIV errors, followed by a discussion of the errors associated with the source and source conditions. It concludes in §3.5.4 by summarising the total experimental error associated with the results presented within this thesis. Note that, as all the quantitative results given in this thesis have been obtained from planar PIV, herein we only quantify the error associated with quantities obtained from planar PIV measurements.

3.5.1 PIV errors

A short discussion on the errors associated with obtaining velocity vectors using the PIV technique follows.

Peak locking

Peak locking is a phenomena that occurs when particle displacements calculated by the PIV algorithm are biased towards integer values. This phenomena therefore prevents the measurements from achieving sub-pixel accuracy (Raffel et al., 2007). The most common cause of peak locking is when the diameter of the particles, as captured by the camera, is smaller than a single pixel. To ensure that this was not the case for our results we examined histograms of the particle displacements, an example of which is displayed in figure 3.9. If peak locking was occurring, the histogram would have peaks situated around integer values. We do not observe any such peaks, and can therefore be confident that our results maintain sub-pixel accuracy. If there were to have been peak locking, one could slightly defocus the image so that the particle image diameter was bigger than a single pixel (Raffel et al., 2007).

Algorithm errors

At this point, the errors associated with the PIV algorithm are considered. These errors arise from the cross-correlation procedure itself and, according to Raffel et al. (2007), the total error ε_{total} can be split into a systematic bias component ε_{bias} and a root-mean-square component ε_{RMS},

$$\varepsilon_{total} = \varepsilon_{bias} + \varepsilon_{RMS}. \tag{3.13}$$

The magnitude of this error is influenced by various parameters, including the particle image diameter, the particle density, and the particle image shift. A full discussion of the quantities

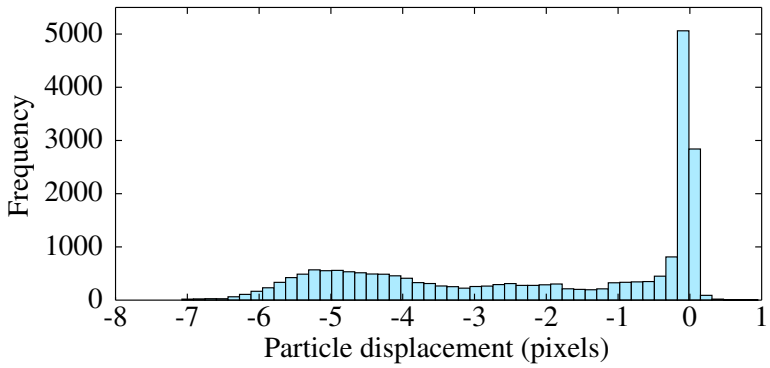

Fig. 3.9: A histogram showing the frequency of various particle displacements for an instantaneous vector field acquired in FOV2 for the jet issuing from source **N4R5V1**. The lack of peaks situated around integer values demonstrates that our data is not peak locked. Histogram bin-width: 0.16 pixel.

influencing the error can be found in Raffel et al. (2007). The algorithm errors are here quantified by displacing a frame from an existing PIV recording by a known amount, then carrying out PIV on the shifted image pair. The pixel movement calculated by the PIV algorithm can then be compared with the known pixel movement, giving the values of ε_{bias} and ε_{RMS} displayed in table 3.4. Note that, as we have shifted an existing image by a fixed amount, we do not account for errors due to the displacement gradient, noise, rogue vectors, or out-of plane motion (these are discussed further in the remainder of this section). Nonetheless, this analysis shows that the error associated with the algorithm is small, never exceeding 0.3%. The total error decreases in magnitude as the pixel displacement is increased, affirming our choice of the duration between successive laser pulses which was set so as to ensure a maximum particle displacement of approximately 7 pixels (see §2.4). Furthermore, the error does not vary appreciably across the different fields of view captured. Finally, the root-mean-square component of the algorithm error ε_{RMS} will reduce on calculating the statistical quantities (e.g. time-averaged velocities, the standard deviation of the velocity fluctuations etc.) and will be captured upon estimating the error associated with statistical quantities in §3.5.2.

Out-of-plane motion

The circumferential velocity component of the flow, which is perpendicular to our measurement plane, may result in the loss of a particle between the first and second images. Such losses reduce the strength of the correlation peak and introduce errors into measurements of the velocity vectors (Raffel et al., 2007). However, given that the mean flow is symmetric about the

FOV		Pixel displacement				
		1	3	5	7	9
NE	ε_{bias}	0.0066%	0.0040%	0.0036%	0.0032%	0.0032%
	ε_{RMS}	0.2934%	0.1082%	0.0675%	0.0512%	0.0421%
1	ε_{bias}	-0.0026%	0.0001%	0.0005%	0.0006%	0.0006%
	ε_{RMS}	0.1456%	0.0539%	0.0370%	0.0280%	0.0221%
2	ε_{bias}	-0.0058%	-0.0039%	-0.0035%	-0.0033%	-0.0033%
	ε_{RMS}	0.1177%	0.0415%	0.0267%	0.0209%	0.0176%
3	ε_{bias}	-0.0030%	-0.0041%	-0.0038%	-0.0040%	-0.0040%
	ε_{RMS}	0.2764%	0.1095%	0.0543%	0.0250%	0.0215%
4	ε_{bias}	-0.0043%	-0.0039%	-0.0035%	-0.0039%	-0.0041%
	ε_{RMS}	0.1484%	0.0939%	0.0660%	0.0374%	0.0222%

Table 3.4: The two components of the algorithm error, ε_{bias} and ε_{RMS}, in each field of view for a range of artificial pixel displacements (see §3.5).

measurement plane (see §3.2.2), there is no mean out-of-plane motion. Thus, any out-of-plane loss of particle pairs will not introduce a bias to time-averaged and higher order measurements of velocity. In addition, the relatively small maximum circumferential turbulence intensity of the jet ($\sigma_w/\bar{u}_{max} \lesssim 30\%$, Hussein et al., 1994) indicates that the out-of-plane velocity component is small relative to maximum axial velocity of the jet. Thus, the value chosen for the duration between two laser pulses, chosen to ensure a maximum displacement of 7 pixels, will not result in a significant out-of-plane motion or particle loss. Finally, a visual inspection of the interrogation windows in an image pair confirmed that the out-of-plane particle loss was low.

Rogue vectors

Rogue vectors are occasionally detected in PIV data due to the detection of an correlation peak from sources other than the particle movement between the two images, such as noise. The magnitude and orientation of these rogue vectors is often at odds with the surrounding vector field. As stated in §2.4.3, the first two passes of the multi-pass cross-correlation algorithm removed rogue vectors using a two-stage median filter and replaced the empty vectors using interpolation, whereas the final pass did not remove or replace rogue vectors. Visual inspection indicated rogue vectors, of which there were very few, were primarily situated towards the corners of our domain and away from the region of interest. The rogue vectors were primarily detected at the corners of the domain due to the vignetting effect of the camera lens and filter. Given the pseudo-random (in time and space) appearance of rogue vectors, our results, which

utilise time-averaged and higher-order velocity statistics, will not be significantly affected by the appearance of rogue vectors (Raffel et al., 2007). The one exception is towards the edge of the far-field measurement domain (FOV4) where the vignette effect is strong enough that rogue vectors are detected regularly. This has an effect on the higher-order velocity statistics (see figure 4.13 for $x/D_o = 12$ and $r/D_o \lesssim -2.5$), but not on measurements of the time averaged velocity (see figure 4.12).

Other error sources

Other error sources primarily have the effect of introducing a random uncertainty to our estimates of the instantaneous velocities. These error sources include uncertainties due the particle image diameter, particle image shift, particle image density, background noise and displacement gradients (Raffel et al., 2007). This random error will reduce on calculating the statistical quantities (e.g. time-averaged velocities, the standard deviation of the velocity fluctuations etc.) and will be captured upon estimating the error associated with statistical quantities in §3.5.2.

Displacement gradients and the particle image shift have the potential to introduce a bias error to measurements of the instantaneous velocity. However, the multi-pass PIV algorithm used (see §2.4.3) accounts for this by using the displacement vectors calculated from the previous pass to shift and deform the interrogation windows (LaVision, 2014). Thus, the bias error arising from displacement gradients and particle image shift is assumed to be negligible.

Calibration and timing errors

For PIV, the calibration procedure is used to map pixel displacements to real world displacement of particles. The time between the laser pulses is then used to calculate the corresponding velocity. To quantify the error in this process we follow the procedure outlined by Lazar et al. (2010).

The error sources contributing to the calibration error include lens distortions and a positioning error between the laser and calibration plate. The lens distortion error ε_{lens} is the quantified by the size of the average deviation (see table 3.2) compared to the visible length of the calibration plate (in pixels). The absolute error in the positioning of the calibration plate is half the size of the laser sheet, i.e. ± 1 mm. The relative positioning error ε_{pos} is then the absolute positioning error compared to the distance between the camera and calibration plate.

As the duration of each laser pulse is small (10 ns, see §2.4), the primary error in calculating the velocities from a physical displacement is associated with the error in the time between two successive laser pulses (Lazar et al., 2010). This error occurs due to jitter in the laser pulse timing, and jitter in the timing of the PTU (programmable timing unit). From the manufacturers'

FOV	ε_{lens}	ε_{pos}	ε_{laser} $\times 10^{-3}$	ε_{PTU} $\times 10^{-3}$	$\varepsilon_{conversion}$
NE	0.01%	0.2%	25.0%	2.50%	0.23%
1	0.03%	0.04%	1.56%	0.16%	0.05%
2	0.05%	0.04%	0.63%	0.06%	0.06%
3	0.03%	0.02%	0.25%	0.03%	0.04%
4	0.03%	0.01%	0.14%	0.01%	0.03%

Table 3.5: The errors associated with converting the pixel displacement into a velocity. The total conversion error $\varepsilon_{conversion}$ includes contributions from a camera distortion ε_{lens}, positioning of the calibration plate ε_{pos}, the timing jitter in the PTU ε_{PTU} and the timing jitter in the laser ε_{laser}.

specification, the laser jitter is at most 0.5 ns (Litron Lasers Ltd, 2010), and the jitter in the PTU is at most 0.05 ns (LaVision, 2014). The relative laser jitter error ε_{laser} and PTU jitter error ε_{PTU} is then the duration of the jitter compared to the duration between successive laser pulses.

Table 3.5 gives values of the individual errors which contribute to the error in converting a pixel displacement to a velocity, and also gives the total error in the conversion procedure $\varepsilon_{conversion}$. Note that the total error in converting pixel displacements to velocities is small.

3.5.2 Set-up errors

A short discussion on the errors associated with the experimental set-up now follows. Note that this discussion does not consider errors associated with the source conditions, these are discussed in §3.5.3.

Alignment errors

While we have made every effort to ensure, and confirmed within reasonable limits (see §3.3.1), that the jet centreline and planar PIV measurement plane are correctly aligned, small misalignments will introduce small errors into our results. These errors will manifest in quantities which have been calculated or inferred using the assumption that the jet centreline and measurement plane are coincident. Within this thesis, these quantities are primarily the time-averaged jet width b, centreline velocity $\bar{u}(x,0)$, volume flux Q and momentum flux M. From the information provided in §2.4.4, at worst the offset distance y_s is 1 mm and the offset angle η_s is 0.00035° (calculated from an offset of 2 mm over 1 m). Using the geometrical model presented

y_s (mm)	η_s °	Υ_b	Υ_{u*}	Υ_Q	Υ_M
1	0.00035	0.02%	0.04%	0.07%	0.13%

Table 3.6: Estimates of the error associated with a perpendicular offset y_s and angular offset η_s between the measurement plane and jet centreline. The quantity Υ_i represents the uncertainty in i, i.e. $i \pm \Upsilon_i$ (and, for clarity, $i = u*$ refers to any measurement of the time-averaged axial velocity). These errors have been calculated using the geometrical model presented in Appendix B and information regarding the alignment of the nozzle and laser sheet in §2.4.4.

in Appendix B (and discussed in §3.3.1), we provide estimates of the errors associated with these offsets in table 3.6. The geometrical model is based on a Gaussian time-averaged axial velocity profile, and thus, where the distance from the source is required, we have conservatively chosen the location at which the time-averaged axial velocity profiles first resemble a Gaussian ($x = 4.5D_o$, see §4.3.5).

Statistical errors

As discussed in §3.3.2, the finite number of samples taken leads to some uncertainty in the statistical estimates obtained. While we have shown that our estimates of the time-averaged quantities are of good quality for meaningful extraction of the velocity statistics, here we quantify the uncertainty associated within the finite number of samples captured. In addition, in quantifying this uncertainty we also quantify the effect of the random instantaneous uncertainties (see §3.5.1) on our statistical quantities (Sciacchitano & Wieneke, 2016). First, we must determine the number of effective samples n_{eff}, that is the number of samples which are independent of one another. The turbulent time-scale τ, calculated in §3.1.2 and shown in table 3.2, provides a measure of the time over which velocities are correlated. Thus, the number of effective samples is calculated from the sampling time t_s (= 83 seconds, see §2.4.2) and τ using

$$n_{eff} = \frac{t_s}{\tau}, \tag{3.14}$$

and shown in table 3.7 Note that n_{eff} is limited by the real number of samples ($n_{av} = 1250$). Thus, where the result of (3.14) is larger than n_{av}, the number of effective samples is set as the number of real samples, i.e. $n_{eff} = n_{av}$.

FOV	n_{eff}	$\Upsilon_{\bar{u}}$	$\Upsilon_{\bar{v}}$	Υ_{σ_u}	Υ_{σ_v}	$\Upsilon_{\overline{u'v'}}$
NE	1250	1.8%	1.7%	2.0%	2.0%	4.0%
1	1250	0.7%	0.6%	2.9%	2.7%	4.0%
2	1140-1250	0.4%	0.3%	2.1%	2.1%	4.2%
3	890-1140	0.9%	0.7%	2.4%	1.7%	4.7%
4	830-890	0.9%	0.7%	2.5%	2.5%	4.9%

Table 3.7: The number of effective samples n_{eff} and the uncertainty, due to a finite number of samples, in our time-averaged measurements of the velocity statistics.

From Sciacchitano & Wieneke (2016), uncertainties in the time-averaged axial velocity $\bar{u}$ and standard deviation of the axial velocity fluctuations σ_u are calculated using

$$\Upsilon_{\bar{u}} = \frac{\sigma_u}{\sqrt{n_{eff}}} \tag{3.15}$$

and

$$\Upsilon_{\sigma_u} = \frac{\sigma_u}{\sqrt{2(n_{eff}-1)}}, \tag{3.16}$$

with analogous equations used for the radial components $\bar{v}$ and σ_v. Finally, the uncertainty in the Reynolds stress is calculated using

$$\Upsilon_{\overline{u'v'}} = \overline{u'v'}\sqrt{\frac{2}{n_{eff}}}. \tag{3.17}$$

The average uncertainty, due to the finite number samples, in the velocity statistics for each planar PIV measurement window is given in table 3.7. These uncertainties have been obtained by calculating the percentage uncertainty for every vector and then averaging these uncertainties over the field of view. The uncertainty in table 3.7 is therefore representative of the field of view. The small uncertainty in our estimates of the time-averaged quantities is in agreement with figure 3.7 and confirms our conclusion in §3.3.2 that our time-averaged estimates are of good quality.

3.5.3 Source errors

Many of the results in §4-6 are scaled on the source conditions and source geometry. The uncertainty associated with the measurements of the source conditions and geometry is discussed

	$\frac{D_i}{D_o}$	Q_0 (m^3/s)	Υ_{Q_0}	l (mm)	Υ_l	A_0 (mm^2)	Υ_{A_0}	U_0 (m/s)	Υ_{U_0}	Υ_{M_0}	$\frac{h}{l}$	$\frac{M_m - M_{TH}}{M_m}$
N1R3V1	0.845	0.0109	1.8%	8.40	0.5%	2645	0.5%	4.1	1.9%	3.6%	1.55	11.6%
N2R3V1	0.894	0.0109	1.8%	5.59	0.8%	1755	0.8%	6.2	2.0%	3.7%	1.97	11.6%*
N3R3V1	0.947	0.0112	1.8%	2.71	1.6%	855	1.6%	13.1	2.4%	3.9%	2.92	9.0%
N4R3V1	0.968	0.0108	1.8%	1.65	2.7%	518	2.7%	20.9	3.2%	4.5%	4.79	5.6%
N5R3V1	0.981	0.0112	1.8%	1.06	4.5%	361	4.5%	31.5	4.8%	5.8%	8.21	5.6%*

Table 3.8: The source conditions, geometry and corresponding uncertainties. The nozzle geometries are detailed in table 2.1 and the source conditions in table 5.1. The quantity Υ_i represents the uncertainty in i, i.e. $i \pm \Upsilon_i$. The final column gives the percentage difference in momentum flux estimates M_{TH} calculated based on a 'top-hat' profile to those calculated from the actual exit velocity profile, see §3.5.3. In this final column, values indicated with a * have not been calculated, but are conservatively assumed to be equal to the value to the source with the most similar smaller contraction ratio.

here. The uncertainties in the measured quantities are related to uncertainties in the calculated quantities using uncertainty propagation methods, i.e. assuming the errors are uncorrelated, the error in quantity $AB = f(A,B)$ is

$$\Upsilon_{AB} = \sqrt{\Upsilon_A^2 + \Upsilon_B^2}, \tag{3.18}$$

where the uncertainty is denoted with Υ and the subscript represents the quantity to which the uncertainty applies, see Taylor (1977) for more details.

This uncertainty analysis is outlined for the different sources, the details of which are summarised in table 3.8. The jets that issue from these sources are examined in §5. The uncertainties associated with the source geometry, fluxes and velocities are given in table 3.8. Excluding Υ_{Q_0}, all the uncertainties increase with the diameter ratio due to the increase in the uncertainty of the slot width - the slot width decreases with increasing D_i/D_o, while the absolute uncertainty in the slot width remains constant, see §2.1.

Calculations of the exit velocity U_0 and source momentum flux M_0 are based on a 'top-hat' velocity profile, see §2.2.1. Profiles of the streamwise velocity immediately downstream of the slot indicate that the assumption of a 'top-hat' velocity profile is reasonable for the flow exiting sources **N3R3V1** and **N4R3V1** (figure 3.10b-c), and less reasonable for the flow issuing from source **N1R3V1** (figure 3.10a). The differences in the velocity profiles are attributed to the different contraction ratios (h/l, see table 3.8) – for our nozzles, as D_i/D_o increases so does h/l. Higher contraction ratios are associated with more uniform exit velocity profiles due

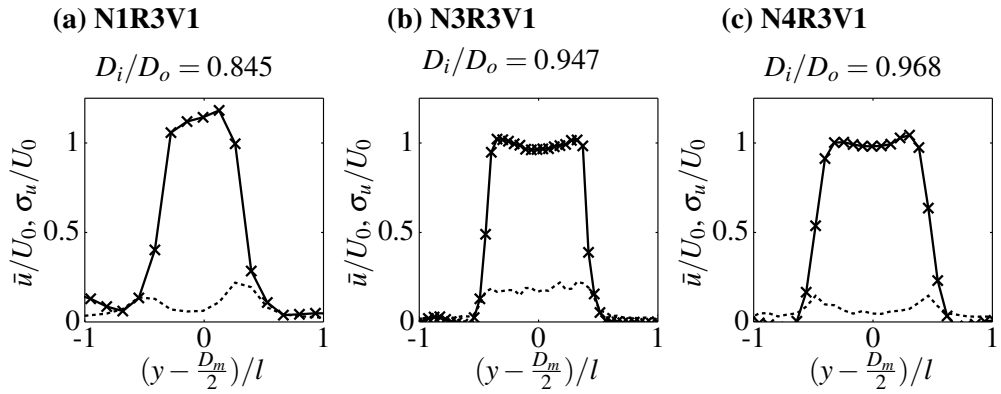

Fig. 3.10: Time-averaged cross-stream profiles of dimensionless streamwise velocity (solid line '–') and associated dimensionless standard deviation (dotted line '···') for sources **N1R3V1**, **N3R3V1**, and **N4R3V1** (as indicated), recorded at: (a) $x/l = 0.6$, (b) $x/l = 0.02$ and (c) $x/l = 0.2$; measurement locations are marked on the solid line with a cross $\times$.

to the larger pressure drop across the orifice, whereas very low contraction ratios ($h/l \approx 1$) are associated with pipe flow velocity profiles (Ball et al., 2012). Closer examination of figure 3.10(b-c) reveals that the exit velocity profile of sources **N3R3V1** and **N4R3V1** more closely resembles the 'saddle-back' velocity profile that occurs in jets issuing from a sharp-edged orifice (Quinn, 2006). It is also evident in figure 3.10(a) that the dimensionless velocity of the fluid exiting the slot in the $x-y$ plane exceeds unity; this is attributed to asymmetries in the flow issuing from the nozzle (§3.2.2).

We also note that the profiles of turbulent intensity σ_u/U_0 in the flow issuing from sources **N1R3V1** and **N4R3V1** are similar (figure 3.10a,c), peaking in the shear layers and having a magnitude of approximately 5% within the core of the jet. In contrast, source **N3R3V1** (figure 3.10b) has a turbulent intensity profile that is approximately constant across the jet, with a magnitude of approximately 20%. The reason for the different profiles of turbulent intensity is unknown but is anticipated to be due to small internal differences in the nozzle geometry.

Estimates of (specific) mean momentum flux calculated from the profiles shown on figure 3.10 and $M_m = 2\pi \int_{-1}^{1} \bar{u}^2 y' \, \mathrm{d}y'$ (where we define the coordinate $y' = (y - D_m/2)/l$) are compared to estimates M_{TH} calculated from a 'top-hat' profile, where the subscript 'TH' refers to 'top-hat' and associated quantities. In the calculation of these estimates we assume that there is no variation in the velocity profile around the circumference of the slot. For the purposes of comparison, the estimate of M_{TH} is calculated using the volume flux Q_{TH} obtained from the profiles given in figure 3.10,

$$M_{TH} = \frac{Q_{TH}^2}{A_{TH}} = \frac{(2\pi \int_{-1}^{1} \bar{u} y' \, \mathrm{d}y')^2}{A_{TH}}, \tag{3.19}$$

where A_{TH} denotes the area associated with the 'top-hat' profile. Given that Q_H is calculated very close to the source we assume that $A_{TH} = A_0$. The relative difference between M_m and M_{TH}, shown in the final column of table 3.8, for sources **N1R3V1**, **N3R3V1** and **N4R3V1**, lends support to the claim that higher contraction ratios result in more uniform velocity profiles. Note that measurements of the velocity profile immediately downstream of the slot were not obtained for sources **N2R3V1** and **N5R3V1**. For these sources, conservatively, the value of M_{TH} is assumed to be equal to the value for the source with the most similar smaller contraction ratio. At worst, the difference between the 'top-hat' and measured velocity profile is under 12%. In addition, our results indicate that at the source profiles of $\overline{u'^2}$ and $\overline{v'^2}$ are identical and thus, at the source, the momentum integral (3.7) is equal to the mean momentum flux. Given the uncertainties in A_0 (table 3.4) and that the variation of the exit velocity profile around the circumference of the annulus is unknown, we continue to assume a 'top-hat' velocity profile when calculating M_0 and U_0. This choice is vindicated by estimates of the momentum integral which indicate $M/M_0 \approx 1$, see figure 3.2.

3.5.4 Error Summary

Here, we provide a summary of the total error associated with the results presented throughout the remainder of the thesis. The errors have been calculated from the errors discussed within this section using standard error propagation methods (see Taylor (1977) for more details). The total error is a function of both the field of view and of the source. As it would be impractical here to list out the error for every field of view and source, in table 3.9 we present a summary of the error for each source (delineated by chapter), and conservatively assume that the error associated with the field of view takes the worst value (ignoring the field of view adjacent to the slot exit (NE) from which quantitative results have not been obtained).

To demonstrate how the errors have been calculated, a few examples follow. The error in the source normalised velocity $\bar{u}/U_0$, $\Upsilon_{\bar{u}/U_0}$, consists of the PIV bias error ε_{bias}, the averaging error $\Upsilon_{\bar{u}}$, the calibration error $\varepsilon_{conversion}$, the alignment error Υ_{u*} and the source error Υ_{U_0}. On assuming the errors are uncorrelated, the error is calculated using

$$\Upsilon_{\bar{u}/U_0} = \sqrt{\varepsilon_{bias}^2 + \Upsilon_{\bar{u}}^2 + \Upsilon_{U_0}^2 + \Upsilon_{u*}^2 + \varepsilon_{conversion}^2}. \tag{3.20}$$

To calculate the error in the centreline normalised velocity $\bar{u}/\bar{u}(x,0)$, $\Upsilon_{\bar{u}/\bar{u}(x,0)}$, we must consider the fact that the errors in $\bar{u}$ and $\bar{u}(x,0)$ are correlated (and in this case, identical). Thus we have

$$\Upsilon_{\bar{u}/\bar{u}(x,0)} = \underbrace{\sqrt{\varepsilon_{bias}^2 + \Upsilon_{\bar{u}}^2 + \Upsilon_{u*}^2 + \varepsilon_{conversion}^2}}_{\Upsilon_{\bar{u}}} + \underbrace{\sqrt{\varepsilon_{bias}^2 + \Upsilon_{\bar{u}}^2 + \Upsilon_{u*}^2 + \varepsilon_{conversion}^2}}_{\Upsilon_{\bar{u}(x,0)}}. \tag{3.21}$$

Errors in the integrals of Q and M_0 have been calculated through propagating the error in the estimates of the velocity through the numerical integration procedure. Due to difficulties quantifying the uncertainties due to jet asymmetry, for the volume flux Q and momentum flux M the uncertainties are only apply for $x/D_o > 4$ (by which point the jet has become axisymmetric, see §3.2.2). These errors vary significantly along the length of the jet, being higher near the source and small further downstream. Thus, for each source on table 3.9, a range of errors has been given for Q/Q_0 and M/M_0.

To use these errors to assess the later measurements, several considerations must be made. For example, on comparing quantities that do not include a source term (e.g. $\bar{u}/\bar{u}(x,0)$) across experiments, we must consider the error in the volume flux estimates Υ_{Q_0} and the error in the slot width Υ_l (see table 3.8). Thus, the error across experiments ε_{iExp} is i.e. using

$$\varepsilon_{iExp} = \sqrt{\Upsilon_i^2 + \Upsilon_{Q_0}^2 + \Upsilon_l^2}, \tag{3.22}$$

where Υ_i is the error in the quantity of interest, obtained from table 3.9. Similarly, because the error in the slot width is systematic, on comparing results from the same nozzle which include a source term (e.g. $\bar{u}/U_0$), the error in the slot width Υ_l should be not be considered (see table 3.8). Thus, the error when comparing measurements from the same nozzle ε_{iN} is

$$\varepsilon_{iN} = \sqrt{\Upsilon_i^2 - \Upsilon_l^2}. \tag{3.23}$$

A special cases arises on comparing results that do not contain a source term and which issue from the same nozzle, across different fields of view. As results in each fields of view have been captured during separate experimental runs, the error associated with comparing results across different fields of view ε_{iFOV} can be calculated from a combination of (3.22) and (3.23), i.e. using

$$\varepsilon_{iFOV} = \sqrt{\Upsilon_i^2 + \Upsilon_{Q_0}^2}. \tag{3.24}$$

	$\frac{\bar{u}}{U_0}$	$\frac{\bar{u}}{\bar{u}(x,0)}$	$\frac{\bar{v}}{\bar{u}(x,0)}$	$\frac{\sigma_u}{\bar{u}(x,0)}$	$\frac{\sigma_v}{\bar{u}(x,0)}$	$\frac{\overline{u'v'}}{\bar{u}(x,0)^2}$	Q/Q_0	M/M_0	Q_a/Q_0
Chapter 3									
N4R1V1	4.9%	1.9%	1.5%	5.8%	5.4%	6.8%	5.1-10.8%	10.3-21.7%	6.9%
N4R2V1	3.8%	1.9%	1.5%	5.8%	5.4%	6.8%	4.0-10.3%	8.4-20.8%	5.4%
N4R3V1	3.4%	1.9%	1.5%	5.8%	5.4%	6.8%	3.5-10.2%	7.5-20.5%	4.6%
N4R4V1	3.3%	1.9%	1.5%	5.8%	5.4%	6.8%	3.4-10.1%	7.2-20.4%	4.3%
N4R5V1	3.2%	1.9%	1.5%	5.8%	5.4%	6.8%	3.3-10.1%	7.1-20.3%	4.1%
Chapter 4									
N4R5V1	3.2%	1.9%	1.5%	5.8%	5.4%	6.8%	3.3-10.1%	7.1-20.3%	4.1%
Chapter5									
N1R3V1	2.1%	1.9%	1.5%	5.8%	5.4%	6.8%	3.5-10.2%	7.0-20.3%	4.6%
N2R3V1	2.2%	1.9%	1.5%	5.8%	5.4%	6.8%	3.5-10.2%	7.0-20.3%	4.6%
N3R3V1	2.6%	1.9%	1.5%	5.8%	5.4%	6.8%	3.5-10.2%	7.2-20.4%	4.6%
N4R3V1	3.4%	1.9%	1.5%	5.8%	5.4%	6.8%	3.5-10.2%	7.5-20.5%	4.6%
N5R3V1	4.9%	1.9%	1.5%	5.8%	5.4%	6.8%	3.5-10.2%	8.3-20.8%	4.6%
Chapter 6									
N4R5V1-4	3.2%	1.9%	1.5%	5.8%	5.4%	6.8%	3.3-10.1%	7.1-20.3%	4.1%
N1R3V4	2.1%	1.9%	1.5%	5.8%	5.4%	6.8%	3.5-10.2%	7.0-20.3%	4.6%
N2R3V4	2.2%	1.9%	1.5%	5.8%	5.4%	6.8%	3.5-10.2%	7.0-20.4%	4.6%
N3R3V4	2.6%	1.9%	1.5%	5.8%	5.4%	6.8%	3.5-10.2%	7.2-20.5%	4.6%
N5R3V4	4.9%	1.9%	1.5%	5.8%	5.4%	6.8%	3.5-10.2%	8.3-20.8%	4.6%
N4R1V4	4.9%	1.9%	1.5%	5.8%	5.4%	6.8%	5.1-10.8%	10.3-21.7%	6.9%
N4R2V4	3.8%	1.9%	1.5%	5.8%	5.4%	6.8%	4.0-10.3%	8.4-20.8%	5.4%
N4R3V4	3.4%	1.9%	1.5%	5.8%	5.4%	6.8%	3.5-10.2%	7.5-20.5%	4.6%
N4R4V4	3.3%	1.9%	1.5%	5.8%	5.4%	6.8%	3.4-10.1%	7.2-20.4%	4.3%

Table 3.9: A table summarising the total error associated with the results presented throughout this thesis (i.e. the total error associated with the quantities denoted by the column headings). The table has been delineated by chapter. Special consideration must be taken on comparing results across experimental runs or when comparing results from the same source, see §3.5.4.

CHAPTER 4

The turbulent jet from a slender annular slot ventilated by a self-induced flow through the open core

4.1 Introduction

4.1.1 Problem outline

The flow of interest herein is that established by an incompressible, turbulent and isothermal jet that issues from a slender open-core annular source (depicted schematically in figure 4.1a) into otherwise quiescent surroundings. The current chapter is intentionally limited to a single value of $D_i/D_o(=0.968)$, which was as close to the limiting slender case ($D_i/D_o=1$) as was feasibly possible with the fabrication technique. In §5 the role of D_i/D_o was examined, and crucially, for these slender annuli the overall structure and behaviour remained unchanged. As we show in §4.3, uniquely, the jet which develops from this source geometry induces a flow in the ambient that passes through the open core in the direction of the jet. This induced flow is observed as the region of ambient fluid bounded by the jet and the nozzle on the flow visualisation presented in figure 4.2.

4.1.2 Layout of this chapter

Based on a review of the literature it is evident that the turbulent jet which forms from an open-core slender annular source has not been considered prior to the current chapter. To advance our understanding we have explored using PIV the streamwise and cross-stream development of such a jet, from the region immediately adjacent to the source to $16D_o$ downstream. Our

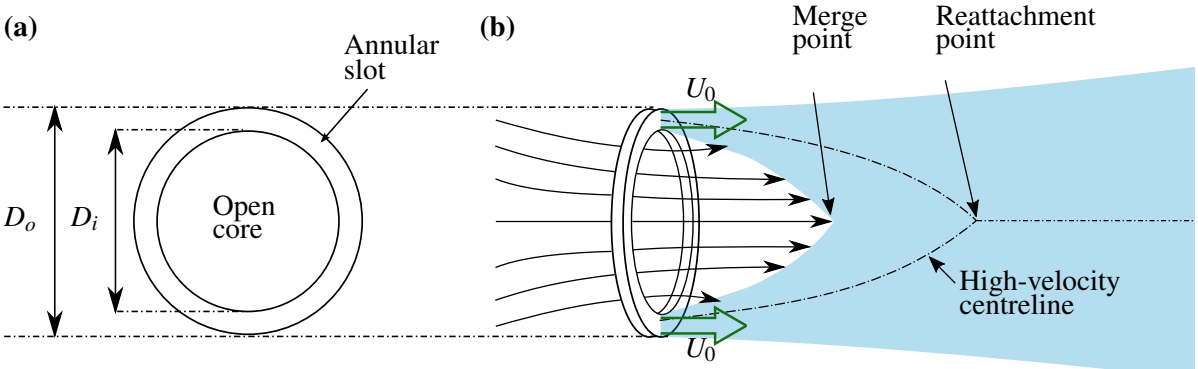

Fig. 4.1: Schematics depicting: (a) an open-core annular-jet source, shown face on to the exit slot of width $l = (D_o - D_i)/2$; (b) time-averaged streamwise section through the jet showing streamlines for the ventilating flow induced through the core of the annulus. The shaded region depicts the main body of the jet. The steady exit velocity U_0 is perpendicular to the plane of the source as indicated. Relative locations of 'merge' and 'reattachment' points (defined in §4.3) are indicated.

results provide entirely new information on the annular jet. We proceed (§4.2) by outlining the experiments and source conditions used to obtain our measurements. This is followed by our results (§4.3) in which we utilise the PIV data to examine the streamwise variation of the momentum integral. We then examine the development towards self-similar behaviour and, in doing so, identify key locations of dynamical interest, e.g. where the jet merges and reattaches. The induced-flow region is also investigated, including a quantification of the volume flux induced through the central core. In §4.4 we summarise our findings and draw our conclusions.

4.2 Experiments

An in-depth discussion regarding the nozzle design, experimental set-up and procedure has been given in §2. A brief outline of the experiments used to obtain the measurements discussed herein, including the details on the source conditions and the measurement windows, is now presented.

This chapter investigates the jet issuing from source **N4R5V1**, or, in other words, issuing from an annulus with $D_i/D_o = 0.968$, $D_v/D_i = 0.90$ and $Re_s = 3200$ (see table 4.1, or, for detail on the nozzle, table 2.1). Notably, this source has a near ideal slender diameter ratio ($D_i/D_o \approx 1$) and an almost fully open core ($D_v/D_i \approx 1$). A volume flux Q_0 was supplied to the nozzle through an intake bell mouth with pressure fluctuations indicating a variation in the flow

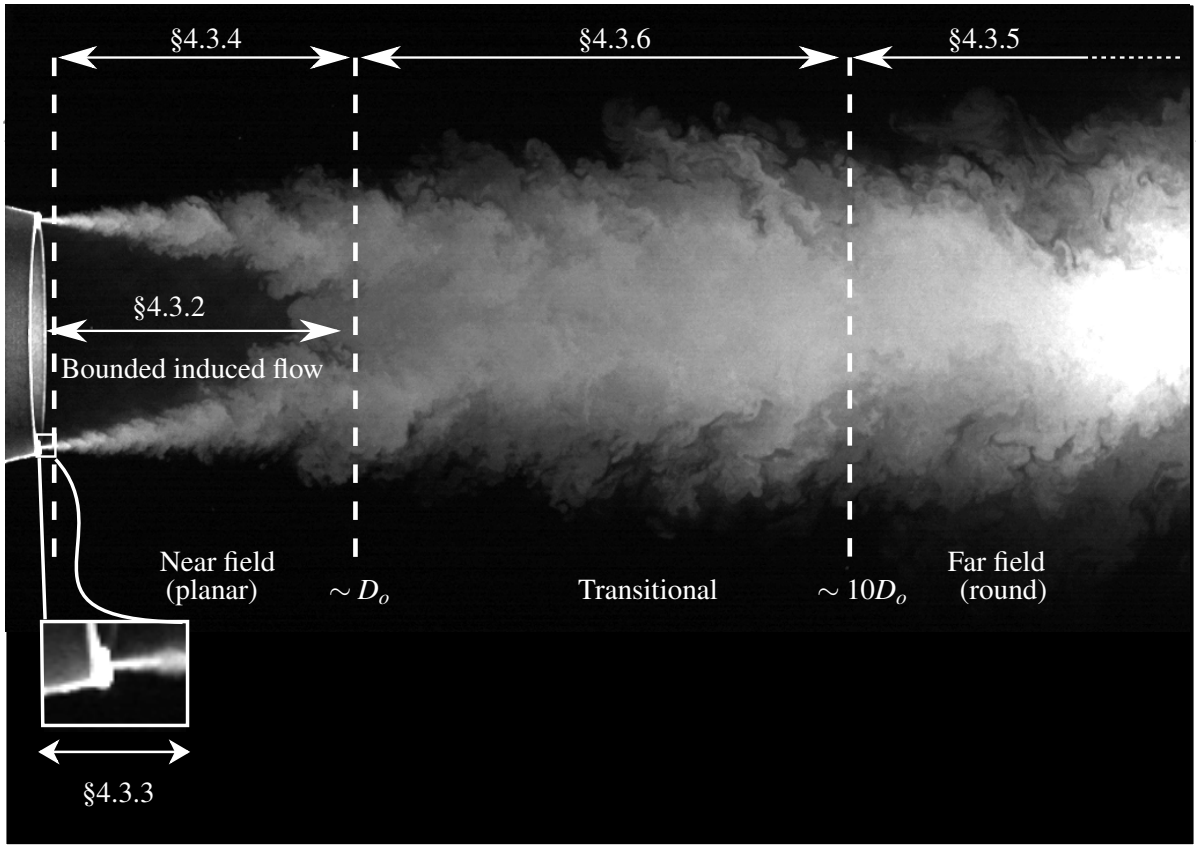

Fig. 4.2: Flow visualisation of a ventilated annular air jet from an open-core prototype slender annular source ($D_i/D_o = 0.981$ and Reynolds number based on the slot width of $Re_l \approx 1800$). The flow was visualised using vaporised olive oil particles fed directly into the intake of the supply pump. The image, taken of the instantaneous flow in the mid-plane of the jet, clearly shows a near-field region of jet coalescence that bounds an internal region of induced flow that is drawn through the open core in the direction of the jet (left to right). The jet is partitioned (not to scale) into the distinct regions of flow identified (see §4.3.2–4.3.6). The insert shows a zoomed in view of the region immediately adjacent to the slot exit, and indicates the planar-jet development region discussed in §4.3.3.

rate of ± 0.0001 m^3 s^{-1} (i.e. $Q_0 = 0.0153$ m^3 s^{-1} $\pm 1\%$). Despite the temperature difference $\Delta T = 15$°C between the source and ambient fluid, the jet length L_j is large (compared to the measurement domain $0 \lesssim x/D_o \lesssim 16$) and, as discussed in §2.2.3 and §3.2.3 the effect of buoyancy on our results may be regarded as negligible.

The results presented herein were predominantly captured using planar PIV on the $x-y$ plane of the nozzle (i.e. slices along the jet). Four overlapping windows (centred on the nozzle axis) and a single secondary window (adjacent to and centred on the slot) were used to capture details of the flow from both far from the source and in the near field, as illustrated on figure 2.5. Specific details on the positioning and size of these windows is given in table 4.2.

Source	$\frac{D_i}{D_o}$	$\frac{D_v}{D_i}$	Re_l	Re_f	U_0 (m s^{-1})	ΔT (°C)	L_j/D_o
N4R5V1	0.968	0.90	$3200 \pm 5\%$	$45000 \pm 5\%$	29.5	15	61

Table 4.1: Source conditions for the open-core jet issuing from nozzle **N4** (see table 2.1) examined in this chapter. Reynolds numbers, $Re_l = U_0 l/\upsilon$ (1.1) and $Re_f = \sqrt{M_0}/\upsilon$ (1.2), are those estimated based on a kinematic viscosity for air at 20°C of $\upsilon = 1.5 \times 10^{-5}$ m^2 s^{-1} (Batchelor, 1967) and on assuming a uniform exit velocity $U_0 = Q_0/A_0$; $Q_0 = 0.0153$ m^3 s^{-1} $\pm 1\%$ denotes the source volume flux and $A_0 = \pi(D_o^2 - D_i^2)/4 = 518.4$ mm^2 the area of the nozzle exit.

FOV	x_{min} (mm)	x_{max} (mm)	y_{min} (mm)	y_{max} (mm)	$\frac{x_{min}}{D_o}$	$\frac{x_{max}}{D_o}$	$\frac{y_{min}}{D_o}$	$\frac{y_{max}}{D_o}$	Spatial resolution (mm)
NE	0.3	20.4	41.6	58.4	0.00	0.20	0.41	0.57	0.1
1	2.5	181.5	-76.3	74.9	0.02	1.79	-0.75	0.74	1.1
2	148.1	454.5	-130.5	128.0	1.46	4.47	-1.28	1.26	1.9
3	414.6	955.1	-229.7	226.3	4.08	9.40	-2.26	2.23	3.4
4	885.7	1635.2	-321.5	310.9	8.71	16.09	-3.16	3.06	4.7

Table 4.2: PIV measurement domains. Entries give the coordinates for the fields of view (FOVs) used in these experiments (and illustrated on figure 2.5). NE refers to the field of view immediately adjacent to the nozzle exit.

4.3 Results and discussion

The flow visualisation shown in figure 4.2 reveals a number of distinguishing features that are characteristic of this class of jet. The image captures an instantaneous snapshot of the $x-y$ plane extending from the source to approximately $5D_o$ downstream. In the near nozzle region, the fine jet issuing horizontally from the slender annular slot can be clearly seen, as can the open core of the nozzle. Immediately apparent is an inward curvature of this jet which subsequently coalesces to bound an internal region of induced flow. Entrainment into the inner shear layer of the jet is responsible for inducing this flow through the open core in the direction (left to right) of the jet. The resulting bullet-shaped internal induced-flow region is unique to these open-core ventilated jets. In contrast with observations of closed-core annular jets

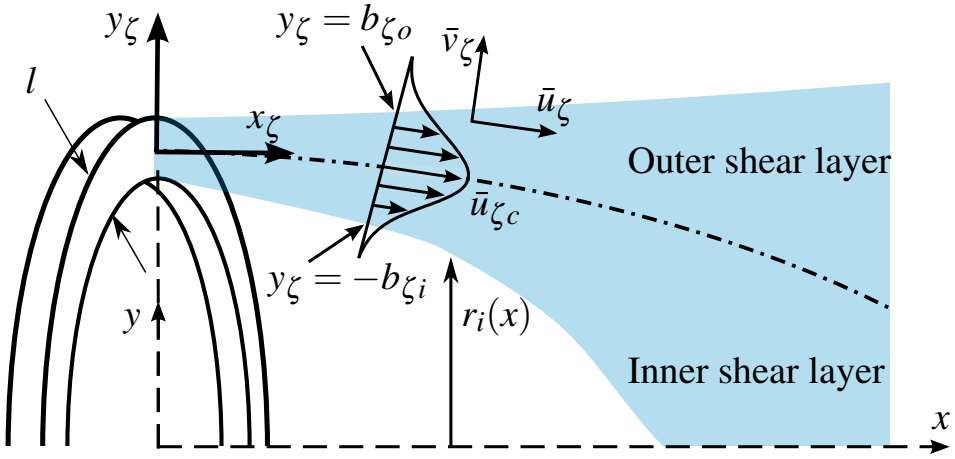

Fig. 4.3: Local coordinate system (x_ζ, y_ζ) for the near-field region. The dot-dashed line indicates the 'centreline' along which the streamwise velocity takes a maximum value $\bar{u}_\zeta(x_\zeta, 0) = \bar{u}_{\zeta c}$. The coordinate system follows this high-velocity centreline from the slot such that x_ζ is tangential to, and y_ζ is perpendicular to, this centreline. The velocities $\bar{u}_\zeta$ and $\bar{v}_\zeta$ are those in the streamwise and cross-stream directions, respectively.

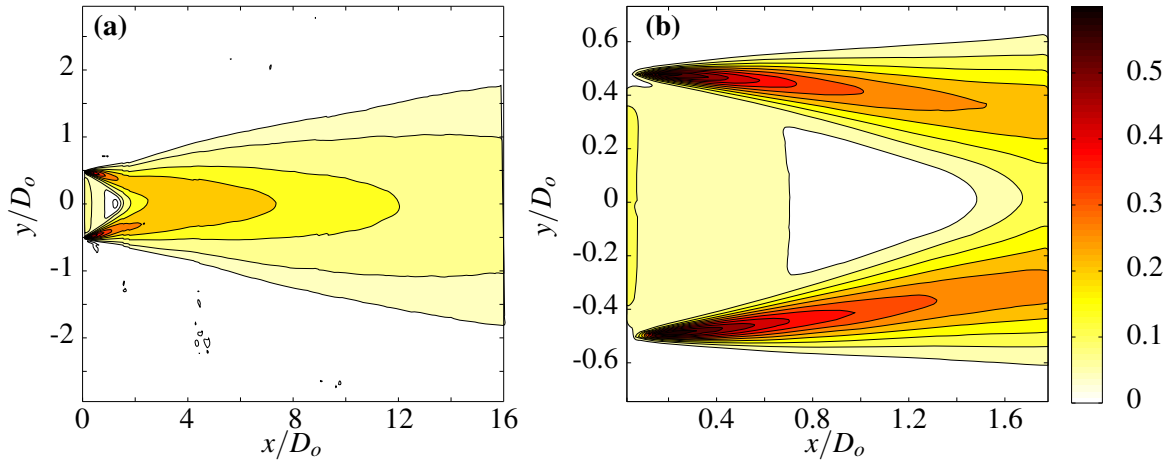

Fig. 4.4: Contour plots of the time-averaged axial velocity $\bar{u}(x,y)$ for the ventilated annular jet ($D_i/D_o = 0.968$, $Re_l \approx 3200$) in the $x-y$ plane. (a) The entire measurement domain using plotted data from FOV1-FOV4. (b) Region adjacent to the nozzle corresponding to FOV1. The colour bar indicates the non-dimensional streamwise velocity $\bar{u}/U_0$. Close to the slot ($x \lesssim 0.1D_o$) the velocities in the jet are not adequately captured by the PIV measurements due to the relatively thin jet ($O(l = 1.65$ mm$)$) when compared to the resolution of FOV1 ($R_s = 1.1$ mm, table 4.2).

(e.g. Chigier & Beer, 1964a; Ko & Chan, 1978), a large-scale unsteady recirculation region immediately downstream of the nozzle is not observed. Pre-coalescence, the external envelope of the jet does not vary significantly in width, however, further downstream the jet expands and is similar in appearance to a classic round jet that develops from a circular orifice. These general features of the annular-jet flow are confirmed in the complementary contour plots of time-averaged axial velocity $\bar{u}/U_0$; figure 4.4(a) depicts the entire measurement domain and figure 4.4(b) the near-field region of jet convergence and bounded region of induced flow. The variation of velocity within the jet and ambient is examined in the subsections that follow.

Regarding terminology, we refer to the high-velocity core of the curved merging jet and of the merged jet as a 'centreline'. With respect to the near field, development of the flow in the direction of the centreline is referred to as 'streamwise' and sections perpendicular to the centreline as 'cross stream'. Figure 4.3 shows such a high-velocity centreline as a dot-dashed line and introduces the local coordinate system for the near field (x_ζ, y_ζ) that follows the centreline; the subscript ζ signifies values in this coordinate system so that, for example, $u_{\zeta c}$ denotes the centreline streamwise velocity. With respect to the far field, where the time-averaged position of the high-velocity centreline is coincident with the longitudinal axis of the nozzle, flow development in the direction of this axis is referred to as 'axial' and sections perpendicular to this axis as 'radial', so as to distinguish from the near-field descriptions.

To identify the location of the reattachment point, i.e. where the high-velocity centreline merges (figure 4.1), in figure 4.5 we plot the axial velocity $\bar{u}(x, y = 0)$ between $0 < x/D_o \lesssim 9.5$. Note that the axial velocity increases for $1.5 \lesssim x/D_o \lesssim 4.5$ and thereafter decreases. According to Warda et al. (1999), the increase in velocity corresponds with the coalescing of the jet, however, once the jet has completely coalesced, i.e. beyond the reattachment point, the velocity along the nozzle axis decays. This locates the reattachment point at $x_{re} \approx 4.5D_o$.

The results of Ko & Chan (1978) suggest that an *unventilated* annular jet (with an identical diameter ratio to that examined herein) reattaches approximately $1.1D_o$ downstream of the nozzle. The reattachment of the ventilated annular jet further downstream is readily attributed to the open core of the annulus; fluid is induced through the core, reducing the pressure difference between the central region and the ambient, resulting in a diminished jet curvature and consequently reattachment further downstream.

The observations above, and results that follow, show that the ventilated annular jet can be split into four regions, as indicated on figure 4.2, each with a distinct behaviour: a bounded induced-flow region (§4.3.2), a near-field region of coalescence (§4.3.3, §4.3.4), a transitional region (§4.3.6) and a far-field round-jet-like region (§4.3.5). The geometry of an annular nozzle offers multiple lengths on which one could choose to scale the data. When considering the near-field development of the flow (§4.3.3, §4.3.4) we scale on the slot width l. The

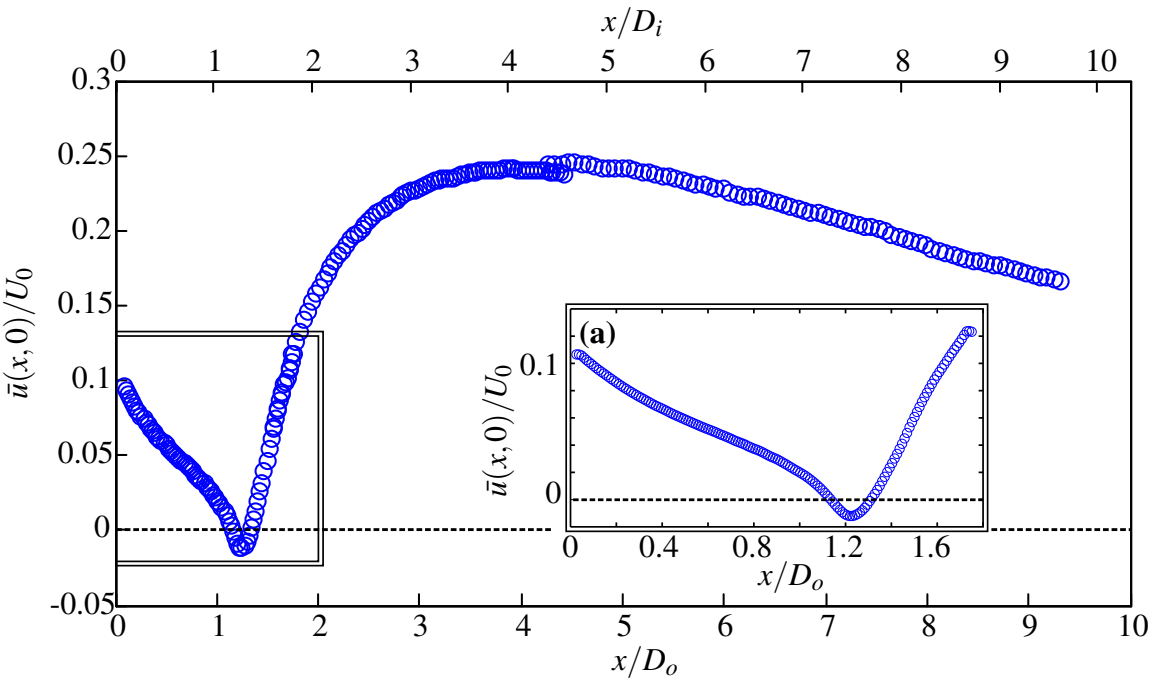

Fig. 4.5: Dimensionless axial velocity along the longitudinal nozzle axis $\bar{u}(x,0)/U_0$ for $0 < x/D_o \lesssim 9.5$. The reattachment point is located at $x/D_o \approx 4.5$ where the velocity is at a maximum. The internal bounded region of induced flow extends for $0 \leq x/D_o \lesssim 1.2$ (cf. figure 4.7). Insert (a) shows a zoomed view for $0 \leq x/D_o \lesssim 1.8$. Note the region of flow reversal (negative velocity) for $1.11 \lesssim x/D_o \lesssim 1.30$. The small discontinuity at $x/D_o \approx 4.5$ is due to errors in our estimate of $\bar{u}(x,0)/U_0$, see §3.5.4.

streamwise development in the far field (§4.3.5) is scaled on the round-jet length scale $\sqrt{A_0}$. In the remaining regions we scale on the outer diameter D_o as is standard in the unventilated annular jet literature. While we note that for the bounded induced-flow region (§4.3.2), D_i characterises the distance separating the opposite sides of the inner shear layer at the source, for our slender source $D_i \approx D_o$ and therefore we scale this region on D_o for consistency. Before examining the flow within the four regions, we assess the fidelity of our measurements by evaluating the momentum integral $M(x)$.

4.3.1 Momentum integral

For an isothermal free jet, the momentum integral is independent of the distance downstream of the source (Schlichting, 1968). To the second order, the momentum integral

$$M(x) = \underbrace{\pi \int_{-\infty}^{\infty} \bar{u}^2 r \, \mathrm{d}r}_{M_m(x)} + \underbrace{\pi \int_{-\infty}^{\infty} (\overline{u'^2} - \overline{v'^2}) r \, \mathrm{d}r}_{M_{tp}(x)}, \tag{4.1}$$

(cf. Wang & Law, 2002) was evaluated based on our planar PIV measurements of $\bar{u}$, u' and v'. In (4.1), u' and v' denote the axial and radial fluctuating velocity components, respectively.

The resulting estimates of $M(x)$, scaled on the source momentum flux M_0, are plotted in figure 4.6; also shown are the variation of the mean flow component $M_m(x)$, and the contribution $M_{tp}(x)$ attributed to the turbulent quantities and axial pressure integral.

For $x \gtrsim 4D_o$, $M/M_0 \approx 1$ indicating that the momentum integral of the jet is indeed conserved. Moreover, there is no sign of a decay in the momentum integral for the measurements made furthest downstream, indicating that the test chamber was sufficiently large, and specifically that the jet was not unduly influenced by a return flow in the chamber. Evidently, on moving downstream the turbulent contribution M_{tp} increases and attains approximately 5–7% of the source momentum flux. This downstream increase is attributed to the increase in the turbulent intensities (see figure 4.14 in §4.3.5) as the jet evolves towards a state of approximate self-similarity.

For $x \lesssim 4D_o$, the normalised momentum integral estimates fall significantly below unity. Drawing firm conclusions as to the reasons for the trend observed is not straightforward due to: the near-source flow asymmetries; the dynamics associated with jet coalescence (the reattachment point falling at $x \approx 4.5D_o$); the chosen fields of view (which overlap at $x \approx 4D_o$); the error in our estimates of the momentum integral (7-20%, §3.5.4 and table 3.9); and the fact that the assumption that the jet is thin, made when deriving (3.7), does not hold in the near-field of the jet (see §1.4.1). Whilst $M(x)/M_0 < 1$ is not expected on physical grounds as no forces were acting on the jet, momentum integral estimates calculated from measurements made on the single $x-y$ plane are not representative of the true momentum integral. Although it is unclear as to what degree the jet is symmetrical before $x/D_o = 4$, these findings suggest the jet is symmetrical for $x/D_o \gtrsim 4$.

4.3.2 Induced flow

The pattern of time-averaged streamlines characteristic of the near-field flow is shown in figure 4.7. The region shown extends from the nozzle exit into the coalescence region and

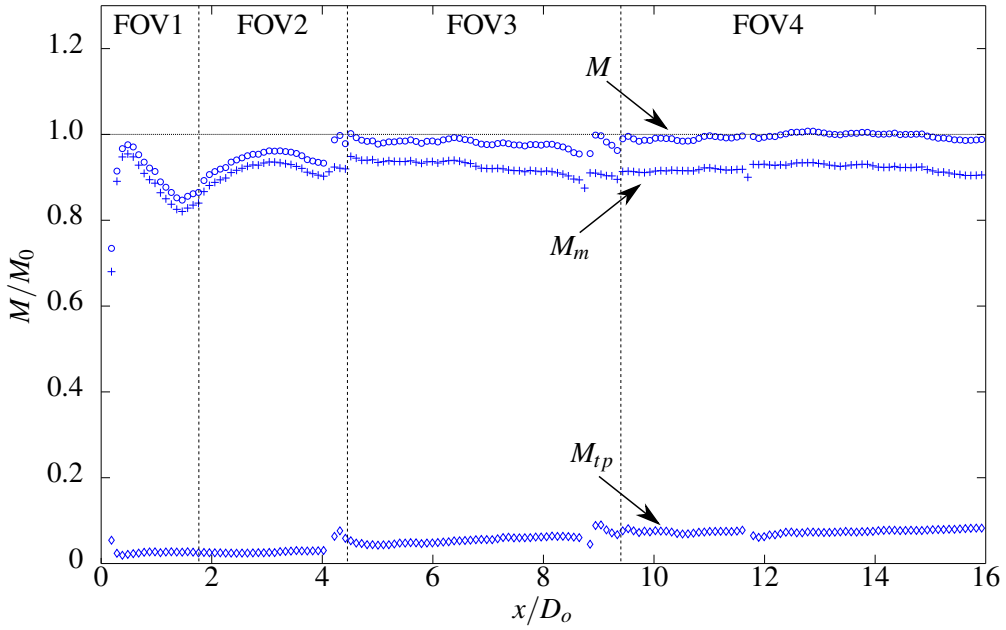

Fig. 4.6: Variation of the dimensionless momentum integral M/M_0 with distance downstream, from (4.1), for the ventilated annular jet. Also shown are the contributions from the mean flow, M_m/M_0, and from the turbulent fluctuations and axial pressure integral, M_{tp}/M_0. The source momentum flux was estimated as $M_0 = Q_0^2/A_0$. The vertical dotted lines indicate the downstream extents of the fields of view (cf. table 4.2). The discontinuities near the window edges are due to errors in our estimate of M/M_0, see §3.5.4

shows the flow within and induced by the annular jet. The streamlines were calculated using MATLAB's built in streamline function, hence the distance separating neighbouring streamlines does not correspond to a constant change in the stream function. The stream function is not used for displaying the streamlines as it is not trivial to accurately calculate the stream function from the PIV vectors as any noise or errors present within the PIV data will tend to propagate on integration. The streamline pattern reveals that the entrainment of ambient fluid into the outer shear layer of the jet (external jet perimeters at top and bottom of image) induces a flow in a direction perpendicular (approx.) to the local high-velocity centreline. By contrast, entrainment into the inner shear layer induces a flow perpendicular to this, drawing fluid through the open core in the direction of the nozzle axis.

(i) Inner shear layer

One of the distinguishing features of the streamline pattern for the internal induced flow is a relatively small-scale region of recirculation situated along the axis of symmetry for $1.1 \lesssim x/D_o \lesssim 1.3$. Examination of the flow visualisation image (figure 4.2) shows that the

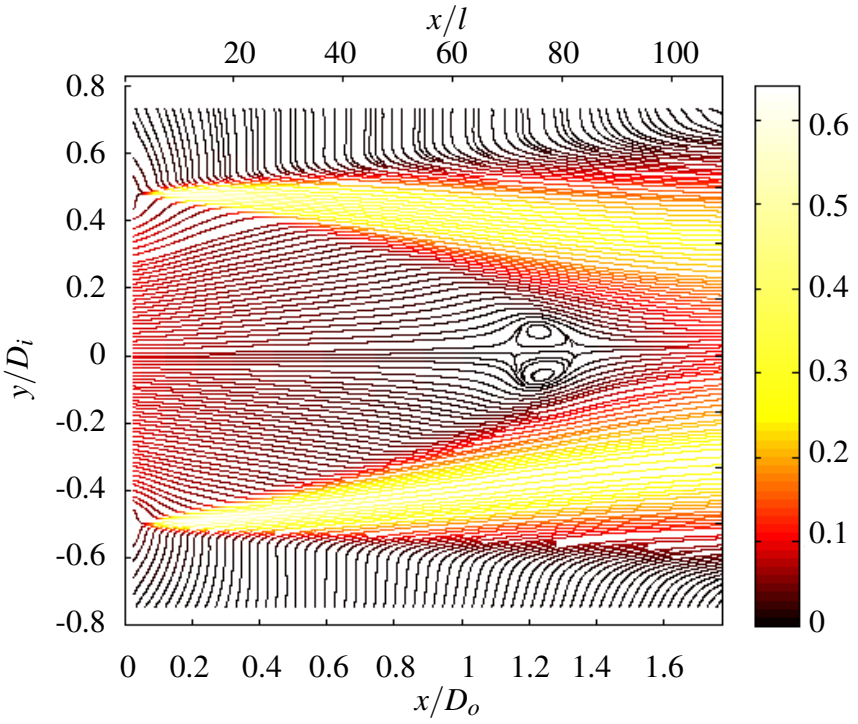

Fig. 4.7: Time-averaged streamline pattern shown on a section through the ventilated annular jet that extends along the longitudinal axis from the nozzle exit to the jet-coalescence region. Colour indicates the non-dimensional velocity magnitude $\sqrt{\bar{u}^2+\bar{v}^2}/U_0$ along streamlines.

converging jet does not coalesce at a point, rather the downstream limit of the induced-flow region appears 'blunt' ended. Observations of the flow here showed complex self-interactions within the inner shear layer, with eddies crossing the longitudinal nozzle axis - in other words, a region where the jet self-entrained. As such, we believe the recirculation region seen in figure 4.7 to be a consequence of shear-layer interactions. Figure 4.5(a), which plots the normalised velocity $\bar{u}(x,0)/U_0$ along the nozzle axis, reveals that the recirculating region comprises a region of reverse flow ($\bar{u}(x,0)/U_0 < 0$) bounded by two stagnation points, one at $x/D_o \approx 1.11$ and the other at $x/D_o \approx 1.30$. Moreover, the induced flow decelerates from a maximum velocity at the exit plane of the nozzle to a weakly negative velocity in the recirculation region and subsequently accelerates into the region of jet coalescence. This time-averaged picture implies that pressure is lowest at the plane of the open core, increases to a local maxima at the stagnation points, before decreasing again as the jet coalesces. To elaborate, the upstream stagnation point is expected to be at atmospheric pressure given that the upstream flow (induced through the core of the annulus) is inviscid. Due to the highly turbulent

motions within the recirculating vortex, the downstream stagnation point is expected to be at a pressure below atmospheric.

Defining the streamwise extent (x_m) of the bounded induced-flow region to be the point at which the inner shear layer first self-interacts based on the time-averaged picture of the flow, i.e. as the upstream end of the recirculation region, gives $x_m/D_o \approx 1.11$. Alternatively, on specifying the perimeter of the inner shear layer as the locus of points along which the streamwise velocity has fallen to $1/e$ (where ln(e)=1) of the peak high-velocity centreline value, a second estimate of $x_m/D_o = 1.60$ can be obtained from the intersection of the loci.

The flow induced through the open core of the annulus is subsequently entrained into the jet and thereby serves to enhance the volume flux in the near field when compared with the closed-core case. On calculating the mean velocity of the flow induced through the r-θ plane at $x/D_o = 0.5$ (figure 3.3a), using (3.3) and (3.4) with an estimate of $r_i/D_o = 0.35$, yields $\bar{u}_i/U_0 = 0.056$ with a standard deviation of $\pm 2\%$ ($\sigma_i/U_0 = 0.001$). Therefore, although the jet has a weak θ-dependence in the near field (§3.2.2), it appears that the induced flow has no such θ-dependence. We may then reliably estimate the volume flux induced through the core of the annulus by evaluating $Q_a = \int_0^{2\pi} \int_0^{D_i/2} \bar{u}(x=0) r \, \mathrm{d}r \, \mathrm{d}\theta = \pi \int_{-D_i/2}^{D_i/2} \bar{u}(x=0) y \, \mathrm{d}y$. Based on this we obtain $Q_a/Q_0 = 1.2$.

(ii) Outer shear layer for $x \leq x_m$

Having now estimated the total volume flux entrained by the inner shear layer as $Q_a = 1.2Q_0$, it is of interest to compare this with the total volume flux Q_e that is entrained by the outer shear layer over a comparable streamwise distance, namely for $0 \leq x \leq x_m$. To estimate Q_e we first note that the volume flux of the flow at $x = x_m$, $Q(x_m)$, consists of contributions from the source Q_0, from fluid induced through the open core Q_a and fluid entrained into the *outer* shear layer Q_e. It follows that

$$\frac{Q_e}{Q_0} = \frac{Q(x_m)}{Q_0} - \frac{Q_a}{Q_0} - 1, \tag{4.2}$$

where the volume flux of the jet Q is calculated within a region bounded by a perimeter located at $y = \pm y_w$, defined such that $y_w > |D_o/2|$ and $\bar{u}(x, y_w)/\bar{u}_{max} = 0.05$. This definition of y_w, obtained through a process of trial and error, bounds the external jet perimeter such that estimates of volume flux remain continuous at the boundary of two measurement windows. Thus,

$$Q(x) = \pi \int_{-y_w}^{y_w} \bar{u}(x, y) y \, \mathrm{d}y. \tag{4.3}$$

As this definition encompasses all the fluid contained between the limits of integration, the internal induced flow is included in the resulting estimate of $Q(x)$. Evaluating (4.3) at $x = x_m$, by which point the entirety of the internal induced flow has been entrained by the inner

shear layer, allows us to estimate the volume flux entrained by the outer shear layer between $0 \leq x \leq x_m$. Taking $x_m = 1.11D_o$ we obtain $Q_e/Q_0 = 1.5$. Alternatively, on taking $x_m = 1.60D_o$ we obtain $Q_e/Q_0 = 2.0$. Both estimates are approximate due to the asymmetries in the jet near the nozzle (see §3.2.2).

Evidently, both the inner and outer shear layers entrain different amounts of fluid. This difference in entrainment can be explained by the differing surface areas of the interfaces over which this fluid is entrained – the area of the inner entrainment surface being the smaller (figure 4.2). On characterising the perimeter of both shear layers by the $1/e$ velocity contours (and therefore with $x_m = 1.60D_o$), we obtain a surface of area $ISL = 4.2\pi(D_o/2)^2$ for the inner shear layer and of $OSL = 7.1\pi(D_o/2)^2$ for the outer shear layer. The ratio of surface areas for these shear layers is approximately equal to the ratio of volume fluxes entrained (at $x_m = 1.60D_o$), i.e. $Q_e/Q_a = 1.66 \approx 1.69 = OSL/ISL$, where the small difference can be attributed to experimental uncertainty.

4.3.3 Jet development adjacent to the nozzle exit

We proceed by examining the development of the jet immediately downstream of the slot, i.e. the region indicated by the zoomed in insert on figure 4.2. We recall the slot has dimension l and planar PIV measurements were recorded between $x/l = 0.2$ and $x/l = 12$ (table 4.2, i.e. for $0.3 \leq x \leq 20.4$ mm). At first sight, the cross-stream variation in $\bar{u}_\zeta$ recorded immediately downstream of the slot (at $x_\zeta/l = 0.2$), figure 4.8(a), appears to indicate that the velocity profile at the source could be reasonably approximated by a 'top-hat'. Closer examination reveals that the profile more closely resembles the 'saddle-back' velocity profile that occurs in jets issuing from a sharp-edged orifice (Quinn, 2006). The standard deviation σ_{ζ_u} of the streamwise velocity (figure 4.8a dotted line) shows that the turbulence intensities peak within the shear layers and are approximately 5% ($\sigma_{\zeta_u}/\bar{u}_\zeta \approx 0.04/0.85$) within the core of the jet.

The colour map of axial velocity $\bar{u}$, figure 4.8(b), indicates that the trajectory of the jet in this region remains close to horizontal. The coordinate y has been translated in the plot so that the longitudinal axis ($(y-(D_i+D_o)/4)/l = 0$) bisects the slot. Moreover, measurements of the time-averaged streamwise velocity along the high-velocity centreline $\bar{u}_{\zeta_c}/U_0$, figure 4.8(c), indicate that the velocity within the core remains almost unchanged for a distance of approximately 4-5l downstream; a potential core of a length between 4-6l is in good agreement with the planar-jet literature (e.g. Krothapalli et al., 1981; Thomas & Goldschmidt, 1986). It is also evident in figure 4.8(c) that the dimensionless velocity of the fluid exiting the slot in the $x-y$ plane is not equal to unity; this is attributed to asymmetries in the flow issuing from the nozzle (§3.2.2).

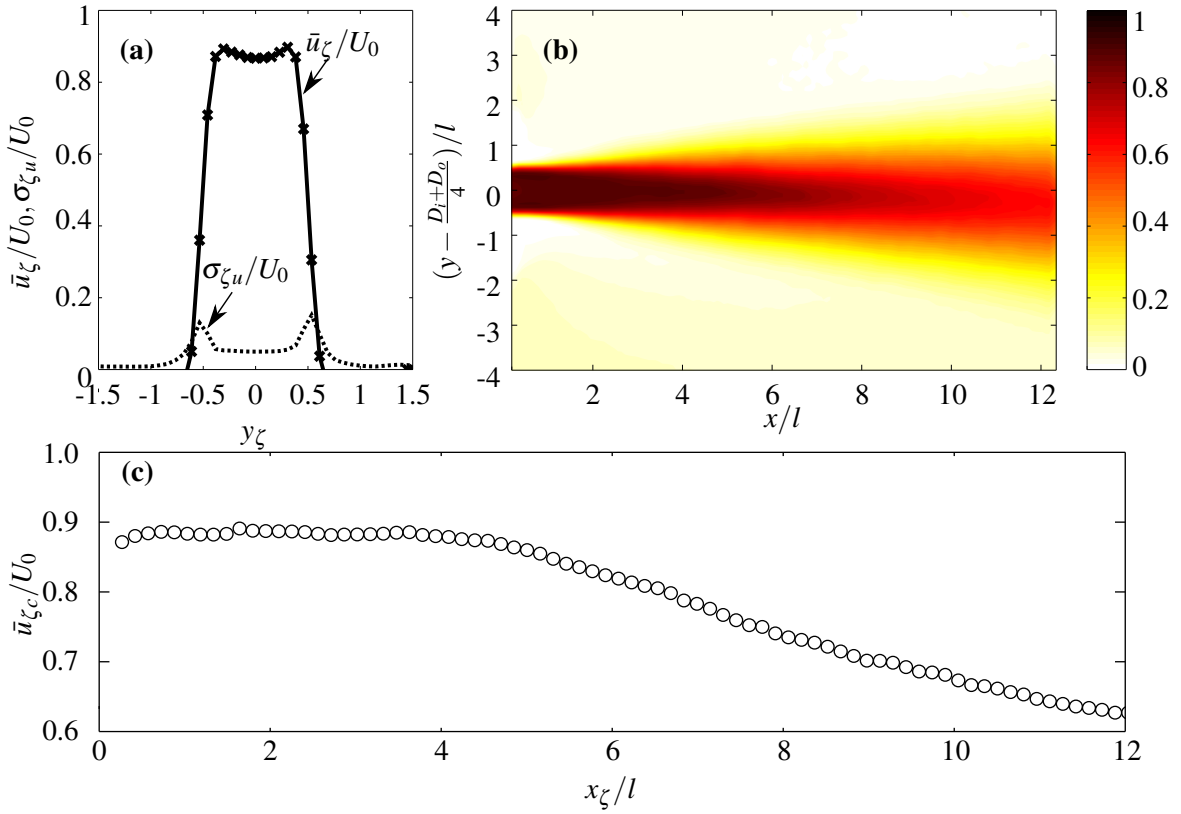

Fig. 4.8: Near-slot region. (a) Time-averaged cross-stream profile of streamwise velocity recorded immediately downstream of the exit plane at $x_\zeta/l = 0.2$; measurement locations are marked with a cross $\times$. (b) Colour map of time-averaged axial velocity downstream of the exit plane; the colour bar shows $\bar{u}/U_0$. (c) Time-averaged dimensionless streamwise velocity $\bar{u}_{\zeta_c}/U_0$ along the high-velocity centreline exiting the slot; x_ζ denotes the distance along this centreline, figure 4.3.

4.3.4 The near-field jet

We now examine the flow further from the slot ($x/l > 12$ or, equivalently, $x/D_o > 0.2$), where the curvature of the jet becomes significant, and into the region in which the shear layer coalesces. Our primary focus is on the streamwise development of velocity and turbulent intensity (§4.3.4–4.3.4).

Moving away from the source the annular jet collapses towards the longitudinal axis of the nozzle and we attribute this to the pressure difference between the ambient and the internal region of induced flow (§4.3.2). For this 'near-field' region we introduced a coordinate system (x_ζ, y_ζ) which follows the high-velocity jet centreline (figure 4.3), such that $y_\zeta > 0$ represents locations within the outer shear layer and the ambient, and $y_\zeta < 0$ represents locations within the inner shear layer and the internal induced-flow region. Within the near-field region, the

high-velocity centreline merges at the reattachment point and is therefore not coincident with a streamline, i.e. we anticipate some cross-centreline flow. For sufficiently small x_ζ/l the jet appears to be horizontal in the flow visualisation (see also figure 4.8b) and thereafter its curvature increases. To follow the curving high-velocity centreline, a curve defined by a first-order Fourier series of the form $a_0 + a_1\cos(px) + a_2\sin(px)$, for constants a_i $(i = 0, 1, 2)$ and p, was fitted to the data points with the largest velocity magnitude. Profiles were found by performing cubic interpolation perpendicular to this curve.

For the profiles that follow in §4.3.4 (figures 4.9, 4.10), velocity is scaled on $\bar{u}_{\zeta_c}$, the cross-stream coordinate y_ζ is scaled on the width b_ζ of the outer shear layer (where b_ζ is defined such that $\bar{u}_\zeta(x_\zeta, b_\zeta) = \bar{u}_{\zeta_c}(x_\zeta)/e$), and we continue to scale distances in the streamwise direction on the slot width l. Note that on profiles for which $x_\zeta/l \geq 85$, the data point marked at the largest negative value of y_ζ/b_ζ lies on the symmetry axis of the nozzle (i.e. on $y = 0$).

Velocity and intensity profiles

From the profiles of time-averaged streamwise velocity $\bar{u}_\zeta(x_\zeta = const., y_\zeta)$ plotted in figure 4.9(a), it is evident the structure of the outer shear layer ($y_\zeta > 0$) remains relatively unchanged over the measurement domain considered ($15 \leq x_\zeta/l \leq 265$). The profiles appear to be approximately self-similar and follow closely the Gaussian $\bar{u}_\zeta/\bar{u}_{\zeta_c} = \exp(-y_\zeta^2/b_\zeta^2)$. Whilst there is some evidence that a subset of the corresponding profiles for the inner shear layer show a partial collapse (see profiles for $x_\zeta/l = \{15+, 30\bigcirc, 50*\}$), there is clear evidence that, further downstream, the form of the profiles is influenced by the merging of the jet. Notably, the scaled velocities within the inner induced-flow region first decrease as the jet proceeds past the recirculation region (see $y_\zeta/b_\zeta \lesssim -2$ for $x_\zeta/l = \{70\bullet, 85\times\}$ and §4.3.2) before increasing as the inner shear layer combines. The streamwise velocity distribution in the outer shear layer is not noticeably affected by the merging of the jet.

We now turn our attention to the profiles of time-averaged cross-stream velocity $\bar{v}_\zeta(x_\zeta = const., y_\zeta)$ plotted in figure 4.9(b). Merging has a significant effect on the cross-stream velocities as neither the structure of the inner nor the outer shear layer approach self-similar forms. The negative cross-stream velocity at the outer perimeter of the jet ($y_\zeta/b_\zeta \gtrsim 2$) is a signature for the flow induced in the ambient. The positive cross-stream velocity at the inner perimeter of the jet ($y_\zeta/b_\zeta \lesssim -2$) represents fluid that has been induced through the open core of the annulus. A notable feature apparent in figure 4.9(b) is the positive cross-stream velocity across the jet centreline for $x_\zeta/l \geq 30$, signifying a transport of fluid from the inner to the outer shear layer. While small compared to the streamwise velocity ($\bar{v}_\zeta/\bar{u}_\zeta \ll 1$), this positive cross-stream velocity is not insignificant when compared to the maximum cross-stream velocity ($\bar{v}_{\zeta,max}$) in

Symbol	+	◯	∗	•	×	□	◊	▷	◁	△	▽	☆
x_ζ/l	15	30	50	70	85	105	115	145	175	205	235	265
x/D_o	0.25	0.50	0.81	1.14	1.38	1.70	1.87	2.35	2.85	3.30	3.80	4.30

Table 4.3: Symbol with corresponding dimensionless streamwise distance downstream of the slot x_ζ/l used in the velocity and turbulent intensity profiles (figures 4.9, 4.10). The approximate axial location x/D_o of the velocity and turbulent intensity profiles is also given. On travelling in the downstream direction, the colour of the symbols transmutes from blue to red.

the jet with $\bar{v}_\zeta(x_\zeta,0)/\bar{v}_{\zeta,max}(x_\zeta) \approx 0.4-1.0$. Our data indicates that for $30 \leq x_\zeta/l \leq 85$, the cross-centreline velocity is almost constant, with a value of $\bar{v}_\zeta(x_\zeta,0)/\bar{u}_{\zeta c}(x_\zeta) \approx 0.01$.

The non-zero velocity across the centreline suggests that the inner shear layer is being absorbed into the outer shear layer. Although, at a glance, one might be tempted to interpret this cross-centreline velocity as indicating that the inner shear layer entrains fluid at a greater rate than the outer shear layer, the analysis in §4.3.2 indicates that the entrained volume flux is solely a function of the shear layers surface area.

Once the inner shear layer has merged, the magnitude of the velocity across the centreline $\bar{v}_\zeta(x_\zeta,0)$ increases (note the profiles between $x_\zeta/l = \{115\text{◊}\}$ and $x_\zeta/l = \{265\text{☆}\}$). Still further downstream, the high-velocity centreline merges (the reattachment point located at $x_\zeta/l \approx 277$ or, equivalently, $x/D_o \approx 4.5$, §4.3). Thereafter, a single high-velocity centreline persists; after reattachment there is zero time-averaged volume flux across the centreline (see §4.3.5).

Profiles of streamwise $I_{\zeta u}(=\sigma_{\zeta u}/\bar{u}_{\zeta c})$ and cross-stream $I_{\zeta v}(=\sigma_{\zeta v}/\bar{u}_{\zeta c})$ turbulent intensity, where $\sigma_{\zeta u}$ and $\sigma_{\zeta v}$ denote the standard deviation of the respective velocity fluctuations, are plotted in figure 4.10. Although the furthest reaches of the outer shear layer $(y_\zeta/b_\zeta \gtrsim 1)$ are approximately self-similar for downstream distances exceeding $x_\zeta/l = 30$, the furthest reaches of the inner shear layer $(y_\zeta/b_\zeta \lesssim -1.5)$ are self-similar only for the short span $30 \lesssim x_\zeta/l \lesssim 70$ and deviate from self-similarity as the inner shear layer begins to merge. Further downstream $(x_\zeta/l \gtrsim 115)$, the profiles closer to the axis $(y_\zeta = 0)$ begin to evolve as the shear layer mixes and merges.

Streamwise dependence

Given the annular nozzle geometry considered, for which the nozzle radius is large compared with the width of the slot through which the jet issues $(D_o/2 \gg l)$, and the existence of

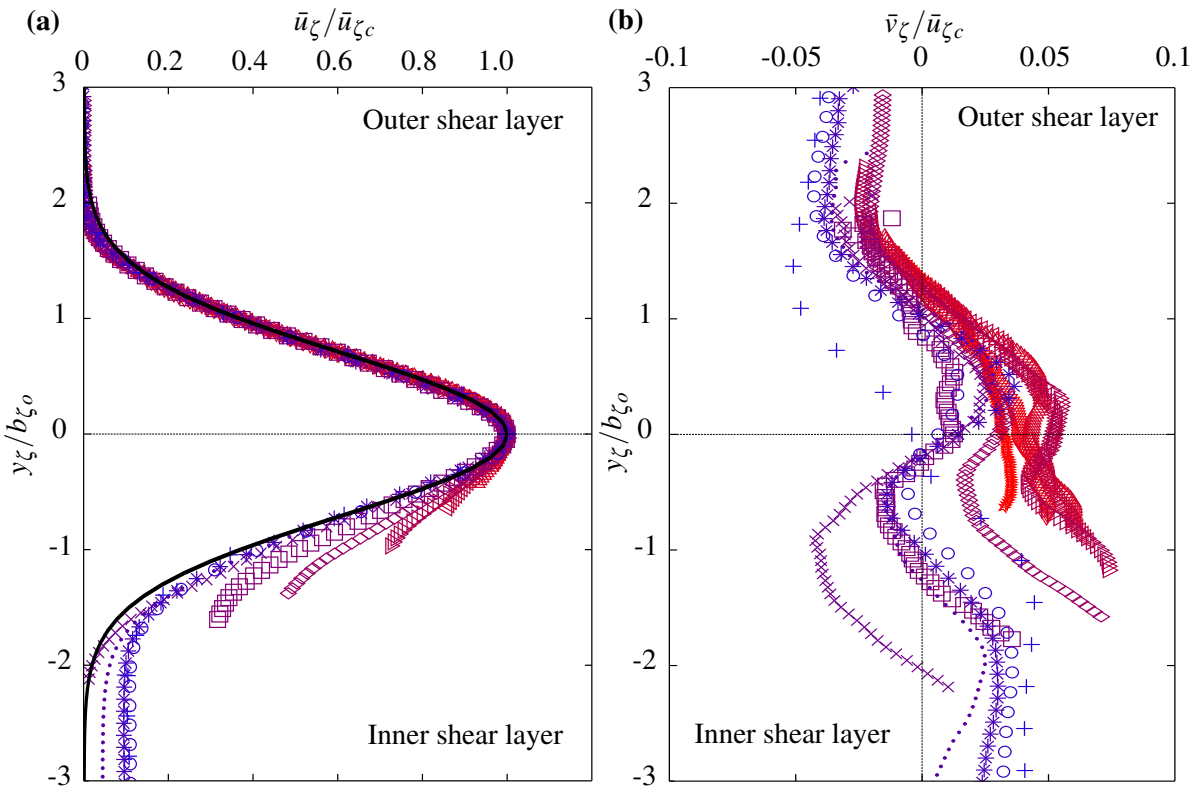

Fig. 4.9: Exit slot to reattachment region of the ventilated annular jet. Profiles of time-averaged: (a) streamwise velocity $\bar{u}_\zeta$ and (b) cross-stream velocity $\bar{v}_\zeta$ recorded at downstream distances from $x_\zeta/l = 15$ (+) to $x_\zeta/l = 265$ (☆). Refer to table 4.3 for downstream location corresponding to each symbol. The solid line in (a) is the Gaussian $\bar{u}_\zeta/\bar{u}_{\zeta c} = \exp(-y_\zeta^2/b_{\zeta o}^2)$.

quasi self-similar streamwise velocity profiles (§4.3.4), one might reasonably anticipate a resemblance between the near-field jet from the annulus and the classic planar jet that issues from a slender rectangular slot. Indeed, as we shall see, planar-jet-like behaviour persists over a significant distance downstream of the exit slot. To enable direct comparisons with the classic results on planar jets we again scale lengths on the slot width l.

Figure 4.11(a) plots the variation of the normalised width of the inner shear layer, $b_{\zeta i}/l$, and the outer shear layer, $b_{\zeta o}/l$, with distance along the high-velocity centreline x_ζ/l. Data is plotted between the source and the location at which the high-velocity centreline merges (the reattachment point at $x_\zeta/l \approx 277$). The solid line shows the linear planar-jet scaling from Fischer et al. (1979) with a gradient (growth rate) of 0.116. Sufficiently close to the source, the growth rates of both the outer (○) and inner (□) shear layers are approximately linear and closely follow the growth rate of a planar jet.

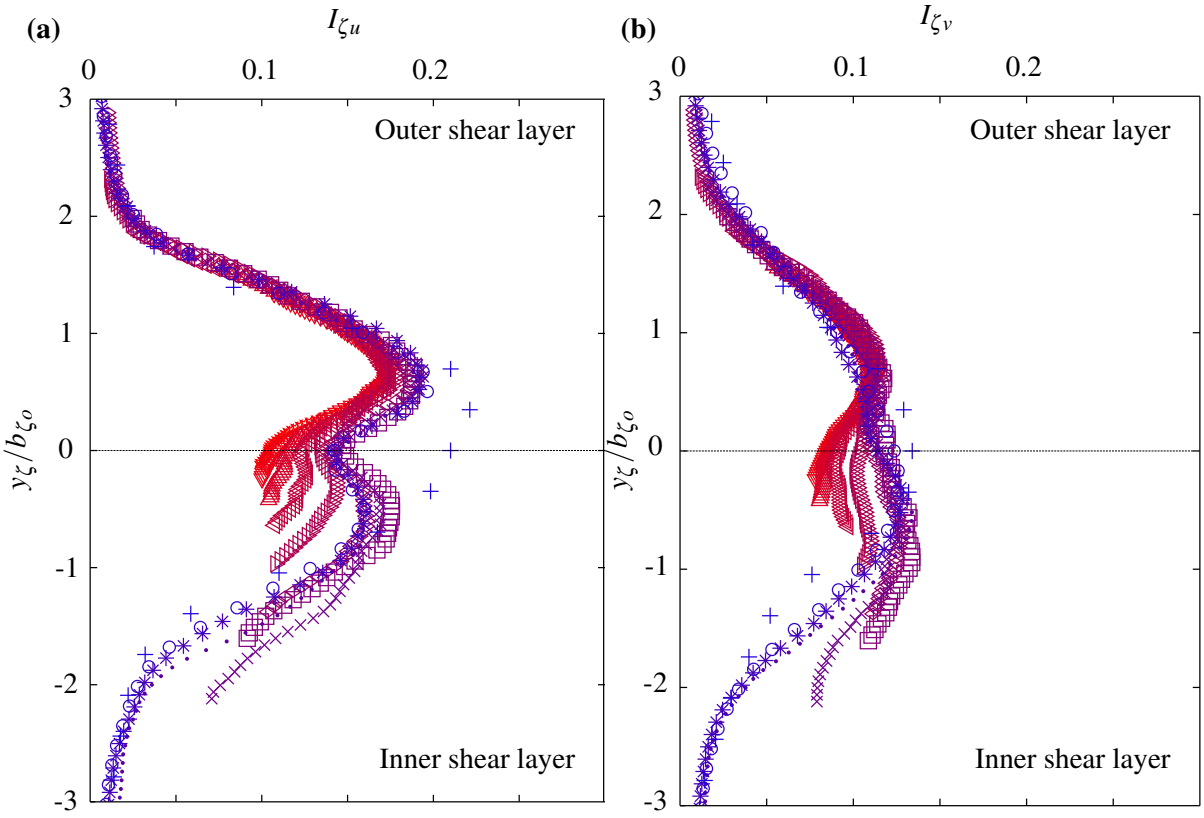

Fig. 4.10: Exit slot to reattachment region of the ventilated annular jet. Profiles of time-averaged: (a) streamwise turbulent intensity $I_{\zeta u} = \sigma_{\zeta u}/\bar{u}_{\zeta c}$ and (b) cross-stream turbulent intensity $I_{\zeta v} = \sigma_{\zeta v}/\bar{u}_{\zeta c}$. Refer to table 4.3 for downstream location corresponding to each symbol.

For $x_\zeta/l \gtrsim 60$ the inner shear layer begins to rapidly widen, behaviour we attribute to self-interactions. Further evidence of this local interaction is the presence of the recirculation region at $x_\zeta/l \approx 70$ (or, equivalently, at $x/l \approx 70$, see figure 4.7 and §4.3.2). The data (□) on figure 4.11(a) is plotted until the inner shear layer begins to coalesce at $x_\zeta/l \approx 100$. This value yields the alternative estimate for the streamwise extent of the bounded induced-flow region discussed in §4.3.2, of $x_{\zeta m}/l \approx 100$, or, equivalently, $x_m/D_o \approx 1.60$.

For $x_\zeta/l \gtrsim 70$ the growth rate of the outer shear layer increases gradually, reaching a growth rate of 0.137 for $x_\zeta/l > 150$ (dashed line on figure 4.11a). The increase in growth rate above that of the planar jet coincides with the merging of the annular jet. Still further downstream, the spreading rate begins to transition to that of a round jet; evidence of this behaviour is described in §4.3.5 and §4.3.6.

Based on growth rates, we therefore assert that the annular jet closely resembles the planar jet for $0 < x_\zeta/l \lesssim 60$. This assertion is further supported by the streamwise centreline velocity

(figure 4.11b) which scales as $\bar{u}_{\zeta_c}/U_0 \propto (x_\zeta/l)^{-1/2}$ (solid line) for $x_\zeta/l < 60$. For planar jets, it has long been established that $\bar{u}_{\zeta_c}/U_0 = const.(x_\zeta/l)^{-1/2}$ (Fischer et al., 1979). For our annular jet, the constant of proportionality is 2.5, whereas Fischer et al. (1979) report a value of 2.41 for planar jets.

For $x_\zeta/l > 100$ the rate of velocity decay in the jet from the annular slot is noticeably slower than for a planar jet. We attribute this to the transfer of momentum between the coalescing inner shear layer (annular case) rather than to transfers with the ambient (planar case). As we will see in §4.3.5, sufficiently far downstream (for $x_\zeta/l \gtrsim 540$) the streamwise velocity decays linearly, as is characteristic of a round jet (Fischer et al., 1979). In the range $60 \lesssim x_\zeta/l \lesssim 540$ our data suggests the annular jet may be regarded as in transition from planar to round-jet behaviour.

As a final note, the close agreement between classic scalings for a planar jet and our measurements provides us with a strong lead, namely the persistence of planar-jet-like behaviour indicates that the annular jet for $x_\zeta/l < 60$ (or, equivalently, for $x/D_o < 1$) is influenced primarily by the local geometry (via the length scale l) rather than by the annular geometry. However, the streamwise extent over which planar-jet behaviour holds is expected to be controlled by the dominant length scales of the nozzle (D_i and D_o), as these scales characterise the distance separating opposite sides of the (inner and outer) shear layers and of the jet centreline at the source.

4.3.5 The far-field jet

Turning our attention to the behaviour of the jet downstream of the region of coalescence, a natural question that arises concerns how the jet develops towards classic round-jet behaviour, as might reasonably be anticipated in the far field. Given this expectation, we revert to the global coordinate system (x,y). We address this question by examining radial profiles of the first- and second- order velocity statistics, exploring the development towards a state of self-similarity. Our results (§3.2.2) indicate that the flow shows no discernible swirl, may be regarded as axisymmetric at modest distances downstream and, as such, the $x-y$ plane interrogated, and on which the results of this section are based, is a representative plane. For the profiles considered (figures 4.12, 4.13, 4.15), velocity is scaled on the centreline axial velocity $\bar{u}_c$ and the radial coordinate is scaled on the local width b of the external jet envelope.

Velocity and intensity profiles

A visual inspection of the profiles of time-averaged axial velocity shown in figure 4.12(a), which extend to $x/D_o = 14$ (recall that $D_o \approx 62l$, table 4.1), suggests that a far-field state of

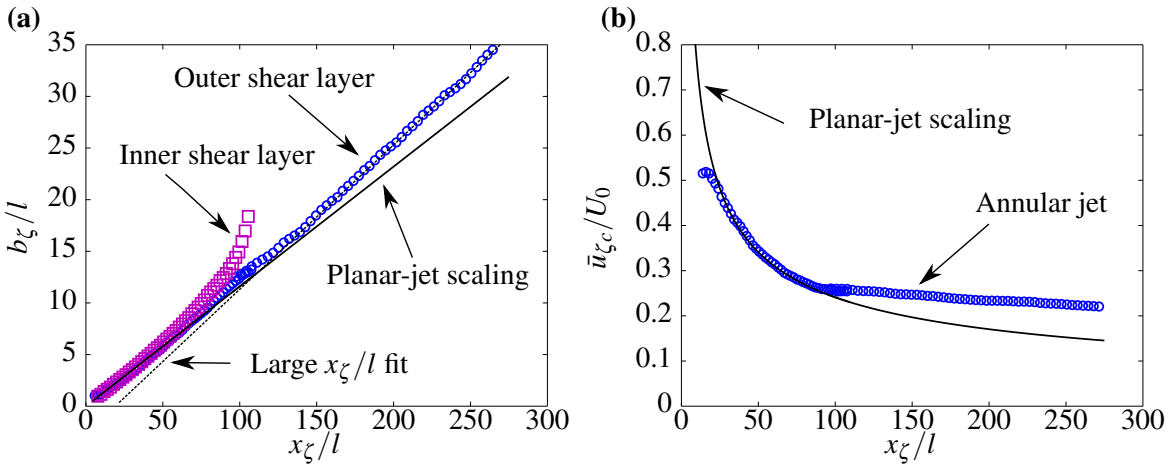

Fig. 4.11: (a) Normalised width of inner shear layer $b_{\zeta i}/l$ (□) and outer shear layer $b_{\zeta o}/l$ (○) versus streamwise distance x_ζ/l (see figure 4.3). The solid line with gradient 0.116 shows the linear shear layer growth for an idealised planar jet (Fischer et al., 1979, p. 328). The dashed line represents a linear best fit to our ventilated annular-jet data for $x_\zeta/l > 150$ and has a gradient of 0.137. (b) Streamwise centreline velocity for our ventilated annular jet (○). The solid line plots the planar-jet velocity $\bar{u}_{\zeta c}/U_0 = const.(x_\zeta/l)^{-1/2}$ (Fischer et al., 1979) with a constant of proportionality of 2.5. For reference, the locations $x_\zeta/l = \{100, 250\}$ are equivalent to $x/D_o \approx \{1.6, 4.0\}$ on the longitudinal nozzle axis.

approximate self-similarity is attained for $x/D_o \gtrsim 5$. Returning to figure 4.9(a) we note that the outer shear layer of the final profile (☆ at $x_\zeta = 265l$, or, equivalently, $x \approx 4.5D_o$) is also Gaussian and self-similar, suggesting that the outer shear layer transitions, without a break in self-similarity, into the single shear layer observed after the jet has merged.

For the profiles of time-averaged radial velocity, figure 4.12(b), there is no close collapse of the data, although for $x/D_o \gtrsim 7$ the profiles begin to more closely overlap. As noted in §4.3.4, the cross-stream velocity $\bar{v}_\zeta$ profiles of the coalescing jet are not self-similar due to the influence of merging, and it was therefore to be expected that the radial velocity profiles $\bar{v}(x = const., y)$ of the coalesced jet appear to be approaching self-similarity downstream of the axial velocity profiles $\bar{u}(x = const., y)$. Figure 4.12(b) clearly shows that the jet entrains fluid from the ambient (velocities towards the jet centreline in the ambient) and that fluid within the core of the jet moves outwards (velocities away from the centreline in the jet).

Dimensionless profiles of axial ($I_u = \sigma_u/\bar{u}_c$) and radial ($I_v = \sigma_v/\bar{u}_c$) turbulent intensities are shown in figure 4.13. Although the profiles are qualitatively similar to those observed in round jets (Hussein et al., 1994; Wang & Law, 2002), the peak turbulent intensities for the annular jet ($I_{u,max} = 0.24$ and $I_{v,max} = 0.17$ at $x/D_o \approx 14$) are significantly lower (for the round jet of Hussein et al. (1994) $I_{u,max} \approx 0.29$ and $I_{v,max} \approx 0.23$), at least for the downstream distances

Symbol	+	◯	∗	●	×	□	◊	▷	◁	△	▽	☆
x/D_o	1	2	3	4	5	6	7	8	9	10	12	14
$x/\sqrt{A_0}$	4.5	8.9	13.4	17.9	22.3	26.8	31.3	35.7	40.2	44.6	53.6	62.5

Table 4.4: Symbol with corresponding dimensionless axial distance downstream of the nozzle exit plane used in the velocity, turbulent intensity, Reynolds stress and turbulent viscosity profiles (figures 4.12, 4.13, 4.15a-b). On travelling downstream, the colour of the symbols transmutes from blue to red.

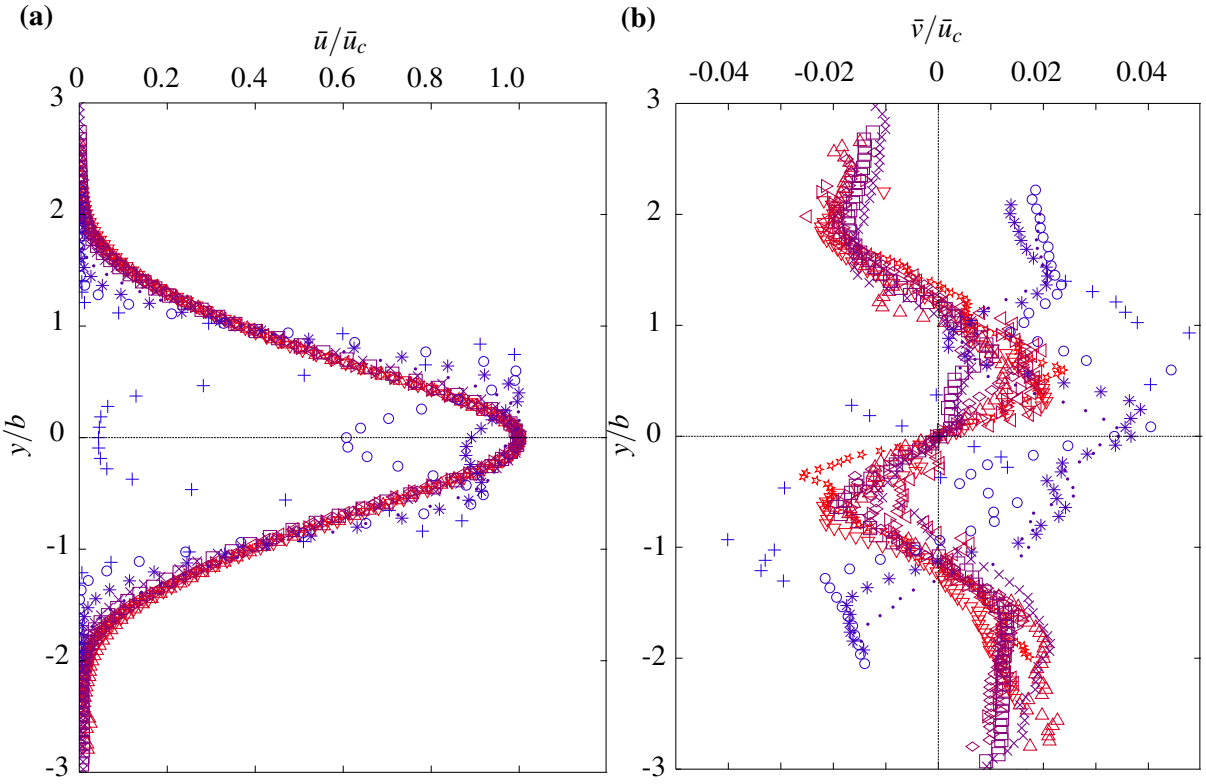

Fig. 4.12: Time-averaged velocity profiles for the ventilated annular jet: (a) axial velocity $\bar{u}/\bar{u}_c$ and (b) radial velocity $\bar{v}/\bar{u}_c$ at downstream distances from $x/D_o = 1.0$ (+) to $x/D_o = 14.0$ (☆). See table 4.4 for the downstream location corresponding to each symbol.

that were possible for us to make measurements. These differences indicate that the turbulence statistics do not reach a fully self-similar state within $16D_o$ of the source. This claim is further supported by the results of figure 4.14 which show that the peak axial turbulent intensity $I_{u,max}$ is not independent of x/D_o within our measurement domain.

It is prudent here to check at what distance from the source the turbulent statistics reach self-similarity in round jets, and to compare this distance with the measurement domain of our experiment. To enable comparisons between round jets and annular jets we scale on the characteristic round-jet length scale $Q_0/M_0^{1/2} = \sqrt{A_0}$ (Fischer et al., 1979). Ferdman et al. (2000) find self-similarity of the turbulence statistics in round jets at approximately 40 diameters downstream (for their nozzle $40D \approx 45\sqrt{A_0}$). Ko & Chan (1978) observed that the *unventilated* annular jet attained a self-similar state beyond approximately $5D_o$ downstream (for their nozzle $5D_o \approx 6.3\sqrt{A_0}$). The corresponding measurements within our *ventilated* annular jet, even as far downstream as $15.7D_o(\approx 70\sqrt{A_0})$, are not fully self-similar, suggesting that the open-core slender annular geometry and the resulting internal region of induced flow have a significant influence on the development of a jet.

Figure 4.15(a) shows normalised radial profiles of Reynolds stress $\overline{u'v'}/u_c^2$, a quantity which represents the turbulent shear stresses within the annular jet. As one would expect, the Reynolds stress profiles indicate that momentum is transferred away from the jet axis towards the ambient. Although the profiles appear to be progressing towards a self-similar state, similarity is not reached. These profiles, while qualitatively similar to the round-jet observations of Hussein et al. (1994), exhibit marginally reduced peak Reynolds stresses $(\overline{u'v'}/u_c^2)_{max} \approx 0.02$ (for round jets $(\overline{u'v'}/u_c^2)_{max} \approx 0.025$) due to the aforementioned reduced peak turbulent intensities. These reduced peak Reynolds stresses indicate that, within our measurement domain $0 < x/D_o < 16$, the magnitude of momentum transferred away from the jet centreline for the ventilated annular jet is less than for a fully developed round jet.

As we shall see below, evaluating the turbulent viscosity,

$$\nu_T(x,y) = \frac{-\overline{u'v'}}{\partial\bar{u}/\partial y}, \tag{4.4}$$

a measure of the radial momentum transport within the jet, lends support to the conclusion that the ventilated annular jet has a reduced momentum transport when compared to self-similar round jets, at least as far downstream as $x = 16D_o$. Radial profiles of normalised turbulent viscosity $\hat{\nu_T} = \nu_T/(\bar{u}_c b)$, figure 4.15(b), are qualitatively similar to those of Hussein et al. (1994) for round jets (their results plotted as the continuous line) although with a reduced magnitude and, therefore, a reduced radial momentum transport. The profiles suggest that the momentum transfer occurs primarily for $|y/b| < 1$, and reduces with distance from the jet

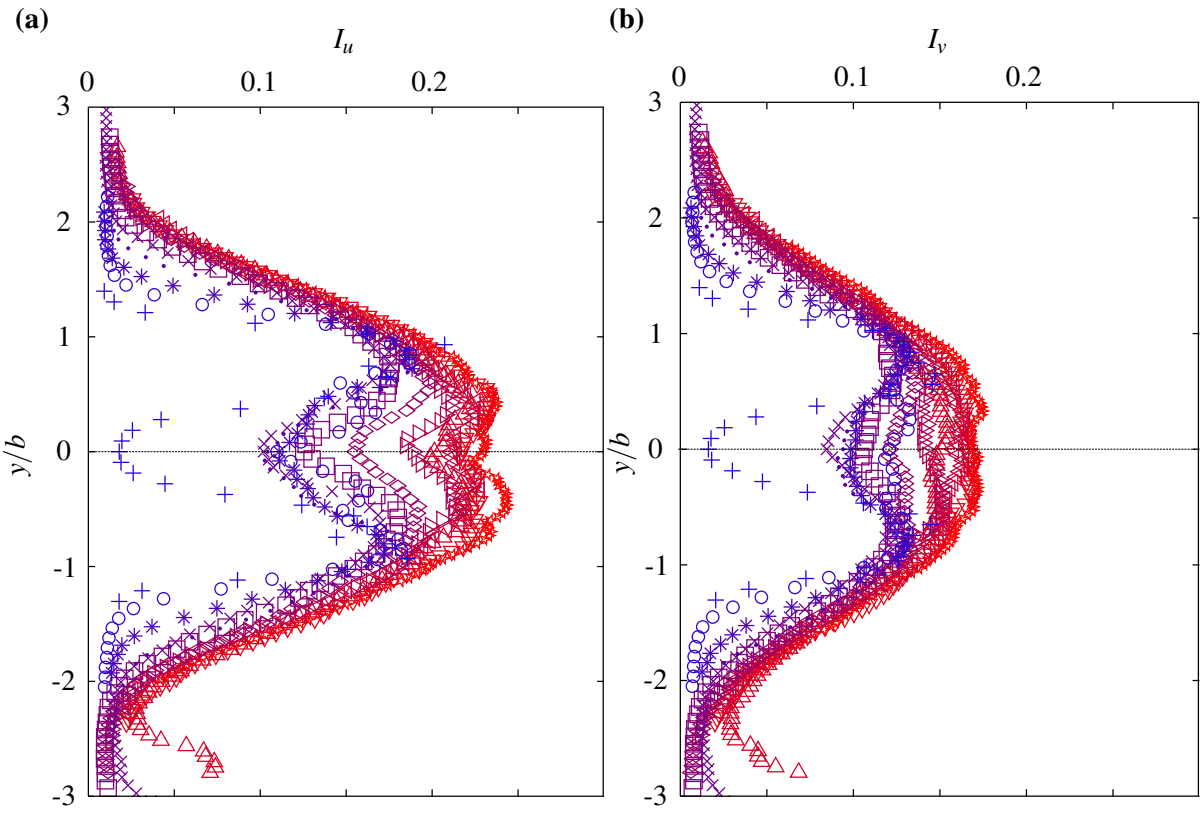

Fig. 4.13: Turbulent intensity profiles for the ventilated annular jet: (a) axial turbulent intensity $I_u(x,y) = \sigma_u(x,y)/\bar{u}_c(x)$ and (b) radial turbulent intensity $I_v(x,y) = \sigma_v(x,y)/\bar{u}_c(x)$. The downstream location corresponding to each symbol is given in table 4.4. The uncharacteristicly high turbulent intensities for $y/b < -2$ on the profile at $x/D_o = 12$ are due to the regular appearance of rogue vectors at the window extremities due to the vignetting effect of the lens and filter, see §3.5 for further discussion.

centreline for $|y/b| > 1$. The scatter near the jet axis occurs because the Reynolds stress is divided by a very small velocity gradient and thus small errors are amplified in this region. The implications of the reduced momentum transport are discussed in §4.3.5.

The development of radial momentum transport along the length of the jet becomes clear on plotting the axial variation in turbulent viscosity. This was achieved by calculating the dimensionless bulk turbulent viscosity $\langle \hat{\nu}_T \rangle$. The quantity $\langle \hat{\nu}_T \rangle$ represents an average of $\hat{\nu}_T$ across the jet and is calculated using the fit proposed by Ezzamel et al. (2015) and van Reeuwijk et al. (2016), whereby a Gaussian velocity profile is assumed and the experimental profiles are fitted to the function

$$F = 2\langle \hat{\nu}_T \rangle \frac{y}{b} \exp\left(-\frac{y^2}{b^2}\right). \tag{4.5}$$

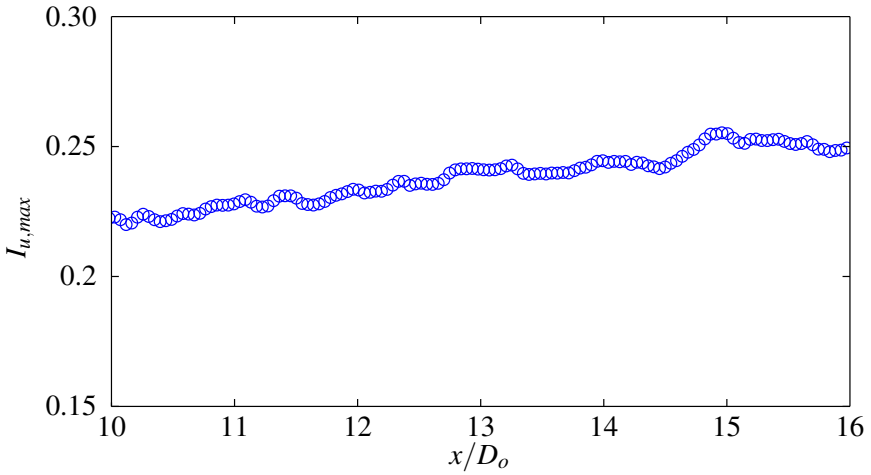

Fig. 4.14: Peak axial turbulent intensity $I_{u,max}$ in the ventilated annular jet versus downstream distance x/D_o.

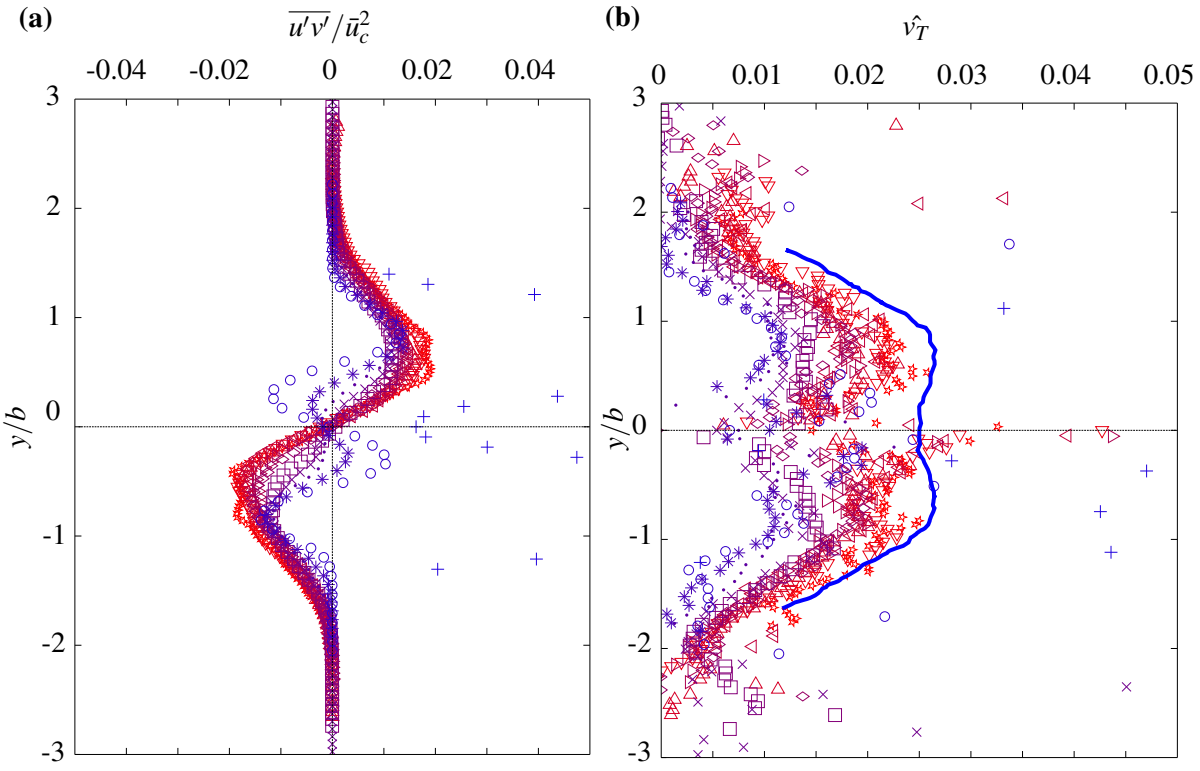

Fig. 4.15: Radial profiles of dimensionless: (a) Reynolds stress $\overline{u'v'}/\bar{u}_c^2$ and (b) turbulent viscosity $\hat{\nu_T} = \nu_T/(\bar{u}_c b)$. In (b) the line represents the fit of Hussein et al. (1994) to their experimental data for a round jet. See table 4.4 for the downstream location corresponding to each symbol.

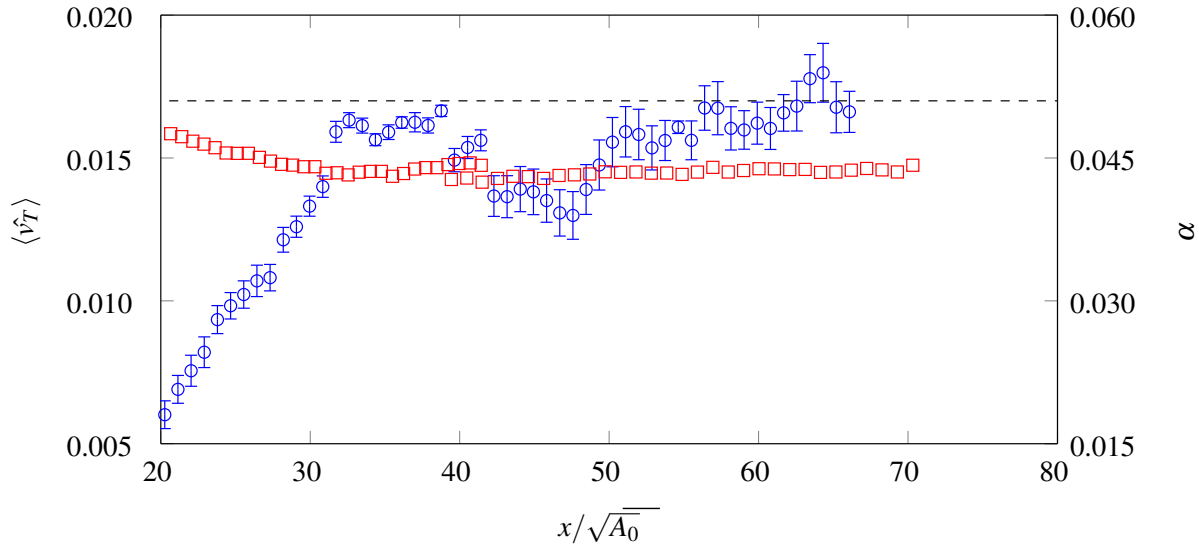

Fig. 4.16: Bulk turbulent viscosity $\langle \hat{\nu_T} \rangle$ (○) versus downstream distance $x/\sqrt{A_0}$. The errror bars represent the 95% confidence interval obtained when fitting the data to (4.5). The entrainment constant $\alpha \approx 3\langle \hat{\nu_T} \rangle$ (Ezzamel et al., 2015; van Reeuwijk et al., 2016), and as such, the axis on the right-hand side represents the conversion from $\langle \hat{\nu_T} \rangle$ to α. Also plotted (□) is the entrainment constant worked out from the volume flux using (4.6) and (- - - -) the entrainment constant calculated from $\alpha = c_1/2$ (Fischer et al., 1979).

For $x/\sqrt{A_0} \lesssim 30$ estimates of $\langle \hat{\nu_T} \rangle$ are inaccurate due to the continuing development of the jet which renders the assumptions used in the derivation of (4.5) invalid. Further downstream, despite the uncertainty shown, figure 4.16 (○) indicates that $\langle \hat{\nu_T} \rangle$, and therefore radial momentum transport, increases with downstream distance.

Much of the work on the subject of entrainment by jets follows on from the classic work of Ricou & Spalding (1961) in which they developed elegant experiments to satisfy the 'entrainment appetite' of the jet. Morton et al. (1956) parameterise this entrainment by means of an entrainment constant α, which links the radial velocity of the induced flow to the velocity along the jet centreline Morton et al. (1956), so that for the far field of our annular jet

$$\frac{dQ}{dx} = 2\pi b \alpha \bar{u}(x,0). \tag{4.6}$$

Typically, the entrainment coefficient for jets falls within the range $0.045 < \alpha < 0.056$ Ezzamel et al. (2015). Neglecting the contributions from higher order terms, from Ezzamel et al. (2015), the entrainment constant $\alpha \approx 3\langle \hat{\nu_T} \rangle$. Thus, the axis on the right of figure 4.16 shows that for $x/\sqrt{A_0} \gtrsim 30$ the estimates of $\langle \hat{\nu_T} \rangle$ give values of α that are consistent with those from the literature. Also plotted (- - - -) is $\alpha = c_1/2$ (Fischer et al., 1979), and (□) values of α

	c_1	c_2	c_3
Ventilated annular jet	0.102	7.5	0.231
Round jet	0.113	6.5	0.353
Fischer et al. (1979)	0.107	7.0	-
Hussein et al. (1994)	-	6.5	-

Table 4.5: Coefficients for (4.7a), (4.7b) and (4.7c) for the ventilated annular jet and the round jet.

calculated using (4.6) and values of b, $u(x,0)$ and dQ/dx from figure 4.17, where dQ/dx has been estimated using the linear best fit line. For $x/\sqrt{A_0} \gtrsim 30$, estimates of α from the turbulent viscosity fall between the estimates of α calculated using the spreading rate and volume flux.

Axial dependence

To compare the far-field development of the annular jet with the classic round jet, we examine the axial dependence of their width b, axial velocity $\bar{u}(x,0)$ and volume flux Q (figure 4.17). For the round jet we performed independent PIV measurements as discussed in Appendix A. To enable direct comparisons, we once again scale the downstream distance on the characteristic round-jet length scale $\sqrt{A_0}$ (Fischer et al., 1979). For our annular nozzle $D_o \approx 4.5\sqrt{A_0}$.

Our data for the annular jet shown in figure 4.17(a-c) confirms that, as for a round jet, far from the nozzle, jet width, inverse axial velocity, and volume flux increase linearly with x and can be described by

$$b = c_1(x - x_0), \quad (4.7a) \qquad \bar{u}(x,0) = c_2 U_0 \left(\frac{x - x_0}{\sqrt{A_0}}\right)^{-1}, \quad (4.7b) \qquad Q(x) = c_3 Q_0 \frac{x - x_0}{\sqrt{A_0}}, \quad (4.7c)$$

where x_0 denotes the virtual origin (see §4.3.5). Estimates of volume flux were calculated using (4.3). The constants c_1, c_2 and c_3 describing the far-field behaviour of the round and annular jets are given in table 4.5. Although from these entries it would appear that the decay rate (c_2) of the annular jet velocity exceeds that of our round jet (and the round jets of Hussein et al. (1994) and Fischer et al. (1979)), the turbulent quantities within our measurement domain have not reached self-similarity and, therefore, the decay rate would likely evolve further with downstream distance. The increasing turbulent intensities and turbulent viscosity with distance downstream, reported in §4.3.5, indicate an increasing radial momentum transfer, which will result in a reducing decay constant (a larger decay constant c_2 signifying a lower decay rate) and an increasing bulk entrainment rate c_3 in the annular jet.

Nearer to the nozzle ($x/\sqrt{A_0} \lesssim 40$), the volume flow rates of the annular and round jets differ significantly. This difference is in part an artefact of (4.3) which, for the annular jet, includes the contribution of the internal induced flow in $Q(x)$, a contribution that is not strictly part of the jet but rather of the induced flow. To exclude the internal induced-flow region in our comparisons of annular- and round- jet flow rates, we may compare flow rates at the merge point. The volume flux of the annular jet at the merge point (located at either $5.0\sqrt{A_0}(\approx 1.11D_o)$ or $7.2\sqrt{A_0}(\approx 1.60D_o)$, see §4.3.2) exceeds that of the round jet by 200 - 210 % (figure 4.17c), suggesting that entrainment of this internal induced flow serves to increase the volume flux of the annular jet near the nozzle. Estimates of the volume flux (Q/Q_0) very near the source ($x/\sqrt{A_0} \lesssim 1.5$) are inaccurate due to a combination of the large velocity gradients and the spatial resolution of the data. Downstream of the merge point, the bulk entrainment rate of the jet decreases (compare the gradient of the ventilated annular jet measurements for $x \leq 7.2\sqrt{A_0}$ and $x > 7.2\sqrt{A_0}$). This suggests that the increased bulk entrainment in the near field is primarily due to entrainment of the induced flow. Far from the source, for $x/\sqrt{A_0} \gtrsim 40$, the volume flux Q and the dilution rate dQ/dx of the annular jet is below that of the corresponding round jet. This reduced far-field dilution is due to the reduced momentum transport within our measurement domain, as signified by the reduced decay constant in the round jet ($c_2 = 6.5$ in the round jet as opposed to $c_2 = 7.5$ in the ventilated annular jet, see figure 4.17). This reduced momentum transport is also discussed with respect to the turbulent viscosity in §4.3.5. However, the turbulent quantities within our measurement domain have not reached self-similarity and, therefore, the dilution rate would likely evolve further with downstream distance.

For the ventilated annular jet, all three quantities ($b/\sqrt{A_0}$, $(\bar{u}(x,0)/U_0)^{-1}$, Q/Q_0) attain an approximately linear behaviour for $x/\sqrt{A_0} \gtrsim 40$; for the round jet we estimate for $x/\sqrt{A_0} \gtrsim 20$. This difference is attributed to the near-field planar-jet region and the distance over which the annular jet coalesces prior to asymptoting to round-jet behaviour.

A note on virtual origins

The position of the virtual origin $x = x_0$ for the ventilated annular jet proved to be sensitive to the downstream distance at which we assumed the far-field linear behaviour (4.7a-c) to commence. As discussed earlier, we believe this stems from the fact that the jet has not yet reached a fully self-similar state. There are, however, trends of note. The annular nozzle geometry shifts the virtual origin upstream relative to both the round jet and the nozzle itself. From fitting data in the range $40 < x/\sqrt{A_0} < 70$, we locate the virtual origin at $x_0/\sqrt{A_0} = -4.0 \pm 0.9$, where ± 0.9 represents the variation in the virtual origin between the different quantities considered. This upstream shift occurs due to the relatively large nozzle diameter D_o when compared with the slot width l.

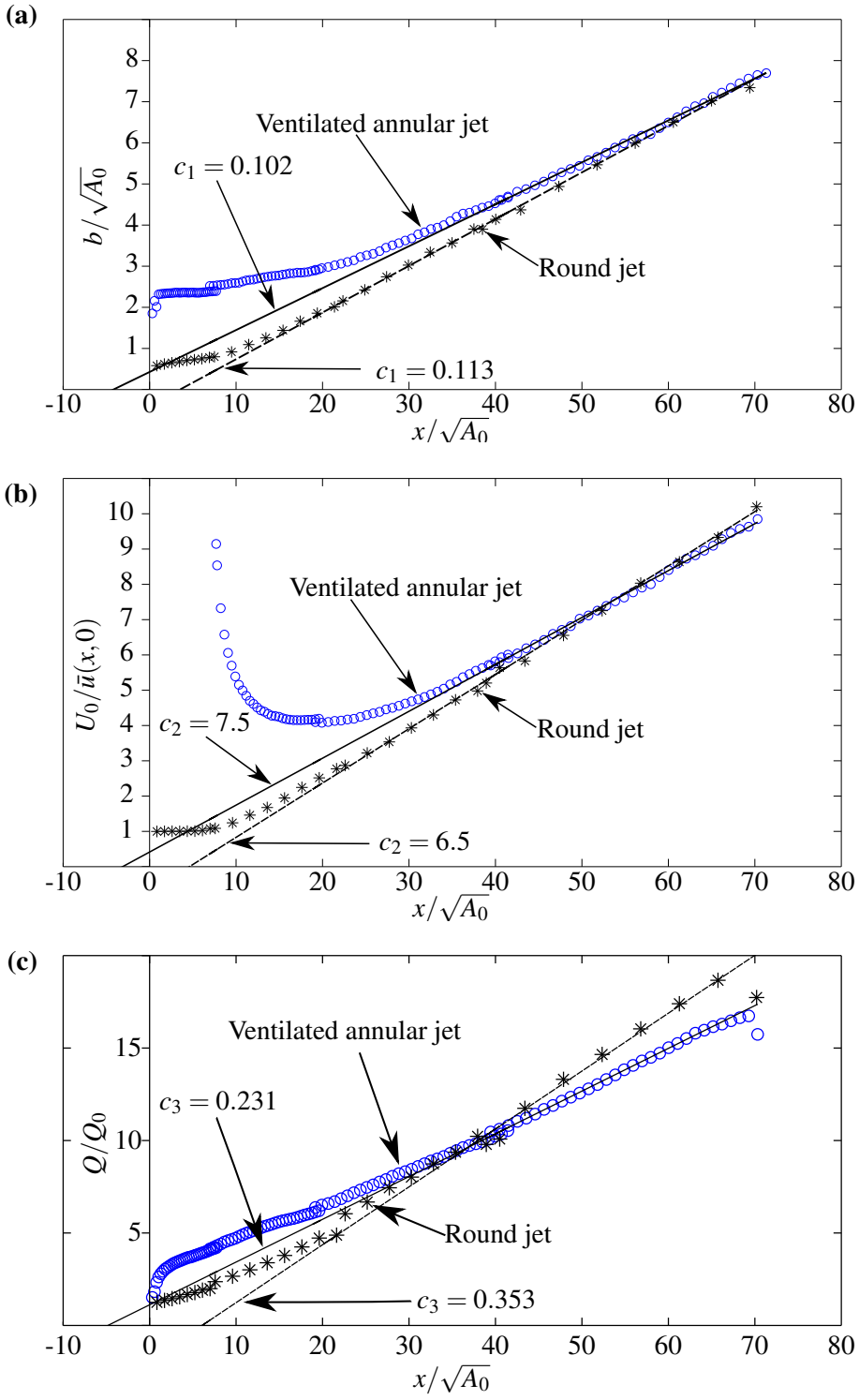

Fig. 4.17: Dimensionless variation with distance downstream $x/\sqrt{A_0}$ of: (a) jet width $b/\sqrt{A_0}$; (b) inverse axial velocity $(\bar{u}(x,0)/U_0)^{-1}$; and (c) volume flux Q/Q_0 (calculated using (4.3)). Ventilated annular jet data ($\circ$) and best linear fit to this data for $x/\sqrt{A_0} \geq 40$ (solid line). Round-jet data ($*$) and best linear fit to this data for $x/\sqrt{A_0} \geq 20$ (dashed line) as measured in our validation experiments (see Appendix A for details). The best fit lines are given by (4.7a), (4.7b), (4.7c) with the constants c_1, c_2, and c_3 given on the figures. The virtual origin x_0 is the location at which the best fit lines cross the x-axis.

4.3.6 Transition $(1 \lesssim x/D_o \lesssim 10)$

Between the near-nozzle region, where the jet exhibits planar-jet behaviour ($x_\zeta/l < 60$ or, equivalently, $x/D_o < 1$, §4.3.4), and the far field, where the jet exhibits round-jet behaviour ($x/\sqrt{A_0} > 45$ or, equivalently, $x/D_o > 10$, §4.3.5), the flow may be regarded as in transition between these two states. The profiles of time-averaged streamwise $\bar{u}_\zeta(x_\zeta = const., y_\zeta)$ and axial $\bar{u}(x = const., y)$ velocity in the outer shear layer (for $y_\zeta/b_\zeta \geq 0$ in figure 4.9a and $x/D_o \geq 5$ in figure 4.12a) remain self-similar throughout this transitional region, suggesting that the influence of the coalescence on the structure of the outer shear layer is small. However, the absence of full self-similarity in the profiles of the time-averaged cross-stream $\bar{v}_\zeta(x_\zeta = const., y_\zeta)$ and radial $\bar{v}(x = const., y)$ velocities (figures 4.9b and 4.12b) demonstrates that the jet is evolving dynamically along our entire domain of measurement. It is within the transitional region that the high-velocity centreline extending from the annular slot merges. Beyond the reattachment point, located at $4.5D_o$ downstream, the jet can be regarded as having completely coalesced; the outer shear layer has absorbed the entirety of the inner shear layer, although the flow continues to develop downstream (§4.3.5).

Clear indicators for the transition are also evident in the turbulent intensity profiles, where a local self-similarity is observed near the nozzle (see profiles in figure 4.10 for $30 \leq x_\zeta/l \leq 105$ or, equivalently, $0.5 \leq x/D_o \leq 1.75$) and a second local self-similarity is evident far downstream (figure 4.13). Between these regions, the turbulent intensities within the inner shear layer tend to decrease as the jet merges (see $y_\zeta/l \leq 0$ on profiles in figure 4.10 for $x_\zeta/l \geq 105$) as a result of the reduced velocity gradient in the inner shear layer (see profiles in figure 4.9 for $x_\zeta/l \geq 105$). Once the inner shear layer has been absorbed, the turbulent intensities begin to increase (see profiles in figure 4.13 for $x/D_o \geq 5$). The transition is also noted on examining the variation of the jet width and centreline velocity with distance downstream (figures 4.11, 4.17). The regions of planar-jet behaviour and of local self-similarity near the nozzle terminate at the same location ($x_\zeta/l \approx 100$) due to the link between the jet development and its turbulent properties. We anticipate that the extents and characteristics of the transitional region to be primarily influenced by the inner D_i and outer D_o diameters of the nozzle, as these length scales characterise the separation between the opposite sides of the (inner and outer) shear layers and of the jet centreline at the source.

4.4 Conclusions

The dynamics of a turbulent jet produced on ejecting fluid steadily through a slender annular slot surrounding an open core into an otherwise quiescent uniform environment have been studied.

Using high-resolution velocity measurements obtained from particle image velocimetry we have identified four regions of flow, each characterised by a distinct behaviour and dominant length scale. Herein we targeted a slender annulus, the ratio of internal to external diameters $D_i/D_o = 0.968$ being close to the theoretical idealised limit of $D_i/D_o = 1$. Moreover, the core was almost fully open with a ventilation ratio of $D_v/D_i \approx 0.9$.

Unique to the open-core, or ventilated, annular geometry is an internal region of induced flow that is bounded by the jet itself. This bounded induced-flow region is driven by entrainment into the inner shear layer of the jet and its extent characterised by the internal diameter D_i. Our measurements indicate that the volume flux entrained into the jet from this internal flow region is comparable with the source volume flux ($\approx 1.2Q_0$) and, as a consequence, near-field dilution is enhanced compared with a classic round jet. This feature could potentially be put to good effect in applications where there is a need, or benefit, to rapidly dilute the source fluid. For example, effluent discharges into the ocean often take the form of a round jet (Fischer et al., 1979) and near-field dilution could be significantly increased through the use of a slender ventilated annular nozzle geometry. However, for $x/\sqrt{A_0} \gtrsim 40$, the volume flux of the ventilated annular jet falls below that of the round jet, indicating that the open-core source would not be suitable for applications which require enhanced far-field dilution. Given the near-idealised geometry considered, the aforementioned volume flux induced through the core represents a practical upper limit, this flux reducing as the ventilation ratio D_v/D_i decreases.

The annular jet itself consists of a near-field planar-jet-like region, a transitional region and, ultimately, a far-field round-jet region. Within the planar-jet region, the behaviour of the flow is characterised by the slot width $l = (D_o - D_i)/2$; our results suggest that the jet has no knowledge of the annular nature of the source until merging begins. Far downstream, we observe behaviour characteristic of a round jet, namely a linear spreading rate, a linear decay of inverse axial velocity and a linear increase in volume flux. Based on comparisons made with classic round jets it appears that the relevant length scale of this far-field region is the square root of the slot area $\sqrt{A_0}$. While there is approximate self-similarity of the time-averaged axial velocities, the turbulent quantities continue to evolve with downstream distance indicating true self-similarity has not yet been achieved despite the scale of our measurement domain extending to $16D_o$. Nonetheless, it is clear that existing scalings for planar jets and round jets apply to the near-field and far-field regions respectively. With respect to the far field, the annular jet may be replaced with a round jet at the virtual origin – our results suggest the origin is located at $x/\sqrt{A_0} = -4.0$.

CHAPTER 5

The coalescence of a turbulent slender open-core annular jet - the role of the diameter ratio

5.1 Introduction

The measurements and flow visualisations of a turbulent jet from a slender annular source with an open centre, presented in §4, revealed the presence of an internal region of induced flow that is bounded by the jet itself. This region is comprised of unmixed ambient fluid which has been drawn through the open centre (or open core) of the annulus, prior to being mixed into the jet. Of primary interest herein is to characterise the bounded induced-flow region and the associated coalescing behaviour of the jet. The specific quantities of interest are the location at which the perimeter of the inner shear layer may be regarded as having first intersected (i.e. location $x = x_m$ in figure 5.1b), the location at which the jet has completely coalesced ($x = x_{re}$), and the volume flux Q_a and velocity U_a of the flow induced through the open core. At the outset of this work, the dependence of these quantities on the source geometry was unknown. Thus, here our focus is to address the question of how the diameter ratio D_i/D_o influences the bounded induced-flow region and the coalescing of the jet. The approach we take is two-fold: in §5.3 we develop a simplified theoretical model guided by the visualisation of the flow presented in §5.2; and in §5.5 we present the results of a complementary experimental investigation of the annular jet in air. The latter was then used to validate the theoretical model and provide further physical insights.

This chapter is structured as follows. In §5.2, streamline plots from the PIV experiments are presented in order to gain a first insight into the role of the nozzle geometry on the development

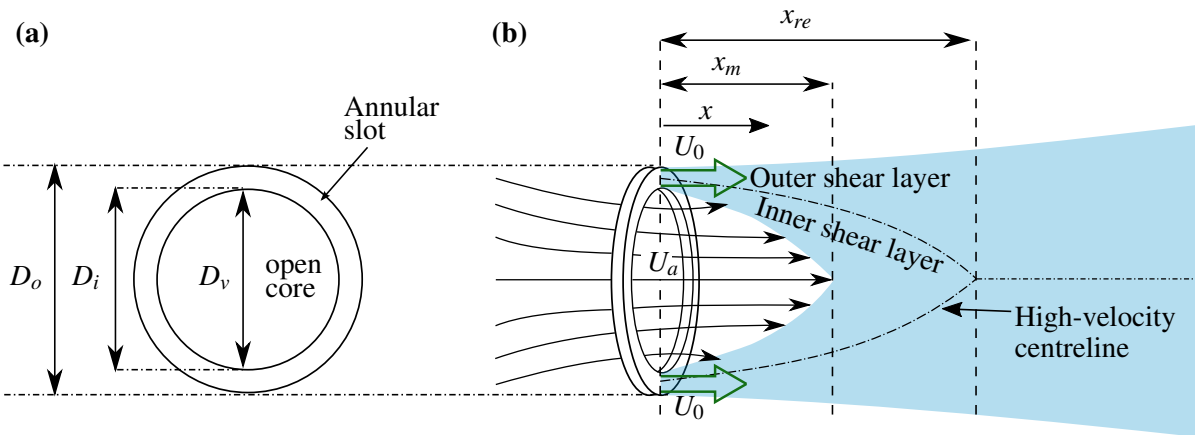

Fig. 5.1: Schematics depicting: (a) a fully open-core ($D_v/D_i = 1$) annular-jet source, shown face on to the exit slot of width $l = (D_o - D_i)/2$; (b) a time-averaged streamwise section through the jet showing streamlines for the flow induced through the open core. The shaded region indicates the main body of the jet. The inner and outer shear layers are separated by the high-velocity centreline (dot-dashed). The steady exit velocity U_0 is perpendicular to the plane of the source as indicated. Locations at which the perimeter of the inner shear layer merges ($x = x_m$) and at which the high-velocity centreline merges ($x = x_{re}$) are indicated. The bounded induced flow refers to the bullet-shaped region (unshaded) that extends a distance x_m downstream of the nozzle.

of the near field of the jet and to guide the mathematical modelling which follows. In §5.3, a theoretical model, inspired by the work of Marsters (1977) on parallel plane jets, is developed in order to predict Q_a, U_a, x_m and x_{re} for the open-core annular jet. In §5.4, the PIV experiments used to investigate the influence of the diameter ratio on jet coalescence are described. The predictions and measurements are compared in §5.5.1. In §5.5.2 the effect of the diameter ratio on the far field of the annular jet is assessed. Finally, in §5.6 we summarise our findings and draw our conclusions.

5.2 Flow visualisation

To guide the theoretical developments it is informative to first visualise the flow and identify the main flow features. The pattern of time-averaged streamlines for five open-core annular jets with diameter ratios spanning $0.845 \leq D_i/D_o \leq 0.981$, obtained from our planar PIV measurements (§5.4), are shown in figure 5.2. For these five nozzles the mean diameter remained approximately constant and the diameter ratio was varied by modifying the slot width (see table 5.1 for details). As can be seen, all five nozzles produce a jet which coalesces

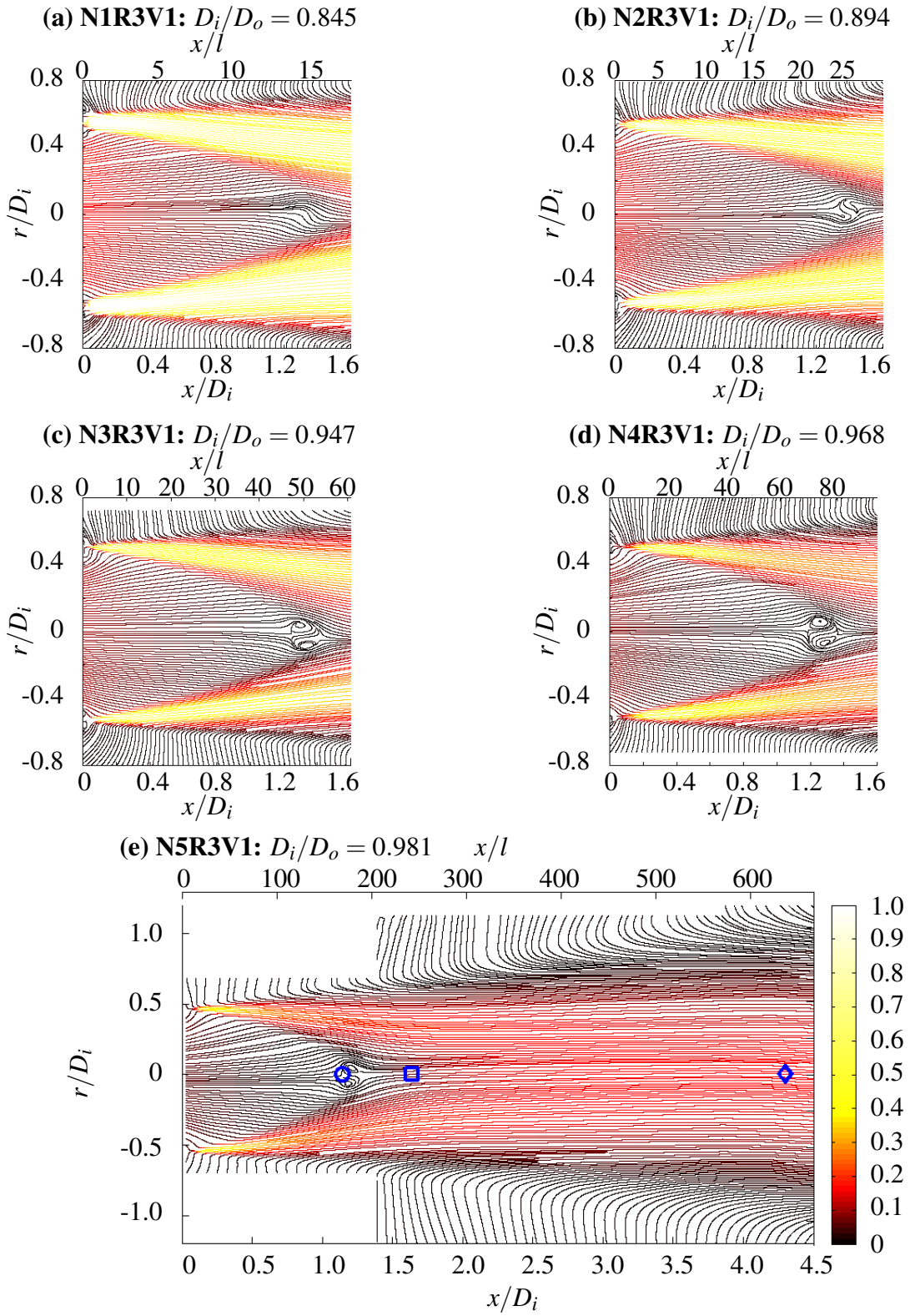

Fig. 5.2: Streamlines of the time-averaged flow for sources **N1-5R3V1** in order of increasing diameter ratio D_i/D_o (details in table 5.1). Colours indicate the non-dimensional velocity magnitude along the streamline $\sqrt{\bar{u}^2+\bar{v}^2}/U_0$, where $\bar{u}$ and $\bar{v}$ are the time-averaged axial and radial velocity components, respectively. The streamlines have been plotted using an inbuilt Matlab function, hence the distance separating neighbouring streamlines does not represent a constant change in the stream function. In (e) the symbol '$\circ$' indicates the location of the upstream stagnation point, '$\square$' the location at which the velocity thresholds intersect (see §5.5.1) and '$\diamond$' the reattachment point (cf. the equivalent symbols on figure 5.8. The location of the symbols has been extracted from the experimental measurements presented in §5.5.1).

downstream of the source, and each induces a flow through the open core of the annulus – a flow which is subsequently entrained and mixed into the jet. The main body of the jet and the region of induced flow are readily distinguished. When scaled on D_i, the axial extent of the bounded induced-flow region is approximately $1.5D_i$ and does not vary appreciably with diameter ratio; the extent of this region reduces marginally as D_i/D_o increases. In figure 5.2 and later in §5.5.1, where we are primarily concerned with the bounded induced-flow region, distances are scaled on the inner diameter of the annulus D_i as this length scale separates opposite sides of the inner shear layer at the source.

In contrast to closed-core annular jets, a large-scale recirculation region is not produced. Air entrained into the outer shear layer (external jet perimeter at top and bottom of the images) induces a flow in a direction that is approximately perpendicular to the local high-velocity centreline. The curvature of the centreline is relatively low, the trajectory of the jet being almost horizontal. On noting the variation in colour along the x-axis, one may make the additional observation that the dimensionless velocity in the jet decays more rapidly as D_i/D_o increases. This may be explained as follows: near the nozzle, the jet is planar-like, as established in PHJ17, and hence the length scale governing the decay of centreline velocity is the slot width l $(= (D_o - D_i)/2)$. Now $2l/D_i = (D_o/D_i) - 1$ and thus increasing D_i/D_o results in a decrease in l relative to D_i (compare the x/D_i and x/l axis scales of the plots in figure 5.2). Thus, when comparing the identical dimensionless axial distances x/D_i, as on figure 5.2, the velocity appears to decay more rapidly as D_i/D_o increases.

Figure 5.2(b-e) reveals a small-scale recirculation region on the nozzle axis, between $1.2 \lesssim x/D_i \lesssim 1.4$, where the inner shear layer of the jet strongly interacts and self entrains. A recirculation region is not visible on the streamline plot for source **N1R3V1**, figure 5.2(a), although the flow along the nozzle axis is clearly redirected at $x/D_i \approx 1.3$. These streamline plots suggest then that the small-scale recirculation region reduces in intensity and ultimately disappears as D_i/D_o is reduced. We anticipate that the formation and intensity of the small-scale recirculation region are governed by the relative magnitudes of the pressure and inertial forces at the downstream end of the bounded induced-flow region. As the diameter ratio increases, the relative magnitude of the inertial force decreases, cf. (1.5). Moreover, the streamline patterns indicate that once D_i/D_o exceeds a certain threshold, the pressure force overcomes the inertial force and redirects some fluid upstream. The relative magnitudes of the inertial and pressure forces $F_I/(kF_P)$, calculated at the source using (1.5) are plotted in figure 5.3. This reveals in excess of a two-fold reduction in $F_I/(kF_P)$ as the diameter ratio increases (by contrast, only marginally) from 0.845 to 0.981. Furthermore, the presence of the small-scale recirculation region can be used to isolate the slender regime of the open-core

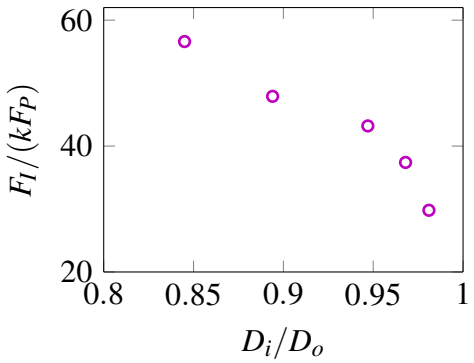

Fig. 5.3: Variation of the ratio of inertial and pressure forces $F_I/(kF_P)$ with D_i/D_o. The values plotted have been calculated using (1.5) and the experimental measurements of U_a/U_0 (the latter are shown in figure 5.7a).

annular jet. Based on our observations, this pins down the critical slender diameter ratio to the range $0.845 < (D_i/D_o)_S < 0.894$.

The locations of interest, which we have used to characterise the coalescing behaviour of the jet, are marked on figure 5.2(e). The two definitions of the merge point x_m, as discussed in §5.5.1, are indicated with the symbols '$\circ$' and '$\square$', and the location of the reattachment point x_{re} with '$\diamond$'. We return to a discussion of these symbols in §5.5.1.

5.3 Model development

5.3.1 Outline

Our objective is to develop a predictive capability so as to quantify the influence of the diameter ratio on the quantities that characterise the coalescing behaviour and bounded induced-flow region of a slender annular jet from a nozzle with an open core.

The turbulent jet considered is an incompressible and isothermal flow that originates from an annular slot, of area A_0, which circumnavigates a fully open core (so that $D_v/D_i = 1$) of area A_a. The density of the jet and environment are denoted ρ. The source momentum flux of the jet is denoted by ρM_0. As we consider the time-averaged behaviour of the jet, we treat the flow as axisymmetric. Figure 5.4 shows a schematic of this jet, together with a section through a cylindrical control volume, labelled $\mathbf{BCC'B'}$, of radius $r = r_{CV}$. The upstream end of the control volume is coincident with the slot exit (section $\mathbf{BB'}$) and the downstream end (section $\mathbf{CC'}$) is at $x = x_C$, where $x_C \gg x_{re}$. We proceed by examining the fluxes of momentum

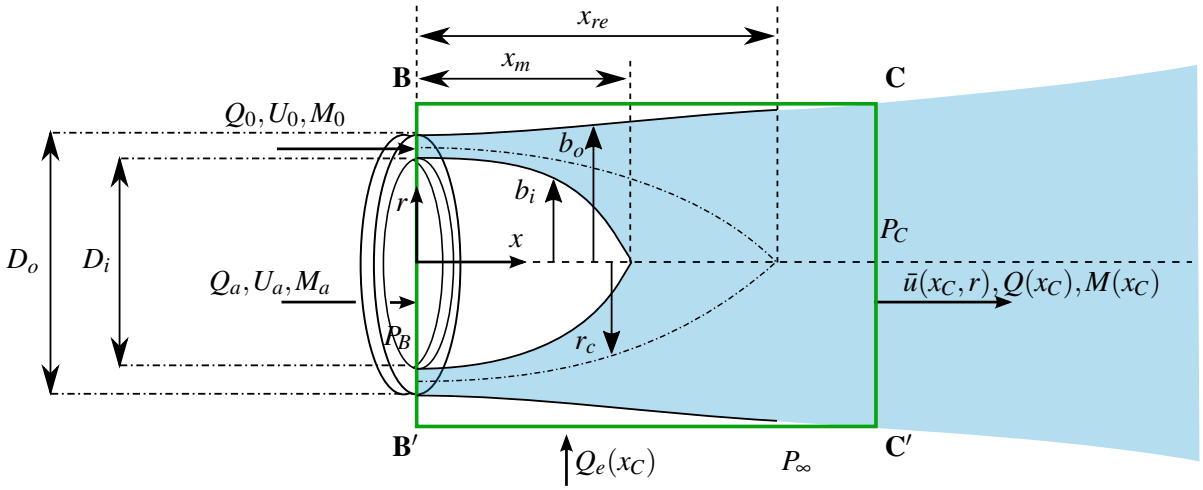

Fig. 5.4: The schematic depicts an $x-r$ plane through the jet and control volume **BCC′B′**. Key dimensions, velocities and the fluxes into and out of the control volume are marked. The dot-dashed curve with radius r_c represents the high-velocity centreline.

and volume through the control volume. Our analysis is based on the mean flow and does not include the turbulent contribution to the fluxes.

5.3.2 Governing equations

At section **CC′**, the volume flux of the jet $Q(x_C)$ consists of contributions from the source volume flux Q_0, from the volume flux induced through the open core Q_a, and from the volume flux entrained into the outer shear layer $Q_e(x_C)$ between the source at $x = 0$ and $x = x_C$. Conservation of volume flux thereby requires

$$Q(x_C) = Q_0 + Q_a + Q_e(x_C). \tag{5.1}$$

In addition to the source momentum flux (ρM_0), the momentum flux in the jet at section **CC′** (denoted $\rho M(x_C)$) consists of contributions from the flux induced through the core (ρM_a) and the pressure force acting on the control volume. The momentum equation in the x-direction (figure 5.4) may therefore be written

$$2\pi \int_0^{r_{CV}} P_B(r) r \, \mathrm{d}r - 2\pi \int_0^{r_{CV}} P_C(r) r \, \mathrm{d}r = \rho M(x_C) - \rho M_0 - \rho M_a, \tag{5.2}$$

where the static pressures $P_B(r)$ and $P_C(r)$ act over the upstream (**BB′**) and downstream (**CC′**) sections of the control volume, respectively.

As we focus on high Reynolds number releases that yield turbulent jets, the velocity profiles at the slot exit and across the open core of the annulus are assumed to be 'top-hat'. This assumption is supported by PHJ17 who recorded approximately uniform velocity profiles in these locations. The velocity of the flow induced through the open core U_a and slot exit velocity U_0 can now be expressed in terms of the fluxes Q_a and Q_0 as

$$U_a = \frac{Q_a}{A_a}, \qquad U_0 = \frac{Q_0}{A_0}, \tag{5.3a,b}$$

where

$$A_a = \pi(D_i/2)^2 \qquad \text{and} \qquad A_0 = \pi(D_o/2)^2 - \pi(D_i/2)^2. \tag{5.4a,b}$$

The specific momentum fluxes are thus

$$M_a = U_a^2 A_a, \qquad M_0 = U_0^2 A_0, \qquad M(x) = 2\pi \int_0^\infty \bar{u}(x,r)^2 r \, \mathrm{d}r, \tag{5.5a,b,c}$$

and the volume flux of the jet

$$Q(x) = 2\pi \int_0^\infty \bar{u}(x,r) r \, \mathrm{d}r, \tag{5.6}$$

where $\bar{u}$ denotes the time-averaged axial velocity in the jet. Substituting for (5.3), (5.5) and (5.6) into (5.1) and (5.2), volume and momentum conservation reduce to

$$2\pi \int_0^\infty \bar{u}(x_C,r) r \, \mathrm{d}r = U_0 A_0 + U_a A_a + Q_e(x_C) \tag{5.7}$$

and

$$2\pi \int_0^{r_{CV}} P_B(r) r \, \mathrm{d}r - 2\pi \int_0^{r_{CV}} P_C(r) r \, \mathrm{d}r = 2\pi\rho \int_0^\infty \bar{u}(x_C,r)^2 r \, \mathrm{d}r - \rho U_0^2 A_0 - \rho U_a^2 A_a, \tag{5.8}$$

respectively. Before attempting to solve (5.7) and (5.8) simultaneously, both expressions are simplified.

5.3.3 The momentum equation

To simplify the LHS of the momentum equation (5.8) several assumptions can be made. First, we assume that there is zero mass flux through section **BB′** beyond the nozzle boundaries

(i.e. zero mass flux along $x = 0$ for $r > D_o/2$) and, therefore, that the static pressure outside the nozzle boundaries on section **BB′** is atmospheric. This assumption is supported by the streamline plots in figure 5.2, which clearly show that air entrained into the outer shear layer is induced in a direction perpendicular to the jet flow. The approximately uniform velocity profile at the slot measured by PHJ17 indicates that the jet is issuing into a region of constant pressure. For simplicity, we assume that the pressure immediately downstream of the slot is equal to the pressure that spans the open core of the annulus. Therefore, within the nozzle boundaries, considering a particle of fluid accelerated through the open core, from rest far upstream of the nozzle, without a change in elevation, application of the Bernoulli equation gives

$$P_B(r) = \begin{cases} P_\infty - \frac{1}{2}\rho U_a^2 + P_L & \text{for } 0 \leq r \leq D_o/2 \\ P_\infty & \text{for } r > D_o/2 \end{cases} \tag{5.9}$$

where P_∞ denotes atmospheric pressure and P_L the pressure losses associated with the induced flow upstream of section **BB′**. Pressure losses stem from the presence of the nozzle, and include the effects of friction and contraction of the induced flow as it passes through the open core. We may reasonably neglect the presence of the nozzle and, therefore, for simplicity assume $P_L = 0$ (Appendix C.1). Section **CC′** is located sufficiently far downstream that the static pressure is uniform and atmospheric, i.e. $P_C(r) = P_\infty$. Thus the LHS of (5.8) becomes

$$2\pi \int_0^{r_{CV}} P_B(r) r \, \mathrm{d}r - 2\pi \int_0^{r_{CV}} P_C(r) r \, \mathrm{d}r = -\frac{1}{2}\rho U_a^2 \pi \left(\frac{D_o}{2}\right)^2. \tag{5.10}$$

We now introduce two dimensionless quantities, the ratio of the core and slot areas

$$\hat{A}_a = A_a/A_0, \tag{5.11}$$

and the ratio of the induced and source velocities

$$\hat{U}_a = U_a/U_0. \tag{5.12}$$

Combining (5.8) and (5.10), the dimensionless form of the momentum equation reduces to

$$\frac{M(x_C)}{M_0} = 1 + \gamma \quad \text{where } \gamma = \frac{\hat{U}_a^2}{2}(\hat{A}_a - 1). \tag{5.13}$$

For our slender annular jets, $\hat{A}_a \approx \{2.0,\ 3.2,\ 3.6,\ 11.8,\ 20.3\}$ and so $M(x_C) > M_0$. As is expected for an isothermal jet that is free from outside influences, (5.13) indicates that the local momentum flux of the coalesced jet is solely a function of the source geometry (via $\hat{A}_a$ and $\hat{U}_a$)

and (specific) source momentum flux. Given $M(x_C)$ is independent of x_C, hereinafter we drop the reference to x_C, replacing $M(x_C)$ with M.

5.3.4 The continuity equation

We now return to the continuity equation, (5.7), and first consider the volume flux entrained into the outer shear layer $Q_e(x_C)$. PHJ17 observed planar-jet-like behaviour for $0 \lesssim x/D_o \lesssim 1$, transitional behaviour for $1 \lesssim x/D_o \lesssim 10$ and round-jet-like behaviour for $x/D_o \gtrsim 10$; flow in the planar- and round- jet regions closely followed the classic scalings for round and planar jets. Due to the absence of such a robust scaling for the zone of flow establishment and the transitional region, the jet is simplified and modelled in two parts: from the source to the reattachment point[1] ($0 \leq x \leq x_{re}$) the jet is modelled as a fully developed planar jet; and downstream of this point ($x > x_{re}$), the jet is modelled as a fully developed round jet. Thus,

$$Q_e(x_C) = \int_0^{x_C} \frac{dQ_e}{dx}\,\mathrm{d}x = \underbrace{\int_0^{x_{re}} \frac{dQ_e}{dx}\,\mathrm{d}x}_{\text{Planar jet}} + \underbrace{\int_{x_{re}}^{x_C} \frac{dQ_e}{dx}\,\mathrm{d}x}_{\text{Round jet}}. \tag{5.14}$$

A discussion regarding the region of flow development of the planar jet together with the implications of assuming this region to be well developed are given in §5.5.1 and Appendix C.2.

Far-field round-jet region

Expressed in terms of the entrainment velocity $v_e(x)$ and jet width $b(x)$, the volume flux in the round-jet region, i.e. for $x > x_{re}$, increases due to entrainment as

$$\frac{dQ_e}{dx} = 2\pi b v_e, \qquad v_e(x) = \alpha \bar{u}(x,0), \tag{5.15}$$

(Fischer et al. (cf. 1979)) where α denotes the entrainment coefficient. We define the jet width $b(x)$ as the radial coordinate at which $\bar{u}(x,r)/\bar{u}(x,0) = 1/e$, where $\ln(e) = 1$. In a fully developed round jet, both the jet width and the inverse axial velocity along the longitudinal nozzle axis increase linearly with x, i.e. $b(x) = c_1(x - x_0)$ and $\bar{u}(x,0) = c_2 M^{1/2}(x - x_0)^{-1}$ where c_1 and c_2 represent the spreading rate and velocity decay constants, respectively, and x_0 the virtual origin of the round-jet behaviour (Fischer et al., 1979). Thus

$$\int_{x_{re}}^{x_C} \frac{dQ_e}{dx}\,\mathrm{d}x = 2\pi M^{1/2} \alpha c_1 c_2 (x_C - x_{re}). \tag{5.16}$$

[1] We recall from §4 that the reattachment point was located at $x \approx 4.3 D_o$, i.e. in the transitional region.

Values of the constants used in the predictions (§5.5) are given in table 5.2.

Entrainment surfaces

Before one is able to estimate the volume flux entrained into the near-nozzle planar-jet region, i.e. for $x \leq x_{re}$, it is necessary for our model to describe the (time-averaged) shape of the entrainment surfaces. Two entrainment surfaces are present in this region: an outer entrainment surface, of radius $r = b_o(x)$, between the jet and the ambient; and an inner entrainment surface, of radius $r = b_i(x)$, between the jet and the bounded induced-flow region. These surfaces and the high-velocity jet centreline, of radius $r = r_c(x)$, are illustrated on figure 5.4. Although the high-velocity centreline curves within this region, for simplicity we make the assumptions that the distance along the centreline is equal to the horizontal distance from the source, and that the outer shear layer of the jet spreads away from the centreline in the direction perpendicular to the x-axis. The former assumption is supported qualitatively by the streamlines in figure 5.2, in which the trajectory of the near-field jet appears to be approximately horizontal and quantitatively in figure 5.5 which plots the distance along the (curved) high-velocity centreline x_ζ against the corresponding x-coordinate along the longitudinal nozzle axis. The data falls on the line $x_\zeta = x$, confirming that this assumption is justified. Similar results were obtained for all five nozzles tested.

Following Sawyer (1960), who investigates the attachment of thin planar jets to a flat boundary, we assume the high-velocity centreline follows a circular arc. The centreline begins in the centre of the exit slot, i.e. $r_c(0) = D_c/2$ where

$$D_c = (D_o + D_i)/2 \tag{5.17}$$

and intercepts the x-axis at the reattachment point so that $r_c(x_{re}) = 0$. Thus, the centreline follows a circular arc described by

$$r_c(x) = \sqrt{R_c^2 - x^2} + \frac{D_c}{2} - R_c, \qquad \text{for } 0 \leq x \leq x_{re}, \tag{5.18}$$

where the radius of curvature of this arc

$$R_c = \frac{x_{re}^2 + D_c^2/4}{D_c}. \tag{5.19}$$

PHJ17 observed that the outer entrainment surface spreads linearly away from the high-velocity centreline. Hence, we write

$$b_o(x) = r_c(x) + d_1 x. \tag{5.20}$$

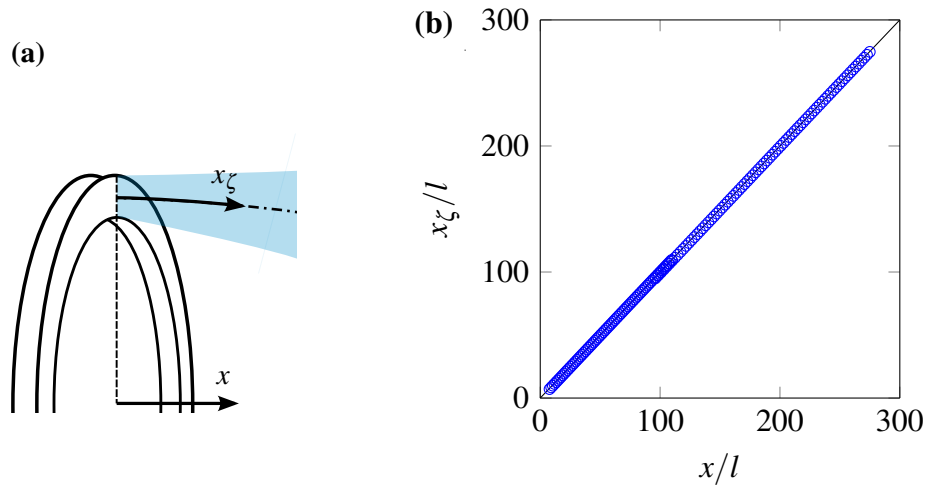

Fig. 5.5: (a) The two coordinate axes x and x_ζ. The x coordinate as measured along the longitudinal nozzle axis and the x_ζ coordinate measured along the curved high-velocity jet centreline. (b) The variation of x_ζ/l with x/l, inferred from the PIV data using the method described in §4.3.4, for the slender open-core annular jet issuing from source **N4R3V1** (see table 5.1). The data '$\circ$' has been plotted between the source and the reattachment point. The straight line shows $x_\zeta = x$.

The constant d_1 is the spreading rate of the planar-jet perimeter and we shall use d_2 to denote the planar velocity decay constant. Note that the notation b_o is intentionally distinct from b due to the dependence of b_o on $r_c(x)$. Following the classic scalings (Fischer et al., 1979), the jet perimeter is defined as the $\bar{u}(x,r)/\bar{u}_c(x) = 1/e$ velocity contour and the time-averaged velocity along the centreline as

$$\bar{u}_c(x) = d_2 M_p^{1/2} x^{-1/2} \approx d_2 \left(\frac{M_0}{\pi D_c}\right)^{1/2} x^{-1/2}. \tag{5.21}$$

The term M_p denotes the specific momentum flux per unit length of the planar jet exiting the slot and is approximated as $M_p = M_0/(\pi D_c)$ on assuming that the slot is thin. The aforementioned velocity contour has been chosen so as to be consistent with the definition of width b given in §5.3.4. Once again, the notation denoting the velocity along the high-velocity centreline $\bar{u}_c$ is intentionally distinct from that denoting the velocity along the longitudinal nozzle axis $\bar{u}(x,0)$ despite the coincidence of the nozzle axis and high-velocity centreline in the far field, so as to easily distinguish between the two definitions.

Next we consider the bounded induced-flow region of radius $r = b_i(x)$. In a steady state, a volume flux equal to that which is induced through the core of the annulus must be entrained

across the curved surface of the inner shear layer and we note that at $x = x_m$, $b_i(x_m) = 0$ (figure 5.4). Clearly, the inner shear layer must begin to merge upstream of the jet reattachment point, thus introducing the coefficient β we have

$$x_m = \beta x_{re} \qquad \text{where } 0 < \beta < 1. \tag{5.22}$$

According to PHJ17 the inner shear layer does not follow the planar-jet spread as closely as the outer shear layer and, as such, we wish to uncouple the merging of the inner shear layer from the jet centreline. Therefore, rather than relate the inner entrainment surface directly to the jet centreline, we make the assumption that the inner entrainment surface follows a circular arc. The arc begins at the inner lip of the nozzle where $b_i(0) = D_i/2$ and ends at the merge point where $b_i(\beta x_{re}) = 0$. The radial location $r = b_i(x)$ of the inner entrainment surface is then

$$b_i(x) = \sqrt{R_i^2 - x^2} + \frac{D_i}{2} - R_i, \qquad \text{for } 0 \le x \le \beta x_{re}, \tag{5.23}$$

where the radius of curvature of this arc

$$R_i = \frac{(\beta x_{re})^2 + D_i^2/4}{D_i}. \tag{5.24}$$

Near-nozzle planar-jet region

With reference to (5.14), for the region $0 \le x \le x_{re}$,

$$\frac{dQ_e}{dx} = 2\pi b_o v_{ep}, \tag{5.25}$$

where $v_{ep}(x) = \alpha_p \bar{u}_c(x)$ is the entrainment velocity into this planar-jet region and α_p the planar-jet entrainment coefficient. Substituting in (5.21) and (5.5b),

$$v_{ep}(x) = \alpha_p d_2 \left(\frac{U_0^2 A_0}{\pi D_c}\right)^{1/2} x^{-1/2}. \tag{5.26}$$

Therefore, on integrating (5.25),

$$\int_0^{x_{re}} \frac{dQ_e}{dx}\,\mathrm{d}x = 2\pi\alpha_p \int_0^{x_{re}} \bar{u}_c(x) b_o(x)\,\mathrm{d}x = 2\pi\alpha_p d_2 \left(\frac{U_0^2 A_0}{\pi D_c}\right)^{1/2} \int_0^{x_{re}} b_o(x) x^{-1/2}\,\mathrm{d}x. \tag{5.27}$$

Eliminating x_C

Substituting (5.16) and (5.27) into (5.14), and then (5.14) into (5.7) yields for volume conservation

$$\begin{aligned} 2\pi\int_0^\infty \bar{u}(x_C,r)r\,\mathrm{d}r =& U_0A_0 + U_aA_a + 2\pi M^{1/2}\alpha c_1c_2(x_C-x_{re}) \\ &+ 2\pi\alpha_p d_2\left(\frac{U_0^2A_0}{\pi D_c}\right)^{1/2}\int_0^{x_{re}} b_o(x)x^{-1/2}\,\mathrm{d}x, \end{aligned} \tag{5.28}$$

where we recall M denotes the momentum flux at the section **CC′**.

In order to recast (5.28) in a form which is independent of the location of section **CC′**, i.e. seeking to eliminate x_C, we begin by evaluating the integral on the LHS of (5.28). At $x = x_C$ the jet is round and expected to have a Gaussian velocity profile $\bar{u}(x,r) = \bar{u}(x,0)e^{-r^2/b^2}$ (Fischer et al., 1979). On recalling that $b = c_1(x-x_0)$ and $\bar{u}(x,0) = c_2M^{1/2}(x-x_0)^{-1}$ we have

$$2\pi\int_0^\infty \bar{u}(x_C,r)r\,\mathrm{d}r = \pi\bar{u}(x_C,0)b(x_C)^2 = \pi M^{1/2}c_1^2c_2(x_C-x_0). \tag{5.29}$$

The similarities between (5.29) and the penultimate term of (5.28) are evident and indicate that simplifications could be made on relating the entrainment constant α to the spreading rate c_1. To do this, rather than relating M to M_0 directly using (5.13), we make the assumption that $M = M_0$. This approximation is supported by the PIV measurements in §4.3.1 which show $M(x) \approx M_0$ for a slender open-core annular nozzle, see figure 4.6. Indeed, for the five nozzles tested, $0.02 \lesssim \gamma \lesssim 0.07$[2], these values being small compared to unity and thus supporting the assumption. On substituting the round-jet scalings for width and the velocity along the longitudinal nozzle axis into (5.15) we obtain

$$\frac{dQ_e}{dx} = 2\pi b\alpha\bar{u}(x,0) = 2\pi\alpha c_1c_2M_0^{1/2} \quad \text{for} \quad x > x_{re}. \tag{5.30}$$

Fischer et al. (1979) give the volume flux of a round jet as $Q_e = \pi c_1^2c_2Q_0A_0^{-1/2}x$, hence,

$$\frac{dQ_e}{dx} = \pi c_1^2c_2\frac{Q_0}{\sqrt{A_0}}. \tag{5.31}$$

Using (5.3b) and (5.5b) to express the length scale $\sqrt{A_0}$ in terms of the specific source momentum flux and source volume flux ($\sqrt{A_0} = Q_0/M_0^{1/2}$), combining (5.30) and (5.31) gives

$$\alpha = \frac{c_1}{2}. \tag{5.32}$$

[2] calculated using (5.13) with values of $\hat{U}_a$ extracted from the measurements shown in figure 5.7(a)

Finally, combining (5.28), (5.29) and (5.32) allows us to eliminate x_C and write, for volume conservation,

$$\sqrt{\frac{M}{M_0}}\frac{\pi c_1^2 c_2 (x_{re}-x_0)}{\sqrt{A_0}} - \frac{2\pi\alpha_p d_2}{(\pi A_0 D_c)^{1/2}}\int_0^{x_{re}} b_o(x)x^{-1/2}\,\mathrm{d}x = 1+\hat{A}_a\hat{U}_a. \tag{5.33}$$

Relating α_p to d_1

To further simplify (5.33) we next relate the entrainment coefficient α_p to the spreading rate of the planar jet d_1. The approach taken is almost identical to that above by which α and c_1 were related. Following Fischer et al. (1979), the volume flux per unit length of the planar jet can be expressed as

$$Q_p = d_1 d_2 \sqrt{\pi} M_p^{1/2} x^{1/2}. \tag{5.34}$$

The volume flux Q_p is equal to the volume flux entrained into the jet, i.e. substituting $\bar{u}_c$ from (5.21), we require

$$\int_0^x \frac{dQ_p}{dx}\,\mathrm{d}x = \int_0^x 2\alpha_p \bar{u}_c\;\mathrm{d}x = 4\alpha_p d_2 M_p^{1/2} x^{1/2}. \tag{5.35}$$

Equating (5.34) and (5.35) then gives

$$\alpha_p = \frac{d_1\sqrt{\pi}}{4} \tag{5.36}$$

and (5.33) becomes

$$\sqrt{\frac{M}{M_0}}\frac{\pi c_1^2 c_2 (x_{re}-x_0)}{\sqrt{A_0}} - \frac{\pi d_1 d_2}{2(A_0 D_c)^{1/2}}\int_0^{x_{re}} b_o(x)x^{-1/2}\,\mathrm{d}x = 1+\hat{A}_a\hat{U}_a. \tag{5.37}$$

The induced flow

For a fixed source geometry (via fixed D_i and D_o), (5.37) has two unknowns (x_{re} and $\hat{U}_a$) and no unique solution. To close the problem we consider the volume flux Q_a induced through the open core of the annulus. This closure relates the reattachment location $x = x_{re}$ to $\hat{U}_a$. We have assumed that the entrainment into the inner shear layer is planar-jet-like with entrainment constant $\alpha_p = d_1\sqrt{\pi}/4$, (5.36), thus, the volume flux induced through the annulus is

$$Q_a = \int_0^{\beta x_{re}} 2\pi b_i v_{ep}\,\mathrm{d}x = \frac{\pi^{3/2} d_1 d_2}{2}\left(\frac{U_0^2 A_0}{\pi D_c}\right)^{1/2}\int_0^{\beta x_{re}} b_i(x)x^{-1/2}\,\mathrm{d}x, \tag{5.38}$$

where v_{ep} is given by (5.26). Substituting for $Q_a = U_a A_a$ from (5.3a) into (5.38) and rearranging yields a second relationship linking $\hat{U}_a$, x_{re} and β, namely

$$\hat{A}_a \hat{U}_a = \frac{\pi d_1 d_2}{2\sqrt{D_c A_0}} \int_0^{\beta x_{re}} b_i(x) x^{-1/2} \, \mathrm{d}x. \tag{5.39}$$

Substituting for (5.39) into (5.33) gives the final form of the continuity equation, namely

$$\sqrt{\frac{M}{M_0}} \frac{\pi c_1^2 c_2 (x_{re} - x_0)}{\sqrt{A_0}} - \frac{\pi d_1 d_2}{2\sqrt{D_c A_0}} \int_0^{x_{re}} b_o(x) x^{-1/2} \, \mathrm{d}x = 1 + \frac{\pi d_1 d_2}{2\sqrt{D_c A_0}} \int_0^{\beta x_{re}} b_i(x) x^{-1/2} \, \mathrm{d}x, \tag{5.40}$$

for the unknowns $\hat{U}_a$, x_{re} and β. The ratio M/M_0 $(= f(\hat{U}_a))$ is given by (5.13). For a given value of β, only a single positive combination of $\hat{U}_a$ and x_{re} satisfies (5.40).

The model developed may now be used to predict how the volume flux and associated velocity induced through the open core, the location of the merge point and reattachment point vary with diameter ratio.

5.3.5 Solution procedure

Although a constraint linking $\hat{U}_a$ and x_{re} was developed in (5.40), the unknown β was introduced. To obtain a solution, we make use of the work of Sawyer (1960) which provides an expression for the radius of curvature at the source of a thin planar jet, R_S, using the ratio of the source momentum flux per unit length $(\rho U_0^2 A_0/(\pi D_c))$ and the pressure difference across the jet $(\rho U_a^2/2)$. Accordingly, for the slender open-core annular jet, which behaves as a planar jet near the nozzle,

$$R_S = \frac{\rho U_0^2 A_0}{\rho U_a^2 \pi D_c/2} = \frac{2A_0}{\pi \hat{U}_a^2 D_c}. \tag{5.41}$$

With reference to the geometry shown in figure 5.6, we write

$$D_c = 2R_S(1 - \cos\phi) + 2\delta\cos\phi, \tag{5.42}$$

where ϕ is the angle between a line perpendicular to the jet centreline and the nozzle exit plane, and δ is the width of the planar jet at $x = x_m$, which is defined as $\delta = d_1 x_m$. Geometrically

$$x_m = R_S \sin\phi. \tag{5.43}$$

After some algebra, (5.41) - (5.43) yield

$$x_m = \frac{2A_0}{\pi \hat{U}_a^2 D_c} \sin\left[\cos^{-1}\left(\frac{D_c - 4A_0/(\pi \hat{U}_a^2 D_c)}{2\delta - 4A_0/(\pi \hat{U}_a^2 D_c)}\right)\right]. \tag{5.44}$$

To solve for x_m using (5.44) we require values for $\hat{U}_a$ of δ, both of which have a dependence on x_m.

We note that other approaches may have been used to close (5.40). For example, one could link x_{re} and $\hat{U}_a$ by setting $R_c = R_S$, and thus solve (5.33) without the need for an iterative procedure. However, it is important to acknowledge that in real jets the radius of curvature of the jet centreline R_c is not constant and will increase with distance downstream (Lund, 1964). By avoiding the coupling of R_S and R_c in our solution, we allow R_c to be an 'average' radius of curvature which more accurately describes the overall coalescing behaviour of the jet. We have coupled R_S and R_i – clearly the value of x_m calculated using this method represents the minimum distance at which the shear layer merges. Given the constraint imposed in (5.39), we can use this coupling to iterate towards the final solution. Firstly, we made an initial guess of $\beta = 0.5$ and $\delta = 0$. Following this, we selected the only positive combination of x_{re} and $\hat{U}_a$ which satisfied (5.40). The integrals in (5.40) were solved numerically using the composite Simpson's rule. Using (5.44), this value of $\hat{U}_a$ was used to calculate x_m. A new value of β was calculated using $\beta_{n+1} = (\beta_n + x_m/x_{re})/2$ where n represents the iteration step. When the change in β was within a specified tolerance (i.e. $|\beta_{n+1} - \beta_n|/\beta_n < \varepsilon$), the iteration was stopped; otherwise new values of δ (calculated using the previous iterations value for x_m, i.e. $\delta_n = d_1(x_m)_{n-1}$), x_{re} and $\hat{U}_a$ were calculated for the new value of β and the iteration procedure repeated. Typically, the solution converged for a tolerance of ε =0.1% in under 10 iterations. Smaller values of ε resulted in no change in the first three significant figures of the predictions. The predictions shown herein are based on $\varepsilon = 0.1\%$.

The theoretical model developed does not provide a solution for all possible diameter ratios D_i/D_o. The model only produces valid solutions in the range $0.77 < D_i/D_o < 1$ due to the thin slot assumption made. The range of D_i/D_o for which solutions are valid is apparent in the plots shown in §5.5.1.

5.4 Experiments

To validate the theoretical model developed in §5.3 we require measurements of $\{Q_a, U_a, x_m, x_{re}\}$ for a range of D_i/D_o corresponding to slender annuli. To this end, experiments were performed with five nozzles spanning a range of diameter ratios. An in-depth discussion regarding the

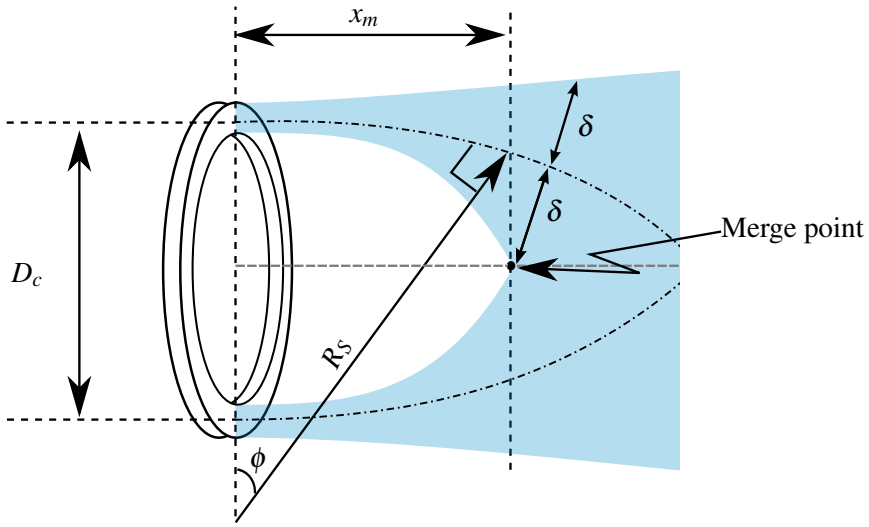

Fig. 5.6: The nozzle and flow-field geometry used to estimate the location of the merge point x_m using the radius of curvature of the high-velocity centreline (dot-dashed line). The radius of curvature R_S is evaluated using the expression deduced by Sawyer (1960) for a thin planar jet (5.41).

nozzle design, experimental set-up and procedure has been given in §2. A brief outline of the experiments used to obtain the measurements discussed herein, including the details on the source conditions, is now presented.

This chapter investigates the jets issuing from sources **N1-5R3V1**, or, in other words, issuing from an annuli with $0.845 \leq D_i/D_o \leq 0.981$, $D_v/D_i = 0.90$ and $Re_s \approx 2300$ (see table 5.1, or, for detail on the nozzles, table 2.1). A volume flux Q_0 was supplied to the nozzle through an intake bell mouth with pressure fluctuations indicating a variation in the flow rate of ± 0.0001 m^3 s^{-1}. Despite the source dependent temperature difference $10.2°\text{C} \leq \Delta T \leq 20.0°\text{C}$ between the source and ambient fluid, the jet length L_j is large and, as discussed in §2.2.3 and §3.2.3 the effect of buoyancy on our results may be regarded as negligible. For the experiments described herein we chose an (approximately) constant value of $Re_l \approx 2300$ and let Re_f vary; the rationale being that Re_l is both smaller and applicable to the near-field region in which the jet coalesces and in which our primary interest lies.

The results presented herein were captured using planar PIV on the $x-y$ plane of the nozzle (i.e. slices along the jet). Four overlapping windows (centred on the nozzle axis) were used to capture details of the flow from both the near to the far field, as illustrated on figure 2.5.

	$\frac{D_i}{D_o}$	Q_0 (m^3/s)	$\sqrt{A_0}$ (mm)	U_0 (m/s)	l (mm)	Re_l ($\pm 5\%$)	Re_f ($\pm 5\%$)	ΔT (°C)	$\frac{L_j}{D_o}$
N1R3V1	0.845	0.0109	51.4	4.1	8.40	2300	14000	12.2	14
N2R3V1	0.894	0.0109	41.9	6.2	5.59	2300	17000	12.2	18
N3R3V1	0.947	0.0112	29.2	13.1	2.71	2400	25000	15.0	34
N4R3V1	0.968	0.0108	22.8	20.9	1.65	2300	32000	10.2	52
N5R3V1	0.981	0.0112	19.0	31.5	1.06	2200	40000	20.0	50

Table 5.1: Source conditions for the five sources **N1-5R3V1**, listed in order of increasing D_i/D_o. Detail regarding thethe nozzle design is given in §2.1, with dimensions in table 2.1. Reynolds numbers, $Re_l = U_0 l/\upsilon$ and $Re_f = \sqrt{M_0}/\upsilon$, were estimated based on a kinematic viscosity for air at 20°C of $\upsilon = 1.5 \times 10^{-5}$ m^2 s^{-1} (Batchelor, 1967) and for a uniform exit velocity $U_0 = Q_0/A_0$. The ventilation ratio $D_v/D_i = 0.9$ for all five nozzles.

	c_1	c_2	x_0	d_1	d_2
Fischer et al. (1979)	-	-	-	0.116	2.41
PHJ17	0.102	7.5	$-4.0\sqrt{A_0}$	-	-

Table 5.2: Constants and virtual origin used in the predictions of the model developed in §5.3.

5.5 Results and discussion

This section is split into two parts. First in §5.5.1 the predictions of our model are compared with the experimental results. Following this examination of the near-field coalescing region of the jet, we investigate in §5.5.2 whether the far-field flow shows a dependence on the diameter ratio. The far field is of interest given that, in the theoretical developments, we assume a single value for the decay and spreading rates and for the virtual origin of the open-core annular jet in this region.

To obtain predictions from the model, values for the constants c_1, c_2, x_0, d_1 and d_2 are required. Naturally, one would be inclined to choose values obtained from experiments on slender open-core annular jets, such as those recorded by PHJ17. However, therein we note that the presence of near-field flow asymmetries may significantly influence estimates of d_2. Moreover, estimates of d_1 were not made. Given the near-field planar-jet-like behaviour, one could reasonably advocate for the use of values extracted from the existing literature on planar jets. Thus, we implement the theoretical model using round-jet constants (c_1, c_2) and virtual

origin (x_0) extracted from PHJ17, and planar-jet constants (d_1, d_2) from the literature. These values are given in table 5.2. Implicit in selecting a fixed value for x_0 is that the virtual origin for the round-jet region of the slender open-core annular jet does not vary with D_i/D_o. A discussion regarding the validity of this assumption is given in §5.5.2. The sensitivity of the predictions to the choice of values for these constants is addressed in Appendix C.3 and indicates that, with the exception of x_{re}, predictions are insensitive to the choice of c_1, c_2 and x_0, and are only marginally influenced by the choice of d_1 and d_2.

5.5.1 Comparison with theory

Predictions are possible and shown for diameter ratios $0.77 < D_i/D_o < 1$ (cf. §5.3.5). Our discussion below focusses on comparisons between the predictions and the measurements, and on establishing the role of the diameter ratio.

Velocity and volume flux induced through the open core

Figure 5.7 plots the variation of the velocity U_a/U_0 and volume flux Q_a/Q_0 induced through the open core with the diameter ratio D_i/D_o. As the diameter ratio increases, our results indicate that U_a/U_0 decreases and Q_a/Q_0 increases. With regards to the induced velocity U_a/U_0, figure 5.7(a), the predictions are in good agreement with the measurements for larger diameter ratios, i.e. those for which the thin slot assumption is most valid. The thin slot assumption and the assumption that the flow is a fully developed planar jet on exiting the annular slot are directly related. As the diameter ratio is reduced, l/D_i increases (see discussion in §5.2), and the axial extent of the region of planar-jet-like flow establishment increases relative to the extent of the bounded induced-flow region. The increasing discrepancy, as the diameter ratio is reduced, between the predictions and the experimental measurements is thus attributed to the decreasing validity of the assumption that the jet is a fully developed planar jet on exiting the annular slot. With regards to the induced volume flux Q_a/Q_0, figure 5.7(b), the theory over-predicts as expected. This over-prediction is, in part, due to the higher ventilation ratio of the model ($D_v/D_i = 1$, '——') when compared to the experiments ($D_v/D_i = 0.9$, '○'). On making the assumption that the induced flow velocity U_a does not change significantly with small changes in the ventilation ratio, we can correct for the different ventilation ratios. This assumption is supported by measurements of U_a (given in §6.3.3) for jets issuing from nozzles with a range of ventilation ratios; in these measurements U_a changes by approximately 5% as the ventilation ratio D_v/D_i is varied between 0.90 and 0.75. Thus, on multiplying our experimental measurements of U_a by A_a, and dividing by the source volume flux Q_0, we obtain the corrected volume fluxes, plotted using '•' on figure 5.7(b). Once again, at high diameter

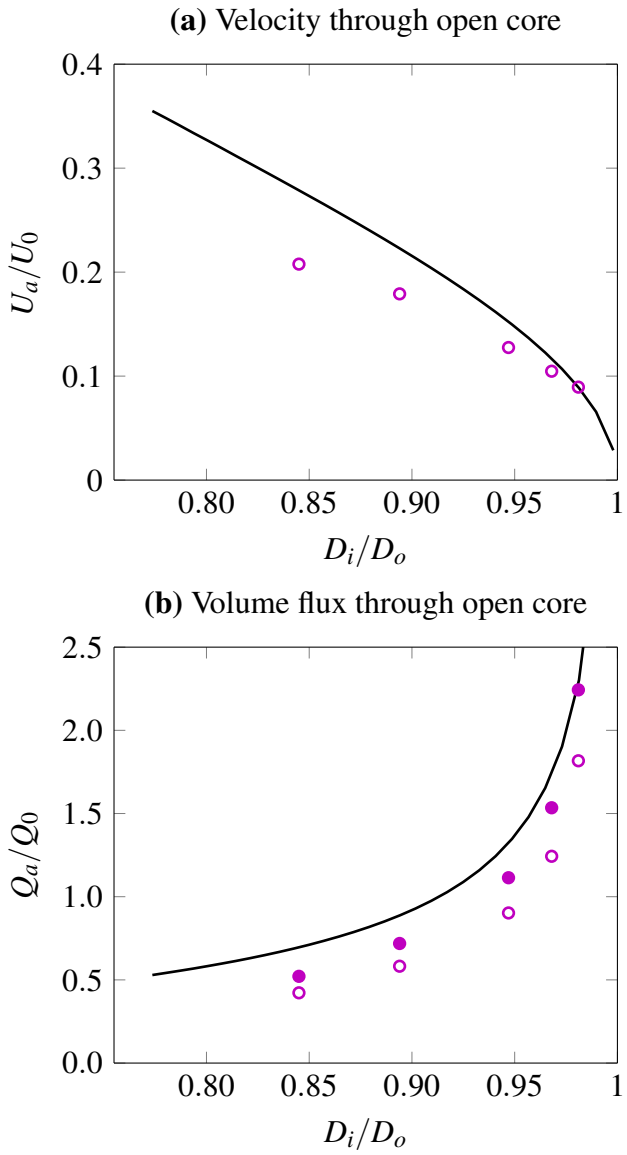

Fig. 5.7: Variation with diameter ratio D_i/D_o of (a) normalised velocity induced through the open core U_a/U_0, and (b) normalised volume flux induced through the open core Q_a/Q_0. Theoretical prediction '—'. Measurements for sources **N1-5R3V1** are marked by the symbol '○'. Measurements corrected for the ventilation ratio are marked using '●'. The error in these measurements is approximately 4.6%, see table 3.9.

ratios, at which the thin slot assumption is most valid, the prediction agrees well with the corrected volume fluxes.

To explain the trends shown in figure 5.7, one may consider a nozzle for which the source volume flux Q_0 and mean diameter D_c $(= (D_o + D_i)/2)$ remain constant. As the diameter ratio D_i/D_o increases towards unity, the width of the slot l $(= D_o(1 - D_i/D_o)/2)$ must decrease. For a given source volume flux Q_0, and noting $A_0 = \pi D_c l$, the source velocity of the jet U_0 $(= Q_0/A_0)$ must therefore also increase, such that $U_0 \to \infty$ as $l \to 0$. Velocities at the source U_0, along the centreline $\bar{u}_c$ $(\propto U_0 x^{-1/2})$, entrained v_{ep} $(\propto \bar{u}_c)$ and induced through the core U_a $(\propto v_{ep})$ are interdependent and increase together. Thus, specifically the increase in U_0 leads to an increase in U_a. The volume flux induced through the open core Q_a $(= U_a A_a)$ thereby increases, as both U_a and (on recalling that D_c is fixed) A_a $(= \pi(D_i/2)^2)$ increase as $D_i/D_o \to 1$. Given that the source volume flux is fixed in this argument, as indicated on figure 5.7(b), $Q_a/Q_0 \to \infty$ as $D_i/D_o \to 1$. At first glance, this may seem to contradict the trend shown on figure 5.7(a). However, while the model predicts $U_a/U_0 \to 0$ as $D_i/D_o \to 1$, as discussed above, the individual components of this ratio approach infinity, i.e. $U_0 \to \infty$ and $U_a \to \infty$. This plot therefore indicates that, on increasing the diameter ratio, the source velocity U_0 approaches infinity more rapidly than the velocity of the fluid induced through the open core U_a.

Although (5.40) has no valid solutions for low diameter ratios, it is reasonable to expect that $Q_a/Q_0 \to 0$ as $D_i/D_o \to 0$; in the limit $D_i/D_o = 0$ the annular nozzle has become a circular source without a central opening and would not establish a bounded internal region of induced flow. Moreover, although the predicted values of U_a/U_0 and Q_a/Q_0 are unphysical as $D_i/D_o \to 1$, a source with $D_i/D_o = 1$ is also unphysical. In practice, as $D_i/D_o \to 1$, the assumption of incompressibility will no longer be valid (due to the magnitude of U_0), rendering our model invalid for this extreme case.

Locations of merge and reattachment points

We next consider the axial extent of the bounded induced-flow region as characterised by the merge point $(x_m, 0)$. As we noted in PHJ17, there are multiple ways to define the merge point. One possible definition locates the merge point at the upstream stagnation point of the small-scale recirculation region that forms where the inner shear layer strongly self interacts; this position is marked by the symbol '$\circ$' on the streamlines in figure 5.2(e) and on figure 5.8(a)[3], which plots x_m/D_i against D_i/D_o. Alternatively, defining the jet width as the radius at which

[3]The point '$\circ$' for $D_i/D_o = 0.845$ is not the upstream stagnation point but indicates the approximate location of the flow redirection. For this flow, our results indicate that there is no recirculation region (see figure 5.2a and §5.2)

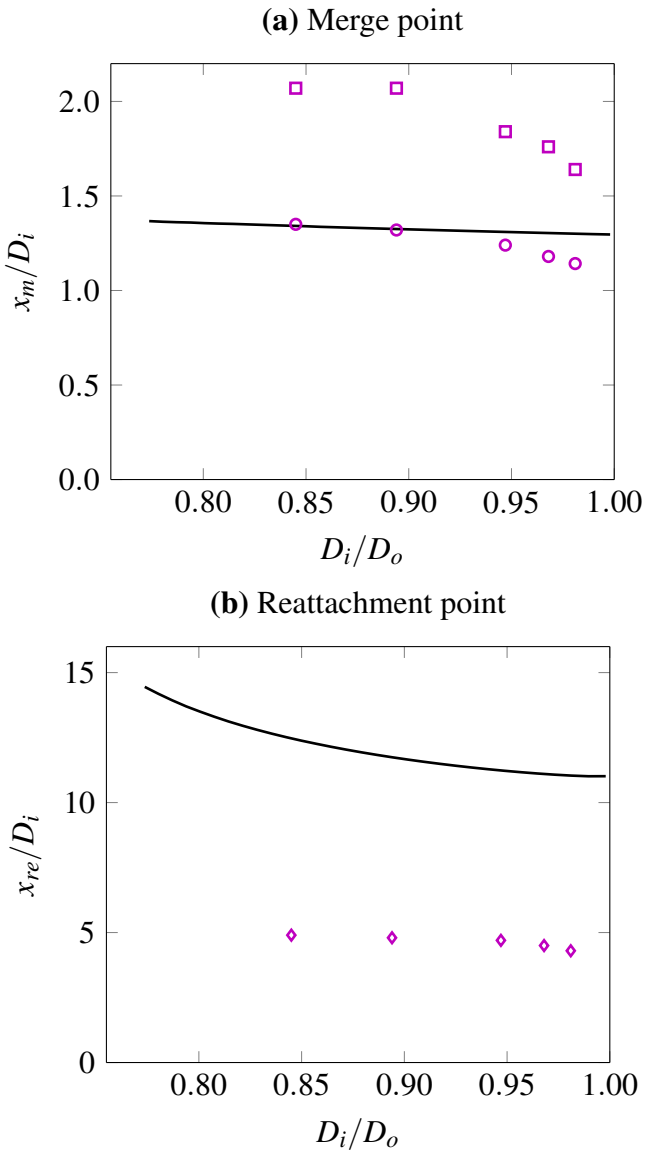

Fig. 5.8: Variation with diameter ratio D_i/D_o of (a) the merge point x_m/D_i, and (b) the reattachment point x_{re}/D_i. Theoretical prediction '—'. Symbols indicate measurements for: the '○' merge point based on the location of the upstream stagnation point; '□' the merge point based on the location where the time-averaged velocity contours defined by $\bar{u}(x,r)/\bar{u}_c(x) = 1/e$ in the inner shear layer meet; and '◇' the reattachment point (cf. equivalent symbols on figure 5.2e). The error in these measurements is related to the spatial resolution of the PIV measurements and is smaller than the size of the symbols.

the axial velocity has fallen by a factor of e, the symbols '□' on figure 5.2(e) and figure 5.8(a) indicate estimates for x_m based on the intersection of the resulting velocity contours. While the intersection of the velocity contours '□' is consistently located downstream of the stagnation point '○', both move upstream as the diameter ratio D_i/D_o is increased.

Despite the fact that estimates of the merge point in (5.44) use the jet width, the similarity between the predictions and the stagnation points on figure 5.8(a) suggests that the stagnation point bounds the axial extent of the bounded induced-flow region. This observation is explained on arguing, based on the streamline plots in figure 5.2, that the entire volume flux induced through the open core has been entrained by the inner shear layer before the upstream stagnation point. Further evidence linking the stagnation point and model prediction is given by the similar trends observed with D_i/D_o. The prediction for x_m/D_i, the point at which the velocity contours intersect '□', and the stagnation point '○' are all relatively insensitive to D_i/D_o. This insensitivity when the data has been scaled on D_i (figure 5.8a), confirms our expectation that the length scale D_i characterises the bounded induced-flow region.

The reattachment point, $x = x_{re}$, describes the location at which the high-velocity jet centreline exiting the annular slot merges. Our predictions and measurements of the variation in x_{re}/D_i with D_i/D_o are plotted on figure 5.8(b) which shows that the jet reattaches closer to the source as the diameter ratio is increased. This trend is consistent with the decrease of F_I/F_P as D_i/D_o is increased (cf. (1.5) and figure 5.3), the increased magnitude of the pressure force F_P relative to the inertial force F_I resulting in the jet coalescing closer to the source. Ko & Chan (1978) identified similar behaviour in *closed-core* annular jets. Additionally, while figure 5.3 indicates a two-fold decrease in the inertial force relative to the pressure force over the range $0.845 \leq D_i/D_o \leq 0.981$, over the same range, measurements indicate that the reattachment point shifts only marginally upstream (by approximately 15%). This difference in magnitude is a consequence of directly coupling the pressure difference driving the induced flow (at the source) and the pressure difference acting on the jet itself. While, in reality, these pressure differences are linked, the pressure acting on the slender open-core jet will reduce with distance downstream due to the entrainment of the induced flow. Evidently, the location of the reattachment point predicted by the model differs significantly from the experimental measurements. We suspect that this is because the reattachment point resides in the transitional region that links the planar-jet and round-jet behaviours (PHJ17), and which is not included in the model formulation.

5.5.2 Far downstream of the nozzle

In the development of the model (§5.3) we specified the far-field round-jet behaviour with the constants c_1, c_2 and x_0, which denote the spreading rate, decay rate and virtual origin,

respectively. A sensitivity analysis (Appendix C.3) shows that, with the exception of x_{re}, the quantities predicted are insensitive to the choice of c_1, c_2 and x_0. Given that the constants specified affect our predictions, it is pertinent to examine whether, and to what extent, the diameter ratio D_i/D_o influences the far-field region. If the diameter ratio significantly influences the far-field region, the constants chosen will not be universal and our use of universal constants (see §5.5) for obtaining predictions from the theoretical model will be invalid. We examine the data for **N3-5R3V1** due to their relatively large jet lengths (compared to **N1-2R3V1**) and their correspondingly larger measurement domains ($0 \leq x \lesssim 16D_o$, see §5.4), which extend into what may be regarded as the far field.

Upstream of the reattachment point the jet has not attained its final self-similar form and continues to develop with distance downstream (PHJ17). Therefore, it is natural to expect that the development towards a self-similar state is characterised by the dimensions of the nozzle, D_i and D_o, these dimensions controlling the coalescing behaviour (figures 5.7-5.8). Downstream of the reattachment point, i.e. after the jet has coalesced, we expect the influence of D_i to diminish. For this reason, to examine the development towards self-similarity we scale x on D_o. Figure 5.9 shows this development by comparing the idealised Gaussian profile e^{-y^2/b^2} with the time-averaged axial velocity profiles measured by means of their root-mean-square deviation (RMSD), where

$$\mathrm{RMSD}(x) = \sqrt{\frac{\int_{-y_E}^{y_E} \left(e^{-y^2/b^2} - \bar{u}(x,y)/\bar{u}(x,0)\right)^2 \, \mathrm{d}y}{2y_E}}. \tag{5.45}$$

In (5.45), y_E represents the coordinate corresponding to the edge of the measurement window. Figure 5.9 indicates that, at least for the slender annuli examined herein, the choice of diameter ratio has little influence on the development of the time-averaged axial velocity profiles. All three flows (**N3-5R3V1**) converge to a self-similar state at $x \approx 5D_o$. The collapse of the data and the simultaneous convergence suggest that our choice of D_o, as the dominant length scale characterising the development towards self-similarity, is appropriate.

When considering the development, with downstream distance x, of the jet width b and longitudinal axial velocity $\bar{u}(x,0)$ in the far-field region, the choice of length scale on which to scale the data is more complex. In PHJ17, the round-jet length scale $\sqrt{A_0}$ was used when making comparisons between the far field of round and annular jets. When considering quantities that have a dependence on the source fluxes, such as the velocity along the longitudinal nozzle axis, this scaling is necessary to collapse the data. However, when considering quantities that do not depend on the source fluxes, for example the jet width, a collapse over a greater range of x can be obtained by scaling on D_o. We elaborate on these scaling considerations further where appropriate.

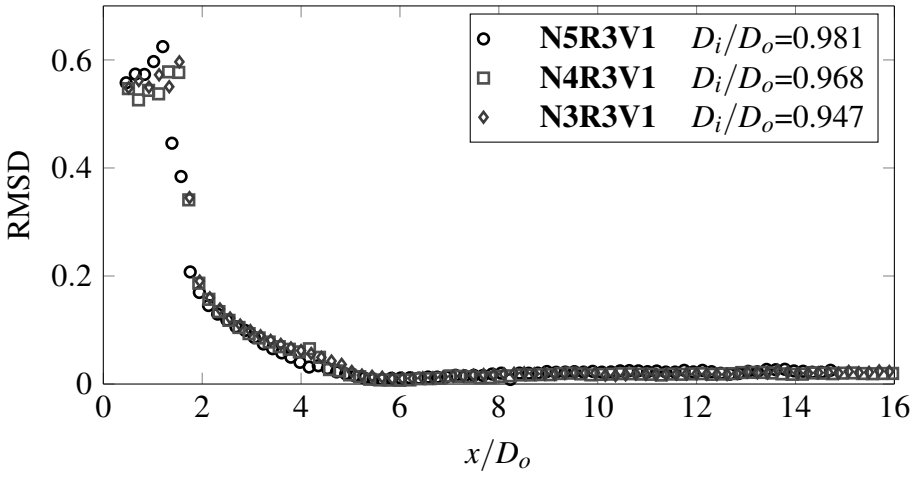

Fig. 5.9: The variation with distance downstream x/D_o of the root-mean-square deviation (RMSD) between the measured (time-averaged) axial velocity profiles for sources **N3-5R3V1** and the idealised Gaussian profile e^{-y^2/b^2}.

	D_i/D_o	c_1	$x_{01}/\sqrt{A_0}$	x_{01}/D_o	c_2	$x_{02}/\sqrt{A_0}$	α
N3R3V1	0.947	0.106	-1.6	-0.45	7.5	-2.6	0.530
N4R3V1	0.968	0.105	-1.3	-0.30	7.5	-6.5	0.525
N5R3V1	0.981	0.104	-3.7	-0.65	7.8	-2.8	0.520
Mean		0.105	-2.2	-0.47	7.6	-4.0	5.25

Table 5.3: Constants and virtual origins for (5.46a) and (5.46b), extracted from the PIV measurements of the jets issuing from nozzles **N3-5R3V1**. The relevant values of $\sqrt{A_0}$ and D_o are given in table 5.1. Also included are estimates of α calculated from (5.30), cf. figure 4.16.

The axial development of the jet width and the longitudinal axial velocity are plotted in figures 5.10 and 5.11, respectively. The current set of measurements confirm the finding of PHJ17, namely, that the jet width and inverse axial velocity increase linearly with x in the far field as

$$b = c_1(x - x_{01}), \qquad \bar{u}(x,0) = c_2 U_0 \left(\frac{x - x_{02}}{\sqrt{A_0}}\right)^{-1}, \qquad (5.46a,b)$$

where x_{01} and x_{02} represent the location of the virtual origin for the respective quantities. Figure 5.10 plots the variation of jet width with distance downstream; in figure 5.10(a) lengths are shown scaled on $\sqrt{A_0}$ and in figure 5.10(b) on D_o. While both scalings lead to a collapse of the data, scaling on D_o leads to a collapse over the entire range of data presented. We may appreciate better this enhanced collapse if we consider that: (5.46a) does not prescribe a scaling

and so the choice of length scale on which to scale the data is unrestrained; the outer perimeter of the jet at the source coincides with the outside edge of the slot, i.e. from the experimental data $b(0) = D_o/2$; and the location of the reattachment point x_{re} does not vary significantly with D_i/D_o (figure 5.8b) and, therefore, neither does the shape of the high-velocity centreline. The best fit to the jet widths has been plotted in figures 5.10(a-b) using (5.46a) and the mean values for the spreading rate c_1 and virtual origin x_{01} given in table 5.3. While the location of the virtual origin x_{01}, for nozzles **N3-5R3V1**, varies from the mean value by a maximum of 39% (when the data is scaled on D_o), the variation from the mean value of the spreading rate c_1 is small (<1%).

Figure 5.11 plots the variation of the inverse axial velocity with x; in figure 5.11(a) distances are scaled on $\sqrt{A_0}$ and in figure 5.11(b) on D_o. Of the two scalings, the scaling on $\sqrt{A_0}$ leads to a far better collapse of the data. This is understood when we note the presence of the source length scale $\sqrt{A_0}$ in (5.46b). We include the best fit line for the collapse shown in figure 5.11(a) using (5.46b) and the mean values for the constants (given in table 5.3).

When scaling on $\sqrt{A_0}$ (figures 5.10a and 5.11a), the location at which data for each jet may be regarded as having collapsed onto the linear best fit line differs. As the diameter ratio is increased, the location at which the velocity in the jet collapses onto the linear best fit line shifts downstream. This is because the collapse is governed by the development towards self-similar behaviour and therefore scales on D_o (cf. figure 5.9) rather than on $\sqrt{A_0}$.

The small differences in the constants (c_1, c_2, x_{01} and x_{02}) between each jet could be attributed to a number of factors. These include experimental uncertainty, the influence of the diameter ratio and the fact that the jet had not reached full self-similarity within our measurement domain. While it is possible that the diameter ratio has some influence on the far-field flow, PHJ17 noted that, at the extreme downstream end of the measurement domain ($x \approx 16D_o$), the turbulent quantities had not reached full self-similarity and, therefore, that the coefficients obtained were still slowly developing. Indeed, the values acquired for the coefficients c_1, c_2, x_{01} and x_{02}, using linear fits to our data for $9 < x/D_o < 15$, proved to be sensitive to the location at which we assumed the far-field behaviour to begin. This is in line with the observations of PHJ17, and indicates that each jet is still evolving. Despite this, the variation of the data is within experimental uncertainty and thus we conclude that the far-field behaviour of a slender open-core annular jet is independent of diameter ratio. However, in contrast to the findings of PHJ17, there is a significant difference between the virtual origins x_{01} and x_{02}. While this may be again related to the ongoing flow development, careful consideration must be given before representing the far field of a slender open-core annular jet as a universal round jet. Crucially, there does not appear to be a systematic variation in the virtual origin

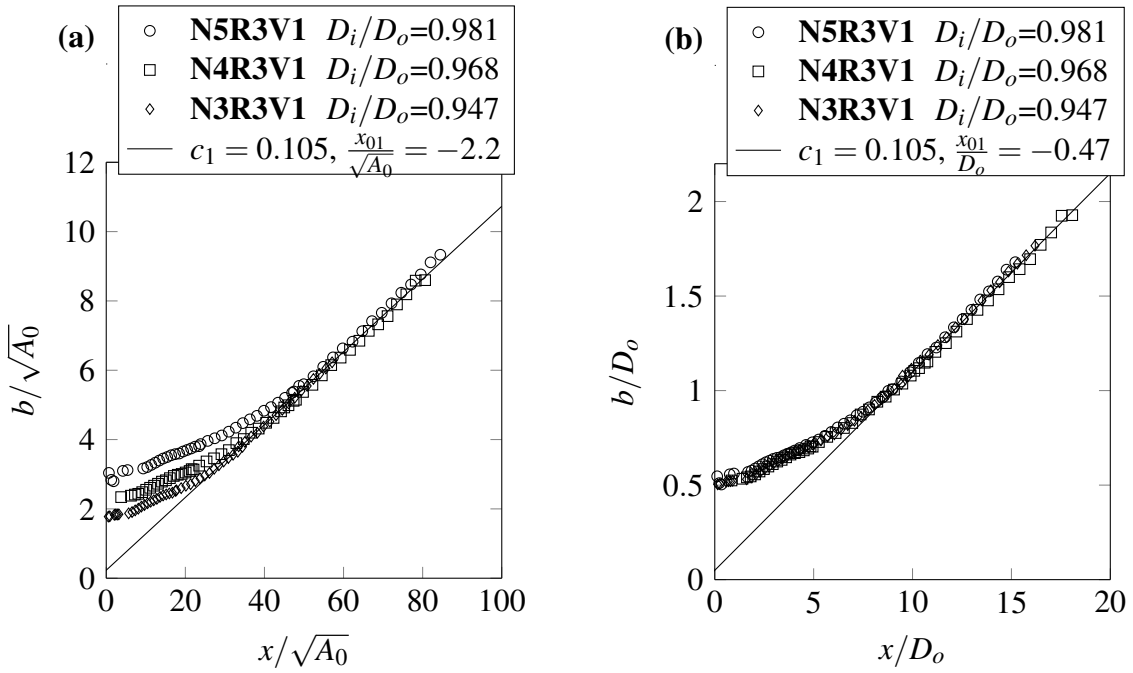

Fig. 5.10: The variation of jet width b with distance downstream for sources **N3-5R3V1**. In (a) the data is scaled on $\sqrt{A_0}$ and in (b) the data is scaled on D_o. Both (a) and (b) show the linear line of best fit, given by (5.46a), for the constants given in the legends. The error in these measurements is smaller than the size of the symbols.

location with diameter ratio for the slender open-core annular jets examined, justifying the use of a non-varying virtual origin in the theoretical model.

5.6 Conclusions

Our primary objective was to establish the effect of the diameter ratio D_i/D_o on the locations, fluxes and velocities that characterise the bounded induced-flow region and coalescing behaviour of a turbulent open-core annular jet. We achieved this by developing a theoretical model which was validated by means of comparison with complementary experimental measurements using particle image velocimetry on five nozzles with diameter ratios of $D_i/D_o = \{0.845,\ 0.894,\ 0.947,\ 0.968,\ 0.981\}$. There are two overarching methods by which the diameter ratio appears to influence the flow. First, for a nozzle with fixed mean diameter $D_c = (D_i + D_o)/2$, increasing D_i/D_o decreases the slot width l. The effect of the change in the slot width l cascades down from the exit velocity to the induced flow velocity and volume

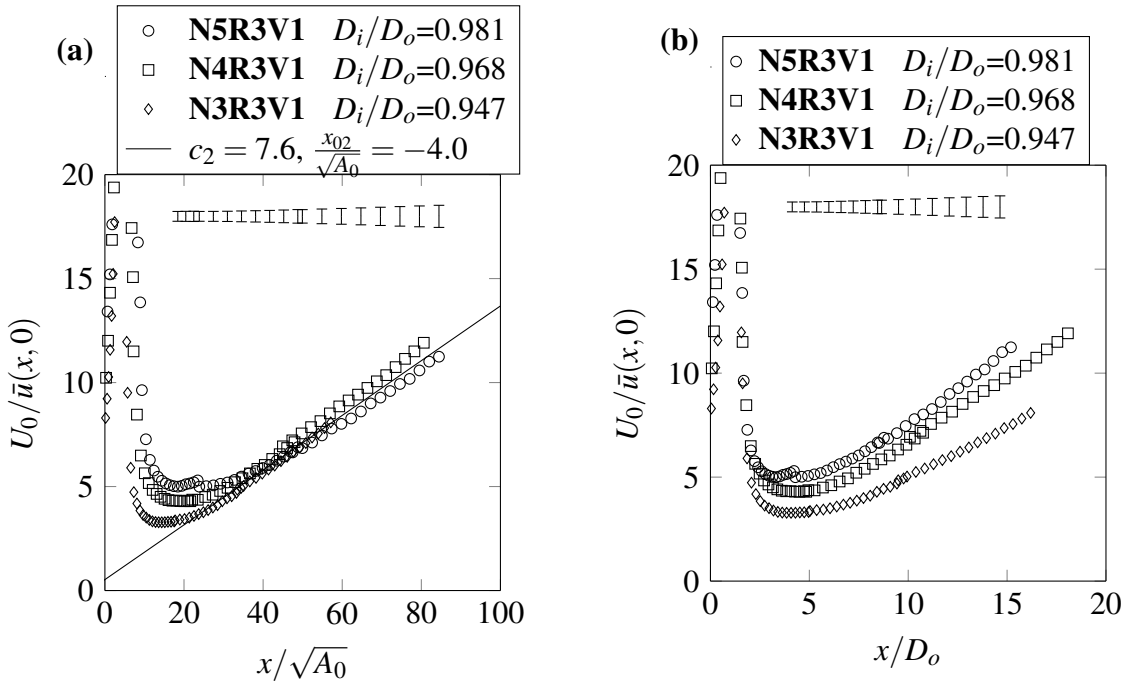

Fig. 5.11: The variation of the inverse velocity along the longitudinal axis of the nozzle $U_0/\bar{u}(x,0)$ for sources **N3-5R3V1**. In (a) the coordinate is scaled on $\sqrt{A_0}$ and the constants for the linear line of best fit, (5.46b), given in the legend. In (b) the coordinate is scaled on D_o. Error bars shown represent the estimated error in $U_0/\bar{u}(x,0)$, see §3.5.4 and table 3.9. Error bars shown are those estimated for nozzle **N5R3V1**, where the relative uncertainty in the slot width is the largest, and thus represent the largest error margins (of the three sources).

fluxes. The second relates to the relative magnitude of the inertial and pressure forces that govern the coalescing behaviour of the jet.

A comparison of the predictions and measurements reveals that the model accurately predicts the velocity U_a induced through the open core of the annulus at diameter ratios approaching unity. As the diameter ratio is reduced, the validity of the assumptions suffers and the model's accuracy reduces. Despite the loss of accuracy in predictions of U_a, the model qualitatively captures the trends observed in U_a, the merge point x_m, and the volume flux induced through the open core Q_a suggesting that it captures well the key physics. The large inaccuracies in predicting the location of the reattachment point x_{re} can be attributed to the fact that this point resides in the region where the jet is transitioning from planar-jet to round-jet behaviour, a region which was not modelled. We conclude that the theoretical model can be regarded as a first-order predictive tool for annular sources with diameter ratios close to unity.

Both the theoretical predictions and the experimental results show that the ratio D_i/D_o, of the inner and outer diameters of the annulus, has a considerable influence on the flow in the

near-source region of the jet. Increasing D_i/D_o increases the volume flux Q_a induced through the open centre of the annulus and causes the location at which the jet coalesces x_{re} to shift upstream. By contrast, our experimental results indicate that, in the far field, the effect of D_i/D_o on the jet width and velocity is minimal. The sources examined showed a very similar development towards self-similarity, we observe far-field round-jet behaviour, with similar spreading c_1 and decay rates c_2. However, the choice of length scale on which to scale the far-field data obtained is not necessarily intuitive. Previously, in §4, we suggested scaling on the round-jet length scale $\sqrt{A_0}$. While this scaling lead to a collapse, in the far field, of the data for the jet width b and for the velocity along the longitudinal nozzle axis $\bar{u}(x,0)$, our results herein clearly suggest that scaling the jet width b on D_o is most appropriate.

As a final comment, although in the development of the theoretical model (§5.3) both the coalescing and subsequent far-field regions were considered, one is able to replicate our predictions without consideration of the latter, i.e. without reference to the second integral in (5.14). However, imposing, for example, a constant pressure at the downstream end of the resulting control volume (i.e. at $x = x_{re} = x_C$) is not readily justified.

CHAPTER 6

The coalescence of a turbulent slender open-core annular jet - the role of the ventilation ratio

6.1 Introduction

Thus far, the focus of the work herein has been the turbulent jet issuing from a slender (almost fully) open-core source into an unbounded and otherwise quiescent environment. Comparing observations of the (almost fully) open-core jet (§4) with those of the closed-core jet ($D_v/D_i = 0$, e.g. Ko & Chan, 1978) reveals significant differences in the behaviour of the flow. These differences primarily manifest in the near-source region, i.e. typically for $x/D_o \lesssim 1$. For closed-core jets, a large-scale recirculation region exists immediately downstream of the core, whereas, in open-core jets, the region downstream of the core is dominated by a classic induced flow. We anticipate that the ventilation ratio D_v/D_i, illustrated in figure 6.1, controls the transition between these limiting behaviours, see §1.3. The combination of the induced-flow and recirculation region is hereinafter referred to as the *bounded near-source region*. Note that the *bounded near-source region* is distinct from the bounded induced-flow region described in the earlier chapters, as it explicitly includes the recirculation region.

The current chapter is concerned with how the ventilation ratio influences the bounded near-source region, on the location at which the jet has coalesced x_{re}, and on the resulting far-field behaviour. The existing literature on slender closed-core annular jets has focussed entirely on the symmetry breaking behaviour first observed by Del Taglia (2002) (see §1.3). It is established in §6.3.1 that the jets that issue from the closed-core nozzles examined herein do not exhibit this symmetry breaking behaviour. Thus, in addition to examining the role of D_v/D_i

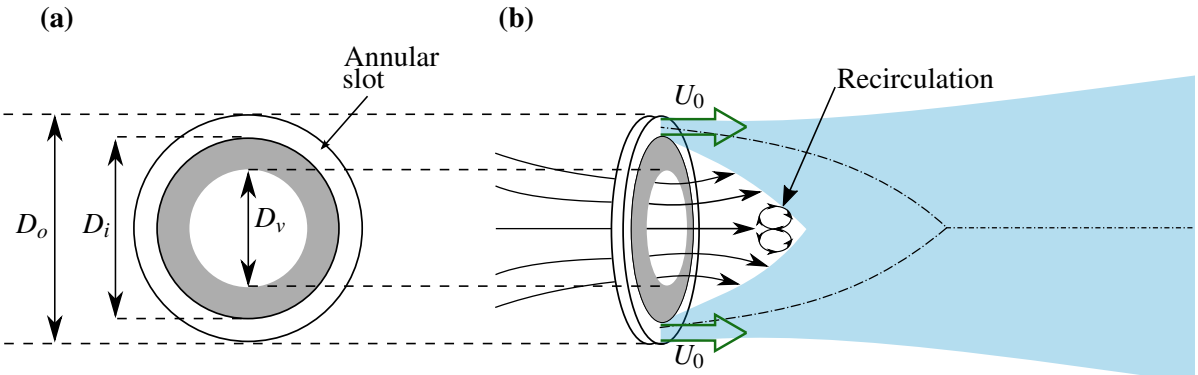

Fig. 6.1: Schematics depicting an open-core slender annular-jet source: (a) shown face on to the slot, with exit slot width $l = (D_o - D_i)/2$ and with a circular central opening of diameter D_v; (b) streamlines for the flow induced through the open core of the annulus, the recirculation region, and a time-averaged streamwise section through the jet (shaded in blue). The region shaded in grey depicts the blocked area of the core, and the unshaded region bounded by the jet and the nozzle (containing the induced-flow and recirculation region) represents the bounded near-source region. The steady exit velocity U_0 is perpendicular to the plane of the source as indicated. The dot-dashed lines represent the high-velocity centrelines issuing from the slot.

on open-core jets, we examine the role of the D_i/D_o on the development of slender closed-core ($D_v/D_i = 0$) annular jets.

The motivations for the work are threefold. Firstly, by exploring a wider range of source geometries our physical understanding of the slender open-core annular jet will be increased. Secondly, this work will allow us to gain an understanding of whether the ventilation ratio D_v/D_i can be used to control the flow issuing from slender annular sources. Finally, a practical motivation arises from a common use of the slender open-core annular source as a device intended for personalised cooling (Mason et al., 2010). These devices have the potential to be placed in locations which, among other things, restrict the ventilation of the core (i.e. near or against a wall), the effect of which is currently unknown.

The current chapter is structured as follows. In §6.2 the source conditions are outlined and elements which were unique to this set of experiments, and thereby departed from the standard methodology, are discussed. In §6.3 the results are presented and discussed. Finally, in §6.4 we offer our conclusions.

6.2 Experiments

Details of the experimental equipment, design and technique are given in §2. Here we elucidate on the specific source geometry and source conditions, discuss modifications made to the nozzles which allowed the investigation of a range of ventilation ratios D_v/D_i, and describe the method by which measurements of the pressure difference across the nozzle blockage were obtained.

6.2.1 Nozzle ventilation and source conditions

For the investigation presented herein, two sets of modifications were made to the annular nozzle. The purpose of the first set of modifications was to allow the investigation of jets issuing from slender closed-core annular sources $D_v/D_i = 0$ (across a range of D_i/D_o), and the second to allow the examination of jets issuing from sources with a range of ventilation ratios D_v/D_i (at a fixed D_i/D_o).

The first set of modifications involved completely sealing, with adhesive tape, the upstream end of the open core for nozzles **N1-N3** and **N5** (i.e. the core was blocked at $x = -0.7D_c$, see figure 6.2b). The adhesive tape was stretched taut which ensured that it did not flex during the experiments. With the exception of the ventilation ratio, the source conditions, outlined in table 6.1, are almost identical to those discussed in §5.4. Differences between these two sets of experiments primarily manifest in the source volume flux Q_0 and are less than 10%.

The second set of adjustments sought to modify the ventilation ratio of a single nozzle. Nozzle **N4** was modified to complement the earlier investigation (§4) of the slender almost fully open-core ($D_v/D_i = 0.90$) annular jet. For these alterations, a series of annular disks, of outer diameter $D_p = 96.35$ mm and inner diameter $D_v = \{0,\ 48.2,\ 72.3\}$ mm, were cut from a 1 mm thick aluminium sheet using a water jet cutter. These disks allowed us to obtain $D_v/D_i = \{0,\ 0.50,\ 0.75\}$ and were affixed, with an adhesive tack, to the upstream end ($x = -0.7D_c$) of the nozzles core, see figure 6.3. With the exception of the ventilation ratio D_v/D_i, the source conditions, summarised in table 6.2, are almost identical to the experiments discussed in §4.2. Differences between these two sets of experiments also primarily manifest in the source volume flux Q_0 and are less than 5%.

The measurements presented herein were primarily captured using planar PIV on the $x-y$ plane of the nozzle (i.e. slices along the jet). Four overlapping measurement windows (centred on the nozzle axis and extending from the source to $x = 16D_o$, cf. figure 2.5) were used to capture details of the flow from the near to the far field. In addition, measurements captured on the $r-\theta$ plane at $x/D_o = \{0.25,\ 1.0,\ 3.0,\ 5.0,\ 10.0\}$ using stereoscopic PIV are discussed.

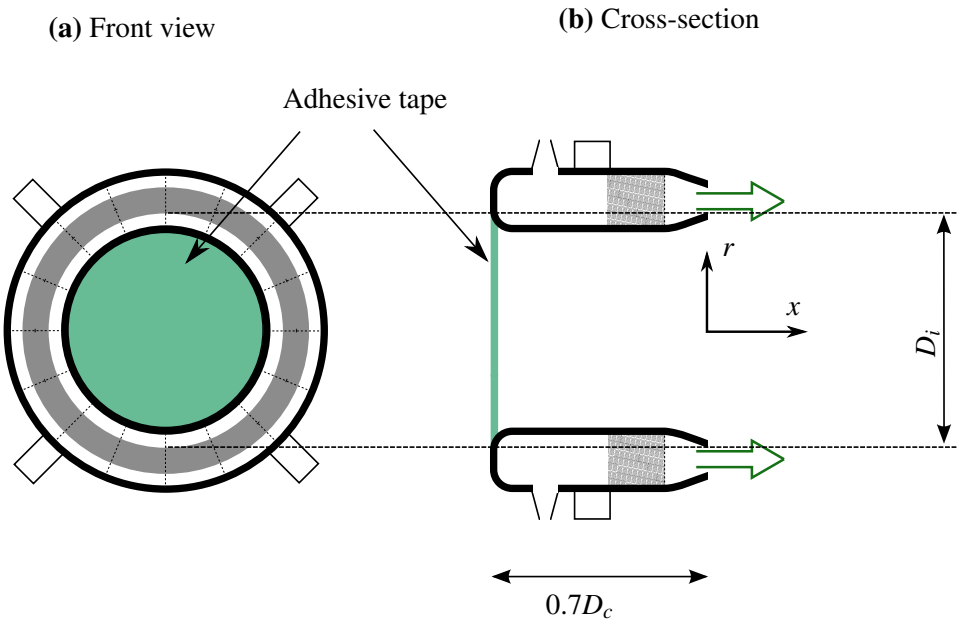

Fig. 6.2: Schematic illustrating the location of the adhesive tape (shaded in green) used to completely block the core of the annular source, i.e. to modify the source such that $D_v/D_i = 0$. This adhesive tape is located at the upstream end of the nozzle, i.e. at $x = -0.7D_c$. Nozzle details are given in §2.1.

	$\frac{D_i}{D_o}$	$\frac{D_v}{D_i}$	Q_0 (m^3/s)	U_0 (m/s)	Re_l ($\pm 5\%$)	Re_f ($\pm 5\%$)	ΔT (°C)	$\frac{L_j}{D_o}$	λ
N1R3V4	0.845	0	0.0109	4.1	2300	14000	12.2	14	5.4
N2R3V4	0.894	0	0.0109	6.2	2300	17000	12.2	18	8.4
N3R3V4	0.947	0	0.0112	13.1	2400	25000	15.0	34	17.8
N5R3V4	0.981	0	0.0124	34.5	2400	43000	20.0	49	51.0

Table 6.1: Geometry and source conditions, listed in order of increasing D_i/D_o, for the experiments where the nozzles **N1-N3** and **N5** (§2.1) were used to investigate the effect of blocking the core of the annulus ($D_v/D_i = 0$). The upstream end ($x = -0.7D_c$) of the nozzles core was blocked with adhesive tape, see §6.2.1 and figure 6.2. The dimensionless length λ, calculated using (1.3), quantifies the non-dimensional shift of the stagnation point and is used by Del Taglia (2002) to predict the onset of symmetry breaking behaviour (see §1.3).

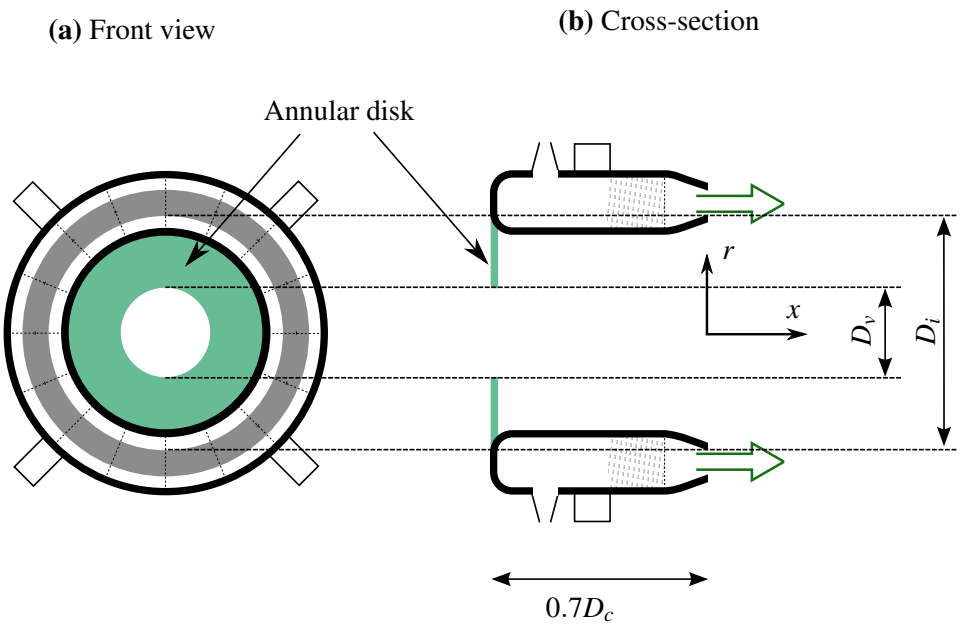

Fig. 6.3: Schematic illustrating the location of the annular disk (shaded in green) used to modify the ventilation ratio D_v/D_i of the annular nozzle. This disk is located at the upstream end of the nozzle, i.e. at $x = -0.7D_c$. Nozzle details are given in §2.1.

	$\frac{D_i}{D_o}$	$\frac{D_v}{D_i}$	Q_0 (m^3/s)	U_0 (m/s)	Re_l ($\pm 5\%$)	Re_f ($\pm 5\%$)	ΔT (°C)	$\frac{L_j}{D_o}$	λ
N4R5V1	0.968	0.90	0.0153	29.5	3200	45000	15.0	64	-
N4R5V2	0.968	0.75	0.0159	30.5	3400	47000	20.0	56	-
N4R5V3	0.968	0.50	0.0159	30.5	3400	47000	20.0	56	-
N4R5V4	0.968	0	0.0153	29.5	3300	45000	22.5	50	30.0

Table 6.2: Geometry and source conditions, listed in order of decreasing D_v/D_i, for the experiments where nozzle **N4** (§2.1) was used to investigate the effect of the ventilation ratio D_v/D_i on the jet issuing from a slender annular source. The ventilation ratio was altered by means of annular aluminium disks at the upstream end ($x = -0.7D_c$) of the nozzles core, see §6.2.1 and figure 6.3. Note that λ is not calculated for **N4R5V1-3** as (1.3) is only applicable to closed-core jets.

6.2.2 Pressure measurements

To complement the PIV measurements, the difference in the pressure between the upstream and downstream faces of the disk used to completely block the core of the annulus was measured. For these measurements, an aluminium disk was fabricated (as described in §6.2.1) with six pressure taps. These pressure taps were located, as illustrated on figure 6.4, so as to determine the dependence of the pressure difference on the radial coordinate r. Given the negligible influence of the return flow in the chamber (§3.2.1), the pressure on the upstream face of the disk was assumed to be equal to the ambient pressure (denoted as P_∞). Thus, the pressure difference was measured between a tap located in the ambient and the 6 taps located on the downstream face of the annular disk. Measurements were acquired using an in-house array of 2 kPa pressure transducers which allowed simultaneous recording at the six pressure taps. Prior to recording, the pressure sensors were zeroed, the mixed flow impeller fan was activated and measurements allowed to stabilise. Then, measurements were sampled at 10 Hz for a period of 60 seconds. This recording interval was found to be suitable for obtaining good quality estimates of the time-averaged pressure difference.

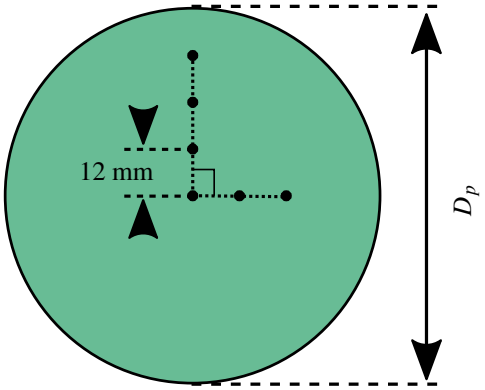

Fig. 6.4: The location of the six pressure taps '•' on the aluminium disk used to block the core of the nozzle, at which measurements of the pressure difference ΔP between the upstream and downstream faces of the disk were measured. The pressure taps are located 12 mm apart.

Recordings of the pressure difference were made for closed-core jets with $0.845 \leq D_i/D_o \leq 0.981$ and $Re_l \approx 2200$, i.e. for sources **N1-3R3V4** and **N5R3V4** detailed in table 6.1. In addition, recordings were made for the closed-core ($D_v/D_i = 0$) nozzle **N4** ($D_i/D_o = 0.968$) with $1100 \leq Re_l \leq 3000$, i.e. sources **N4R1-5V4** as detailed in table 6.3.

Source	Re_l	Re_f	Q_0 (m^3/s)	U_0 (m/s)	ΔT (°C)	L_j/D_o
N4R1V4	1100	15000	0.0049	9.6	3.5	48
N4R2V4	1600	22000	0.0076	14.5	7.2	42
N4R3V4	2300	32000	0.0108	20.9	10.2	52
N4R4V4	2800	37000	0.0127	24.6	15.3	53
N4R5V4	3200	45000	0.0153	29.5	15.0	64

Table 6.3: Details of the Reynolds numbers and accompanying source conditions, listed in order of increasing Re_l, for which measurements of pressure (§6.2.2) across the disk used to block nozzle **N4** were taken.

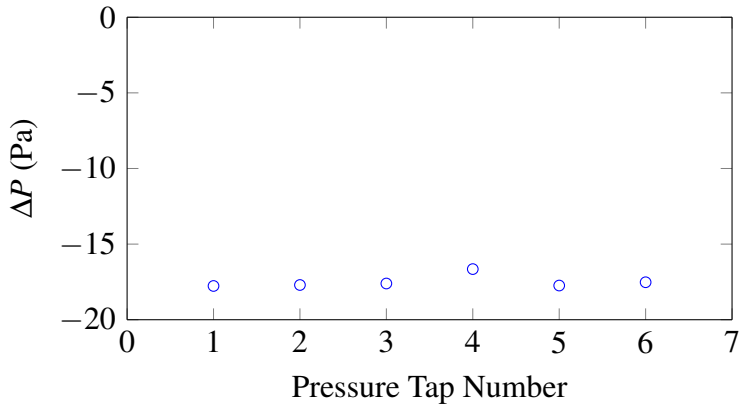

Fig. 6.5: The time-averaged pressure difference ΔP as measured at each of the 6 pressure taps for the flow issuing from source **N4R5V4**.

Given that our measurements indicated that the time-averaged pressure differences were independent of the location of the pressure tap (differing by less than 5%, see figure 6.5), for each nozzle a single value for the pressure difference acting on the disk is obtained by averaging values recorded at the six pressure taps.

6.3 Results and discussion

We begin by qualitatively examining instantaneous snapshots, figure 6.6, of a turbulent slender closed-core annular jet issuing from source **N5R3V4**, i.e. with $D_i/D_o = 0.981$ and $D_v/D_i = 0$, obtained using flow visualisation on the $x-y$ plane. Near source, the jet can be distinguished

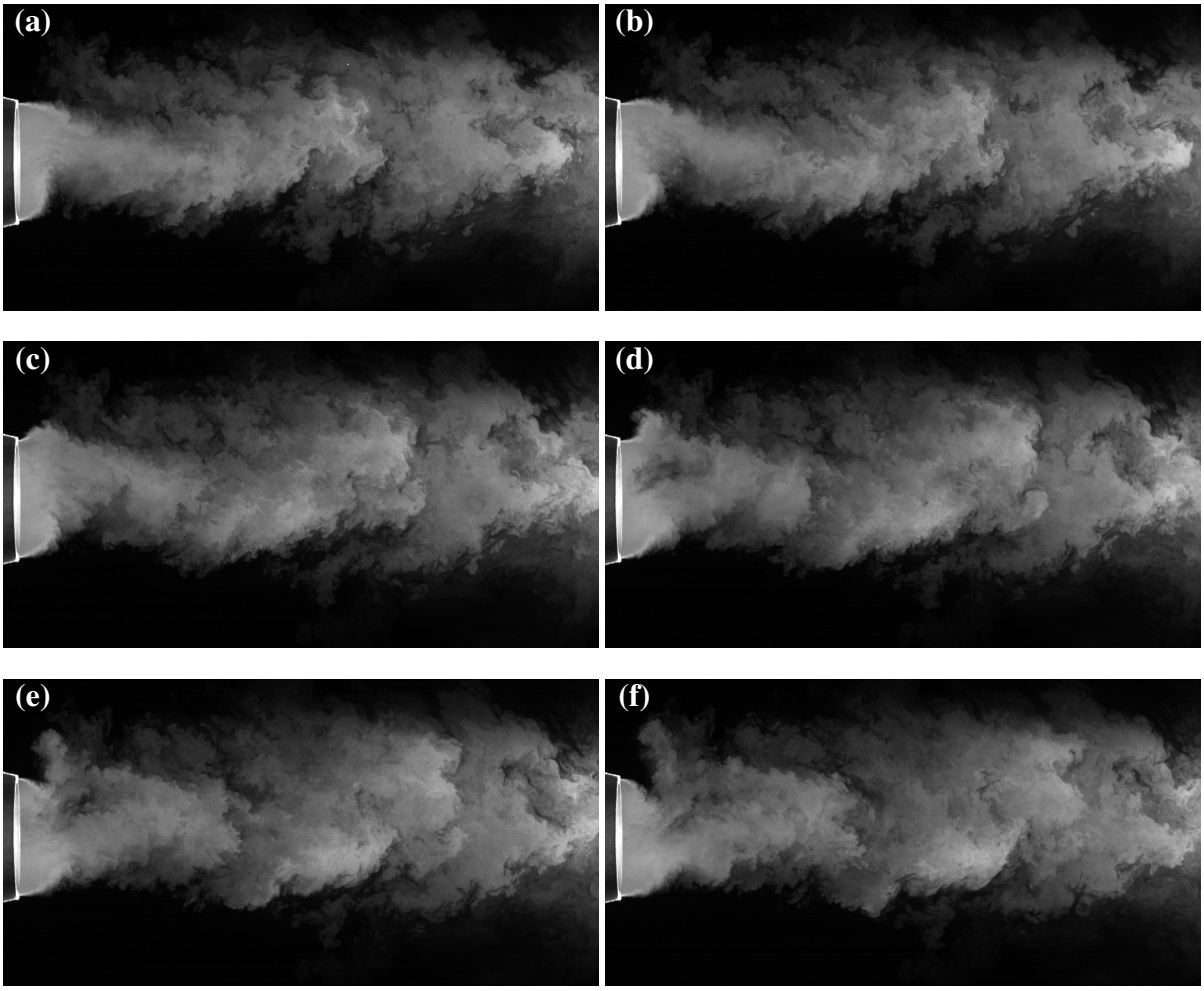

Fig. 6.6: Instantaneous snapshots of the mid-plane of the jet issuing from the closed-core slender annular source **N5R3V4** (see tables 2.1 and 6.1 for details). The snapshots shown (a-f) are 0.005 seconds apart. Note the highly unsteady nature of the flow, the near-source flapping behaviour and the meandering of the jet produced.

from the recirculation region by the increased light intensity which represents an increased smoke concentration in comparison to the surroundings. The recirculation region is the smoke filled region adjacent to the nozzle and bounded by the jet. These snapshots, captured 0.005 seconds apart, reveal that the flow is highly unsteady. These snapshots qualitatively suggest that fluid contained within the wake vortices, shed from the recirculation region (Lam et al., 1986), accounts for a significant proportion of the downstream jet volume flux. The jet meanders on travelling downstream, which we attribute to the fact that the location of vortex shedding changes randomly in time (cf. Lam & Ko, 1986). There was no evidence of meandering in

the open-core jet (§4) as the open core prevented the formation of the large-scale recirculation region. Thus, the meandering motion has some dependence on the ventilation ratio D_v/D_i.

Ko et al. (1998) noted that the passage of a shed vortex induced a velocity in the jet itself. For their jet, this velocity induction resulted in the formation of an additional vortex train (in the jet). For our slender annular jet the effect is large enough to cause the jet itself to flap. By 'flapping' we refer to the time variation in the curvature of the jet issuing from the slot (note changes in trajectory of the jet issuing from the slot at the top of the snapshots in figure 6.6a-f). As discussed in §1.3, the influence of vortex shedding is directly related to the relative streamwise extents of the potential core and recirculation region. For the slender jet examined here, the relative extent of the potential core when compared to the recirculation region is small, and so the effect of vortex shedding is much more significant (than in the non-slender jets examined in the literature).

The remainder of this section is structured as follows. First, in §6.3.1 we examine the symmetry of the jets produced by the closed-core annular nozzles. This is followed in §6.3.2 by a discussion of the momentum integral. We then proceed to discuss the coalescing behaviour of the jet, focussing on the bounded near-source region (§6.3.3) and the location at which the jet reattaches (§6.3.4). In §6.3.5 we explore the effect of the ventilation ratio on the near-field planar-jet-like behaviour. Finally, in §6.3.6 we examine the far field of the flow issuing from our sources.

A note on scalings

The distances presented herein have been non-dimensionalised using the scalings established in §4-5. The bounded near-source region has been scaled on D_i (cf. §4.3.2 and §5.2), the development of the jet and the jet width on D_o, and the inverse centreline velocity on $\sqrt{A_0}$ (cf. §5.5.2).

6.3.1 Symmetry

Del Taglia (2002) observed symmetry breaking behaviour in slender closed-core annular jets and related this behaviour to the non-dimensional shift of the stagnation point λ, see discussion in §1.3. Calculating values of λ for sources **N3R3V4**, **N5R3V4** (final column of table 6.1) and **N4R5V4** (final column of table 6.2) using (1.3) reveals $\lambda > 16$. On recalling that $3.18 < \lambda_{crit} < 16$, this indicates that the jets issuing from these sources should exhibit symmetry breaking behaviour. However, stereoscopic PIV measurements of the axial velocity $\bar{u}(r,\theta)$ on the r-θ plane of source **N4R5V4** at $x/D_o = 1$, figure 6.7(a), indicate that the time-averaged

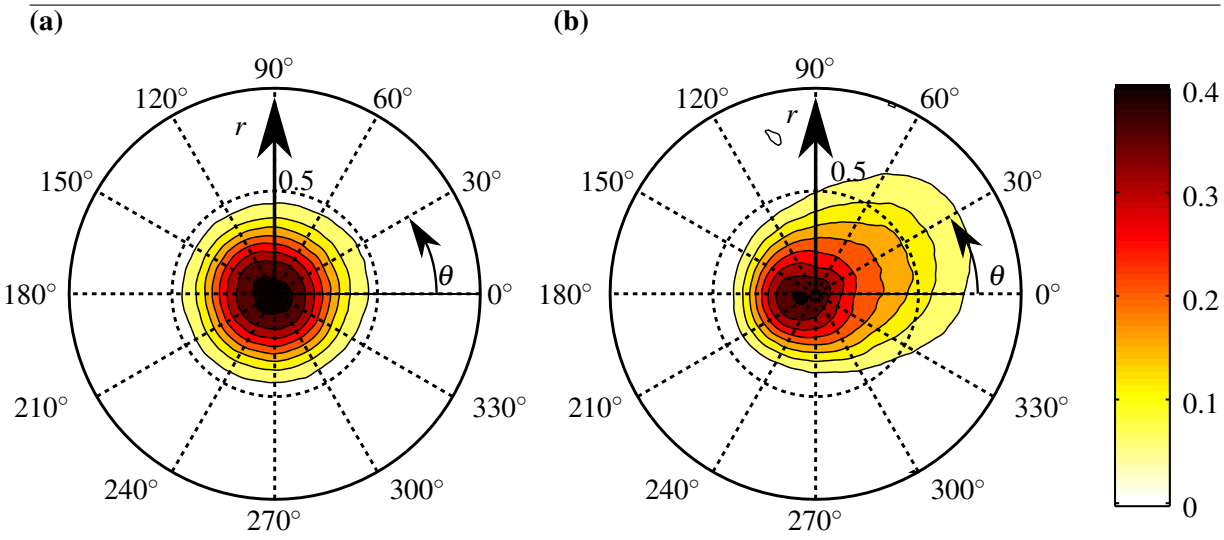

Fig. 6.7: Contour plots of time-averaged axial velocity $\bar{u}(r,\theta)$ captured using stereoscopic PIV on an $r-\theta$ section located at $x/D_o = 1$ for the closed-core sources (a) **N4R5V4** as described in §6.2, and (b) **N4R5V4*** where the blockage has been applied to the front of the nozzle (see §6.3.1). Note the change in the symmetry that occurs on altering the position of the blockage.

flow is approximately axisymmetric. The primary difference between the nozzle geometry examined herein and those investigated in the literature is the x location of the blockage. The sources examined herein are blocked at $x = -0.7D_c$ (i.e. blocked at the back, see figure 6.3), whereas the sources from which symmetry breaking jets issue have been blocked flush with the nozzle exit (i.e. blocked at the front, at $x = 0$, e.g. Del Taglia, 2002). Our results therefore suggest that the symmetry breaking behaviour is dependant on the blockage location. This dependence is confirmed by the asymmetry of the time-averaged flow (at $x/D_o = 1$) when source **N4R5V4*** is blocked flush with the nozzle exit, figure 6.7(b). The mechanism by which symmetry breaking behaviour is dependent on the blockage location is unknown. Symmetry breaking was not investigated further given the more fundamental aspects for study laid out in the objectives.

'Handle bars' (shown on figure 6.8) indicate that the range of momentum integral estimates M_θ, calculated using (3.8) on a virtual planar PIV plane rotated about the stereoscopic $r-\theta$ sections of the flow issuing from source **N4R5V4**, are small and provide further evidence that the flow is symmetrical. Crucially these small 'handle bars' indicate that the $x-y$ plane of the jet issuing from a source whose core has been closed at the back is representative of the flow.

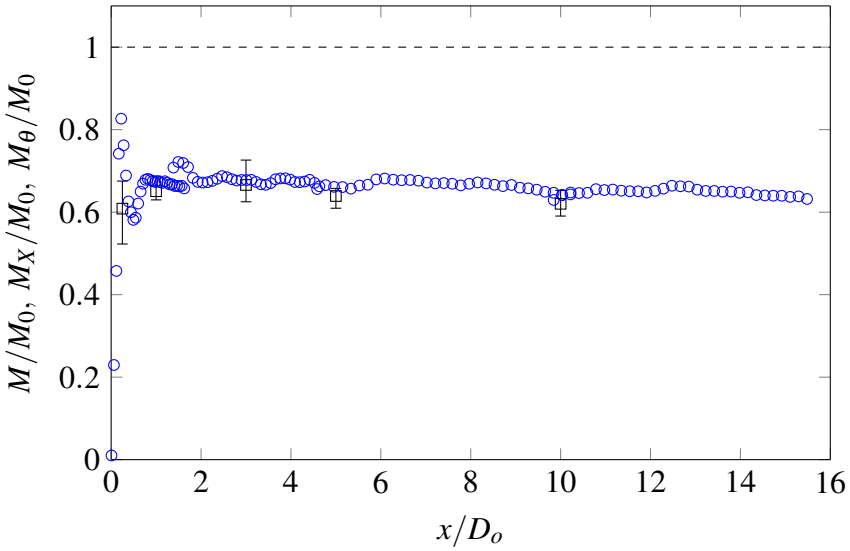

Fig. 6.8: Variation of the specific momentum integral with distance downstream for **N4R5V4**. Estimates of M from planar PIV measurements (on an $x-y$ plane) using (3.7) '$\circ$', estimates of M_X from stereoscopic measurements (on an $r-\theta$ plane) using (3.9) '$\square$'. 'Handle bars' represent the range of values obtained by calculating the specific momentum integral M_θ from the $r-\theta$ sections along lines of constant θ using (3.8), see §3.2.2.

6.3.2 Momentum integral

Upon calculating estimates of the specific momentum integral M using (3.7) on the $x-y$ plane, shown using the symbol '$\circ$' on figure 6.8, we immediately notice that the momentum integral of the jet is less than expected given the volume flux supplied to the nozzle (i.e. $M_0 = Q_0^2/A_0$ and $M/M_0 \approx 0.66 < 1$). These estimates coincide with estimates (from stereoscopic PIV on the $r-\theta$ plane and (3.9)) marked with the symbol '$\square$' on figure 6.8, confirming that this is not an alignment issue. Note that extremely near the source, for $x/D_o \lesssim 0.5$, estimates of the momentum flux calculated from the PIV data are inaccurate due to the relatively high velocities and relatively narrow slot (when compared to the vector resolution, see table 2.3). Despite the deficit, the momentum integral is conserved with distance downstream, and a single value for the momentum integral deficit M_D $(= M_0 - M(x))$ is obtained by averaging over $2 \leq x/D_o \leq 16$. Values of M_D are plotted for $0.845 \leq D_i/D_o \leq 0.981$ on figure 6.9(a). This plot shows a clear increase in M_D with D_i/D_o and moreover, suggests that the momentum integral deficit is negligible for the non-slender sources (for $D_i/D_o \lesssim 0.85$) that have been the focus of the literature (§1.3). As anticipated, from comparing the momentum integral in the open-core (figure 4.6) and closed-core (figure 6.8) jets, figure 6.9(b) reveals that the deficit M_D is dependent on the ventilation ratio D_v/D_i.

To explain the momentum integral deficit we consider similarities between closed-core annular jets and flows past bluff bodies. In the region immediately downstream of a bluff body, a large-scale recirculation region exists from which vortices are shed (e.g. Perry et al., 1982). This region and shedding behaviour resemble the near-field behaviour of a closed-core jet. A major focus in the bluff body literature is the estimation of the drag force. For bluff body flows, the drag force consists of a frictional contribution and a contribution from the pressure difference between the upstream and downstream faces of the body. On acknowledging that a drag force is dimensionally equivalent to a (non-specific) momentum integral and that a pressure difference ΔP exists across the blockage, it becomes clear that the momentum integral deficit is a result of a 'drag force'. Typically, the drag force is modelled using

$$\rho M_D = \underbrace{-\frac{1}{2}\rho U_0^2 C_D A_R}_{\Delta P}, \tag{6.1}$$

(e.g. Tennekes & Lumley, 1972), where C_D is the drag coefficient and A_R the projected area perpendicular to the primary flow direction[1]. As the primary flow is not passing over the external surface of the closed-core source, the term $-\rho U_0^2 C_D/2$ represents the pressure difference across the blockage ΔP. For simplicity and because, for slender sources in which drag is significant, the area of slot is much smaller than the area of the blockage, i.e. $A_0 \ll (1-D_v^2/D_i^2)\pi(D_i/2)^2$, herein we assume that pressure difference acting on the slot is equal to ΔP. Thus, we can write $A_R = (1-D_v^2/D_i^2)\pi(D_i/2)^2 + A_0$ and normalise (6.1) by ρM_0 ($= \rho A_0 U_0^2$), giving

$$\frac{|M_D|}{M_0} = \frac{1}{2} C_D \underbrace{\left[\left(1-\frac{D_v^2}{D_i^2}\right)\frac{\pi(D_i/2)^2}{A_0} + 1\right]}_{A_R}. \tag{6.2}$$

A drag coefficient of $C_D = 0.035$, see '——' on figure 6.9, is obtained empirically by fitting (6.2) to measurements of M_D. The predictions and experimental data have similar trends, indicating that we can suitably model the momentum integral deficit as a drag force acting on the nozzle. In the model, when a constant value of $C_D = 0.035$ is used, the pressure difference is solely dependent on the exit velocity U_0. Bluff body literature has noted that the drag coefficient is sensitive to geometry of the bluff body and the Reynolds number of the flow (Roos & Willmarth, 1971). Thus, for the annular jet, C_D is likely to vary with D_i/D_o, D_v/D_i and Re_l. This changing drag coefficient goes some way to explain the inaccuracies of the predictions particularly with regards to the limits of the parameter space: for $D_i/D_o = 0$, i.e. a round jet, the model falsely predicts a non-zero momentum integral deficit; for $D_i/D_o > 0.99$ the model

[1] For the bluff body case, U_0 refers to the free stream velocity.

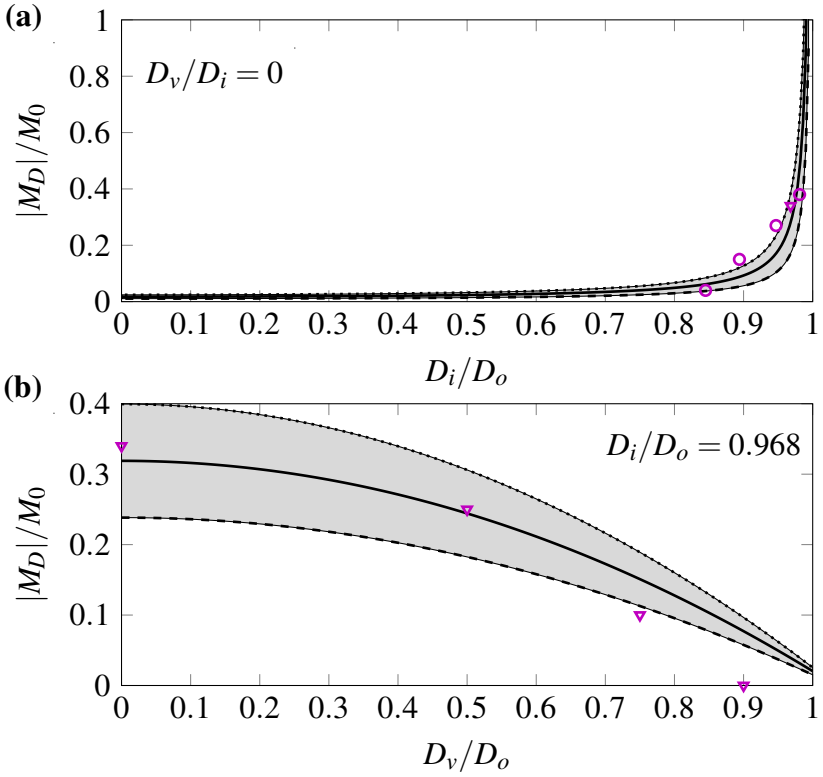

Fig. 6.9: Variation of the momentum integral deficit M_D/M_0 with (a) diameter ratio D_i/D_o (for $D_v/D_i = 0$) and (b) ventilation ratio D_v/D_i (for $D_i/D_o = 0.968$). The values for '$\circ$' are extracted from our PIV measurements on the jets issuing from sources **N1-3R3V4** and **N5R3V4**, and the values for '$\triangledown$' from sources **N4R5V1-4**. Predictions from the theoretical model (6.2): best fit $C_D = 0.035$, '——'; the 95% confidence intervals of this fit are shaded in grey and bounded by $C_D = 0.021$ '- - - -' and $C_D = 0.048$ '.....'.

predicts $M_D > M_0$, clearly a non-physical result. Equally, with regards to the ventilation ratio, the model appears to over-predict the momentum integral deficit for $D_v/D_i \gtrsim 0.5$.

Verification of the relationship between the momentum integral deficit and the pressure difference was obtained by comparing, on figure 6.10, measurements and predictions of ΔP (see §6.2 and (6.1)). Given the dependence of ΔP on U_0^2 (cf. (6.1)), plotting ΔP against U_0^2 allows results for $0.845 \leq D_i/D_o \leq 0.981$ and $1100 \leq Re_l \leq 3200$ to be displayed on a single axis. Clearly, the value of $C_D = 0.035$ predicts ΔP very well, particularly on considering the 95% confidence intervals (grey shaded region).

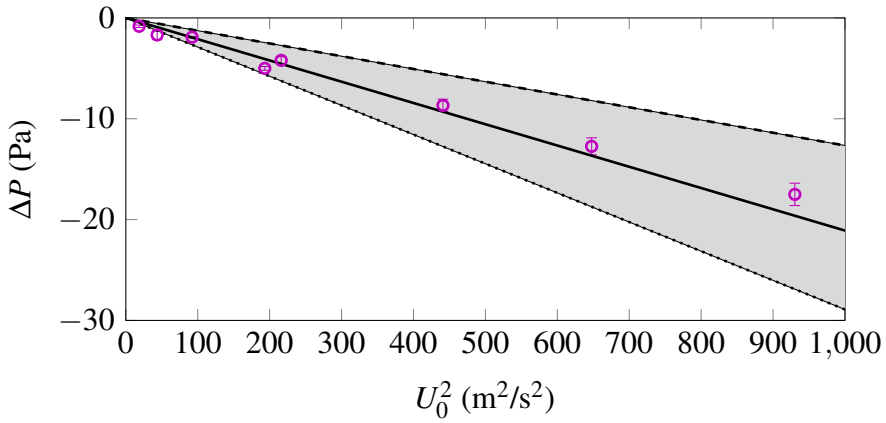

Fig. 6.10: The pressure difference ΔP across the blockage for closed-core annular sources **N4R1-5V4** and **N1-3R3V4** (see tables 6.1 and 6.3), where the sources have been compared by means of the square of the exit velocities U_0^2. Mean of the time-averaged measurements from an array of pressure tappings '○'. 'Handle bars' indicate the standard deviation of these measurements. Predictions from (6.1) using: $C_D = 0.035$ from a best fit of (6.2) to the experimental data in figure 6.9 '——'; the 95% confidence intervals of this fit are shaded in grey and bounded by $C_D = 0.021$ '- - - -' and $C_D = 0.048$ '·····'.

6.3.3 Bounded near-source region

Figure 6.11, which plots the pattern of the time-averaged streamlines in the near field of the jets issuing from sources **N4R5V1-4** (i.e. with $D_v/D_i = \{0,\ 0.50,\ 0.75,\ 0.90\}$), demonstrates that flow behaviour in the bounded near-source region is dependent on the ventilation ratio D_v/D_i. For $D_v/D_i = 0$ (figure 6.11a) this region is dominated by a large-scale recirculation, and for $D_v/D_i = 0.90$ (figure 6.11d) this region almost entirely consists of the induced flow. Between these two extreme cases, streamline plots for $D_v/D_i = 0.50$ and $D_v/D_i = 0.75$ (figures 6.11b-c) show a region of induced flow upstream of the recirculation region. In figure 6.11(b) this region of induced flow extends to $x \approx 0.2D_o$ and in figure 6.11(c) to $x \approx 0.6D_o$. The recirculation region decreases in size as the ventilation ratio D_v/D_i is increased. The behaviour of the bounded near-source region as D_v/D_i is decreased is reminiscent of the behaviour of coaxial jets as the flow rate through the core is decreased (§6.1). This similarity indicates that the restriction of the induced flow is the primary mechanism by which D_v/D_i effects the bounded near-source region.

From these streamline plots, it is apparent that reducing D_v/D_i increases the curvature of the jet issuing from the annular slot. The inertial force F_I projects the jet downstream and the pressure force F_P causes the inward curvature of the jet (see §5 and (5.41)). Therefore, given

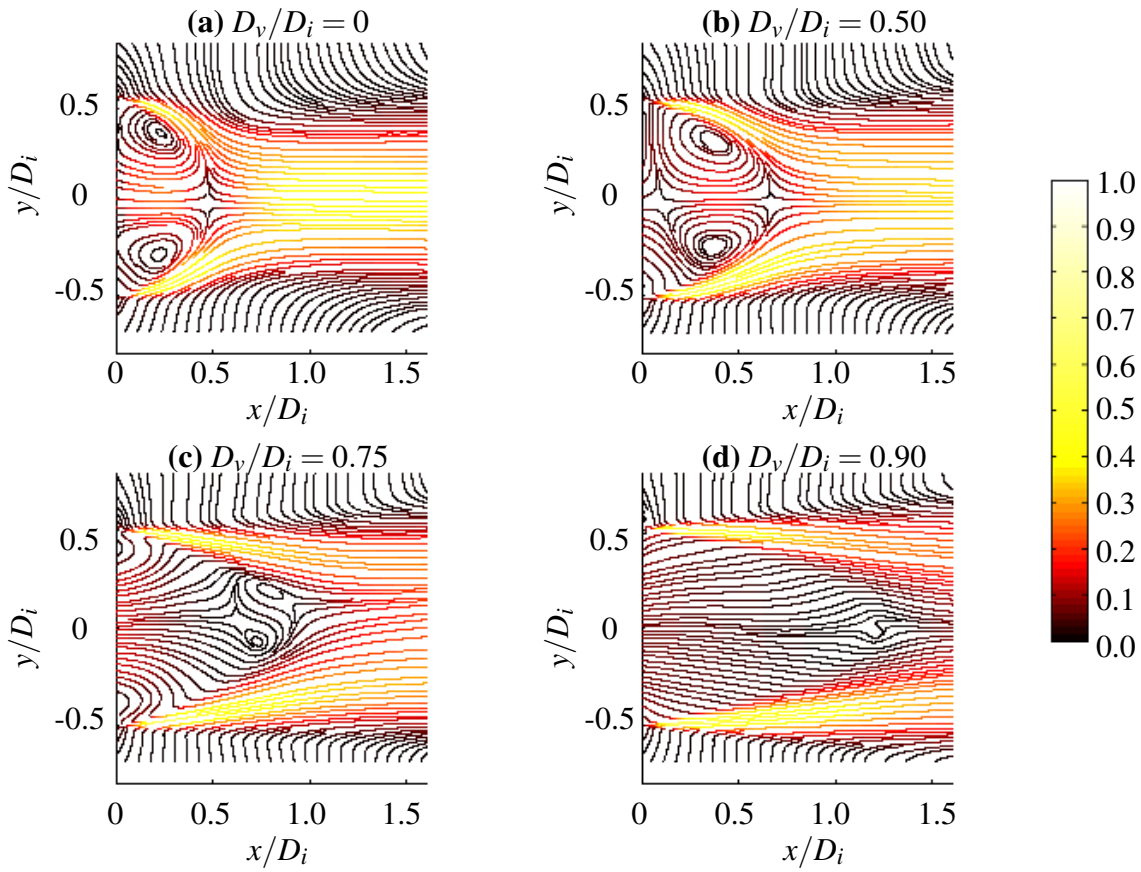

Fig. 6.11: Effect of the ventilation ratio. Time-averaged streamline pattern in the near field of jets issuing from sources (a) **N4R5V4** with $D_v/D_i = 0.00$, (b) **N4R5V3** with $D_v/D_i = 0.50$, (c) **N4R5V2** with $D_v/D_i = 0.75$ and (d) with **N4R5V1** $D_v/D_i = 0.90$, see table 2.2. Colour represents the non-dimensional velocity magnitude $\sqrt{\bar{u}^2 + \bar{v}^2}/U_0$.

that curvature increases with increasing D_v/D_i, it can be inferred that restricting the open core increases the relative size of the pressure force responsible for jet coalescence.

Recirculation region

This section, §6.3.4 and §6.3.6 first discuss the behaviour of the symmetrical closed-core annular jet for a range of slender diameter ratios, and subsequently discuss how the behaviour changes as the ventilation ratio D_v/D_i of the core is varied.

Although the toroidal recirculating vortex is bounded by stagnation points (at $x = x_s$) at its upstream and downstream extents, for the closed-core jets examined the upstream stagnation point is located upstream of the slot exit (and thus upstream of our measurement domain, see figure 6.11a). Figure 6.12(a) plots the location of the downstream stagnation point with the diameter ratio in closed-core annular jets. Our estimates are marked with '$\circ$' and '$\triangledown$', and the

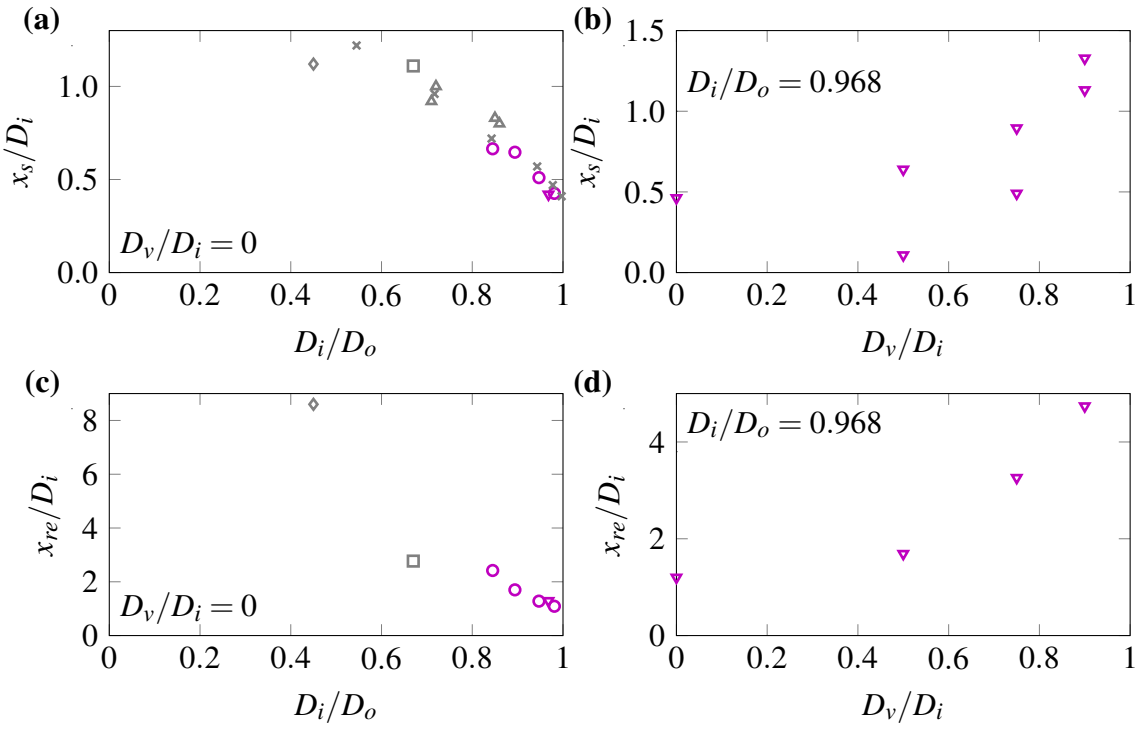

Fig. 6.12: (a) & (b) The variation in the location of the stagnation points with D_i/D_o and D_v/D_i, respectively. (c) & (d) The variation in reattachment point location with D_i/D_o and D_v/D_i, respectively. The values marked '○' are extracted from our PIV measurements on sources **N1-3R3V4** and **N5R3V4**, and the values marked '▽' from source **N4R5V1-4**. Figure 6.12(a,c) includes a selection of data from the literature: '□' Chigier & Beer (1964a), '◇' Ko & Chan (1978), '△' Li & Tankin (1987) and '×' Del Taglia (2002).

light grey symbols denote values extracted from the literature (see caption for details). As the diameter ratio is increased, the normalised location of the stagnation point x/D_i shifts upstream. Our estimates (for nozzles which have been blocked at the back) coincide well with values extracted from the literature (in which the nozzles were blocked at the front). This agreement indicates that the location of the blockage does not influence the downstream extent of the recirculation region.

Figure 6.12(b), which plots estimates for the locations of the stagnation points against the ventilation ratio D_v/D_i, indicates that on increasing D_v/D_i both stagnation points move downstream and the axial distance separating them decreases. These behaviours are symptomatic of the mechanism by which the induced flow is related to the jet curvature, and is discussed in the following section.

Induced flow

Figure 6.13(a) plots estimates '$\circ$' of the non-dimensional volume flux induced through the core Q_a/Q_0 against D_v/D_i, calculated from PIV measurements using (3.5). As anticipated, the ventilation ratio regulates the amount of fluid induced through the open core of the annulus - as D_v/D_i increases, so does Q_a/Q_0. In other words, the larger the area of the open core, the greater the induced volume flux. Given that we expect the induced volume flux to scale with the area of the open core, i.e. $Q_a \propto \pi D_v^2/4$ and $Q_I \propto \pi D_i^2/4$ where Q_I is used here to denote the volume flux at the theoretical fully open-core limit ($D_v/D_i = 1$), we have the ratio

$$\frac{Q_a}{Q_0} = \frac{Q_I}{Q_0}\left(\frac{D_v}{D_i}\right)^2, \tag{6.3}$$

where Q_I/Q_0 $(= f(D_i/D_o))$. Values acquired using (6.3) are plotted with a solid line on figure 6.13(a), using $Q_I/Q_0 = 1.498$ obtained from the best fit to the experimental data. On figure 6.13(a) this value of Q_I/Q_0 corresponds to Q_a/Q_0 at the open-core limit $D_v/D_i = 1$. The good agreement between the fit and the experimental data is surprising, suggesting that despite variation in the ventilation ratio D_v/D_i the pressure difference driving fluid through the open core of the jet remains approximately constant. This assertion is clear from the absence of the ventilation ratio on rewriting (6.3) in terms of U_a/U_0, as

$$\frac{U_a}{U_0} = \frac{Q_I}{Q_0}\left(\frac{D_o^2}{D_i^2} - 1\right), \tag{6.4}$$

and noting that

$$\frac{\Delta P_a}{\Delta P_0} = \frac{\rho U_a^2/2}{\rho U_0^2/2} = \frac{U_a^2}{U_0^2}, \tag{6.5}$$

where ΔP_a is the pressure difference driving fluid through the core and ΔP_0 is the pressure difference driving fluid from the annular slot. Figure 6.13(b) plots experimental estimates '$\circ$', obtained using (3.1.1), of U_a/U_0 against D_v/D_i and includes a solid line which plots the constant value of $U_a/U_0 \approx 0.10$ obtained using (6.4) and $Q_I/Q_0 = 1.498$. Despite the variation in the experimental measurements, they fall within the 95% confidence intervals of the fit (grey shaded region) and thus can be regarded to be constant. However, we have not yet considered the effect of the momentum integral deficit on our measurements.

The pressure difference driving the induced flow is related to the 'entrainment appetite' of the inner shear layers, and thus to the momentum integral of the jet. To determine whether a change in pressure difference with the ventilation ratio is masked by changes in the momentum integral deficit, a correction for the momentum integral is applied to the exit velocity of the

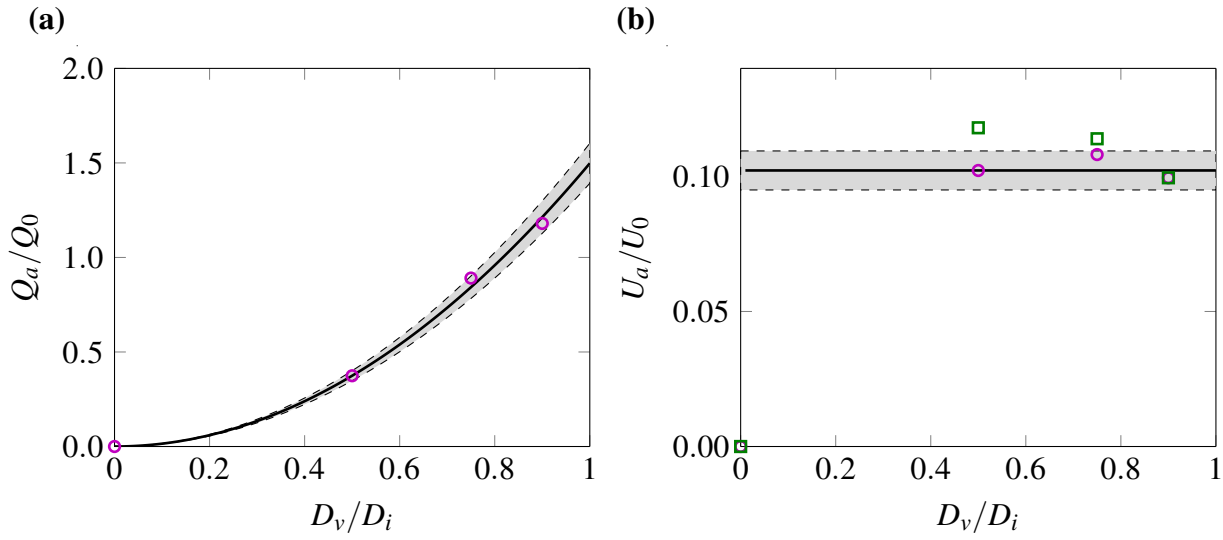

Fig. 6.13: Variation with ventilation ratio D_v/D_i of (a) Q_a/Q_0 and (b) U_a/U_0 induced through the open core for sources **N4R5V1-4**. Data directly extracted from PIV measurements is shown using the symbol '○'. On (a) the solid line '——' represents the best fit to this data using $Q_I/Q_0 = 1.498$ and (6.3). On (b) the solid line '——' represents the best fit to this data using $Q_I/Q_0 = 1.498$ and (6.4), and '□' represents data corrected for the momentum integral deficit. The 95% confidence intervals of the fits are shaded in grey and bounded by a dashed line '- - - -'.

source, i.e. $U_{0*} = \sqrt{(1 - M_D/M_0)U_0^2}$. On applying this correction to the experimental data, see '□' on figure 6.13(b), we observe a decrease in U_a/U_{0*} as the ventilation ratio increases. However, on calculating the ratio of the induced and driving pressure differences $\Delta P_a/\Delta P_0$ using (6.5) and U_a/U_{0*}, the variation between $D_v/D_i = 0.50$ and $D_v/D_i = 0.90$ is small, being less than 3%. From this small variation in the corrected driving pressure we conclude that the primary mechanism by which the ventilation ratio regulates the induced flow is through the modification of the central opening area.

As previously stated, the jet curvature is related to the ratio of pressure and inertial forces that control coalescence. At this stage, one may wonder how to reconcile the low variation in the pressure difference driving the induced flow and the significant variation in jet curvature (figure 6.11) as the ventilation ratio changes. The significant changes in jet curvature are not linked to the driving pressure difference but rather to the volume flux induced through the core. On reducing the ventilation ratio, the non-dimensional volume flux through the core reduces (see figure 6.13). However, the 'entrainment appetite' of the jet remains unchanged. Thus, the degree to which the jet self-entrains increases and the recirculation region grows in size (see figure 6.12b). The recirculation region is associated with a sub-atmospheric

pressure and thus contributes to the pressure force acting on the jet (Ko & Chan, 1978). Larger recirculation regions are associated with larger pressure drops (Rehab et al., 1997), and thus, as the recirculation region grows in size the pressure force acting on the jet increases and the inward curvature of the jet increases.

6.3.4 Reattachment point

The reattachment point, located at $x = x_{re}$, identifies the location at which the high-velocity centreline merges and at which the jet has completely coalesced. Figure 6.12(c), which plots the variation of x_{re}/D_i against D_i/D_o for closed-core jets, shows that increasing the diameter ratio shifts the reattachment point upstream. Our estimates, marked with '$\circ$' and '$\triangledown$', agree with those extracted from the literature (light grey symbols, see caption for details), suggesting that the location of the blockage does not significantly influence the ratio of inertial and pressure forces which control jet coalescence. The upstream shift of the reattachment point indicates that as the diameter ratio increases, the ratio of inertial and pressure forces F_I/F_P controlling jet coalescence decreases. On assuming that the pressure difference responsible for jet coalescence is proportional to the square of the jet exit velocity, i.e. $\Delta P \propto \rho U_0^2$ (cf. (6.1)), (1.4) becomes

$$\frac{F_I}{F_P} \propto k\left[\left(\frac{D_o}{D_i}\right)^2 - 1\right]. \tag{6.6}$$

From (6.6) it is then clear that increasing the diameter ratio results in a reduction of the relative size of inertial force in comparison to the pressure force.

Figure 6.12(d), which plots the variation of x_{re}/D_i with the ventilation ratio D_v/D_i, shows that as the D_v/D_i increases the jet reattaches further downstream. The variation in the reattachment point is consistent with the variation in jet curvature observed on the streamline patterns in figure 6.11. This upstream shift supports the earlier deduction that increasing the area of the open core (i.e. increasing D_v/D_i) increases F_I/F_P.

6.3.5 The near-field jet

It is sensible here to ask how the ventilation ratio influences the near-field planar-jet behaviour. For this, as in §4.3.4, we examine the streamwise development of the jet width along the high-velocity centreline which exits from the annular slot (see figure 4.3). Figure 6.14 shows that the width of the inner (solid symbols) and outer (hollow symbols) shear layers increases with distance downstream. Fischer et al. (1979) note that planar jets spread linearly and in §4.3.4 we observed that the planar-jet-like behaviour exhibited in the near field of the slender open-core annular jet terminated at the point at which the spread was no longer linear. While

the outer shear layers of all four jets spread linearly (approx.) over the measurement domain, as the jet travels past the recirculation region the growth rate of the inner shear layer increases rapidly. Reducing the ventilation ratio results in an increase in the size of the recirculation region (§6.3.3). The increase in size (and increase in jet curvature) causes the upstream boundary of the recirculation region to shift upstream. Correspondingly, the location at which the growth rate of the inner shear layer becomes non linear shifts closer to the source. This increase in growth rate is thus attributed to the self-interaction of the jet, which manifests as the recirculation region. Figure 6.14 therefore suggests that the recirculation region signals the end of the planar-jet-like flow, and the start of the transitional region.

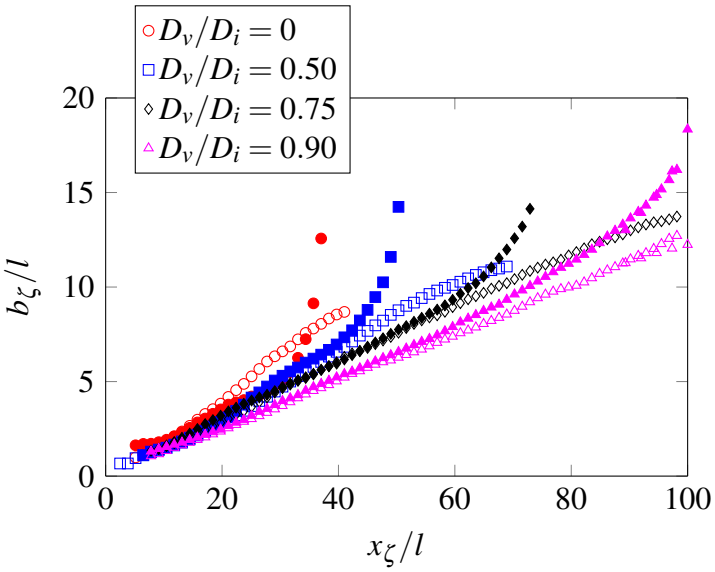

Fig. 6.14: The variation in the jet width for the inner (solid symbols) and outer (hollow symbols) shear layers. Data for the jet exiting the slender ($D_i/D_o = 0.968$) annular slot at a range of ventilation ratios (indicated). Measurements have been taken in a coordinate system aligned with the high-velocity centreline, see figure 4.3.

6.3.6 The far-field jet

One might naturally expect that the significant differences in the near field of closed- and open-core jets extend downstream into the far field. With regards to the closed-core annular jet, we examine sources **N3R3V1** and **N5R3V1** due to their relatively large jet lengths of $L_j \geq 34$ (compared to sources **N1-2R3V1** which have jet lengths of $L_j \leq 18$).

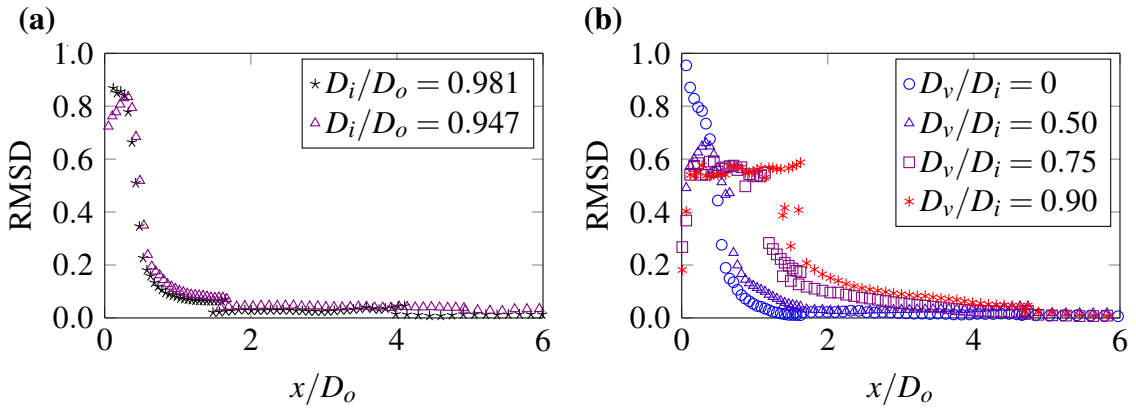

Fig. 6.15: Variation in the RMSD (as evaluated using (5.45)) between the time-averaged velocity profiles $\bar{u}(y)$ and the idealised Gaussian e^{-y^2/b^2} with distance downstream. (a) The effect of varying the diameter ratio (with $D_v/D_i = 0$) for sources **N3R3V4** and **N5R3V4**. (b) The effect of varying the ventilation ratio (with $D_i/D_o = 0.968$) for sources **N4R5V1-4**.

Approach to self-similarity

Annular jets can only reach self-similarity after they have completed coalescing, and thus the location at which far-field behaviour begins will have some dependence on the location of the reattachment point, and consequently, on the ventilation ratio D_v/D_i and diameter ratio D_i/D_o.

To examine the approach towards far-field behaviour, on figure 6.15 we compare profiles of time-averaged axial velocity $\bar{u}(y)$ and the idealised Gaussian e^{-y^2/b^2} by means of the root-mean-square deviation (5.45). Figure 6.15 plots the variation of the root-mean-square deviation (RMSD) with distance downstream. Figure 6.15(a), which plots values for the RMSD extracted from the closed-core jets issuing from sources **N3R3V1** and **N5R3V1**, indicates that the profiles of time-averaged axial velocity attain self-similarity at $x \approx 2D_o$. Given that both jets reattach at approximately the same location ($x_{re}/D_o \approx 1.2$, see figure 6.12c) it is no surprise that the time-averaged velocity profiles achieve self-similarity at similar locations.

Figure 6.15(b), which plots RMSD extracted from jets issuing from sources with $D_v/D_i = \{0, 0.50, 0.75, 0.90\}$, shows that the ventilation ratio significantly influences the location at which the time-averaged velocity profiles attain self-similarity. This was expected given the influence of the ventilation ratio D_v/D_i on the reattachment point (figure 6.12d).

More information on the evolution towards a fully developed state is gleaned, in figure 6.16, on examining the evolution of the peak turbulent intensities $I_{u,max}$ with distance downstream[2].

[2]The turbulent intensity $I_u = \sigma_u/\bar{u}_c$, where σ_u is the standard deviation of the axial velocity fluctuations

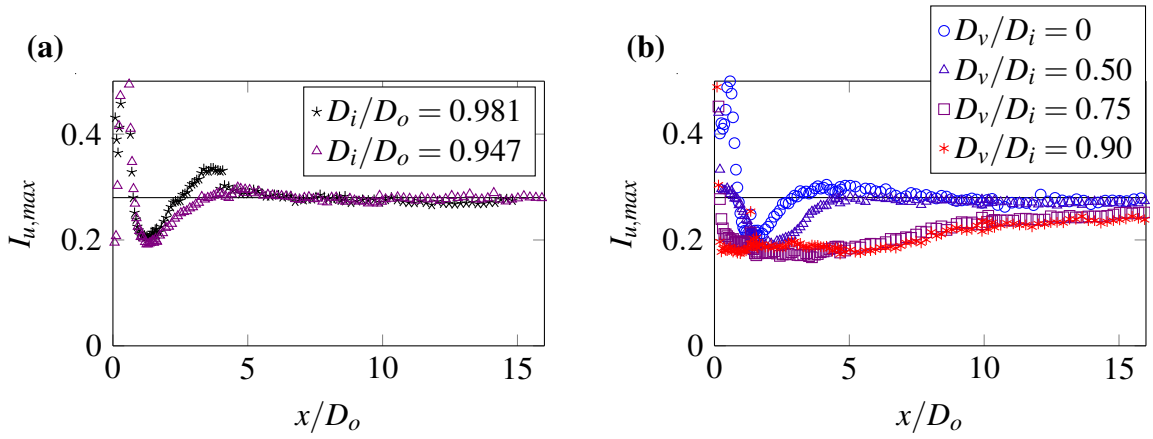

Fig. 6.16: Variation of peak axial turbulent intensity $I_{u,max}$ with distance downstream. (a) The effect of varying the diameter ratio (with $D_v/D_i = 0$) for sources **N3R3V4** and **N5R3V4**. (b) The effect of varying the ventilation ratio (with $D_i/D_o = 0.968$) for sources **N4R5V1-4**. The solid black line represents a constant value of $I_{u,max} = 0.28$. The 10% discontinuity at $x/D_o \approx 4$ in the measurement of $I_{u,max}$ for source **N5R3V4** is within the experimental uncertainty of $\pm 6.1\%$ (see the 5.8% uncertainty in I_u ($= \sigma_u/\bar{u}(x,0)$) in table 3.9, and include the uncertainty across measurement windows using (3.24) – for more information refer to §3.5.4).

Figure 6.16(a) indicates that both the closed-core jets examined develop similarly and that the peak axial turbulent intensity is approximately constant for $x \gtrsim 6D_o$.

As anticipated from the streamwise velocity profiles (figure 6.15(b)), figure 6.16(b) demonstrates that the ventilation ratio D_v/D_i has a profound effect on the streamwise development of the turbulent intensities. Clearly, the greater the restriction of the core, the closer to the source the peak turbulent intensities become approximately constant. Indeed, $I_{u,max}$ in the jets issuing from sources with $D_v/D_i = \{0,\ 0.50\}$ is approximately constant for $x \gtrsim 6D_o$ (see solid black line on figure 6.16(b) which marks $I_{u,max} = 0.28$), whereas $I_{u,max}$ is still evolving at the downstream extent of our measurement domain in jets issuing from sources with $D_v/D_i = \{0.75,\ 0.90\}$. The difference in the development of the turbulent intensities is attributed to differences in the extent of the highly turbulent recirculation region (see figure 6.12b). The larger the recirculation region, the greater the influence on the jet and the closer to the source the turbulent intensities reach a state of approximate self-similarity.

Axial development

The axial development of the jet width b and inverse axial velocity $\bar{u}(x,0)^{-1}$ are plotted in figures 6.17 and 6.18, respectively. As before, the jet width is defined as the distance between the x-axis and $\bar{u}(x,0)/e$ velocity contour. Unsurprisingly, in the region far from the nozzle, the

evolution of these quantities is linear and the flows resemble an axisymmetric jet. Thus,

$$b = c_1(x - x_{01}), \qquad \bar{u}(x,0) = c_2 U_0 \left(\frac{x - x_{02}}{\sqrt{A_0}}\right)^{-1}, \qquad (6.7a,b)$$

where x_{01} and x_{02} represent the locations of the virtual origin for the respective quantities. The constants c_1, c_2 and virtual origins x_{01}, x_{02} in tables 6.4 and 6.5 were found on fitting (6.7) to the data over the range $9 \leq x/D_o \leq 15$. This range of fitting is consistent with the range used in §4 and §5. The resulting best fit lines are included on figures 6.17 and 6.18. For the jets issuing from sources with $D_v/D_i = \{0.75,\ 0.90\}$ the constants describing the spread and inverse centreline velocity are sensitive to the location at which we consider far-field behaviour to begin (and to which we fit (6.7)). This sensitivity is attributed to the fact that the turbulent intensities within these jets are still evolving at the downstream extent of our measurement domain, as established in figure 6.16. For consistency, despite this continuing development, the data is once again fitted over the range $9 \leq x/D_o \leq 15$.

As a result of the scalings established in §5.5.2, the jet width and associated downstream distance are scaled on D_o, and the downstream distance associated with the inverse centreline velocity on $\sqrt{A_0}$.

	D_i/D_o	c_1	x_{01}/D_o	c_2	c_2*	$x_{02}/\sqrt{A_0}$	$x_{02}*/\sqrt{A_0}$	α
N3R3V4	0.947	0.139	-1.19	5.0	5.8	-4.5	-3.8	0.0695
N5R3V4	0.981	0.143	-0.45	4.5	5.7	-9.5	-7.5	0.0715

Table 6.4: Constants extracted from the PIV measurements of the closed-core ($D_v/D_i = 0$) jets issuing from sources **N3R3V4** and **N5R3V4** by fitting (6.7a) and (6.7b) over the range $9 \leq x/D_o \leq 15$. Starred values are those corrected for the momentum flux deficit. Entries in the final column, the entrainment constant α, were calculated using (5.32).

(a) Closed-core jets: Near the source, the width of the closed-core jets decreases before subsequently increasing, see figure 6.17(a) for $x/D_o < 3$. This decreasing width is symptomatic of the strong inward curvature of the jet (see §6.3.3-6.3.4). In the region far from the nozzle the variation in the spreading rate c_1 is small ($< 3\%$), see table 6.4, and is attributed to experimental error. We attribute the larger spread of these closed-core jets ($c_1 \approx 0.14$), when compared to the open-core jet ($c_1 = 0.102$, see §4) and round-jet ($c_1 = 0.113$, see §4) to the meandering behaviour (§6.3). The similar spreading rates for the jets issuing from sources **N3R3V4** and **N5R3V4** indicate that the magnitude of the meandering motion does not vary significantly in

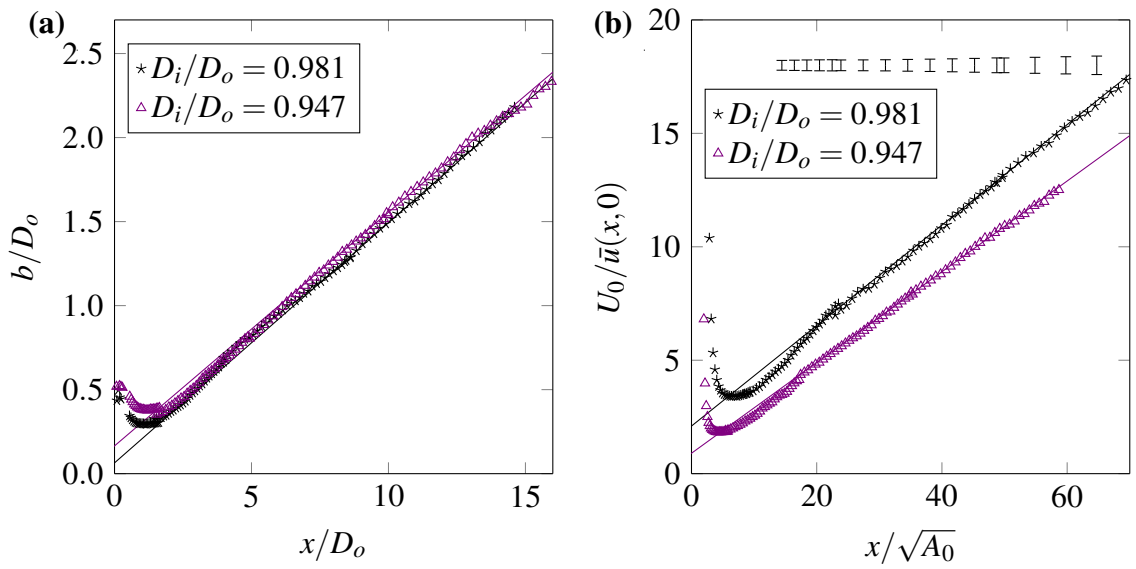

Fig. 6.17: Closed-core jets. Variation with distance downstream of (a) the jet width and (b) the inverse axial velocity along the longitudinal nozzle axis for the jet issuing from sources **N3R3V4** and **N5R3V4**. The best fit lines are given by (6.7a) and (6.7b) with the constants given in table 6.4. On (a) the error is smaller than the size of the symbols. The error bars in (b) represent the estimated error in $U_0/\bar{u}(x,0)$ due to the uncertainty in measurements of the slot width. The error bars shown are those estimated for **N5R3V4** (see table 3.9), where the relative uncertainty in the slot width is largest, and thus represent the largest error margins (of the two sources).

the range $0.947 \leq D_v/D_i \leq 0.981$. We anticipate that for sufficiently low diameter ratios, when the influence of the vortex shedding on the jet is small (see §1.3), the meandering motion will almost entirely cease. The cessation of the meandering motion will correspond with a reduction of the spreading rate. Evidence for a reduced spreading rate at lower diameter ratios arises on considering that the spread ($c_1 \approx 0.14$) of the slender closed-core jet exceeds that of the round jet ($c_1 \approx 0.113$), whereas Chan & Ko (1978) state that the spread of their non-slender jet (with $D_i/D_o = 0.45$) is less than that of a round jet. Our results, combined with their comparison of the spreading rate of annular and round jets, suggests that no meandering occurs in the closed-core jet with $D_i/D_o = 0.45$.

The inverse axial velocity $\bar{u}(x,0)^{-1}$ varies significantly with diameter ratio in closed-core annular jets, see figure 6.17(b). The decay constant c_2 of the jet issuing from the source with $D_i/D_o = 0.981$, '$\star$', is 10% larger than that in the jet issuing from the source with $D_i/D_o = 0.947$, '$\triangle$', see table 6.4. Expressing the centreline velocity in terms of a momentum integral (see (1.16)) makes it clear that the momentum integral deficit should be considered

when estimating values of c_2. This consideration yields

$$u(x,0) = c_2(M_0 - M_D)^{1/2}(x - x_{01})^{-1}. \tag{6.8}$$

On reviewing (6.8), the 10% variation of c_2 is unsurprising due to the 40% variation in the momentum integral deficit (§6.3.2). Values of c_2 corrected for the momentum integral deficit are denoted as c_2* in table 6.4 and are similar for both jets, varying by only 2%. Thus, the differences in the normalised velocity $U_0/\bar{u}(x,0)^{-1}$ are primarily attributed to the momentum integral deficit. The 12% difference between the closed-core decay rate ($c_2 \approx 5.8$) and round-jet decay rate ($c_2 = 6.5$, see §4), is in part attributed to the smearing of the jet that occurs upon time-averaging a meandering flow.

For the closed-core annular jets examined, the virtual origins x_{01} and x_{02} reside upstream of the nozzle and vary marginally with the diameter ratio D_i/D_o.

(b) Varying the ventilation ratio: Increasing the ventilation ratio D_v/D_i reduces the contraction of the jet near the source, figure 6.18(a). This reduction is because the magnitude to which the jet curves inwards decreases on increasing D_v/D_i (§6.3.3-6.3.4). Despite this decreasing inward curvature, increasing the ventilation ratio appears to shift the virtual origin upstream (compare the virtual origins of $D_v/D_i = \{0,\ 0.50\}$ and $D_v/D_i = \{0.75,\ 0.90\}$ on table 6.5 and figure 6.18). While this seems somewhat unintuitive it is attributed to the fact that the greater the restriction of the core, the closer to the source the jet achieves self-similarity (figure 6.15b). Figure 6.18(a) demonstrates that, over the range $0 \leq D_v/D_i \leq 0.75$, increasing the ventilation ratio reduces the spreading rate c_1 by approximately 20%. This reduction in the spreading rate suggests that increasing the ventilation ratio decreases the magnitude of the meandering motion. Further evidence for the decrease in the meandering motion is obtained on comparing flow visualisations of an almost fully open-core jet ($D_v/D_i = 0.90$, figure 1.2), in which no meandering is observed, with the closed-core jet ($D_v/D_i = 0$, figure 6.6), in which a significant meandering motion is present. Between $D_v/D_i = 0.75$ and $D_v/D_i = 0.90$ the spreading rate does not vary, suggesting that no meandering motion is occurring for $D_v/D_i \gtrsim 0.75$.

Upon changing the ventilation ratio D_v/D_i, figure 6.18(b), and prior to accounting for the momentum integral deficit, the decay of the velocity varies significantly. This significant variation is observed in the decay constant c_2, which varies by 50% as the ventilation ratio is increased from $D_v/D_i = 0$ to $D_v/D_i = 0.90$, see table 6.5. Even after accounting for the momentum integral deficit, c_2* in table 6.5, the decay constant c_2 varies by 20%. This is further evidence linking the meandering behaviour of the jet with D_v/D_i; as the meandering motion increases, the time average of the axial velocity along the nozzle axis $\bar{u}(x, y = 0)$ reduces and the perceived decay is larger. Near the source ($x/\sqrt{A_0} < 15$) the velocity along the longitudinal

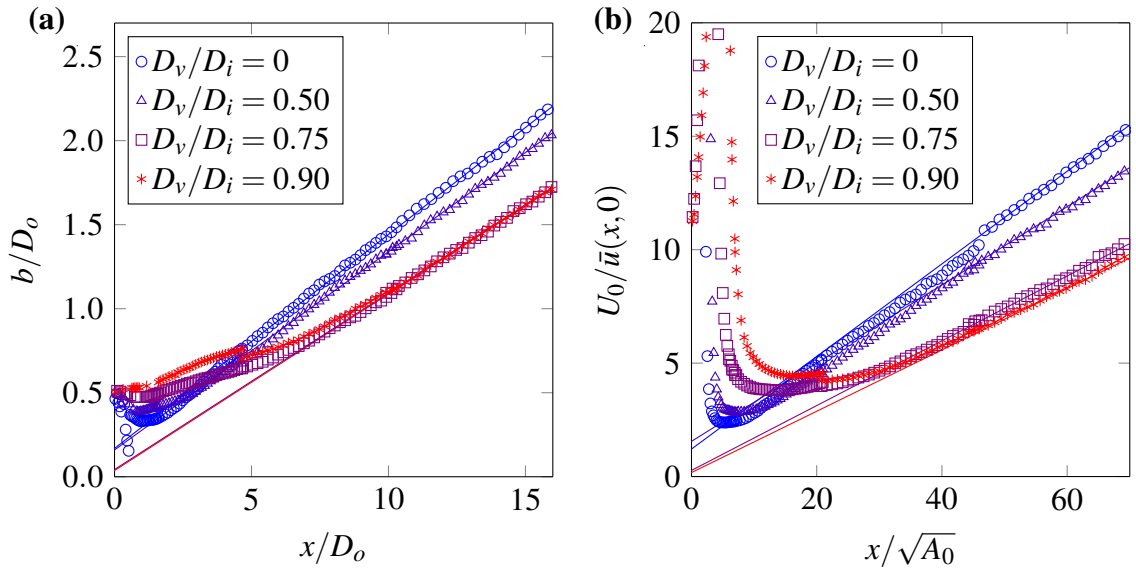

Fig. 6.18: Varying the ventilation ratio. Variation with distance downstream of (a) the jet width and (b) the inverse axial velocity along the longitudinal nozzle axis for the jet issuing from sources **N4R5V1-4**. The best fit lines are given by (6.7a) and (6.7b) with the constants given in table 6.5. On (a) and (b) the error is smaller than the size of the symbols.

nozzle axis is greater in the unventilated annular jet, despite the momentum integral deficit. The larger magnitude of this near-source velocity $\bar{u}(x,0)$ is attributed to the jet coalescing nearer the source as the ventilation ratio is reduced (§6.3.4). In other words the increase in the near-source axial velocity is symptomatic of the fact that the high-velocity centreline is coincident with the longitudinal nozzle axis nearer the source at lower ventilation ratios.

We note that the spreading rate c_1 of source **N4R5V4** (table 6.4) differs from sources **N3R3V4** and **N5R3V4** (table 6.5) by approximately 10%. In addition, even after corrections for the momentum integral deficit, the decay constant c_2 of source **N4R5V4** (table 6.4) differs from sources **N3R3V4** and **N5R3V4** varies by approximately 7%. This difference in the decay constant is larger than the 3.2% uncertainty (approx.) in $\bar{u}(x,0)/U_0$ (see table 3.9 and §3.5.4). The differences between these nominally quite similar sources is possibly due to the effect of the Reynolds number on the vortex shedding behaviour and subsequently on the meandering motion of the jet.

Entrainment

The effect of modifying the ventilation of the core naturally extends to the jet volume flux $Q(x)$, calculated using (4.3) and shown on figure 6.19. Figure 6.19(a), which presents the

	D_v/D_i	c_1	x_{01}/D_o	c_2	c_2*	$x_{02}/\sqrt{A_0}$	$x_{02}*/\sqrt{A_0}$	α
N4R5V1	0.90	0.105	-0.35	7.4	7.4	-1.3	-1.3	0.0525
N4R5V2	0.75	0.105	-0.41	7.0	7.2	-1.9	-1.8	0.0525
N4R5V3	0.50	0.118	-1.35	5.8	6.2	-9.0	-7.8	0.0590
N4R5V4	0	0.127	-1.32	4.9	6.1	-5.9	-4.8	0.0635

Table 6.5: Constants extracted from the PIV measurements of the jets issuing from sources **N4R5V1-4** (i.e. $D_i/D_o = 0.968$) by fitting (6.7a) and (6.7b) over the range $9 \leq x/D_o \leq 15$. Starred values are those corrected for the momentum flux deficit. Entries in the final column, the entrainment constant α, were calculated using (5.32).

variation of the non-dimensional volume flux with downstream distance for the closed-core jets, shows, as expected, that the volume flux of the jets increases on travelling downstream. The total volume flux entrained by the jet with $D_i/D_o = 0.947$ exceeds that entrained by the jet with $D_i/D_o = 0.981$. This difference is explained on considering that a greater proportion of the source momentum integral is conserved (see figure 6.9a) in the jet issuing from the source with $D_i/D_o = 0.947$, and thus the jet is able to entrain more fluid. The discontinuities in the data correspond with the edge of the measurement windows. These discontinuities and the non-linear behaviour at the downstream end of the measurement windows indicate that the width of these windows is too small to directly extract quantitative information of the closed-core jet volume flux. Nonetheless, we can quantitative compare the volume flux of the jets by means of the entrainment coefficient, which was estimated from the spreading rate c_1 using (5.32). Equation (5.32) is valid for this comparison because, despite the momentum integral deficit, the terms which relate to the momentum flux cancel. Comparing values of α for closed-core sources **N3R3V4** and **N5R3V4**, final column of table 6.4, reveals that the entrainment constant of the jet issuing from the source with $D_i/D_o = 0.981$ ($\alpha = 0.0715$) is approximately 3% larger than that from the source with $D_i/D_o = 0.947$ ($\alpha = 0.0695$). This is consistent with the approximately 2% lower decay constant c_2* in the jet issuing from the source with $D_i/D_o = 0.981$. The relatively similar values of α and the significant difference in the momentum integral deficit results in more fluid being entrained in the jet with $D_i/D_o = 0.947$.

Figure 6.19(b), which presents the variation of the volume flux with distance downstream for jets issuing from sources with a range of ventilation ratios, also shows that the volume flux of the jets increases on travelling downstream. Near the source ($x/\sqrt{A_0} \lesssim 15$), the signature of the volume flux induced through the open core is clearly seen, where increases in D_v/D_i result in increases in the near-field dilution of the jet (cf. figure 6.13). Despite the jumps in the data due to insufficient window width, far from the source the volume fluxes of all four

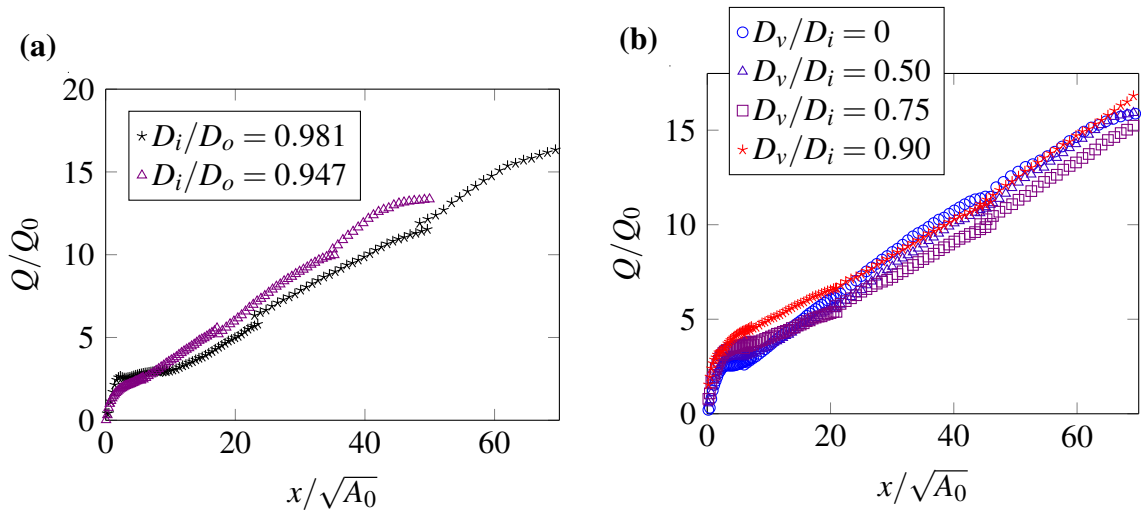

Fig. 6.19: Variation of volume flux Q with distance downstream. (a) The effect of varying the diameter ratio (with $D_v/D_i = 0$) for **N3R3V4** and **N5R3V4**, and (b) the effect of varying the ventilation ratio (with $D_i/D_o = 0.968$) for **N4R5V1-4**.

jets are within 10% of one another, and it is difficult to distinguish systematic differences as the ventilation ratio varies. Given that $Q \propto (M_0 - M_D)^{1/2}x$ (Fischer et al., 1979), the similar volume fluxes and dissimilar momentum integral deficits (with varying D_v/D_i) point towards a significant difference in the entrainment coefficient α. Values of α for sources **N4R5V1-4** are given in the final column of table 6.5 and vary by approximately 20%. These values increase from $\alpha = 0.525$ at $D_v/D_i = 0.90$ to $\alpha = 0.0635$ at $D_v/D_i = 0$. This increase is attributed to the meandering behaviour of the jet, and warrants further investigation in the future. The meandering behaviour results in large-scale motions, and these large-scale motions result in more fluid being engulfed and subsequently entrained. Thus, despite the significant reduction in the conserved momentum integral between $D_v/D_i = 0.90$ and $D_v/D_i = 0$, the increased meandering and therefore the increased entrainment result in similar volume fluxes.

6.4 Conclusions

Herein we have reported on jets issuing from slender annular sources for a range of ventilation ratios, ranging from the closed core ($D_v/D_i = 0$) to the almost fully open core ($D_v/D_i = 0.90$). Far from the source, as anticipated, the jet behaved as an axisymmetric jet. In this region the ventilation ratio influenced the decay of axial velocity, the spreading rate, and the entrainment of the jet. The mechanism for this influence is expected to be through the large-scale structures shed from the bounded near-source region when the ventilation of the core was restricted.

The time-averaged streamlines patterns indicated the manner by which the ventilation ratio controlled the bounded near-source region. These streamline patterns indicated that this region, which resides adjacent to the core, consists of either an induced flow, a recirculation, or some combination of the two. For the open-core jet this region is dominated by the induced flow, and as the ventilation ratio is decreased, the recirculation region grows in size. At the closed-core limit there can be no bounded induced flow. Remarkably, empirical fits indicated that the unphysical, idealised, fully open-core jet (i.e. $D_v/D_i = 1$) with $D_i/D_o = 0.968$ would be able to induce a flow through the core with a volume flux that was approximately 150% of the source flux $Q_a/Q_0 \approx 1.5$. This induced volume flux is approximately 20% larger than the induced volume flux observed in the almost fully open-core sources which had $D_v/D_i = 0.90$. The velocity of the fluid induced through the core did not vary significantly with the ventilation ratio, and was approximately one tenth of the source velocity (i.e. $U_a/U_0 \approx 0.1$) for the jet with $D_i/D_o = 0.968$. This work therefore demonstrated that the restriction of the core was key parameter in controlling the amount of fluid induced through the core, and therefore, the near-field dilution of the jet.

Notably, restricting the ventilation of the nozzle reduced the strength of the jet, as evidenced by estimates of the momentum integral. The restriction of the core resulted in a momentum integral deficit due to a force which acted on the nozzle, and this force was a result of different pressures on upstream and downstream faces of the nozzle. This deficit, which was measured to be as large as 40% of the total source momentum integral for the slender jets of interest, was successfully modelled as a drag force.

The results presented herein indicate that restricting the ventilation of the annulus is a viable method by which to control the flow issuing from a slender annular jet. For example, restricting the ventilation (i.e. reducing D_v/D_i) will produce a jet with a greater spreading rate with the penalty of a reduced momentum integral due to a 'drag force' acting on the nozzle. The momentum integral deficit can be reduced by reducing the slenderness of the source. A greater spreading rate could allow applications of the jet to target a larger area, for example, allowing a personalised cooling device to simultaneously cool more users.

CHAPTER 7

Conclusions and outlook

This thesis has investigated the fluid mechanics of the turbulent jet which issues from a slender annular slot that circumnavigates an open core. The jet of interest issues from the slot into an unbounded and otherwise quiescent environment at a low speed, allowing us to regard the flow as incompressible. This jet coalesces upon travelling downstream and induces a flow through the open core – in other words the core is 'ventilated' by the induced flow. Our investigations sought to characterise the primary flow features and identify the key scalings. The primary flow features refer to those which characterise the bulk time-averaged behaviour of the jets and so include the length over which the jet coalesces, the volume flux induced through the core and the streamwise development of the jet width and centreline velocity. Naturally, upon gaining an understanding of the jet behaviour, the investigations subsequently examined the influence of the source geometry on the jet. Since it was established at the outset of this work that there was an absence of literature regarding the slender open-core annular jet, the decision was made to investigate the problem experimentally so as to gain a physical understanding of the flow.

The sources of interest are uniquely characterised by the source momentum flux M_0, the ratio of the inner D_i and outer D_o diameters of the slot (i.e. the diameter ratio D_i/D_o), and the ratio of the ventilated opening D_v and inner diameter of the slot (i.e. the ventilation ratio D_v/D_i). A source for which $D_i/D_o = 1$ and $D_v/D_i = 1$ is considered to be the idealised slender fully open-core source. Since the idealised slender fully open-core annular source is physically unobtainable, we began by considering the flow issuing from a nozzle which was as close to this limiting case as was feasibly possible. This nozzle was fabricated using 3D printing techniques and had a diameter of approximately 100 mm. Thus, within the experimental chamber, which had horizontal dimensions of 4 m $\times$ 5 m, we were able to explore the development of the jet in both the near and far fields, i.e. from the source to approximately $16D_o$ downstream.

Images obtained from flow visualisation in air, an example of which is shown in figure 7.1, revealed that the near-idealised open-core jet was comprised of distinct regions. Subsequent

measurements of the air jet were made using particle image velocimetry, which allowed the acquisition of high-quality and unobtrusive measurements of the instantaneous velocities. The pattern of the time-averaged streamlines indicated that fluid was induced through the open core before being entrained into the inner shear layer of the jet, this region of induced flow is clearly visible on figure 7.1 as the (dark) ambient region bounded by the jet and nozzle. The downstream extent of this bounded induced-flow region was distinguishable by a small-scale recirculation, which occurred as a result of self-interaction and self-entrainment between opposite sides of the inner shear layer. Further delineation of the jet itself, into three distinct regions, was achieved from the streamwise development of the time-averaged axial velocities. These regions (figure 7.1) are a near-nozzle planar-jet region, a transitional region and far downstream round-jet region. The delineation allowed the identification of the characteristic length scales applicable to the different regions of the flow. As a result, a greater physical understanding was achieved, and the initially daunting leap into theoretically modelling the flow became a natural step.

Thus, the delineation naturally led to the development of a theoretical model for the aspects of the flow that were unique to the slender open-core annular jet, namely the volume flux induced through the open core, and the distances which characterised the bounded induced-flow region and coalescing behaviour of the jet. This model enabled the influence of the diameter ratio D_i/D_o on the flow to be established. Comparison between the predictions and experimental results revealed that the model successfully captured the length of the bounded induced-flow region and the volume flux induced through the core, demonstrating that as the slenderness of the source was increased so does the near-field dilution of the jet. Far from the source, however, the effects of D_i/D_o were much less pronounced.

The influence of the ventilation ratio D_v/D_i was subsequently explored experimentally. The single pre-existing study on jets issuing from annuli with partially restricted cores, namely that of Warda et al. (1999), was not sufficient to characterise or identify the influence of D_v/D_i. The exploration presented herein, for ventilation ratios in the range $0 \leq D_v/D_i \leq 0.9$, indicated the manner by which the flow behaviour gradually changed to produce markedly different flows at the closed- and open- core limits ($D_v/D_i = 0$ and $D_v/D_i = 1$, respectively). As the restriction on the central opening was increased, the volume flux induced through the core reduced, the jet coalesced closer to the source, and the recirculation located at the downstream end of the bounded induced-flow region grew in size. When the restriction of the core was sufficiently large, vortices shed from the recirculation region significantly influenced the jet downstream[1].

[1] Summaries of key results are provided in the Conclusion sections at the end of each chapter.

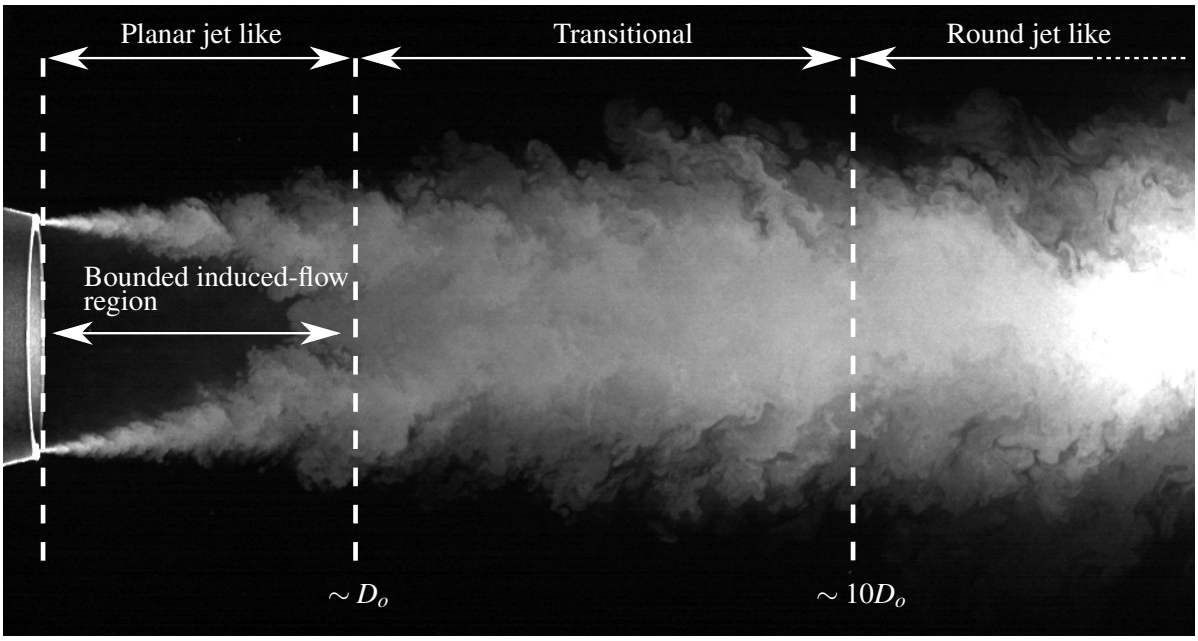

Fig. 7.1: Flow visualisation of a ventilated annular air jet from an open-core slender annular source ($D_i/D_o = 0.981$, $D_v/D_i = 0.90$ and $Re_l \approx 1800$). The jet is partitioned (not to scale) into the distinct regions of flow identified. For this source, the outer diameter of the slot D_o is approximately 100 mm.

Somewhat surprisingly, the existing literature almost exclusively focussed on closed-core jets ($D_v/D_i = 0$), and overlooked the rich behaviours that occur in jets issuing from sources with open cores. This is possibly, in part, due to the difficulty in manufacturing an open-core source, when compared to a closed-core source. To produce closed-core annular jets, the majority of authors have essentially placed a circular blockage in the centre of an existing circular nozzle. The development of a good quality open-core source, as required for the experiments herein, was complex and was facilitated by the ability to 3D print, a relatively novel manufacturing technique which may not have been available to many previous researchers. As with all techniques, 3D printing has its own unique set of limitations, one of which was restricting the choice of fluid medium due to the tendency of the plastics used to absorb water. Nonetheless, the ability to 3D print, on which much progress has been made of late, will no doubt allow experimentalists to examine geometries which were not feasible or cost effective to manufacture using traditional techniques (e.g. highly irregular nozzle geometries).

Despite its simplified foundations, for slender sources, the theoretical model proved to be remarkably good at predicting the velocity of the fluid induced through the open core U_a and the streamwise extent of the bounded induced-flow region x_m, and provided key insights into

the physics of the flow. One such insight is that for a fixed mean diameter ($D_c = (D_i + D_o/2)$) and source volume flux, increasing the diameter ratio leads to an increase the source velocity U_0 and thus and increase in the jet centreline velocity u_c, entrainment velocity v_e and the induced flow velocity U_a. The remarkably good predictions of U_a and x_m, particularly in comparison to the near idealised slender source with $D_i/D_o = 0.981$ where the difference is less than 2% and 10% respectively, indicates that the choice of assumptions which we used to simplify the problem were appropriate. Conversely, where the assumptions are less applicable, e.g. for sources which are less slender, the accuracy of the predictions reduces.

A particularly notable result, obtained from experimental measurements, was that restricting the ventilation of the core reduced the strength of the jet due to the pressure difference acting on the nozzle, as observed from estimates of the momentum integral deficit. To our knowledge, the existing literature entirely ignored the deficit, in part due to the focus on non-slender jets where this deficit is negligible. Although modelling this deficit as a drag force made its existence clear, our first observations of the deficit were surprising. The lack of mention in the existing literature probably stems from researchers (including ourselves) naturally approaching the closed-core annular jet from a jet perspective rather than a bluff body perspective.

The near-source region bounded by the jet itself was given significant attention herein as it contained arguably the most interesting flow behaviour, in which the influence of the source geometry was most apparent. This region, which may comprise of an induced-flow region, or a large-scale recirculation region, or indeed some combination of the two, is unique to this class of sources. While similar behaviour has been observed in coaxial jets, where the flow through the centre is prescribed, in annular jets the flow through the core is entirely a function of the two geometrical ratios D_i/D_o and D_v/D_i. The diameter ratio D_i/D_o controls the entrainment appetite of the jet, while the ventilation ratio D_v/D_i controls the degree to which the induced flow can meet the entrainment appetite of the jet.

Further downstream, in the region where the flow is fully developed, as was anticipated, the jet behaved almost identically to a jet issuing from a circular source. This similarity was unsurprising as both flows are axisymmetric in a time-averaged sense and share the same governing equations. As suspected, the influence of the source geometry was primarily observed in the constants which denote the spreading rate c_1, velocity decay c_2 and the virtual origin x_0 (the virtual origin being the location of a hypothetical point source of momentum flux used to represent the origins of the jet). The almost fully slender open-core ($D_v/D_i = 0.90$) annular jet examined had not reached complete self-similarity within our measurement domain and, therefore, it is not clear whether the values of c_1 and c_2 will asymptote towards the range of values typically observed for round jets. To determine this, measurements further downstream are required. However, the greater the restriction of the core, the closer to the source that

approximate self-similarity is achieved. As such, our measurements of centreline velocity and jet width in slender closed-core annular jets are well within the fully developed region, and differ considerably (by up to 30%) to those observed in round jets. These closed-core jets spread and decay faster than their round-jet counterparts, and the influence of the source is advected downstream by the large-scale structures which originate in the vortex shedding behaviour.

While not a focus of the current work, the slender open-core annular jet has many unique properties which could be used in applications. For example, the flow that is induced through the centre of the slender open-core nozzle makes it potentially useful for applications which require rapid near-field dilution of contaminants or heat. Indeed, one of the existing applications, a hair dryer, makes use of the near-field dilution to both increase the volume flux and reduce the temperature of the flow.

As an outlook, this work provides a foundation from which future investigators can base their investigations into other aspects of the slender open-core annular jet. We recommend that future researchers extend the theoretical model to account for the ventilation ratio D_v/D_i. This would allow the predictions to span a larger parameter space, and likely provide further physical insights into the effect of the ventilation ratio on the coalescing behaviour of the jet. A sensible first step in modelling the effect of the ventilation ratio would be the development of model for the closed-core annular jet. Such a model, if developed using the same framework (i.e. using continuity and conservation of momentum flux), could potentially be combined with the existing model for the fully open-core jet to take into account the influence of the ventilation ratio. Furthermore, improvements to the model can be made on reducing the number of assumptions made. Two examples immediately spring to mind, the first involves including the region of transitional behaviour, and the second involves modelling the region in which the planar-jet-like flow is established. Including the region in which the jet transitions from planar-jet-like to round-jet-like behaviour is likely to lead to better predictions of the location at which the jet coalesces. Modelling the region in which the planar-jet-like flow is established has the potential to extend the range for which the model is valid and increase the accuracy of the model at lower diameter ratios.

References

Ball, C., Fellouah, H. & Pollard, A. (2012). The flow field in turbulent round free jets. *Progress in Aerospace Sciences*, 50:1–26.

Batchelor, G. K. (1967). *An introduction to fluid dynamics*. Cambridge University Press, Cambridge, UK.

Boersma, B. J., Brethouwer, G. & Nieuwstadt, F. T. M. (1998). A numerical investigation on the effect of the inflow conditions on the self-similar region of a round jet. *Physics of Fluids*, 10(4):899–909.

Carazzo, G., Kaminski, E. & Tait, S. (2006). The route to self-similarity in turbulent jets and plumes. *Journal of Fluid Mechanics*, 547:137–148.

Carazzo, G., Kaminski, E. & Tait, S. (2008). On the dynamics of volcanic columns : a comparison of field data with a new model of negatively buoyant jets. *Journal of Volcanology and Geothermal Research*, 178:94–103.

Celik, N. & Bayazit, Y. (2011). Investigation of annular free jet flows with various diameter ratios. In *AIChE Annual Meeting*, pages 109–116, Minneapolis. American Institution of Chemical Engineers.

Chan, W. T. & Ko, N. W. M. (1978). Coherent structures in the outer mixing region of annular jets. *Journal of Fluid Mechanics*, 89(3):515–533.

Chigier, N. A. & Beer, J. M. (1964a). The flow region near the nozzle in double concentric jets. *Journal of Basic Engineering*, 86(4):797–804.

Chigier, N. A. & Beer, J. M. (1964b). Velocity and static-pressure distributions in swirling air jets issuing from annular and divergent nozzles. *Journal of Basic Engineering*, 86(4):788–796.

Craven, B. A. & Settles, G. S. (2006). A computational and experimental investigation of the human thermal plume. *Journal of Fluids Engineering*, 128(6):1251–1258.

Danlos, A., Lalizel, G. & Patte-Rouland, B. (2013). Experimental characterization of the initial zone of an annular jet with a very large diameter ratio. *Experiments in Fluids*, 54:1418.

Davidson, P. A. (2004). *Turbulence - an introduction for scientists and engineers*. Oxford University Press, Oxford, UK.

Del Taglia, C. (2002). *Flow behind a disk stabalized burner with large blockage*. PhD thesis, Swiss Federal Institute of Technology Zurich.

Del Taglia, C., Blum, L., Gass, J., Ventikos, Y. & Poulikakos, D. (2004). Numerical and experimental investigation of an annular jet flow with large blockage. *Journal of Fluids Engineering*, 126(3):375–384.

Del Taglia, C., Moser, A. & Blum, L. (2009). Spontaneous break of symmetry in unconfined laminar annular jets. *Journal of Fluids Engineering*, 131(8):081202.

Dimotakis, P. E. (2000). The mixing transition in turbulent flows. *Journal of Fluid Mechanics*, 409:69–98.

Dimotakis, P. E., Miake-Lye, R. C. & Papantoniou, D. A. (1983). Structure and dynamics of round turbulent jets. *Physics of Fluids*, 26(11):3185–3192.

Dosio, A., de Arellano, J. V.-G. & Holtslag, A. A. M. (2005). Relating Eulerian and Lagrangian statistics for the turbulent dispersion in the atmospheric convective boundary layer. *Journal of the Atmospheric Sciences*, 62(4):1175–1191.

Ezzamel, A., Salizzoni, P. & Hunt, G. R. (2015). Dynamical variability of axisymmetric buoyant plumes. *Journal of Fluid Mechanics*, 765:576–611.

Fei, R. & Merzkirch, W. (2004). Investigations of the measurement accuracy of stereo particle image velocimetry. *Experiments in Fluids*, 37(4):559–565.

Ferdman, E., Otugen, M. V. & Kim, S. (2000). Effect of initial velocity profile on the development of round jets. *Journal of Propulsion and Power*, 16(4):676–687.

Fischer, H. B., List, E. J., Koh, R. C. Y., Imberger, J. & Brooks, N. H. (1979). *Mixing in inland and coastal waters*. Academic Press, New York, 1st edition.

Gates, M. F. & Cochran, C. L. (1961). Summary report - phase II program annular nozzle ejector - contract NONR 2840(00). Technical report, Hiller Aircraft Corporation, Palo Alto, California.

George, W. K. (1989). The self-preservation of turbulent flows and its relation to initial conditions and coherent structures. In George, W. K. & Arndt, R. E. A., editors, *Advances in Turbulence*, pages 39–72. Hemisphere, New York.

Haynes, W. M., editor (2012). *CRC handbook of chemistry and physics*. CRC Press, Boca Raton, 93rd edition.

Heiser, W. H. (2010). Ejector thrust augmentation. *Journal of Propulsion and Power*, 26(6):1325–1330.

Hunt, G. R. & Burridge, H. C. (2015). Fountains in industry and nature. *Annual Review of Fluid Mechanics*, 47(1):195–220.

Hussein, H. J., Capp, S. P. & George, W. K. (1994). Velocity measurements in a high-Reynolds-number, momentum-conserving, axisymmetric, turbulent jet. *Journal of Fluid Mechanics*, 258:31–75.

Idelchik, I. E. (1966). *Handbook of hydraulic resistance*. Jaico Publishing House, India.

Jukes, T., Lirvat, J., Nicolas, F., Padhani, S. & Hunt, G. R. (2015). Flow control using annular jets. In *European Drag Reduction and Flow Contol Meeting*, pages 1–2, Cambridge, UK.

Ko, N. W. M. (1980a). Annular jets of large inner diameter. *Journal of Sound and Vibration*, 69(4):616–621.

Ko, N. W. M. (1980b). Annular jets of small inner diameter. *Journal of Sound and Vibration*, 68(3):468–472.

Ko, N. W. M. & Chan, W. T. (1978). Similarity in the initial region of annular jets: three configurations. *Journal of Fluid Mechanics*, 84(4):641–656.

Ko, N. W. M. & Chan, W. T. (1979). The inner regions of annular jets. *Journal of Fluid Mechanics*, 93(3):549–584.

Ko, N. W. M., Lau, K. K. & Lam, K. M. (1998). Dynamics of interaction modes in excited annular jets. *Experimental Thermal and Fluid Science*, 17:319–338.

Kotsovinos, N. E. (1976). A note on the spreading rate and virtual origin of a plane turbulent jet. *Journal of Fluid Mechanics*, 77:305–311.

Krothapalli, A., Baganoff, D. & Karamcheti, K. (1981). On the mixing of a rectangular jet. *Journal of Fluid Mechanics*, 107:201–220.

Kuethe, A. M. (1933). *Investigations of turbulent mixing regions*. PhD thesis, California Institute of Technology.

Kuhlman, J. M. (1987). Variation of entrainment in annular jets. *AIAA Journal*, 25(3):373–379.

Lam, K. M. & Ko, N. W. M. (1986). Investigation of flow structures of a basic annular jet. *AIAA Journal*, 24(9):1488–1493.

Lam, K. M., Ko, N. W. M. & Lau, K. K. (1986). Wake and wake-induced shear-layer excitation in an annular jet. *Physics of Fluids*, 29(10):3121–3134.

LaVision (2014). *Product manual for DaVis 8.2*. LaVision GmbH, Item No. 1105011-4, Gottingen, Germany.

Lazar, E., Deblauw, B., Glumac, N., Dutton, C. & Elliott, G. (2010). A practical approach to PIV uncertainty analysis. In *27th AIAA Aerodynamic Measurement Technology and Ground Testing Conference*, Chicago, Illinois.

Li, K. & Tankin, R. S. (1987). A study of cold and combusting flow around bluff-body combustors. *Combustion Science and Technology*, 52(4-6):173–206.

List, E. J. (1982). Turbulent jets and plumes. *Annual Review of Fluid Mechanics*, 14:189–212.

Litron Lasers Ltd (2010). Lasers for PIV applications.

Lund, T. S. (1964). Augmented thrust and mass flow associated with two-dimensional jet reattachment. *AIAA Journal*, 24(12):1964–1970.

Marsters, G. F. (1977). Interaction of two plane, parallel jets. *AIAA Journal*, 15(12):1756–1762.

Mason, R., Nicolas, F. & Pitt, R. (2010). Bladeless is more. *ANSYS Advantage*, 6(2):5–7.

McKeon, B. J., Swanson, C. J., Zagarola, M. V., Donnelly, R. J. & Smits, A. J. (2004). Friction factors for smooth pipe flow. *Journal of Fluid Mechanics*, 511:41–44.

Mi, J., Nobes, D. S. & Nathan, G. J. (2001). Influence of jet exit conditions on the passive scalar field of an axisymmetric free jet. *Journal of Fluid Mechanics*, 432(2001):91–125.

Morton, B. R., Taylor, G. & Turner, J. S. (1956). Turbulent gravitational convection from maintained and instantaneous sources. *Proceedings of the Royal Society A: Mathematical, Physical and Engineering Sciences*, 234(1196):1–23.

Papanicolaou, P. N. & List, E. J. (1988). Investigations of round vertical turbulent buoyant jets. *Journal of Fluid Mechanics*, 195:341–391.

Patte-Rouland, B., Lalizel, G., Moreau, J. & Rouland, E. (2001). Flow analysis of an annular jet by particle image velocimetry and proper orthogonal decomposition. *Measurement Science and Technology*, 12:1404–1412.

Perry, A. E., Chong, M. S. & Lim, T. T. (1982). The vortex-shedding process behind two-dimensional bluff bodies. *Journal of Fluid Mechanics*, 116:77–90.

Philip, J. & Marusic, I. (2012). Large-scale eddies and their role in entrainment in turbulent jets and wakes. *Physics of Fluids*, 24:055108.

Priestley, C. H. B. & Ball, F. K. (1955). Continuous convection from an isolated source of heat. *Quarterly Journal of the Royal Meteorological Society*, 81(348):144–157.

Quinn, W. (2006). Upstream nozzle shaping effects on near field flow in round turbulent free jets. *European Journal of Mechanics - B/Fluids*, 25(3):279–301.

Raffel, M., Willert, C. E., Wereley, S. T. & Kompenhans, J. (2007). *Particle image velocimetry: a practical guide*. Springer, Berlin, 2nd edition.

Rehab, H., Villermaux, E. & Hopfinger, E. J. (1997). Flow regimes of large-velocity-ratio coaxial jets. *Journal of Fluid Mechanics*, 345:357–381.

Richards, C. & Pitts, W. (1993). Global density effects on the self-preservation behaviour of turbulent free jets. *Journal of Fluid Mechanics*, 254:417–435.

Ricou, F. P. & Spalding, D. B. (1961). Measurements of entrainment by axisymmetrical turbulent jets. *Journal of Fluid Mechanics*, 11(01):21–32.

Roos, F. W. & Willmarth, W. W. (1971). Some experimental results on sphere and disk drag. *AIAA journal*, 9(2):285–291.

Sawyer, R. A. (1960). The flow due to a two-dimensional jet issuing parallel to a flat plate. *Journal of Fluid Mechanics*, 9(4):543–559.

Schlichting, H. (1968). *Boundary-layer theory*. McGraw-Hill, New York.

Sciacchitano, A. & Wieneke, B. (2016). PIV uncertainty propagation. *Measurement Science and Technology*, 27:084006.

Song, H. B., Yoon, S. H. & Lee, D. H. (2000). Flow and heat transfer characteristics of a two-dimensional oblique wall attaching offset jet. *International Journal of Heat and Mass Transfer*, 43:2395–2404.

Suresh, P. R., Srinivasan, K., Sundararajan, T. & Das, S. K. (2008). Reynolds number dependence of plane jet development in the transitional regime. *Physics of Fluids*, 20(4):044105.

Taylor, J. (1977). *An introduction to error analysis*. University Science Books, Mill Valley.

Tennekes, H. & Lumley, J. L. (1972). *A first course in turbulence*. MIT Press, Cambridge, Massachusetts.

Thomas, F. O. & Goldschmidt, V. W. (1986). Structural characteristics of a developing turbulent planar jet. *Journal of Fluid Mechanics*, 163:227–256.

Torrance, M. C., Natsui, G., Ricklick, M. A. & Kapat, J. S. (2011). Hot-wire study on the impact of porous structure on mean and turbulent velocity profiles in the near-field of a high aspect ratio porous filled slot jet. In *47th AIAA/ASME/SAE/ASEE Joint Propulsion Conference & Exhibit*, page 5914, San Diego, California.

Turner, J. S. (1969). Buoyant plumes and thermals. *Annual Review of Fluid Mechanics*, 1(1):29–44.

van Reeuwijk, M., Salizzoni, P., Hunt, G. R. & Craske, J. (2016). Turbulent transport and entrainment in jets and plumes: A dns study. *Phys. Rev. Fluids*, 1:074301.

Vanierschot, M. & Van den Bulck, E. (2008). Influence of swirl on the initial merging zone of a turbulent annular jet. *Physics of Fluids*, 20(10):105104.

Vanierschot, M., Van Dijck, K., Sas, P. & Van den Bulck, E. (2014). A study of the wake dynamics of annular jet flows with and without swirl. In *17th international symposium on applications of laser techniques to fluid mechanics*, Lisbon, Portugal.

Wang, H. & Law, A. W. (2002). Second-order integral model for a round turbulent buoyant jet. *Journal of Fluid Mechanics*, 459:397–428.

Warda, H. A., Kassab, S. Z., Elshorbagy, K. A. & Elsaadawy, E. A. (1999). An experimental investigation of the near-field region of free turbulent round central and annular jets. *Flow Measurement and Instrumentation*, 10(1):1–14.

Wygnanski, I. & Fiedler, H. (1969). Some measurements in the self preserving jet. *Journal of Fluid Mechanics*, 38(3):577–612.

APPENDIX A

Benchmarking PIV experiments

Preamble

This Appendix overviews the 'benchmarking' PIV experiments that were performed to ensure confidence in the measurements obtained herein; for further information, see Jukes et al. (2015). Unlike all other experiments within this thesis, these experiments were carried out by Dr. Timothy N. Jukes using the same equipment and facility with which we carried out the experiments within this thesis, and who kindly provided us with the data. The round-jet experiment of Hussein et al. (1994) and data therein was taken as the benchmark, and their experiment repeated as closely as possible using our PIV system. Our resulting round-jet data is compared with the ventilated annular jet in §4.3.

A.1 Round-jet experimental set-up

The round-jet nozzle used was almost identical to that of Hussein et al. (1994), with a diameter $D = 25.4$ mm, 121:1 contraction ratio and upstream flow conditioning consisting of a honeycomb and three mesh screens. The jet issued from the nozzle (supplied by a variac controlled centrifugal fan) with an approximately top-hat velocity profile and low initial turbulence, at a Reynolds number of $Re_D = U_0 D/\upsilon \approx 95000$. The experimental environment and procedure were identical to that described in §4.2, with 500 PIV velocity fields acquired in order to estimate the time-averaged quantities and turbulence statistics of interest.

A.2 Near field

Planar PIV results were compared to Pitot tube measurements immediately adjacent to ($x/D = 0$) and slightly downstream ($x/D = 0.6$) of the circular orifice. The PIV velocities agreed well with those from the Pitot measurements, with a difference of $\lesssim 2\%$ (≈ 1 m s^{-1}). This small difference in velocities could potentially be related to errors in the Pitot tube measurements, including errors in the pressure transducer, Pitot alignment, blockage effect and uncertainty in the air density - estimated from thermocouple measurements. From our PIV results we estimated a boundary-layer thickness of 0.85 mm, similar to the value of 0.7 mm measured by Hussein et al. (1994) using a hotwire.

Downstream of the nozzle, the approximately uniform exit profile of the jet was penetrated by the shear layers that form at the jet edges, with a potential core extending for 5-6D from the source, again in close agreement with Hussein et al. (1994). Beyond 5-6D, the flow was fully turbulent.

A.3 Far field

To further validate the PIV system, our far-field round-jet PIV measurements were compared with those of Hussein et al. (1994) and of Ricou & Spalding (1961). The centreline velocity $\bar{u}_c$ and spreading rate of the $\bar{u}_c/2$ velocity contour (i.e. jet half width $b_{0.5}$) were within $\pm 2\%$ and $\pm 2.5\%$, respectively, of the results reported by Hussein et al. (1994) who give $U_0/\bar{u}_c = (1/5.8)(x/D-4)$ and $b_{0.5}/D = 0.094(x/D-4)$.

Hussein et al. (1994) did not measure the volume flux and so comparisons were made with the measurements of Ricou & Spalding (1961). Estimates of volume flux obtained far from the nozzle (by integrating the velocity profiles around the streamwise axis) were compared with, and a good agreement (within -7% and $+2\%$) was found with, the values predicted by the fit of Ricou & Spalding (1961), namely, $Q/Q_0 = 0.32x/D$.

A full analysis of the time-averaged velocity profiles and second-order turbulence statistics was also carried out. Hussein et al. (1994) observed self-similarity of the time-averaged profiles at approximately 30D downstream of the nozzle, a result supported by our PIV measurements. While our turbulent intensity measurements are qualitatively similar to those of Hussein et al. (1994), the values are marginally lower ($\sim -5\%$). Several authors have noted that the turbulent intensities do not become self-similar until far from the nozzle. The measurements of Hussein et al. (1994) were taken further downstream ($x/D = 70$) than our planar PIV measurements ($x/D = 55$), which may explain the discrepancy with the turbulent intensities we measure. This

explanation is supported by the continuing evolution of the turbulent intensities within our round jet with downstream distance x.

In conclusion, our PIV results for the round jet match very well with the results of Hussein et al. (1994) and Ricou & Spalding (1961), indicating that the PIV system was performing well, giving us confidence in our measurements of the annular jet.

APPENDIX B

The effect of misalignment on measurements of momentum flux

Throughout the thesis, assuming the flow is axisymmetric (§3.2.2), we have sought to capture planar PIV measurements on a representative plane (the x-r plane). Every effort was made to align the laser and the flow (§2), as misalignment between the laser and the x-r plane would result in erroneous measurements. In this Appendix, the effect of misalignment on measurements of specific momentum flux is determined geometrically.

For this, we make use of the fact that the mean component of momentum flux M_m can be reconstructed (Hussein et al., 1994) from the spreading rate c_1 and velocity decay c_2 through

$$\frac{M_m}{M_0} = \frac{\pi}{2}(c_1 c_2)^2. \tag{B.1}$$

The jet considered for this analysis is an axisymmetric jet issuing from a point source which is assumed to be self-similar over its entire downstream extent. Thus the jet width and centreline velocity are described by

$$b = c_1 x \qquad \text{and} \qquad \bar{u}(x,0) = c_2 U_0 \left(\frac{x}{\sqrt{A_0}}\right)^{-1}. \tag{B.2a,b}$$

To quantify the effect of misalignment, we consider 'virtual' measurements of the jet along a virtual laser plane that is offset from the jet centreline by a perpendicular distance y_s and an angle η_s, see figure B.1. These offsets will modify the virtual spreading rate c_{1s} and velocity decay c_{2s}. For an axisymmetric jet, which has a circular cross section, the virtual spreading

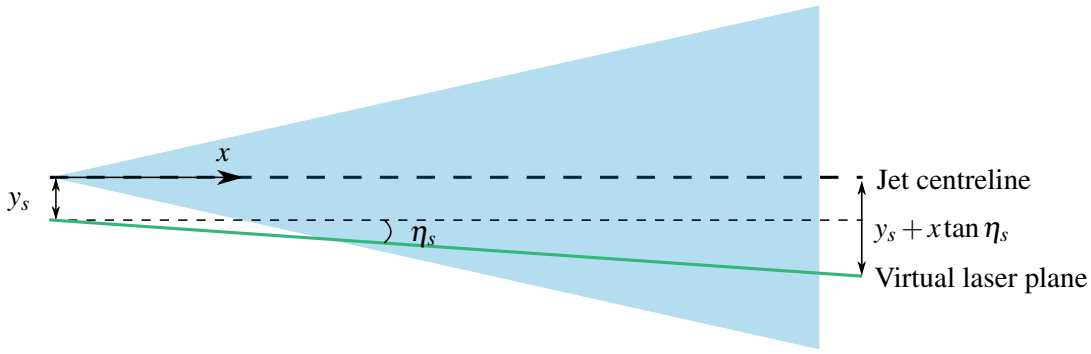

Fig. B.1: A schematic of the misalignment between the longitudinal axis of the round jet and the virtual laser plane, used to determine the influence of misalignment on measurements of momentum flux. The round jet, shaded in blue, issues from a point source and is assumed to be fully self-similar over its entire extent. The virtual laser plane, in green, extends into the page and is offset from the jet centreline by a distance y_s and angle η_s.

rate c_{1s} can be written in terms of the real spreading rate c_1 and offsets y_s and η_s,

$$c_{1s} = \frac{\sqrt{(c_1 x)^2 - (y_s + x\tan\eta_s)^2}}{x}. \tag{B.3}$$

Similarly, on assuming a Gaussian velocity profile and that the velocity along the laser plane is approximately equal to the velocity in the x direction (i.e. a small angle assumption), the virtual velocity decay c_{2s} can be written in terms of the real velocity decay c_2 and offsets y_s and η_s,

$$c_{2s} = c_2 e^{-((y_s + x\tan\eta_s)^2/(c_1 x)^2)}. \tag{B.4}$$

On entering values of c_{1s} and c_{2s} from (B.3) and (B.4) into (B.1) we can determine the effect of misalignment on measurements of momentum flux. Figure B.2 presents the variation of the mean momentum flux M_m/M_0 with distance downstream with a combination of different offsets. The real spreading rate $c_1 = 0.107$ and decay rate $c_2 = 7.0$ have been extracted from Fischer et al. (1979). In the case with no offset ($y_s = 0$ mm, $\eta_s = 0°$, '$\circ$') the virtual (and in this case, the real) mean momentum flux is conserved and makes up approximately 88% of the total momentum flux. While the momentum flux is conserved in the case where the measurement plane is offset by a small angle ($y_s = 0$ mm, $\eta_s = 2°$, '$\square$'), the virtual momentum flux is below the true value. Offsetting the measurement plane by a distance ($y_s = 30$ mm, $\eta_s = 0°$, '$\triangle$') results in the momentum flux asymptoting towards the true amount. Combining both distance and angle offsets ($y_s = 30$ mm, $\eta_s = 2°$, '$\diamond$' or $y_s = 30$ mm, $\eta_s = -2°$, '$*$') results in a combination of the two effects. Crucially, the effect of misalignment on measurements of

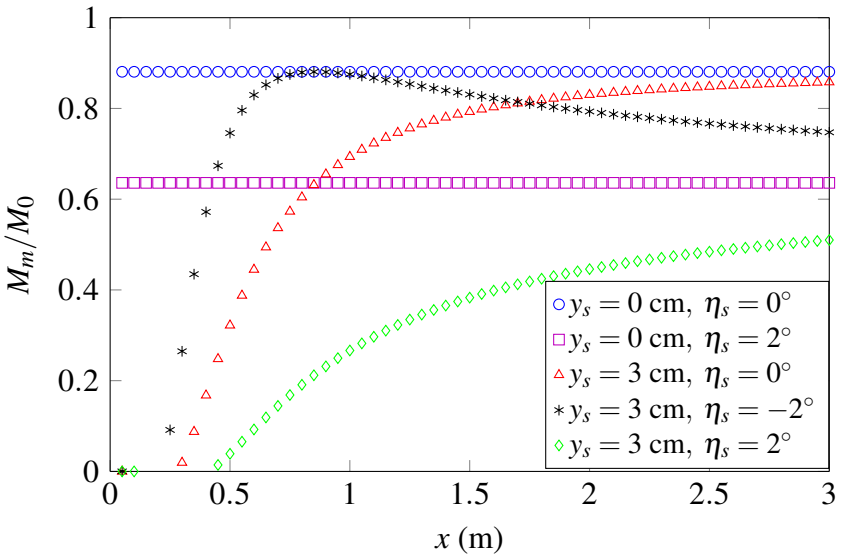

Fig. B.2: The variation of mean momentum flux M_m/M_0 with distance downstream x when the measurement plane is offset by distance y_s and angle η_s from the jet centreline. These values have been calculated from the geometrical model presented in Appendix B.

the momentum flux are clear. Given that the mean momentum flux makes up the majority of total momentum integral (cf. §4.3.1), if the momentum integral estimates, calculated from the planar PIV measurements described in §2, are conserved and equal to the source momentum integral ($M/M_0 \approx 1$), we can be confident that the laser and jet are aligned correctly.

APPENDIX C

Extensions to the theoretical model

Preamble

This Appendix seeks to provide the interested reader with further details of higher-order effects on the predictions made by theoretical model. Specifically, in this Appendix a selection of the assumptions used during the model development are relaxed and the resulting predictions are examined. The structure is as follows: in §C.1 we consider the effects of losses on inducing a flow through the annulus; in §C.2 we consider the effect of a region of flow development for the planar jet exiting the slot; and finally, in §C.3 we present the results of sensitivity analysis examining how the choice of constant influences the nozzle.

C.1 Losses

In the model development (§5.3), and subsequent predictions (§5.5), we regarded the losses associated with the flow induced through the open core of the annulus as negligible. To determine the effect of losses, we now include a pressure loss term P_L in (5.9). The pressure loss term P_L consists of a frictional P_F, contraction P_O and expansion component P_E, hence

$$P_L = P_F + P_O + P_E. \tag{C.1}$$

If we make the assumption that the surface surrounding the open core of the annular nozzle behaves as a pipe, the frictional loss can be quantified using the Darcy-Weisbach equation

$$P_F = f\frac{L}{D_i}\frac{\rho U_a^2}{2}, \tag{C.2}$$

where L is the depth of the nozzle and f is the Darcy-Weisbach friction factor. Since for our nozzle the value of $L/D_c = 0.7 \approx L/D_i$ is small (see figure 2.2), the frictional losses will be relatively small. Including the effects of contraction and expansion is more complex, although one could simply use a smaller effective diameter in place of D_o in (5.10). The effective diameter is introduced by means of a dimensionless discharge coefficient $0 \leq C_D \leq 1$ multiplied by the actual diameter D_o, where $C_D = 1$ would represent the case with no contraction or expansion losses. Equation (5.13) therefore becomes

$$\frac{M(x_C)}{M_0} = 1 + \hat{A}_a \hat{U}_a^2 + \left(\frac{\hat{U}_a^2 C_D (\hat{A}_a + 1)}{2} \right) \left(f \frac{L}{D_i} - 1 \right). \tag{C.3}$$

Equation (C.3) is then implemented into the analysis in §5.3. While the values of f and C_D are unknown, we can use reasonable values to qualitatively assess the effect of losses on the flow. Assuming the annulus is a smooth pipe with a Reynolds number of $Re = U_a D_i/\nu \approx 2 \times 10^4$, from McKeon et al. (2004) we obtain $f \approx 0.025$ and from Idelchik (1966) $C_D \approx 0.8$. On figure C.1 we compare the solution of the original model ($f = 0$ and $C_D = 0$) to the results obtained when $f = 0.025$ and $C_D = 0.8$. Including the losses has a very negligible influence on the vast majority of the quantities considered ($U_a/U_0, Q_a/Q_0, x_m/D_i$); this is shown for the normalised induced volume flux Q_a/Q_0 on figure C.1(a) where the two curves are indistinguishable from each other. Including the losses slightly alters the location of the reattachment point x_{re}/D_o, particularly for lower diameter ratios, as seen in figure C.1(b). Given the extremely small impact on the quantities of interest, for a first approximation we can reasonably assume that there are no losses.

C.2 Region of flow development

In the theoretical development (§5.3) we assumed that the jet behaves as a fully developed planar jet for $0 \leq x \leq x_{re}$. In practice, at the slot the jet has a physical width ($b_i(0) + b_o(0) = l$) and velocity profile which is not fully developed; a zone of flow establishment exists adjacent to the slot (Fischer et al., 1979). As, near the source, the jet displays evidence of planar-jet-like behaviour (PHJ17), we anticipate the streamwise extent of this zone of flow establishment to scale with the slot width l (Thomas & Goldschmidt, 1986). For $D_i/D_o \to 1$, where $l \ll D_i$, neglecting the zone of flow establishment is reasonable. However, as the diameter ratio D_i/D_o is reduced, the relative width of the slot l/D_i increases and thus the streamwise extent of the zone of flow establishment also increases. The conventional method by which to account for this zone of flow establishment is to offset the fully developed jet by a virtual origin correction x_{0p}, such that $\chi = x - x_{0p}$. Using the virtual origin correction (5.27) and (5.38) are modified so

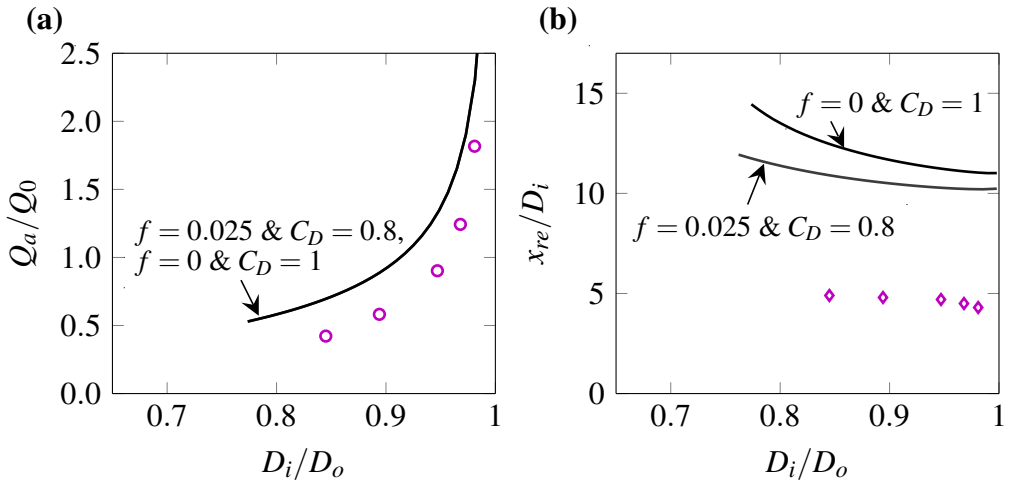

Fig. C.1: A comparison of the predictions with losses ($f = 0.025$ & $C_D = 0.8$) and without losses ($f = 0$ & $C_D = 1$). The variation with the diameter ratio D_i/D_o of (a) the normalised induced volume flux Q_a/Q_0 and (b) the normalised position of the reattachment point x_{re}/D_i. Theoretical prediction '—', measurements for sources **N1-5R3V1** '$\circ$' and '$\diamond$'.

that they, respectively, become

$$\int_{x_0}^{x_{re}} \frac{dQ_e}{dx} dx = 2\pi\alpha_p d_2 \left(\frac{U_0^2 A_0}{\pi D_c}\right)^{1/2} \int_{x_{0p}}^{x_{re}} b_o(\chi)\chi^{-1/2}\,\mathrm{d}x, \tag{C.4}$$

$$Q_a = \frac{\pi^{3/2} d_1 d_2}{2} \left(\frac{M_0}{\pi D_c}\right)^{1/2} \int_{x_{0p}}^{\beta x_{re}} b_i(\chi)\chi^{-1/2}\,\mathrm{d}x. \tag{C.5}$$

In addition, the virtual origin correction is used during the iteration procedure when estimating the width of the planar jet at $x = x_m$, i.e. $\delta = d_1(x_m - x_{0p})$.

Planar-jet literature contains a range of virtual origin corrections x_{0p}, with Kotsovinos (1976) reporting values in the range $-4.2 < x_{0p}/l < 6.5$. For the planar-jet-like region of a slender annular jet, the results of PHJ17 suggest a positive virtual origin correction. Implementing (C.4), (C.5) and the new expression for δ into the model developed in §5.3, with $x_{0p} = \{-4l, 0, 4l\}$, provides us with the plots in figure C.2. Figure C.2(a) demonstrates that the prediction of the induced volume flux Q_a/Q_0 is not notably influenced by the presence of a virtual origin correction. However, the influence of the virtual origin correction on the prediction of x_{re} is much more significant, see figure C.2(b). Both positive ($x_0 = 4l$) and negative ($x_0 = -4l$) virtual origin corrections result in the reattachment point moving upstream as the diameter ratio increases. This movement goes against the trend observed in the experimental data, and suggests that this may not be the most appropriate way to account for the region of flow

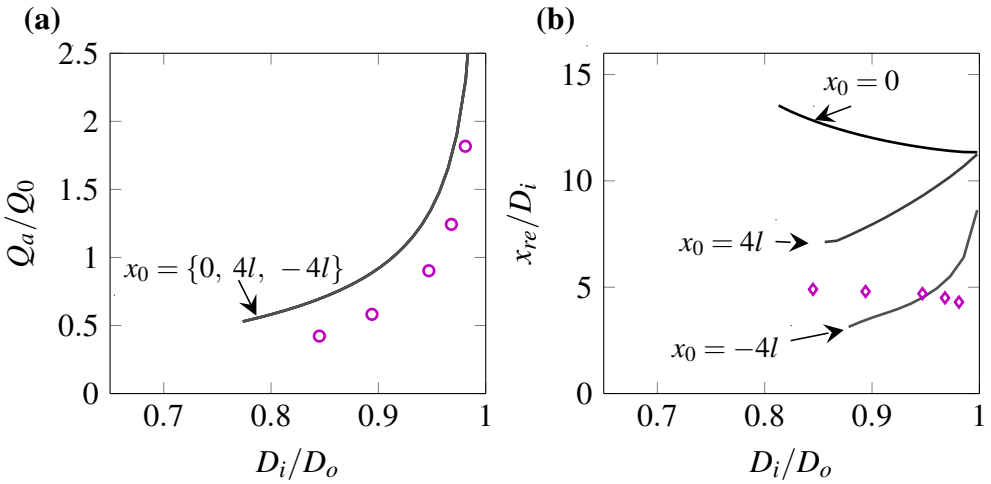

Fig. C.2: A comparison of the predictions with three different virtual origin corrections, $x_0 = \{-4l, 0, 4l\}$. The variation with the diameter ratio D_i/D_o of (a) the normalised induced volume flux Q_a/Q_0 and (b) the normalised position of the reattachment point x_{re}/D_i.

development. Therefore, we exclude the planar virtual origin correction from the model in §5.3.

C.3 Sensitivity

The predictions presented in §5.5 were obtained using round- and planar- jet constants (c_1, c_2, x_0, d_1, and d_2) extracted from §4 and Fischer et al. (1979), see table 5.2. However, there is significant variation in the values of these constants within the literature. Naturally, we would expect the values chosen for these constants to impact the predictions made by the model. Here, we examine the sensitivity of the predictions to the choice of c_1, c_2, x_0, d_1 and d_2. To separate the influence of the round- and planar- jet-like regions, we vary the round-jet constants (c_1, c_2), round-jet virtual origin (x_0) and planar-jet constants (d_1, d_2) separately.

C.3.1 Planar-jet constants

We begin by examining the influence of the planar-jet constants d_1 and d_2, used to model the jet for $0 \leq x \leq x_{re}$, on the predictions. These constants, which describe the spreading rate d_1 and velocity decay d_2 of a planar jet, are linked through to the mean component M_{mp} of the planar-jet momentum flux M_p (Hussein et al., 1994). For the planar jet and where d_1 represents

	-5%	0%	+5%
d_1	0.128	0.116	0.105
d_2	2.29	2.41	2.53
$\frac{M_{mp}}{M_p}$	0.84	0.84	0.84

Table C.1: Values of d_1 and d_2 (see (5.40) and (5.20)) used to examine the sensitivity of the model to the planar-jet constants (see figure C.3). The value of the constant $M_{mp}/M_p = 0.84$ has been calculated using the values of d_1 and d_2 extracted from Fischer et al. (1979) (see central column above or table 5.2). The value of d_2 has been varied by $\pm$ 5% around $d_2 = 2.41$ and d_1 has been calculated from this using (C.6).

the spread of the $\bar{u}(x,r)/\bar{u}_c(x) = 1/e$ time-averaged velocity contour,

$$d_1 = \frac{M_{mp}}{M_p}\sqrt{\frac{2}{\pi}}\frac{1}{d_2^2}. \tag{C.6}$$

Given that momentum flux is conserved within isothermal jets we must vary d_1 and d_2 in such a way that M_{mp}/M_p remains constant. The value of $M_{mp}/M_p = 0.84$ has been calculated using the values of d_1 and d_2 extracted from the literature (see central column of table C.1). In figure C.3, we vary d_2 by $\pm$ 5% relative to the value given in table 5.2 and calculate d_1 from (C.6), see table C.1. The first thing we note is that the model does not converge for the -5% case. Secondly, the variation in Q_0/Q_a (also for U_a/U_0 and x_m/D_i, not shown) between the 0% and +5% cases is small, and the range of diameter ratios for which a solution exists is larger for the +5% case. Finally, increasing d_2 by 5% moves the reattachment point x_{re}/D_i significantly closer to the source. While this movement is significant, in the base model (0% case) predictions of x_{re} are inaccurate (as discussed in §5.5), and the remaining quantities of interest (Q_a, U_a, x_m) are relatively insensitive to changes in d_1 and d_2.

C.3.2 Round-jet constants

We now turn our attention to the round-jet constants, c_1 and c_2, which we have used to model the jet for $x > x_{re}$. Once again, these constants, can be used to reconstruct the mean component M_m of the jet momentum flux M_0 (Hussein et al., 1994). For the case where c_1 represents the

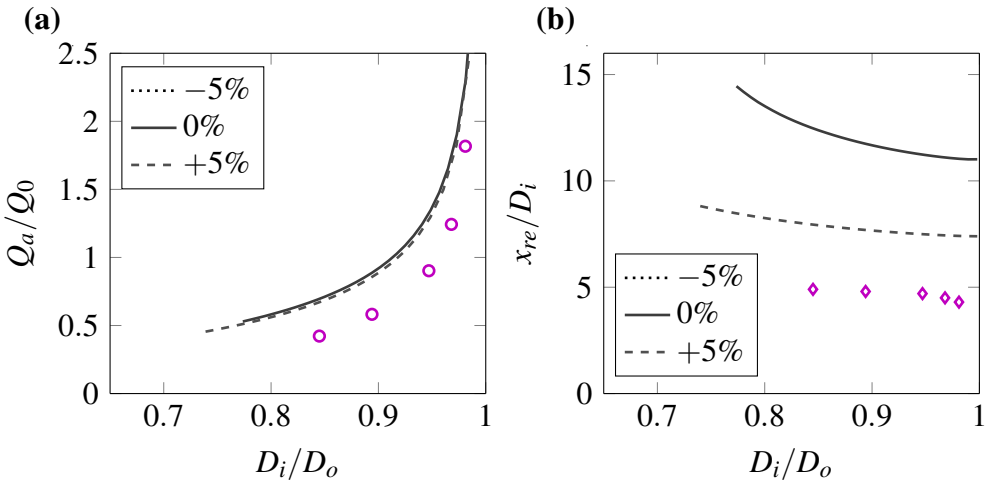

Fig. C.3: Sensitivity of the predictions to the planar-jet constants d_1 and d_2. The variation with the diameter ratio D_i/D_o of (a) the normalised induced volume flux Q_a/Q_0 and (b) the normalised position of the reattachment point x_{re}/D_i. For '·····' and '- - - -' the value of d_2 has been varied by -5% and +5%, respectively, about the base value '——'; values associated with the legend entries are given in table C.1. Note that, for the case where d_2 is varied by -5% the model does not converge and no solutions exist.

spread of the $\bar{u}(x,r)/\bar{u}(x,0) = 1/e$ time-averaged velocity contour,

$$c_1 = \sqrt{\frac{M_m}{M_0}\frac{2}{\pi}\frac{1}{c_2^2}}. \tag{C.7}$$

On examining the sensitivity of the model to the round-jet constants, we must vary c_1 and c_2 together such that M_m/M_0 remains constant. The value of $M_m/M_0 = 0.88$ has been calculated using the values of c_1 and c_2 extracted from PHJ17 (see central column of table C.2).

Figure C.4 presents the model predictions when c_2 is varied by $\pm 5\%$ and c_1 calculated using (C.7), see table C.2. The first thing to note is that the model does not converge for the $+5\%$ case. Secondly, values of Q_0/Q_a (also U_a/U_0 and x_m/D_i, not shown) are highly insensitive to changes in c_1, c_2, and the range of diameter ratios for which a solution exists is larger for the -5% case. This insensitivity is expected, the bounded induced-flow region is upstream of, and therefore has no knowledge of the flow field in the round-jet region. The prediction of the reattachment point location $x = x_{re}$, figure C.4(b), is sensitive to the round-jet constants c_1 and c_2. This sensitivity is explained by considering that, within the theoretical model, the round-jet region begins at the reattachment point.

	-5%	0%	+5%
c_1	0.107	0.102	0.097
c_2	7.13	7.50	7.88
$\frac{M_m}{M_0}$	0.92	0.92	0.92

Table C.2: Values of c_1 and c_2 (see (5.40)) used to examine the sensitivity of the model to the round-jet constants (see figure C.3). The value of the constant $M_m/M_0 = 0.88$ has been calculated using the values of c_1 and c_2 extracted from PHJ17 (see central column above or table 5.2). The value of c_2 has been varied around $c_2 = 7.00$ and c_1 has been calculated from this using (C.7).

Virtual origin

Finally, we turn our attention to the round-jet virtual origin x_0. For the slender open-core annular jet with $D_i/D_o = 0.968$ and $D_v/D_i = 0.90$, in §4 we observed the virtual origin residing at $x_0 \approx -4\sqrt{A_0}$. To examine the sensitivity of the model predictions to the round-jet virtual origin, in figure C.5 we compare the predictions made for virtual origin locations varied by $\pm 5\%$, i.e. with $x_0/\sqrt{A_0} = \{-3.8,\ -4.0,\ -4.2\}$.

Values of Q_0/Q_a shown on figure C.5(a) for the different virtual origin locations are indistinguishable from each other, indicating that the this quantity is highly insensitive to the virtual origin location x_0. An identical quantitative insensitivity is observed in the values of U_a/U_0 and x_m/D_i, although these are not presented here. Once again, this insensitivity is explained by the fact that the bounded induced-flow region is upstream of, and therefore has no knowledge of, the flow field in the round-jet region. The prediction of the reattachment point location $x = x_{re}$, figure C.5(b), is sensitive to x_0 as, within the theoretical model, the round-jet region begins at the reattachment point.

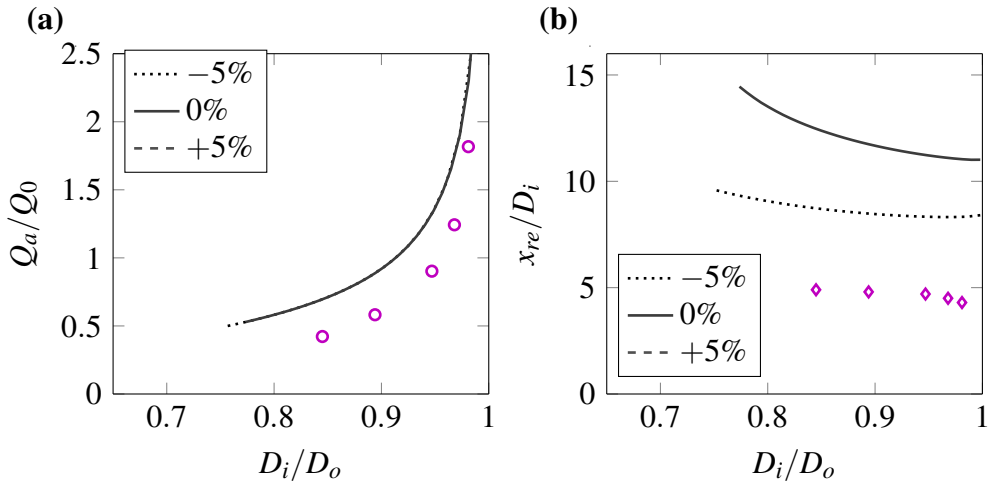

Fig. C.4: Sensitivity of the predictions to the round-jet constants c_1 and c_2. For '.....' and '- - - -' the value of c_2 has been varied by -5% and +5%, respectively, about the base value '——'; values associated with the legend entries are given in table C.2. The variation with the diameter ratio D_i/D_o of (a) the normalised induced volume flux Q_a/Q_0 and (b) the normalised position of the reattachment point x_{re}/D_i. Note that, for the case where c_2 is varied by $+5\%$ the model does not converge and no solutions exist.

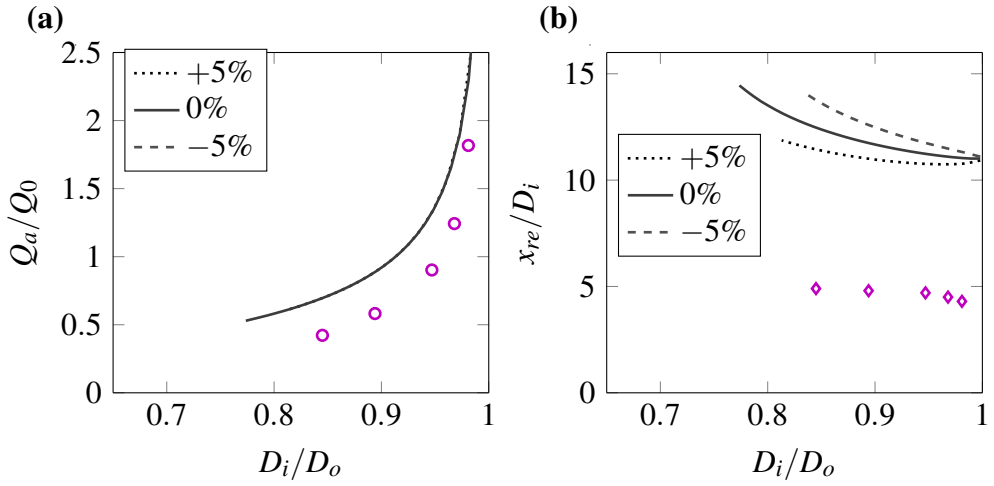

Fig. C.5: Sensitivity of the predictions to the round-jet virtual origin x_0. Predictions have been plotted for virtual origins varied by $\pm 5\%$ of the virtual origin used in the model ($x_0 = -4.0\sqrt{A_0}$), i.e. $x_0 = -3.8\sqrt{A_0}$ '- - - -', $x_0 = -4.0\sqrt{A_0}$ '——' and $x_0 = -4.2\sqrt{A_0}$ '- - - -'. The variation with the diameter ratio D_i/D_o of (a) the normalised induced volume flux Q_a/Q_0 and (b) the normalised position of the reattachment point x_{re}/D_i.